UC Santa Cruz

UC Santa Cruz Electronic Theses and Dissertations

Title

Iron, Manganese and Ruthenium Metal Carbonyls as Photoactive Carbon Monoxide Releasing Molecules (photoCORMS): Ligand Design Strategies, Syntheses and Structure Characterizations

Permalink

https://escholarship.org/uc/item/20s1v5xk

Author

Gonzales, Margarita Andal

Publication Date

2013

Peer reviewed|Thesis/dissertation

eScholarship.org Powered by the California Digital Library
University of California

UNIVERSITY OF CALIFORNIA
SANTA CRUZ

IRON, MANGANESE AND RUTHENIUM METAL CARBONYLS AS PHOTOACTIVE CARBON MONOXIDE RELEASING MOLECULES (PHOTOCORMS): LIGAND DESIGN STRATEGIES, SYNTHESES AND STRUCTURE CHARACTERIZATIONS

A dissertation submitted in partial satisfaction
of the requirements for the degree of

DOCTOR OF PHILOSOPHY

in

CHEMISTRY

by

Margarita A. Gonzales

June 2013

The dissertation of Margarita A. Gonzales is approved:

_____
Professor Scott R. J. Oliver, Chair

_____
Professor Pradip K. Mascharak, Advisor

_____
Professor Glenn L. Millhauser

_____
Tyrus Miller
Vice Provost and Dean of Graduate Studies

Copyright © by:

Margarita A. Gonzales

2013

Table of Contents

Outline of Contents…….. iii

List of Figures…….....viii

Abstract…….....xvii

Acknowledgments……..... .xix

Dedication…….... xxi

Chapter 1. Introduction.....1

1.1. Endogenous Carbon Monoxide (CO) Production from Heme Oxygenase (HO) Activities.....1

1.2. CO-Mediated Vasorelaxation.....5

1.3 CO Signaling.....10

1.4 Utility of Exogenously Applied CO.....12

1.5. Metal Carbonyls as Carbon Monoxide Releasing Molecules (CORMs)....15

1.6. Direction of Research.....27

Chapter 2. Solvent-assisted CO release from Iron Carbonyls Bearing Structurally-Related Pentadentate Ligand Frames.....36

2.1. Background.....36

2.2. Syntheses and X-ray Structures of the Metal Complexes.....40

2.3. Comparison of the Properties of Fe(II) carbonyls bearing Structurally-Related Pentadentate Ligand Frames.....42

2.3.1. IR Spectroscopy

2.3.2. Electronic Absorption Spectra and CO-release in Solution

2.3.3. Delivery of CO to horse heart myoglobin

2.3.4. Kinetic Measurements

2.3.5. Vasorelaxation of mouse aorta

2.4. Experimental Section.....52

2.5. Additional Experimental Data: IR Spectra.....58

2.6. References.....59

2.7 Reprint of Publication.....62

Chapter 3. Photoactive d^6 Metal Carbonyl Complexes Bearing Designed Tridentate Ligand Frames.....71

Part I: Photoactive Manganese Carbonyl Complexes bearing Structurally-related Tripodal Ligand Frames: Investigation of Conjugation Effects on CO Photorelease.....71

3.I.1 Introduction.....71

3.I.2. Syntheses of the Metal Complexes.....75

3.I.2.1. Mn(I) terpyridine carbonyl complexes

3.I.2.2. Mn carbonyls bearing tripodal ligand frames

3.I.3. Characterization of the Photoactive Mn Complexes.....79

3.I.3.1. X-ray Structures of $[Mn(tpa)(CO)_3]ClO_4$ and $[Mn(dpa)(CO)_3]Br$

3.I.3.2. Electronic Absorption Spectra and CO Release in Solution

3.I.3.3. EPR Spectra

3.I.3.4. CO delivery to Myoglobin

3.I.3.5. Kinetic and Quantum Yield Measurements

3.I.3.6. Vasorelaxation of Mouse Aorta

3.I.4. Experimental Section.....93

3.I.5. Additional Experimental Data: IR, ^{1}H NMR and Electronic Absorption Spectra.....99

3.I.6. References.....103

3.I.7. Reprint of Publication.....106

Part II: Ruthenium Carbonyls of the Tridentate NNS ligand qmtpm: Investigation of Auxiliary Ligand Effects on CO Photorelease.....115

3.II.1. Background.....115

3.II.2. Syntheses of the Metal Complexes.....118

3.II.2.1 Characterization of $[Ru(Cl)_2(qmtpm)(PPh_3)]$

3.II.2.2 Characterization of $[Ru(Cl)(CO)(qmtpm)(PPh_3)]BF_4$

3.II.2.3. Characterization of $[Ru(Cl)_2(CO)_2(qmtpm)]ClO_4$

3.II.2.4. Characterization of $[Ru(Cl)(MeCN)(qmtpm)(PPh_3)]BF_4$

3.II.2.5. Characterization of $[Ru(MeCN)_2(qmtpm)(PPh_3)]ClO_4$

3.II.3. Spectroscopic Properties of Ru(II) qmtpm complexes.....125

3.II.3.1. ^{1}H NMR Spectra

3.II.3.2. Electronic Absorption Spectra

3.II.3.3. CO Photorelease in Solution

3.II.4. Conclusions.....132

3.II.5. Experimental Section.....133

3.II.6. Experimental Data: IR, ^{1}H NMR, Electronic Absorption Spectra..137

3.II.7. References.....143

Chapter 4. Density Functional Theory Studies to elucidate origin of CO Photolability in d^{6} Metal Carbonyls bearing the tridentate NNS ligand qmtpm.....145

Part I: DFT and TDDFT Studies of Manganese qmtpm Carbonyl Complexes.....145

4.I.1. Background.....145

4.I.2. Syntheses of the Metal Complexes.....149

4.I.3. Spectroscopic Properties.....151

4.I.4. Structures of the Metal Complexes.....152

4.I.5. Electronic Absorption Spectra and CO Release in Solution.....155

4.I.6. DFT and TDDFT Calculations.....162

4.I.7. Experimental Section.....170

4.I.8. Experimental Data: ^{1}H NMR and IR Spectra.....176

4.I.9. References.....183

4.I.10. Reprint of Publication.....185

Part II: DFT and TDDFT Studies of Ruthenium qmtpm Carbonyl Complexes....197

4.II.1. Background.....197

4.II.2. Geometry Optimizations and Electronic Structure of the Complexes....201

4.II.3. TDDFT calculation and electronic spectra.....207

4.II.4 Conclusions.....213

4.II.5. Computational Methods.....214

4.II.6. Experimental Data: TDDFT Calculated and Experimental Electronic Absorption Spectra.....216

4.II.7. References.....218

Appendix A. Cell Protection Assay Utilizing $[Mn(pqa)(CO)_3]ClO_4$.....219

A.1. Background.....219

A.2. Findings.....219

A.3. Experimental Section.....221

A.4. Experimental Data: Cell Viability Measurements.....224

A.5. References.....226

Appendix B. PhotoCORM Entrapment within an Aluminosilicate Mesoporous Material.....227

B.1. Background.....227

B.2. Findings.....228

B.3. Experimental Section.....232

B.4. References.....236

List of Figures

Chapter 1

Figure 1.1. Sources of endogenously produced CO in mammalian systems

Figure 1.2. Stepwise heme degradation catalyzed by heme oxygenases

Figure 1.3. NO and CO ligands bound to the distal face of heme in cyanobacterial H-NOX

Figure 1.4. Schematic diagram of NO vs. CO-dependent activation of sGC

Figure 1.5. Big conductance calcium activated potassium channels (BK_{Ca}) illustrating the α and β subunits

Figure 1.6. Carbon monoxide signal transduction pathways

Figure 1.7. Effect of exogenous CO gas on mouse-to-rat cardiac transplants

Figure 1.8. Qualitative MO diagram of $Cr(CO)_6$ to illustrate high energy ligand field (LF) excitation and the associated metal-CO bond homolysis

Figure 1.9. The UV/Vis spectrum of $Cr(CO)_6$ in a mixture of ether, pentane and ethanol (EPA) at 298 K and 77K

Figure 1.10. Homoleptic metal carbonyls representing prototypical CORMs

Figure 1.11. Examples of CORMs bearing amino acids and biocompatible groups

Figure 1.12. Fe(II) carbonyl complexes bearing structurally-related pentadentate ligand frames

Figure 1.13. Examples of tripodal ligands utilized in the preparation of *fac*-Mn(I) tricarbonyl complexes as photoCORMs

Figure 1.14. Proposed mechanism for CO release by *fac*-Mn(I) tricarbonyl complexes

Figure 1.15. Miscellaneous photoCORMs

Chapter 2

Figure 2.1. Structures of the designed pentadentate ligands, $PaPy_3H$, $SBPy_3$ and Tpmen, used in this study

Figure 2.2. ORTEP diagram (30% probability level) of the cation of $[(SBPy_3)Fe(CO)](BF_4)_2$

Figure 2.3. Comparison of metric parameters and axial coordination of $[(PaPy_3)Fe(CO)]^+$ and $[(SBPy_3)Fe(CO)]^{2+}$

Figure 2.4. Preliminary structure of the cation of $[(Tpmen)Fe(CO)](ClO_4)_2$

Figure 2.5. Changes in the electronic absorption spectrum of $[(SBPy_3)Fe(CO)](BF_4)_2$ (3.5 mM) upon dissolution (100 mM PBS, pH 7.4)

Figure 2.6. Delivery of CO from $[(Tpmen)Fe(CO)](ClO_4)_2$ to reduced Mb (λ_{max} = 435 nm), resulting in Mb-CO adduct (λ_{max} = 424 nm) in PBS pH 7.4

Figure 2.7. Plot of changes in $\ln([(SBPy_3)Fe(CO)]^{2+})$ vs time in 0.1 M PBS, pH 7.4 as monitored by noting the absorbance values at 450 nm

Figure 2.8. Vasorelaxation of mouse aorta muscle ring using $[(SBPy_3)Fe(CO)](BF_4)_2$ and $[(Tpmen)Fe(CO)](ClO_4)_2$ as a function of concentration

Figure 2.9. Vasorelaxation of mouse aorta muscle rings by $[(SBPy_3)Fe(CO)](BF_4)_2$ and $[(Tpmen)Fe(CO)](ClO_4)_2$ in the absence and presence of ODQ (5 μM)

Figure 2.10. Inhibition of vasorelaxation in the presence of Iberiotoxin using $[(Tpmen)Fe(CO)](ClO_4)_2$ as a CO-donor

Figure 2.11. Effect of Glibenclamide and TEA on $[(Tpmen)Fe(CO)](ClO_4)_2$ – induced vasorelaxation of mouse aortic rings

Figure 2.12. IR Spectrum of $[(SBPy_3)Fe(CO)](BF_4)_2$ in KBr pellet

Figure 2.13. IR Spectrum of $[(Tpmen)Fe(CO)](BF_4)_2$ in KBr pellet

Chapter 3, Part I

Figure 3.I.1. Examples of *fac*- Mn(I) tricarbonyl complexes bearing tripodal ligand frames as photoCORMs

Figure 3.I.2. Structures of the tridentate ligands, terpy, tpa, dpa and pqa utilized in this study

Figure 3.I.3. Absorption spectrum of *mer,cis*-[Re(terpy)$(CO)_2$Cl] in CH_3CN, CH_2Cl_2 and H_2O. Inset shows the region between 350 – 900 nm

Figure 3.I.4. ^{1}H NMR (500 MHz) spectrum of [Mn(pqa)$(CO)_3$]ClO_4 in CD_3CN (3.5- 9.5 ppm range)

Figure 3.I.5. ORTEP diagram (50% probability level) of the cation of [Mn(tpa)$(CO)_3$]ClO_4 with select atom labeling

Figure 3.I.6. ORTEP diagram (50% probability level) of the cation of [Mn(dpa)$(CO)_3$]Br with select atom labeling

Figure 3.I.7. Electronic absorption spectra of [Mn(tpa)$(CO)_3$]ClO_4, [Mn(dpa)$(CO)_3$]Br and [Mn(tpa)$(CO)_3$]ClO_4 in MeCN

Figure 3.I.8. Changes in the electronic absorption spectrum of [Mn(tpa)$(CO)_3$]ClO_4 in MeCN (concentration = 0.07 mM) upon exposure to light ($\lambda > 350$ nm)

Figure 3.I.9. X-band EPR spectrum of $[Mn(pqa)_2]^{2+}$ in frozen DMF/toluene glass (110K). Instrument settings: microwave frequency, 9.443 GHz; power, 31.7 mW; modulation, 100kHz; modulation amplitude, 2G

Figure 3.I.10. Conversion of reduced-Mb to Mb-CO in a mixture of [Mn(dpa)$(CO)_3$]Br and reduced Mb in 100 mM phosphate buffer (pH 7.4) upon exposure to light ($\lambda > 350$ nm)

Figure 3.I.11. Plot of changes in ln ($[Mn(pqa)(CO)_3]^+$) versus time (s) in MeCN upon exposure to visible (($\lambda > 350$ nm, 120 mW) light (concentration = 0.13 mM)

Figure 3.I.12. Vasorelaxation of mouse aorta muscle rings by [Mn(pqa)$(CO)_3$]ClO_4 upon exposure to visible (cold) light and ambient room light

Figure 3.I.13. Vasorelaxation of mouse aorta muscle rings by $[Mn(dpa)(CO)_3]Br$ (top panel) and $[Mn(tpa)(CO)_3]ClO_4$ (bottom panel) upon exposure to visible (cold) light and ambient room light

Figure 3.I.14. IR spectrum of $[Mn(terpy)(CO)_2Br]$ in KBr pellet

Figure 3.I.15. Electronic absorption spectrum of $[Mn(terpy)(CO)_2Br]$ in MeCN (λ_{max} = 730 nm)

Figure 3.I.16. IR spectrum of $[Mn(tpa)(CO)_3]ClO_4$ in KBr disk

Figure 3.I.17. IR spectrum of $[Mn(dpa)(CO)_3]Br$ in KBr disk

Figure 3.I.18. IR spectrum of $[Mn(pqa)(CO)_3]ClO_4$ in KBr disk

Figure 3.I.19. ^1H NMR Spectrum of $[Mn(tpa)(CO)_3]ClO_4$ in CD_3CN

Figure 3.I.20. ^1H NMR Spectrum of $[Mn(tpa)(CO)_3]ClO_4$ in CD_3CN

Figure 3.I.21. Electronic absorption spectrum of $[Mn(dpa)(CO)_3]Br$ in MeCN (λ_{max} = 350 nm); Inset: Electronic absorption spectrum of $[Mn(dpa)_2]^{2+}$ in MeCN

Chapter 3, Part II

Figure 3.II.1. Structures of the qmtpm ligand and the corresponding *fac*-Mn(I) tricarbonyl complexes, $[Mn(qmtpm)(CO)_3Br]$ and $[Mn(qmtpm)(CO)_3(MeCN)]ClO_4$

Figure 3.II.2. ORTEP diagram (50% probability level) of the cation of $[Ru(Cl)(CO)(qmtpm)(PPh_3)]BF_4$

Figure 3.II.3. ORTEP diagram (50% probability level) of the cation of $[Ru(Cl)(CO)_2(qmtpm)]ClO_4$

Figure 3.II.4. ORTEP diagram (50% probability level) of the cation of $[Ru(MeCN)_2(qmtpm)(PPh_3)]ClO_4$

Figure 3.II.5. ^1H NMR Spectrum of $[Ru(Cl)(CO)_2(qmtpm)]ClO_4$ in CD_3CN

Figure 3.II.6. Electronic absorption spectra of $[Ru(Cl)(CO)(qmtpm)(PPh_3)]BF_4$, $[Ru(Cl)(MeCN)(qmtpm)(PPh_3)]BF_4$, and $[Ru(MeCN)_2(qmtpm)(PPh_3)]ClO_4$ in acetonitrile

Figure 3.II.7. Electronic Absorption Spectrum of $[Ru(Cl)(CO)_2(qmtpm)]ClO_4$ in acetonitrile

Figure 3.II.8. Changes in the electronic absorption spectrum of $[Ru(Cl)(CO)(qmtpm)(PPh_3)]BF_4$ (0.25 mM) in acetonitrile with UV light irradiation (power = 5-10 mW/cm^2 ; λ = 310 nm)

Figure 3.II.9. Changes in the electronic absorption spectrum of $[Ru(Cl)(CO)_2(qmtpm)]ClO_4$ (0.25 mM) in acetonitrile with UV light irradiation (power = 5-10 mW/cm^2 ; λ = 310 nm)

Figure 3.II.10. ^1H NMR Spectrum of (1.50-8.75 ppm) of qmtpm in CD_3CN

Figure 3.II.11. IR Spectrum of $[Ru(Cl)_2(qmtpm)(PPh_3)]$ in KBr disk

Figure 3.II.12. Electronic Absorption Spectrum of $[Ru(Cl)_2(qmtpm)(PPh_3)]$ in CH_2Cl_2

Figure 3.II.13. ^1H NMR Spectrum (6.50-10.50 ppm) of $[Ru(Cl)_2(qmtpm)(PPh_3)]$ in $CDCl_3$. Inset: Thioether resonance at 3.11 ppm

Figure 3.II.14. Electronic Absorption Spectrum of $[Ru(Cl)(MeCN)(qmtpm)(PPh_3)]BF_4$ in CH_3CN

Figure 3.II.15. IR Spectrum of $[Ru(Cl)(CO)(qmtpm)(PPh_3)]BF_4$ in KBr disk

Figure 3.II.16. Electronic Absorption Spectrum of $[Ru(Cl)(CO)(qmtpm)(PPh_3)]BF_4$ in CH_2Cl_2

Figure 3.II.17. ^1H NMR Spectrum (7.00-9.90 ppm) of $[Ru(Cl)(CO)(qmtpm)(PPh_3)]BF_4$ in $CDCl_3$. Inset: Thioether resonance at 3.08 ppm

Figure 3.II.18. IR Spectrum of $[Ru(MeCN)_2(qmtpm)(PPh_3)]ClO_4$ in KBr disk

Figure 3.II.19. Electronic Absorption Spectrum of $[Ru(MeCN)_2(qmtpm)(PPh_3)]ClO_4$ in CH_3CN

Figure 3.II.20. ^1H NMR Spectrum (7.00-9.60 ppm) of $[Ru(MeCN)_2(qmtpm)(PPh_3)]ClO_4$ in $CDCl_3$. Inset: Thioether resonance at 2.90 ppm and an additional singlet noted at 2.69 is due to the bound acetonitrile ligands

Figure 3.II.21. IR Spectrum of $[Ru(Cl)(CO)_2(qmtpm)]ClO_4$ in KBr disk

Chapter 4, Part I

Figure 4.I.1. Manganese-based CORMs bearing thiolate and bipyridine ligands

Figure 4.I.2. Structures of the bidentate (pimq) and potentially tridentate ligands (pmtpm and qmtpm) used in this study

Figure 4.I.3. ^{1}H NMR (500 MHz) spectrum of $[Mn(qmtpm)(CO)_3(MeCN)]ClO_4$ in CD_3CN (7.40-9.40 ppm range). Inset: Resonance Signal of unbound -SMe group at 2.56 ppm

Figure 4.I.4. ORTEP diagram (50% probability level) of the cation of $[Mn(pimq)(CO)_3(MeCN)]ClO_4$.

Figure 4.I.5. ORTEP diagram (50% probability level) of the cation of $[Mn(qmtpm)(CO)_3(MeCN)]ClO_4$

Figure 4.I.6. ORTEP diagram (50% probability level) of the cation of $[Mn(pmtpm)(CO)_3(MeCN)]ClO_4$

Figure 4.I.7. ORTEP diagram (50% probability level) of $[Mn(qmtpm)(CO)_3Br]$

Figure 4.I.8. ORTEP diagram (50% probability level) of $[Mn(pmtpm)(CO)_3Br]$

Figure 4.I.9. Electronic absorption spectra of $[Mn(qmtpm)(CO)_3(MeCN)]ClO_4$, $[Mn(qmtpm)(CO)_3Br]$, $[Mn(pmtpm)(CO)_3(MeCN)]ClO_4$, and $[Mn(pmtpm)(CO)_3Br]$ in $CHCl_3$

Figure 4.1.10. Electronic absorption spectra of $[Mn(pimq)(CO)_3(MeCN)]ClO_4$ and $[Mn(qmtpm)(CO)_3(MeCN)]ClO_4$ in MeCN

Figure 4.I.11. Changes in the electronic absorption spectrum of $[Mn(qmtpm)(CO)_3(MeCN)]ClO_4$ in MeCN upon exposure to monochromatic light (λ= 509 nm, 5mW). Inset: Formation of CO-Mb with light induced CO release from $[Mn(qmtpm)(CO)_3(MeCN)]ClO_4$ in 100 mM phosphate buffer (pH 7.4)

Figure 4.I.12. Plot of changes in $\ln[Mn(qmtpm)(CO)_3Br]$ vs. time in THF

Figure 4.I.13. Calculated HOMO/LUMO energy diagram of complexes $[Mn(pimq)(CO)_3(MeCN)]ClO_4$, $[Mn(pmtpm)(CO)_3Br]$, $[Mn(qmtpm)(CO)_3Br]$, and $[Mn(qmtpm)(CO)_3(MeCN)]ClO_4$ (from left to right).

Figure 4.I.14. ^{1}H NMR Spectrum of (6.50-8.90 ppm) of pimq in CD_3CN

Figure 4.I.15. ^{1}H NMR Spectrum of (1.50-9.00 ppm) of $[Mn(pimq)(CO)_3(MeCN)]ClO_4$ in CD_3CN

Figure 4.I.16. IR Spectrum of $[Mn(pimq)(CO)_3(MeCN)]ClO_4$ in KBr pellet

Figure 4.I.17. ^{1}H NMR Spectrum of (1.90-8.90 ppm) of pmtpm in CD_3CN

Figure 4.I.18. ^{1}H NMR Spectrum of (1.50-9.75 ppm) of $[Mn(pmtpm)(CO)_3(MeCN)]ClO_4$ in CD_3CN

Figure 4.I.19. IR Spectrum of $[Mn(pmtpm)(CO)_3(MeCN)]ClO_4$ in KBr pellet

Figure 4.I.20. ^{1}H NMR Spectrum of (2.00-9.50 ppm) of $[Mn(pmtpm)(CO)_3Br]$ in CD_3CN

Figure 4.I.21. IR Spectrum of of $[Mn(pmtpm)(CO)_3Br]$ in KBr pellet

Figure 4.I.22. ^{1}H NMR Spectrum of (1.50-8.75 ppm) of qmtpm in CD_3CN

Figure 4.I.23. ^{1}H NMR Spectrum of (1.50-9.00 ppm) of $[Mn(qmtpm)(CO)_3(MeCN)]ClO_4$ in CD_3CN

Figure 4.I.24. IR Spectrum of $[Mn(qmtpm)(CO)_3(MeCN)]ClO_4$ in KBr pellet

Figure 4.I.25. IR Spectrum of of $[Mn(qmtpm)(CO)_3Br]$ in KBr pellet

Chapter 4, Part II

Figure 4.II.1. Structures of $[Ru(Cl)(CO)(qmtpm)(PPh_3)]BF_4$, $[Ru(Cl)(CO)_2(qmtpm)]ClO_4$, $[Ru(Cl)(MeCN)(qmtpm)(PPh_3)]BF_4$ and $[Ru(MeCN)_2(qmtpm)(PPh_3)]ClO_4$ utilized in DFT and TDDFT studies

Figure 4.II.2. Contour plots of selected molecular orbitals of $[Ru(Cl)(CO)(qmtpm)(PPh_3)]BF_4$

Figure 4.II.3. Contour plots of selected molecular orbitals of $[Ru(Cl)(CO)_2(qmtpm)]ClO_4$

Figure 4.II.4. Contour plots of selected molecular orbitals of

[Ru(Cl)(MeCN)(qmtpm)(PPh_3)]BF_4

Figure 4.II.5. Contour plots of selected molecular orbitals of [Ru($MeCN)_2$(qmtpm)(PPh_3)]ClO_4

Figure 4.II.6. Calculated HOMO/LUMO energy diagram of [Ru(Cl)(CO)(qmtpm)(PPh_3)]BF_4, [Ru(Cl)(MeCN)(qmtpm)(PPh_3)]BF_4 and [Ru($MeCN)_2$(qmtpm)(PPh_3)]ClO_4

Figure 4.II.7. Calculated HOMO/LUMO energy diagram of [Ru(Cl)(CO)(qmtpm)(PPh_3)]BF_4 and [Ru(Cl)$(CO)_2$(qmtpm)]ClO_4

Figure 4.II.8. TDDFT calculated (dashed line) and experimental (solid line) electronic absorption spectrum of [Ru(Cl)(CO)(qmtpm)(PPh_3)]BF_4

Figure 4.II.9. TDDFT calculated (dashed line) and experimental (solid line) electronic absorption spectrum of [Ru(Cl)$(CO)_2$(qmtpm)]ClO_4

Figure 4.II.10. TDDFT calculated (dashed line) and experimental (solid line) electronic absorption spectrum of [Ru(Cl)(MeCN)(qmtpm)(PPh_3)]ClO_4

Figure 4.II.11. TDDFT calculated (dashed line) and experimental (solid line) electronic absorption spectrum of [Ru($MeCN)_2$(qmtpm)(PPh_3)]ClO_4

Appendix A.

Figure A.1. Cell viability of HEK-293T cells after a 4 h exposure to H_2O_2 at 37°C in a humidified atmosphere of 5% CO_2

Figure A.2. Effects of [Mn(pqa)$(CO)_3$]ClO_4 incubation on HEK-293T cells in the absence of light

Figure A.3. Cell viability of [Mn(pqa)$(CO)_3$]ClO_4- preconditioned HEK-293T cells after addition of 200 μM H_2O_2

Figure A.4. Cell viability of [Mn(pqa)$(CO)_3$]ClO_4- preconditioned HEK-293T cells after addition of 500 μM H_2O_2

Appendix B.

Figure B.1. FTIR spectra of Al-MCM-41 (black dashed) and loaded (black solid) {Mn-CO}@Al-MCM-41 in KBR Matrix

Figure B.2. Plot of leaching experiment showing the amount of $[Mn(pqa)(CO)_3]ClO_4$ loss from the Al-MCM-41 matrix

Figure B.3. Changes in Q-band region of horse heart myoglobin (Mb) (PBS, pH 7.4, 100 mM) upon addition of {Mn-CO}@Al-MCM-41 and subsequent irradiation (λ >350 nm)

Figure B.4. Influence of different Al-MCM-41 concentrations on the HeLa cell viability after a 6 h incubation period

Figure B.5. Influence of different {Mn-CO}@Al-MCM-41 concentrations on the HeLa cell viability after a 6 h incubation period

Abstract

IRON, MANGANESE AND RUTHENIUM METAL CARBONYLS AS PHOTOACTIVE CARBON MONOXIDE RELEASING MOLECULES (PHOTOCORMS): LIGAND DESIGN STRATEGIES, SYNTHESES AND STRUCTURE CHARACTERIZATIONS

Margarita A. Gonzales

Recent investigations on the protective aspects of carbon monoxide (CO) have renewed interest in the design and syntheses of a new generation of metal carbonyl complexes as tunable CO-delivery systems. The inherent photosensitivity of transition metal carbonyls has made photochemical metal–CO bond labilization the most promising approach towards controlled CO-delivery to biological targets. This thesis details the design strategies employed in the preparation of photoactive carbon monoxide releasing molecules (photoCORMs) for use as CO donors in physiologically relevant settings. The Introduction (Chapter 1) examines the origins of CO photodissociation in metal carbonyl complexes and describes some photoCORMs known to date.

As an initial step detailed in Chapter 2, we explored whether the design principles we established in the isolation of photolabile metal nitrosyls can be extended to the generation of photoCORMs. We utilized structurally related pentadentate ligand frames in the syntheses of Fe(II)-based carbon monoxide releasing molecules that undergo solvent-assisted CO release under physiologically-relevant conditions.

Chapter 3 covers our research on photoCORMs bearing tridentate ligand frames. The first section focuses on the effects of increasing conjugation and/or number of pyridine donors on a series of *fac*-Mn(I) carbonyl complexes bearing tripodal polypyridine ligands. The resulting UV-active photoCORMs have demonstrated a capacity to function as light-activated vasorelaxing agents. The second section of chapter 3 discusses the synthetic routes towards the preparation of Ru(II) carbonyl complexes of a conjugated ligand frame featuring an NNS donor set. The effect of both σ-donating and π-accepting groups on the photosensitivity of the corresponding Ru(II) compounds are highlighted.

Chapter 4 is centered on the use of density functional theory (DFT) and time-dependent DFT as tools in identifying the ligand design parameters that lead to the observed CO photorelease by some d^6 metal carbonyl complexes. The contributions of auxiliary groups and conjugated moieties to CO photolability are rationalized in terms of their capacity to promote metal to ligand charge transfer processes.

Acknowledgments

First and foremost, I would like to thank my research advisor, Prof. Pradip Mascharak, whose guidance and mentorship made the completion of the projects and publications described herein possible. I had minimal undergraduate research experience, let alone knowledge of organometallic and air-free techniques. But Pradip certainly took the time and effort to train and familiarize me with the intricacies of research and the art of scientific writing. With his supervision, I have come to realize that every reaction in the lab teaches you something and that even unexpected results (i.e. unwanted spectra) can bring you closer to a scholarly outcome.

I would like to thank the rest of my committee members, Prof. Scott Oliver and Prof. Glenn Millhauser, for their guidance and feedback. I appreciate their taking the time to be there for my second year seminar, qualifying exam and other meetings to ensure that I am making progress.

I am especially grateful to those who have helped me obtain crystal structures of my compounds: Dr. Honghan Fei, Dr. Dave Rogow, Dr. Indranil Chakraborty and Prof. Marilyn Olmstead. With their expertise, I have come to appreciate crystal structure solving and solid state characterizations.

I would like to thank those who have helped me get started with the cell work, Walter Bray and Dr. Fernando Postalli-Rodrigues. With their supervision, I now have a good handle on the techniques necessary in cell proliferation and treatment.

I would like to thank past members of the Mascharak lab. Dr. Mike Rose and Dr. Genevieve Halpenny both helped me hit the ground running in terms of getting a

project initiated and taught me a lot about synthetic techniques. Dr. Nicole Fry has been my go-to person for anything project-related such as manuscript submission; crystallization techniques and most importantly, she got me familiarized with DFT and TDDFT analysis. I would like to acknowledge current lab members, Brandon Heilman, Tara deBoer and Sam Carrington (and our newer member Jorge). I know I am quite fortunate to have a group that fosters curiosity, hard work and an overall appreciation of science. I am especially thankful for Sam, who provided the needed expertise in the completion of some DFT-related work. I must also thank my reliable undergraduates: Melanie Yim, Joshua Alvarado and Jose Martinez. Their eagerness and enthusiasm kept me going even on those days when I didn't feel like trying another reaction.

And lastly, I am ever grateful for my family- my parents Mat and Sonia Gonzales and my brother Tom, for their unconditional love and support. They have always recognized my potential and it is their faith in me that kept me going in graduate school. I would not have been able to finish what I started if it wasn't for them.

Dedication

I would like to dedicate this thesis to my parents, Mat and Sonia Gonzales, who have always believed in me and supported me in countless ways. I am well aware of the sacrifices you've made in making sure that we finish college and thus gain access to better career opportunities. Starting over in a new country is not an easy process, but your courage and persistence certainly made it seem so. These are the kinds of values that inspired me to take on new challenges and to maintain progress in graduate school. Papa, your enthusiasm for science and desire to tinker with everyday gadgets helped me see the world as anything but ordinary. Mom, your unending encouragement allowed me to recognize my own accomplishments and gain perspective- especially when I am being my own worst critic. The completion of this thesis would not have been possible if it wasn't for your support and love. Thank you and I love you both.

Chapter 1. Introduction

1. Background

During the past three decades, three small "toxic" molecules namely nitric oxide (NO), carbon monoxide (CO) and hydrogen sulfide (H_2S) have drawn much attention due to their surprising and unexpected roles in numerous physiological processes.[1] Investigations on the biological relevance of CO and H_2S are quite premature when compared that of the radical species NO, which has served as the pioneer in the area of "biologically relevant gases". What once was viewed as an environmental pollutant, NO has now been shown to participate in a myriad of physiological and pathological processes including vasodilation,[2] neurotransmission,[3] immune response[4] and cellular apoptosis.[5] Among this series of gasotransmitters, NO and CO possess the greatest number of similarities – both molecules are ubiquitous ligands in coordination chemistry and are known to interact with metalloproteins, particularly those bearing heme moieties.[6] Consequently, the biological significance and therapeutic potential of CO is emerging at a faster rate in recent years.[7a-d]

1.1 Endogenous CO production from Heme Oxygenase (HO) Activities

With its reputation as a toxin, it is ironic that CO is present in the human body- with levels reaching about 500 μmol/day.[8] Some sources of endogenously produced CO include iron-catalyzed lipid peroxidation[9] and self-inactivation of cytochrome P-450.[10] The majority of CO generated in mammalian systems however, is derived from oxygenases, which exists as two isoforms, inducible (HO-1) and constitutive (HO-2).

1.1.1. Heme Oxygenase and its Isoforms

While both HO-1 and HO-2 catalyze the same rate-limiting step in heme catabolism, these isoforms differ slightly in amino acid sequence, regulation and tissue distribution. As outcome of separate gene expression pathways, human HO-1 and HO-2 share only 45% identical residues in their respective sequences.[11,12] As a result CO levels in the human body are organ and tissue-dependent due to the differential localization of these two different isoforms.

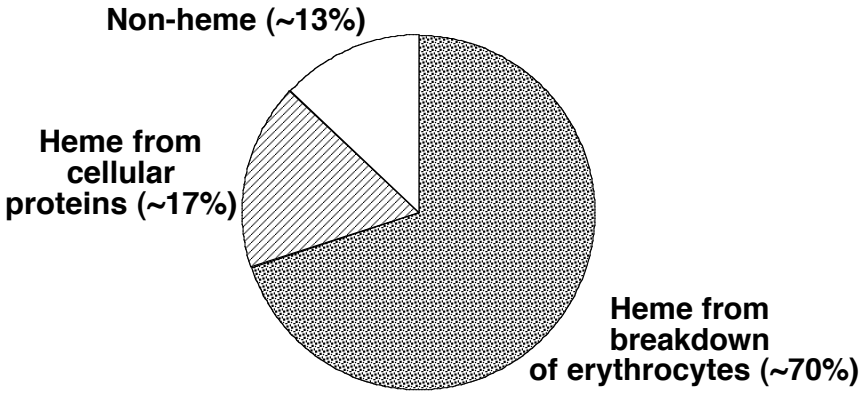

Figure 1.1. Sources of endogenously produced CO in mammalian systems.

Also known as the heat shock protein HSP 32, human HO-1 consists of 288 residues and is found mostly in the spleen and liver, where degradation of senescent erythrocytes occurs.[12] In organs such as the lungs and kidneys that are not primarily facilitating metabolic heme breakdown, increased HO-1 expression has been noted in response to variety of chemical and environmental stresses such as ultraviolet radiation, heavy metals, xenobiotics, reactive oxygen species (ROS)- even heme.[13] In the liver for instance where much of the detoxification processes takes place, HO-1

upregulation has been linked with the production of anti-inflammatory cytokines in both human and rat models of sepsis.[14a] Other pathological conditions that contribute to increased HO-1 expression include atherosclerosis, acute lung injury and renal failure.[14b-d] Mice that are deficient in the HO-1 gene were found to be more susceptible to lipopolysaccharide (LPS) induced endotoxic shock[15a] and exhibit reduced stress defense mechanisms against oxidative damage.[15b] The first reported case of a human HO-1 deficiency was that of a six year old boy exhibiting severe growth retardation and complications relating to vascular function not limited to abnormal coagulation, anemia and erythrocyte fragmentation.[16] The diversity of HO-1 inducing factors suggests the central role of the HO system in anti-inflammatory and immune response. Although no single unifying pathway could be delineated that would account for HO-1 upregulation, it has been determined that an efficient HO-1 system is required to combat a myriad of diseases and to ensure adequate growth. Not surprisingly, the HO-1 system and its by-products, namely CO, have been unambiguously associated with protective functions in mammalian systems.

In addition to the immune response modulated by the HO-1, the second isoform of heme oxygenases, HO-2 serves to maintain regulatory functions in the central nervous system. Primarily expressed in the brain, testes and cerebral vascular systems, HO-2 was only identified when elevated heme oxygenase activity in these organs were noted in the absence of various chemical and environmental stimuli. This constitutive form has been found to modulate cerebral blood flow and promote survival in the event of seizures and hypoxia. Unlike HO-1, which is triggered non-

specifically by external stimuli, HO-2 serves as a primary regulator of cerebral function- maintaining homeostasis and ensuring neuronal survival.[17]

Taken together, these HO isoforms contribute to the observed CO levels in the body. Much like the established signaling molecule NO, CO appears to have been known to catalyze the first and rate-limiting step in heme breakdown, making the endogenous production of CO possible.

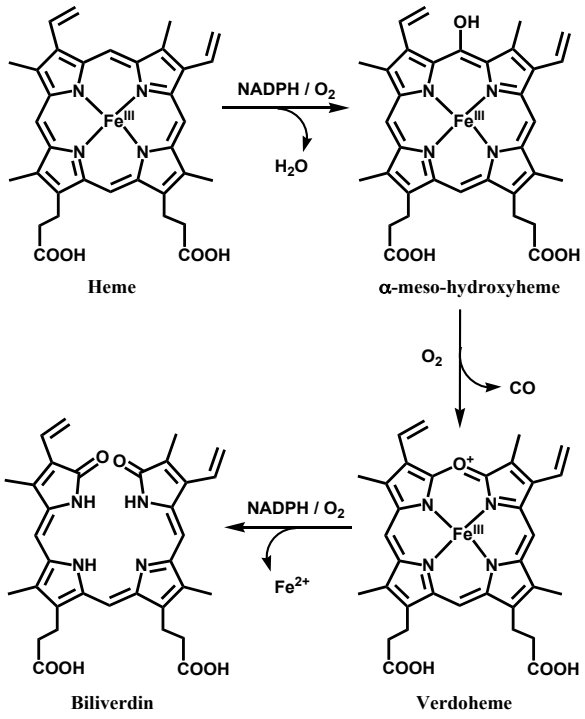

Figure 1.2. Stepwise heme degradation catalyzed by heme oxygenases.

1.1.2. CO from Heme Catabolism

Stepwise heme degradation, first identified by Tenhunen and co-workers, yields ferrous iron (Fe^{2+}), CO and biliverdin.[18] Free iron released in this process is sequestered by the intracellular protein ferritin, while biliverdin is further converted into bilirubin by bilirubin reductase (Figure 1.2).[19] Associated anti-inflammatory and

antioxidant properties of the bile pigments biliverdin and bilirubin have consequently afforded the HO-system its reputation as a vital cell protecting (cytoprotective) machinery, most notably in the cases of HO-1 induction by chemical and environmental stimuli.[20] Initially considered a benign byproduct of HO action, CO was later on ascribed a regulatory role when observations were noted of its capacity to dilate blood vessels. Indeed, much of CO-mediated physiological responses are of vascular origin, which includes inhibition of platelet aggregation[21] and blood vessel dilation.[22]

1.2 CO-Mediated Vasorelaxation

1.2.1. Soluble Guanylyl Cyclase (sGC) as a Target

Early reports by Wang and co-workers suggest that CO could activate both a cyclic guanosine monophosphate (cGMP) pathway and calcium activated potassium (K_{Ca}) channels in vascular tissues leading to an overall dilatory response.[23] Of these two targets, the cGMP pathway was the first to be investigated because cGMP production involves stimulation of soluble guanylyl cyclase (sGC), an intracellular receptor with a known heme binding domain. This heme prosthetic group within sGC typically binds nitric oxide. However a CO-induced rise in cGMP levels resulting from sGC stimulation has also been reported for aortic[24] and visceral smooth muscle cells[25], thus implicating sGC's in CO-mediated vasodilation.

sGC is a heterodimeric protein consisting of an α subunit (73-88 kDa) and a β subunit (70 kDa). An iron-protoporphyrin IX (heme b) prosthetic group is found in the β subunit and allows for substrate binding, leading to enzymatic activity. Nitric

oxide is the primary substrate for this cellular receptor, with sGC activity known to increase by 200-fold upon NO binding.[26] Indeed, sGC stimulation has been established as the exclusive pathway leading to NO-induced vasodilation and has been the target in the development of drugs related to cardiovascular processes.

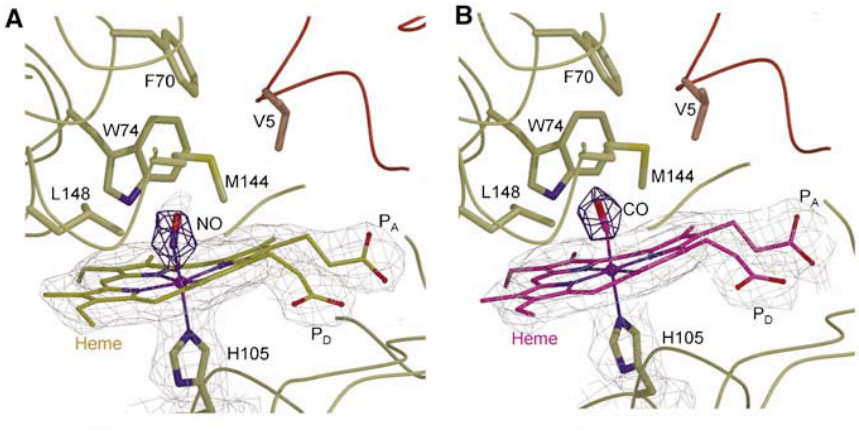

Figure 1.3. (A) NO and (B) CO ligands bound to the distal face of heme in cyanobacterial H-NOX (van den Akker, 2007).[27]

The NO sensing domain of sGC is part of a family of heme sensing nitric oxide oxygen sensing domains (H-NOX), which is conserved among prokaryotes. Taking the H-NOX domain of a cyanobacterial homolog, van den Akker and co-workers determined the crystal structures of the NO-bound and CO bound H-NOX and deduced the molecular basis for weak sGC activation by CO. Typically, sGC stimulation by NO occurs upon binding to heme b and forming a short-lived six-coordinate complex with a proximal histidine (His 105) side chain. Upon heme-His 105 bond cleavage, a five coordinate heme-NO bound species is formed that induces the necessary conformational changes in the enzyme leading to sGC activity (Figure 1.3 and 1.4).[2]

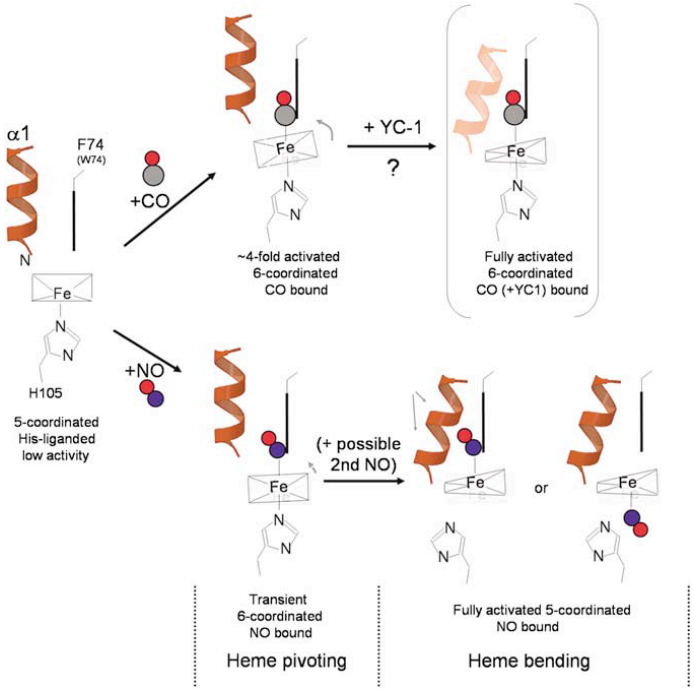

Figure 1.4. Schematic diagram of NO vs. CO-dependent activation of sGC (van den Akker and co-workers, 2007).[27]

The presence of heme b in the β subunit of sGC also allows for the CO-dependent stimulation of this enzyme, as CO's affinity for heme proteins is well established. Unlike NO stimulation that generates a transient six coordinate complex, CO binding to this heme cofactor produces a stable six coordinate complex (Figure 1.3 and 1.4) with the His105 side chain still bound tightly. This only mildly stimulates the enzyme by about four-fold when compared to that of NO. Inability of CO to yield a five coordinate species upon heme ligation is attributed to its increased ionic radii and reduced electronegativity. This apparent ligand discrimination by sGC suggests that much of CO-mediated vasorelaxation proceeds through a different pathway.

1.2.2. Big Conductance Potassium Channels (BK_{Ca}) as targets

BK_{Ca} are expressed in almost every tissue in the body, including vascular smooth muscle cells, and are stimulated by a variety of modulators. Protein kinases, heme and endogenously produced NO and CO all contribute to BK_{Ca} attenuation. Many physiological regulatory processes such as neuronal excitability, muscle contractility, and regulation of vascular tone are outcomes of BK_{Ca} activity. These channels are comprised of a pore-forming α-subunit and an accessory β-subunit, each component facilitating the flux of ions that yield an action potential.[28] The stimulatory effects of NO and CO on BK_{Ca} channels that result in a vasodilatory effect depend on the specific interactions of these two gases on specific subunits of BK_{Ca} channels.

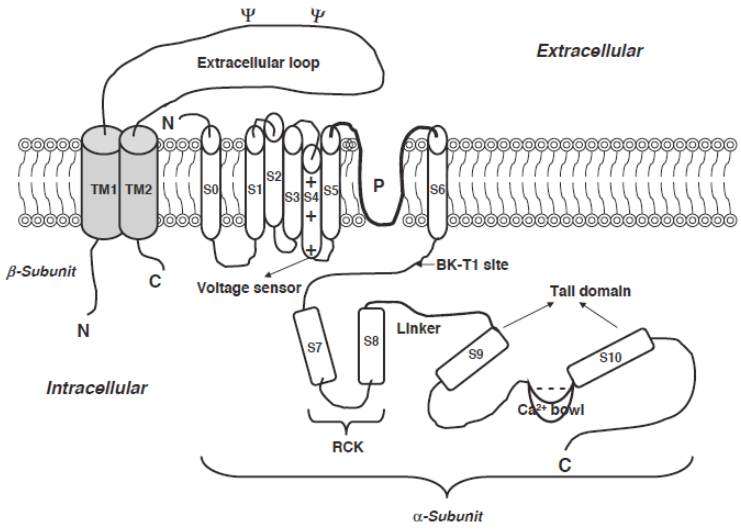

Figure 1.5. Big conductance calcium activated potassium channels (BK_{Ca}) illustrating the α and β subunits (adapted from ref. 28).

Using rat tail artery which bears all three potential targets of CO (sGC, cytochrome P450 and K-channels), Wang and co-workers re-examined the role of CO

in modulating vasodilatory response. Administering the non-specific K^+ channel inhibitor tetraethylammonium (TEA) ion, Wang and co-workers observed complete suppression of CO-induced vasorelaxation, thus implicating K^+ channels in this physiological response.[29] Because potassium channels are among the most common type of ion selective channels involved in cell function, including regulation of blood flow, it is imperative to know which specific type of K^+ channel is responsible for the observed CO-dependent response. Using both large and small conductance channel inhibitors: charybdotoxin and apamin, respectively, this same group has identified the large conductance Ca^{2+}-activated potassium channels (BK_{Ca}) as the primary targets of CO-induced vasodilation.[30]

Jaggar and co-workers postulated that CO is able to directly modify BK_{Ca} by binding to a channel-bound heme domain localized in the α-subunit. This channel-bound heme serves as a BK_{Ca} inhibitor by sensing CO and prevents pore closing.[31] Such interaction increases the open probability of these channels, allowing for smooth muscle relaxation and increased blood flow. Interestingly, such CO-mediated regulation of BK_{Ca} channels and hence of vasodilation, appears to be minimally influenced by endogenously produced NO and by reactive oxygen species such as H_2O_2 and peroxynitrite.[32] These findings confirm the integrity of CO as a potent vasoregulatory molecule which acts on a signaling pathway distinct from that of NO.

1.3 CO Signaling

Compared to the free radical species NO, CO is relatively inert. As a signaling molecule, the substrates of endogenously produced CO are limited to metalloproteins containing heme moieties. In contrast, NO and the subsequent reactive nitrogen species it generates affects not only metalloproteins, but also lipids and amino acid residues such as cysteine and tyrosine. Much of the CO-mediated outcomes that include vasorelaxation and anti-inflammatory responses are attributed to CO interaction with heme-containing proteins implicated in key physiological responses. Figure 1.6 provides an overview of some of the beneficial outcomes associated with CO application, as well as the protein targets associated with each pathway. For instance, CO's interaction with BK_{Ca} –bound heme proteins, discussed in the previous section, illustrates how CO achieves the desired vasoregulatory effect through protein inhibition.

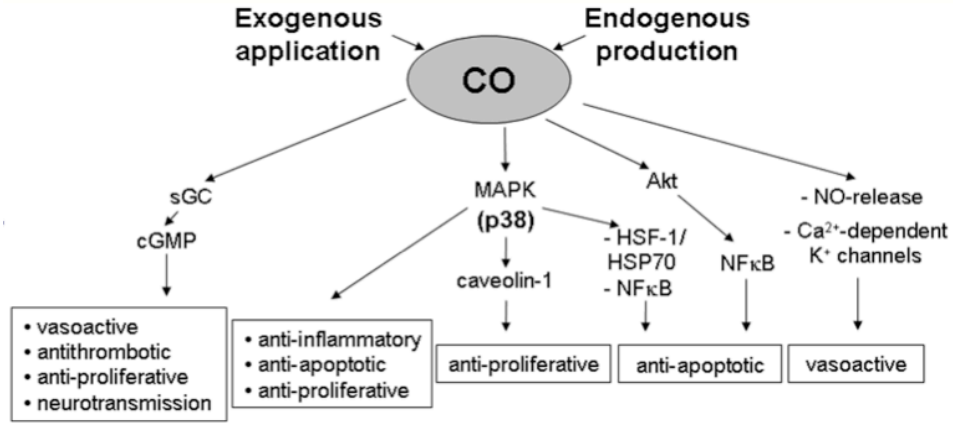

Figure 1.6. Carbon monoxide signal transduction pathways (adapted from ref. 40).

Cytochrome c oxidase, the terminal enzyme of the mitochondrial electron transport chain is another key heme protein that is inhibited by CO. Nontoxic concentrations of exogenously applied CO have been found to trigger a slight increase in mitochondrial reactive oxygen species (ROS),[33] which in turn activate the system's vascular adaptations to reduced oxygen conditions. Such responses to hypoxic environments include upregulation of transcription factors such as HIF-1α[34] and NF-κB,[35] both of which serve to promote survival by producing anti-inflammatory cytokines and chemokines. When administered prior to events of stress, CO is capable of initiating this type of redox (ROS) signaling mechanism thereby functioning as a potent pre-conditioning agent. In a model of brain ischemia, Vieira and co-workers have shown that a CO pre-conditioning step prevents neuronal apoptosis through increased ROS production.[36]

Perhaps the most intriguing signaling pathway modulated by CO is that of mitogen activated protein kinases (MAPKs). This family of proteins initiates signaling cascades in response to stress and external stimuli. Conventional MAPK types include (1) extracellular signal-regulated kinases 1/2 (ERK1/2) (2) c-Jun (N)-terminal kinases 1/2/3 (JNK1/2/3) and (3) p38 isoforms. Although the MAPK family is divided into various subgroups depending on their involvement in physiological and pathological processes, all MAPKs all feature a conserved Serine-Threonine domain, which upon phosphorylation triggers cell signaling.[37]

CO has been found to specifically influence the α and β isoforms of p38 MAPK. In a model of systemic hepatic inflammation, Brugger and co-workers found that the

antioxidant effects of CO are dependent on p38 MAPK activation. The antioxidant properties of CO were sustained despite heme oxygenase deactivation, signifying that exogenously applied CO has the same anti-inflammatory properties as endogenously produced CO in this model.[38] Similarly, the anti-proliferative properties of CO (in the form of $[Ru(CO)_3Cl_2]_2$) has been observed in a model of chronic pancreatitis and was found to proceed via p38 MAPK activation.[39] Despite the increasing evidence on the role of MAPK in CO-mediated protection, the molecular basis for this interaction is still unclear, especially because MAPKs are not known to have heme prosthetic groups. Alternatively, indirect modulation of MAPKs by CO has been proposed to shed light on the role of CO in signaling and immune response.[40]

It is becoming apparent that the influence of CO lies in its capacity to participate in a number of signaling pathways. As a result, this endogenously produced gas could potentially influence a myriad of physiological processes not limited to vasorelaxation. Indeed, the cytoprotective effect of CO, as will be discussed in the following section, can be attributed to its interaction with critical substrates that govern pathways leading to immune response.

1.4 Utility of Exogenously Applied CO

Most notable of these CO-mediated effects is its capacity to promote graft survival as observed in animal models of organ transplantation.[41-43] Much of the injury associated with organ transplant procedures stem from ischemia-reperfusion injury (IRI)- a form of tissue damage resulting from a combination of oxygen deprivation during organ preservation (ischemia) and subsequent restoration of blood

flow (reperfusion) upon transplantation. IRI is initiated when cold preservation of harvested organs disrupts cellular metabolic pathways. Minimal oxygen availability during cold storage causes accumulation of metabolic intermediates, membrane depolarization, depletion of ATP reserves and an overall disruption of the microvasculature within the isolated organ.[44] The recipient's innate immune response then recognizes such molecular patterns of inflammation from the transplanted organ and responds through upregulation of pro-inflammatory mediators such as cytokines, chemokines and macrophages. Although culmination of the organ transplant reestablishes blood circulation, it also brings about a surge of reactive oxygen species. With ischemia-reperfusion injury appearing to be characteristic of organ transplant procedures, further improvements in organ preservation and delivery methods are necessary to minimize graft rejection.

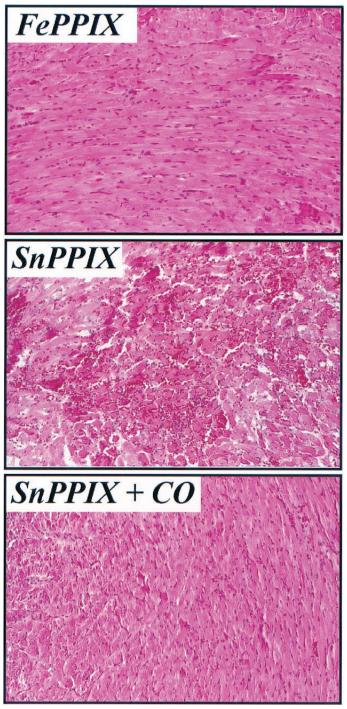

Figure 1.7. Effect of CO gas on heart transplants. Incubation with SnPPIX (middle panel), an HO-1 inhibitor shows increased myocardial infarction as a result of reduced endogenous CO production. Exogenous CO restores graft survival (bottom panel) (adapted from ref. 47).

Among the strategies being investigated, application of CO gas at different stages of organ transplantation has been shown to attenuate host inflammatory response thereby reducing the extent of IRI. When animal donors were provided a

dose of CO gas prior to organ procurement, the said organs were found to better withstand hypoxic conditions as evidenced by the minimal ischemia-reperfusion associated damage.[45] CO preconditioning appears to minimize a variety of pathological markers including T-lymphocytes, tumor necrosis factor (TNFα), interleukin (IL)-1β, and macrophage inflammatory proteins.[46]

Similarly, administration of CO gas to the recipients after transplantation has been found to boost graft tolerance and promote survival. Sato and co-workers concluded that long term survival of mouse-to-rat cardiac transplants was ensured when recipients were exposed to CO gas at different time points after transplantation.[47] Figure 1.7 illustrates how CO in this study suppresses myocardial infarction in the presence of the heme oxygenase inhibitor tin protoporphyrin IX (SnPPIX), thus supporting the notion that exogenously applied CO can act as a graft-promoting agent in lieu of endogenously produced CO. Indeed a number of animal models of cardiac diseases reveal that CO dosage initiates mitochondrial biogenesis due to the anti-coagulative properties of CO. By reducing platelet aggregation due to IRI in transplantation procedures, CO fosters recovery of vascular endothelial cells.[48]

Overall, the capacity of CO to enhance graft survival is attributed to its anti-apoptotic property. Its role in apoptosis, a process of programmed cell death, indicates its even greater significance in signaling mechanisms. As an endogenously produced molecule like NO, CO is able to mediate key pathways conferring protection to the organism.

1.5. Metal Carbonyls as Carbon Monoxide Releasing Molecules (CORMs)

The photosensitivity of metal carbonyls is well established and the mechanisms governing CO release upon illumination has been extensively studied. Due to its exceptional π-accepting character, CO stabilizes low valent metal centers. The strength of the resulting metal-CO bond depends on the ligand frame involved. Irradiation with high-energy radiation induces CO photorelease. Such is the case with homoleptic metal carbonyls, which were the model compounds utilized in elucidating the mechanism of metal-CO bond labilization.

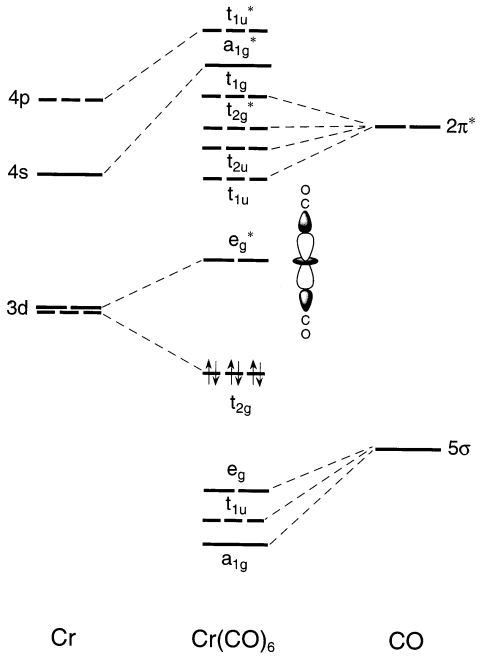

Figure 1.8. Qualitative MO diagram of $Cr(CO)_6$ to illustrate high energy LF excitation and the associated metal-CO bond homolysis.[49b]

Metal carbonyls are known to undergo CO loss via several pathways, with excitation of ligand field (LF) and metal to ligand charge transfer (MLCT) states being the most prominent pathways contributing to CO photodissociation. Using $Cr(CO)_6$ as a representative homoleptic metal carbonyl, the classical interpretation of photoinduced CO dissociation has been attributed to LF excitations. Single electron excitation into the e_g* orbital of $Cr(CO)_6$ reduces the number of bonding electrons in the t_{2g} orbitals, while populating a strongly antibonding Cr-d_z^2 –CO-5σ

e_g* orbital (Figure 1.8). The net effect of LF excitation is loss of an antibonding CO, with concomitant lowering of the d_z^2 orbital energy and loss of symmetry in the formation of $Cr(CO)_5$.[49]

The excitation spectrum of $Cr(CO)_6$ (Figure 1.9) features a low intensity shoulder at ~30,000 cm^{-1}, that corresponds to the ligand field excitation state $^1T_{1g}$, indicating a $t_{2g}^5e_g^1$ configuration. Irradiation onto this low intensity shoulder at ca. 4 eV leads to an observed CO ligand loss.[50] Calculations utilizing the original extended Hückel,[50a] semiempirical INDO/S CI,[51] and *ab initio* RHF methods[52] are consistent with the original assignment of ligand field transitions in $Cr(CO)_6$ corresponding to dissociative CO loss. This standard model of LF excitation leading to photoinduced CO dissociation has been employed thereafter to account for CO loss in various metal carbonyl complexes.

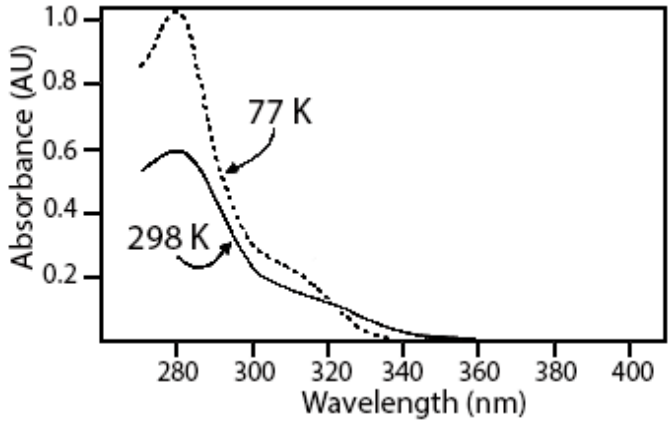

Figure 1.9. The UV/Vis spectrum of $Cr(CO)_6$ in a mixture of ether, pentane and ethanol (EPA) at 298 K and 77K (adapted from ref. 49a).

Later investigations on identifying the primary photoreactions governing metal carbonyls have reexamined the nature of the excited LF state for group 6

hexacarbonyls. Specifically, the metal-CO antibonding e_g orbitals lie at a relatively high energy, such that irradiation at 4 eV is deemed insufficient for $^1A_{1g} \rightarrow {}^1T_{1g}$ transition leading to CO dissociation. Baerends[53] and Pierloot[54] have independently concluded that the previously assigned low intensity shoulder for $Cr(CO)_6$ is actually a symmetry forbidden charge transfer (CT) state as opposed to ligand field. Daniel *et al.* have additionally defined this CT state as ^{1}MLCT character (T_{2u}), the potential energy curve of which crosses over to LF at increasing metal-CO bond lengths.[55] Although CO dissociation is still observed with photolysis, it is now recognized that single electron excitation initially populates a low energy ^{1}MLCT ($d_\pi \rightarrow \pi^*$) state, from which mixing with an excited ^{1}LF ($d_\pi \rightarrow d_{\sigma^*}$) state contributes to the observed metal-CO bond labilization. In the tungsten complex $[W(CO)_5$(piperidine)] for instance, the lowest excited states are W $\rightarrow$ CO MLCT in character, as revealed by time dependent density functional theory (TD-DFT) calculations. Furthermore, no LF excited states have been identified in this complex within a spectroscopically relevant range of 6-7eV, thus suggesting the primary role of MLCT excited states in CO photodissociation.[56]

1.5.1. Homoleptic Metal Carbonyls as prototypical CORMs

The ability of exogenous CO to promote anti-inflammatory and anti-apoptotic activity has prompted a renewed interest in metal carbonyls as carbon monoxide releasing molecules (CORMs) for targeted CO delivery. Not surprisingly, the first compounds to be employed as carbon monoxide releasing molecules (CORMs) were

commercially available homoleptic metal carbonyls due to the well-established photoactivity of this class of compounds (Figure 1.10). Motterlini and co-workers took the representative mono and dinuclear metal carbonyls $Fe(CO)_5$ and $Mn_2(CO)_{10}$ and demonstrated that irradiation with a cold light source leads to CO release. The ability of such compounds to mimic endogenously produced CO was also confirmed by incorporation in vasorelaxation studies involving pre-contracted rat aortic rings.[57]

Mechanisms concerning CO loss can vary depending on the nature of the starting carbonyl and the incoming ligand and may even be further complicated by recombination of the photoproduct(s). For $Fe(CO)_5$, quantum yield measurements by Burkey *et al.* have previously accounted for the formation of both the mono and disubstituted carbonyl species: $Fe(CO)_4L$ and $Fe(CO)_3L_2$ upon UV irradiation, with $Fe(CO)_4$ being the common intermediate leading to each distinct photoproduct.[58] Indeed, $Fe(CO)_5$ is a unique example wherein substitution of two CO groups occurs per photon absorbed. In the case of dimanganese decacarbonyl, CO loss has been recognized to proceed via a dissociative process wherein the transient species $Mn_2(CO)_9$ is generated, as opposed to the typical metal-metal bond cleavage observed during continuous photolysis of dinuclear metal carbonyls.[59]

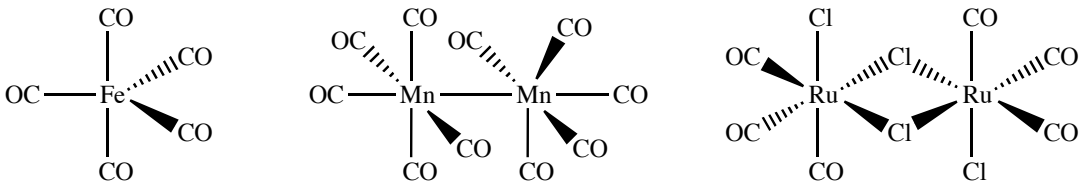

Figure 1.10. Homoleptic metal carbonyls representing prototypical CORMs.

While effective in fostering prolonged vasodilation, these homoleptic metal carbonyls are insoluble in aqueous solutions thus hindering their applicability. The development of metal carbonyls for controlled CO release has therefore been centered on the smart design of ligand frames to sensitize the resulting carbonyls to low energy light, as well as to impart the desired solubility in aqueous media.

1.5.2. Water-Soluble CORMs in solvent-assisted CO release processes

The first water-soluble CORM to be employed in biological studies was [Ru(glycinate)$(CO)_3$Cl] (Figure 1.11), developed by Motterlini and co-workers (often referred to as CORM-3). Facile CO loss from CORM-3 is pH dependent and arises from base (hydroxide) attack on the carbonyl leading to the formation of either $Ru(CO)_2(CO_2Cl(glycinate)]^{2-}$ or $[Ru(CO)_2(CO_2H)(OH)(glycinate)]^-$.[60] Interestingly, Darrensbourg and co-workers[61] have previously determined that incorporation of amino acids and their derivatives as ligands promote CO dissociation from Cr and W

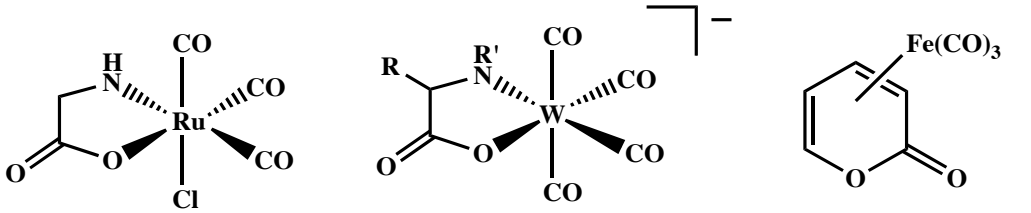

$Ru(CO)_3Cl(glycinate)$ **$[W(CO)_4(O_2CCH_2NHR')]^-$** **$[(\eta^4$ - 2-pyrone)$Fe(CO)_3]$**

Figure 1.11. Examples of CORMs bearing amino acids and biocompatible groups.

amino acid complexes (Figure 1.11). For complexes of the type $[M(CO)_4(OC_2CH_2NR)]^+$ (where M = Cr, W; R= H, CH_3), rates of CO loss are significantly enhanced when R = H, while substituents on the methylene carbon do

not seem to influence the apparent CO release rates. The mechanism points to NH hydrogen abstraction in solution to afford a CO-labilizing amido functionality, which then enhances CO dissociation rates. Metal complexes bearing amino acid, amino ester or non-natural amino acid moieties[62] have since found renewed utility in the area of targeted CO delivery via solvent-assisted CO release mechanisms.

A wide range of ligand frames and ancillary ligands not limited to amino acid functionalities has been utilized in the preparation of CORMs (Figure 1.11). The use of biocompatible functionalities, such as cyanocobalamin, and 2-pyrone (2*H*-pyran-2-one) and its related compounds,[63] appears to be a viable approach in the syntheses of water-soluble CORMS and has yielded CO donors with solvent-dependent CO-releasing profiles. While the incorporation of ligand fragments with inherent bioactivities seems promising in the development of water-soluble CORMS, purposeful ligand design has resulted in CORMs with suitable CO releasing capacities in physiologically relevant media. Mascharak and co-workers have shown that the Fe(II) carbonyls bearing designed structurally-related pentadentate polypyridine ligand frames exhibit CO release in the corresponding iron carbonyl complexes (Figure 1.12) by virtue of a trans-labilizing effect. These iron-based CORMs have been found to induce muscle relaxation of pre-contracted aortic tissue as well as exhibit fast CO-release rates in aqueous and non-aqueous media.[64]

The amount of CO released by solvent-labile CORMs may be quantitative. However the lack of control over CO delivery by such metal carbonyl complexes limits their utility to solvent-dependent CO-release applications. To fully realize the

potential of CORMs as CO donors in biological settings, controlled and site-specific delivery of this otherwise toxic gas is imperative.

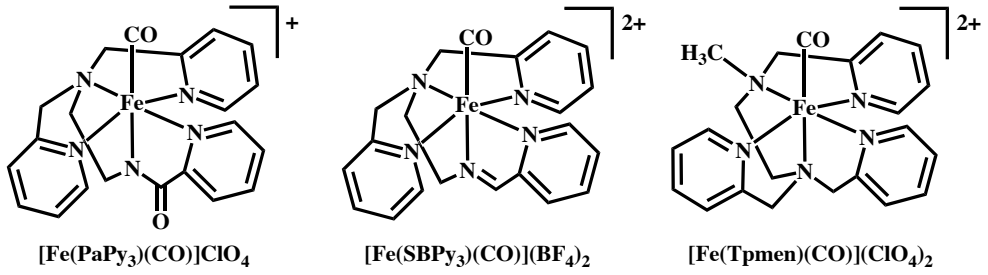

Figure 1.12. Fe(II) carbonyl complexes bearing structurally-related pentadentate ligand frames.[64]

1.5.3. Photoactive Carbon Monoxide Releasing Molecules (photoCORMs)

As noted in the case of prototypical CORMs, the photosensitivity to CO release by transition metal carbonyl complexes can be modulated with the use of ligand frames that foster MLCT excitations. Ford and co-workers reported the photochemical reaction of a water soluble salt $Na_3[W(CO)_5(TPPTS)]$ under UV irradiation and coined the term 'photoCORM' to describe this type of light-triggered CO releasing compound.[65] Subsequent aerobic oxidation after the initial photolysis was found to yield a total of 1.2-1.6 equivalents CO per molecule of $Na_3[W(CO)_5(TPPTS)]$, while recombination reactions further complicates identification of the various photoproduct(s). A number of photoCORMs with diverse ligand frames have been reported since then and the following sections will present the types of photoCORMs identified thus far.

1.5.3.1. fac-Manganese(I) tricarbonyl complexes as photoCORMs

The facile coordination of a variety of lewis bases including arenes, phosphines, thioethers and other heterocyclic moieties onto the $Mn(CO)_3^+$ fragment has led to the characterization of a series of *fac*-Mn(I) tricarbonyl complexes, all of which exhibit CO photodissociation when irradiated with UV to visible light energies. Revisiting the work of Trofimenko, Schatzschneider and co-workers synthesized $[Mn(CO)_3(tpm)]PF_6$ (tpm = tris(pyrazolyl)methane, (Figure 1.13), the first in this series of photoCORMs featuring tripodal ligand frames. This compound was found to release CO when activated by 365 nm light and has demonstrated its potential as a photodynamic therapy (PDT) agent.[66] Although CO release from $[Mn(CO)_3(tpm)]PF_6$ has been applied towards cytotoxic purposes and not in the expected protective assay that CO is known for, $[Mn(CO)_3(tpm)]PF_6$ nonetheless has since found its way into various CO delivery systems including conjugation onto model peptides,[67] nanoparticles,[68] and nanodiamonds.[69]

To elucidate the factors that determine CO release from tricarbonyl manganese(I) complexes, Schatzschneider and co-workers have expanded their series of tripodal ligands to include imidazole moieties and their derivatives. Within the subset of tricarbonyl[tris(imidazolyl)phosphane] manganese(I) complexes, the substitution pattern on the imidazolyl moiety was found to influence the CO-releasing efficiency and stoichiometry of the resulting *fac*-Mn(I) tricarbonyls. Two equiv of CO per mole of complex were released in compounds bearing imidazolyl-2ylphosphane ligand (2-TIP^H) frames (Figure 1.13), while only one CO was released per molecule

when imidazolyl-4ylphosphane was employed.[70] In addition to the substitution pattern on the imidazolyl group, the steric bulk of the substituents was also found to significantly influence CO-release kinetics for the series of tricarbonylmanganese(I) complexes.[71]

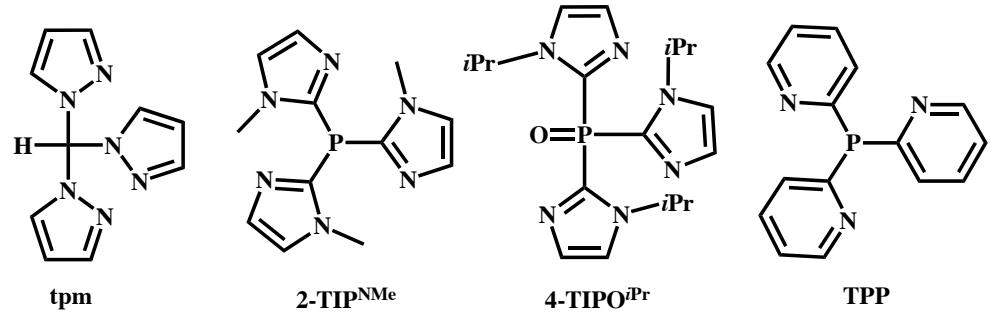

Figure 1.13. Examples of tripodal ligands utilized in the preparation of *fac*-Mn(I) tricarbonyl complexes as photoCORMs.

CO loss from this subset of tricarbonylmanganese(I) photoCORMs was investigated by Berends and Kurz using $[Mn(CO)_3(tpm)](PF_6)$ and $[Mn(CO)_3(bpzaa)]$ (where tpm = tris(pyrazolyl)methane and bpzaa = bis(pyrazolyl) acetic acid) as representative compounds. A generalized scheme detailing CO loss starts with two CO releasing steps followed by oxidation of the manganese center to Mn(II) and finally to Mn(III), with μ-O-Mn^{III} complexes purported to be the final products (Figure 1.14).[72] These findings contrast mechanisms outlined for those of tungsten carbonyls,[65] wherein exhaustive photolysis yields a mixture of photoproducts containing bound CO moieties due to recombination reactions.

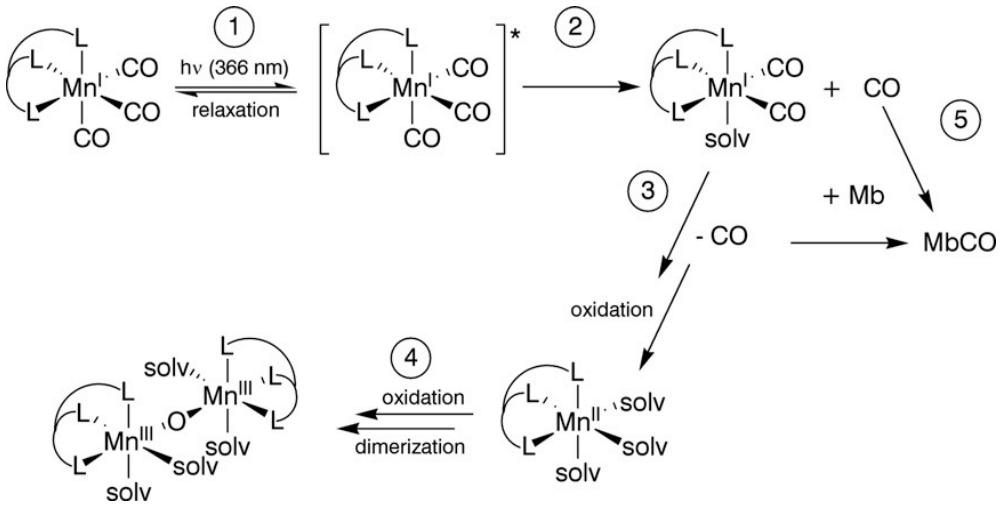

Figure 1.14. Proposed mechanism for CO release by *fac*-Mn(I) tricarbonyl complexes (adapted from ref. 72).

1.5.3.2. Miscelleneous photoCORMs

The rapid developments made in the area of CO donating materials have resulted in a number of metal carbonyl complexes bearing a variety of ligand frames with little resemblance to one another. This section exemplifies some of the photoCORMs that do not fall under the previously mentioned categories.

The compound *fac*-[Mn(his)$(CO)_3$] (where his = histidine, (Figure 1.15) is both water-soluble and undergoes light-induced CO release, unlike previous amino acid complexes that only release CO upon dissolution.[73] Its sensitivity to UV radiation (365 nm) renders it a photoCORM best suited for slow CO release applications due to its half-life of ~ 93 mins. While typical amino acid metal complexes have either mono or bidentate amino acid donors, the deprotonated histidine in *fac*-[Mn(his)$(CO)_3$] acts as a tridentate ligand through the carboxylate oxygen and nitrogen atoms of the amine and the imidazole group.

Not strictly incorporating an amino acid framework, the compound dicarbonyl-bis(cysteamine)iron(II) (referred to as CORM-S1, Figure 1.15) features an N/S ligand donor set derived from cysteine and falls under the classification of photoCORMs.[74] The combination of low-valent iron centers and coordinated thiolates has been known to afford metal carbonyls exhibiting reversible CO desorption properties,[75] making this particular motif suitable for the design of CO carriers. As predicted, CORM-S1 exhibits CO photorelease upon exposure to visible light (λ = 400 nm), yielding two CO molecules per CORM-S1. This compound stimulated voltage and Ca^{2+}-activated potassium channels (BK, Slo1) in a light-dependent manner making it a viable photoCORM for physiological applications.

Kodanko and co-workers have reported a stable iron carbonyl complex featuring a pentadentate ligand, *N*,*N*-bis(2-pyridylmethyl)-*N*-bis(2-pyridyl)methylamine (N4Py). The resulting carbonyl, $[Fe(N4Py)(CO)](ClO_4)_2$ (Figure 1.15) is highly stable in aerobic aqueous solutions and exhibits fast CO release upon irradiation with UV light (365 nm). To enhance targeted CO delivery, $[Fe(N4Py)(CO)](ClO_4)_2$ was attached to the Ala side chain of the peptide Ac-Ala-Gly-OBn, thus ensuring tissue or cell-specific CO delivery.[76]

Metal-alkynyl complexes typically feature strong metal-carbon bonds and the substituents on the alkynyl group can modulate the properties of such complexes. Incorporation of CO ligands in these metal alkynyl complexes could generate photoCORMs for therapeutic applications. The sugar substituted molybdenum complex, [Mo(C$\equiv$CCH$_2$O-β-D-fructopyranose)(η^5-C_5H_5)$(CO)_3$] (Figure 1.15) was

synthesized via the copper-promoted coupling of [Mo(η^5-C_5H_5)Cl$(CO)_3$] to the propargyl-substituted alkyne, [HC≡CCH_2O-(β-D-fructopyranose)]. When exposed to UV light (325 nm, 6 W), this compound undergoes rapid CO release, yielding ca. 2.2 equivalents of CO per photoCORM.[77]

Manganese-based tetracarbonyl complexes of the type $Mn(CO)_4$(C^N) (where C^N = *ortho*-metallated 2-phenylpyridine or benzoquinoline) have been found to

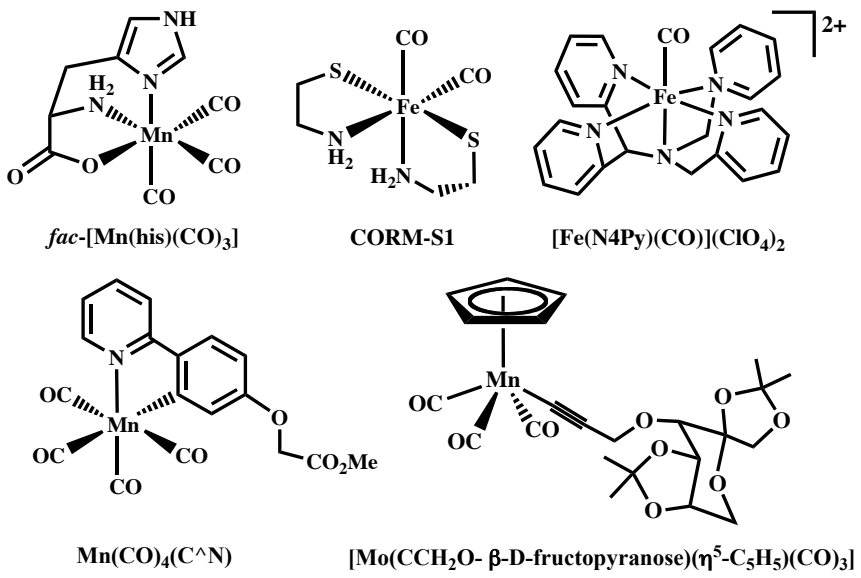

Figure 1.15. Miscellaneous photoCORMs.

exhibit CO photoactivity in the presence of 2-electron donor ligands such as DMSO or PPh_3. In the case of C^N = methyl 4-(pyridin-2-yl) phenyl carbonate, the resulting Mn tetracarbonyl (Figure 1.15) exhibits UV light-dependent CO release (365 nm) and yields approximately three CO ligands per molecule. This photoCORM shows excellent cell viability before and after irradiation, suggesting that its related degradation product(s) are minimally toxic.[78]

Recently, Ford and co-workers reported the synthesis and crystal structure of $[Re(bpy)(CO)_3(thp)]^+$ (where bpy = 2,2′-bipyridine ; thp = tris(hydroxymethyl)phosphine), a rhenium-based photoCORM that is both photoactive and luminescent. $[Re(bpy)(CO)_3(thp)]^+$ yields one CO per molecule when irradiated with 405 nm light and has no apparent cytotoxicity when incorporated into the human prostatic carcinoma cell line, PPC-1.[79]

Overall, the photoCORMs cited in this section represent some of the compounds reported in recent years. As the mechanisms of CO in signaling pathways and its role as a potent cytoprotective agent is better understood, the number of characterized CO-donors is expected to increase. Our understanding of the design principles that govern CO release in biologically relevant conditions will also improve.

1.6. Direction of Research

Facile coordination of CO to electron rich metal centers and the inherent photolability of the resulting metal-CO bond make transition metal carbonyl complexes ideal CO reservoirs to be applied in physiologically relevant conditions. While the principles governing CO photodissociation in this class of compounds has been known for some time, studies on such CO photorelease have been limited to organic and aprotic media, with the use of high energy light to trigger CO release. The main goal of this thesis is *to elucidate the ligand design strategies that impart greater photosensitivity to lights in the visible range and enhanced aqueous solubilities to transition metal carbonyl complexes for use as photoCORMs in biologically relevant conditions.*

Chapter 2 details our initial attempts at developing iron-based photoCORMs using principles previously applied in the preparation of photosensitized metal nitrosyls. Given the success of our group in the preparation of highly photoactive manganese and ruthenium nitrosyls that included pentadentate ligand frames, we synthesized and characterized a series of Fe(II) carbonyls bearing ligands structurally related to $PaPy_3H$, a ligand developed by us to stabilize metal centers in high and low oxidation states. The new Fe(II) carbonyls complexes $[Fe(SBPy)(CO)]BF_4$ (where $SBPy_3$ = *N,N′*-bis(2-pyridylmethyl)amine-N-ethyl-2-pyridine-2-aldimine) and $[Fe(Tpmen)(CO)]ClO_4$ (where Tpmen = *N*-methyl-*N,N′,N′*-tris(2-pyridylmethyl)ethane-1,2-diamine) in chapter 2 yield one equivalent of CO per molecule via a solvent-assisted CO release mechanism.

In research described in Chapter 3, we resorted to the use of tridentate ligand frames that allow for the incorporation of multiple CO ligands per molecule. With the goal of increasing sensitivity to low energy light (Chapter 3, Part I), we explored the effect of increasing conjugation on the metal-CO bond lability of a series of *fac*-Mn(I) tricarbonyl complexes bearing tripodal polypyridine ligand frames. As predicted, a progressive red-shift in the photoband of the corresponding *fac*-Mn(I) tricarbonyl complexes was observed with an increase in the number of pyridine donors and/or conjugation. The most red-shifted compound in this series, $[Mn(pqa)(CO)_3]ClO_4$, was also found to be the most effective at light-induced vasorelaxation of mouse aortic rings.

Part II of Chapter 3 describes our work with the ligand qmtpm, a potentially tridentate ligand frame bearing an NNS donor set, and its use in the syntheses and characterization of Ru(II) carbonyl complexes. In this study, we investigated the effect of a sulfur donor in place of a nitrogen donor on the photosensitivity of the Ru(II) carbonyl complexes derived from qmtpm. In addition, we have also incorporated *trans*-labilizing substituents such as PPh_3 and Cl^- in the design of our compounds to examine the influence of ancillary ligands on the observed CO photorelease.

Finally, chapter 4 includes the results of density functional theory (DFT) and time dependent DFT calculations on a series of manganese and ruthenium carbonyl complexes bearing the qmtpm ligand frame. Results reported herein confirm the role of both ancillary groups and the qmtpm ligand frame in the tuning of metal to ligand charge transfer (MLCT) energies that are key in CO photorelease processes.

1.7. References

(1) *Signal Transduction and the Gasotransmitters: NO, CO and H_2S in Biology and Medicine*; Wang, R. Humana Press: Totowa: New Jersey, 2004.

(2) Ignarro, L. J. *Nitric Oxide: Biology and Pathobiology*; Academic Press: San Diego, 2000.

(3) *Nitric Oxide Free Radicals in Peripheral Neurotransmission*; Kalsner, S., Ed.; Birkhauser: Boston, 2000.

(4) *Nitric Oxide and Infection*; Fang, F. C., Ed.; Kluwer Academic: New York, 1999.

(5) *Nitric Oxide and Cell: Proliferation, Differentiation and Death*; Moncada, S.; Higgs, E. A.; Bagetta, G., Eds.; Portland Press: London, 1998.

(6) *The Smallest Biomolecules: Diatomics and their Interactions with Heme Proteins*; Ghosh, A., Ed.; Elsevier: Amsterdam, 2008.

(7) (a) Wegiel, B.; Hanto, D. W.; Otterbein, L. E., *Trends Mol. Med.*, **2013**, *19*, 3-11. (b) Motterlini, R.; Otterbein, L. E., *Nat. Rev. Drug Discov.*, **2010**, *9*, 728-743. (c) Kaczorowski, D. J.; Zuckerbraun, B. S. *Curr. Med. Chem*. **2007**, *14*, 2720-2725. (d) Kim, H. P.; Ryter, S. W.; Choi, A. M. K. *Ann. Rev. Pharmacol. Toxicol*. **2006**, *46*, 411-449.

(8) Hartsfield, C. L., *Antioxid. Redox. Sign.*, **2002**, *4(2)*, 301-307.

(9) (a) Archakov, A. I.; Karuzina, I. I.; Petushkova, N. A.; Lisitsa, A. V.; Zgoda, V. G., *Toxicol. In Vitro*, **2002**, *16*, 1-10. (b) Vreman, H. J.; Wong, R. J.; Sanesi, C.; Dennery, P. A.; Stephenson, D. K., *Can. J. Physiol. Pharmacol.*, **1998**, *76*, 1057-1065.

(10) (a) *Structure and Function of Cytochromes*, Nishibayashi, H.; Tomura, T.; Soto, R.; Estabrook, R. W.; University Park Press: Baltimore, MD, 1968, p.658. (b) Guengerich, F. P., *Biochemistry*, **1978**, *17*, 3633-3639.

(11) Ryter, S. W.; Alam, J.; Choi, A. M. K., *Physiol. Rev.*, **2006**, *86*, 583-650.

(12) Maines, M. D., *FASEB J.*, **1988**, *2*, 2557-2568.

(13) Keyse, S. M.; Tyrrell, R. M., *Proc. Natl. Acad. Sci.*, **1989**, *86*, 99-103.

(14) (a) Piantadosi, C. A.; Withers, C. M.; Bartz, R. R.; MacGarvey, N. C.; Fu, P.; Sweeney, T. E.; Welty-Wolf, K. E.; Suliman, H. B., *J. Biol. Chem.*, **2011**, *286*, 16374-16385. (b) Wu, M-L.; Ho, Y-C.; Yet, S-F., *Antioxid. Redox Signal.*, **2011**, *15*, 1835-1846. (c) Morse, D.; Lin, L.; Choi, A. M. K.; Ryter, S. W., *Free Radical Bio. Med.*, **2009**, *47*, 1-12. (d) Kirkby, K. A.; Adin, C. A., *Am. J. Physiol. Renal Physiol.*, **2006**, *290*, F563-F71.

(15) (a) Wiesel, P.; Patel, A. P.; DiFonzo, N.; Marria, P. B.; Sim, C. U.; Pellacani, A.; Maemura, K.; LeBlanc, B. W.; Marino, K.; Doerschuk, C. M.; Yet, S-F.; Lee, M-E.; Perrella, M. A., *Circulation*, **2000**, *102*, 3015-3022. (b) Poss, K. D.; Tonegawa, S., *Proc. Natl. Acad. Sci.*, **1997**, *94*, 10925-10930.

(16) Yachie, A.; Niida, Y.; Wada, T.; Igarashi, N.; Kaneda, H.; Toma, T.; Ohta, K.; Kasahara, Y.; Koizumi, S., *J. Clin. Invest.*, **1999**, *103*, 129-135.

(17) Parfenova, H.; Leffler, C. W., *Curr. Pharm. Design*, **2008**, *14*, 443-453.

(18) Tenhunen, R.; Marver, H. S.; Schmid, R., *Proc. Natl. Acad. Sci.,* **1968**, *61*, 748-755.

(19) Kikuchi, G.; Yoshida, T.; Noguchi, M., *Biochem. Biophys. Res. Commun.*, **2005**, *338*, 558-567.

(20) (a) Wu, T-W.; Carey, D.; Wu, J.; Sugiyama, H., *Biochem. Cell. Biol.*, **1991**, *69,* 828-834. (b) Stocker, R.; Yamamoto, Y.; McDonagh, A. F.; Glazer, A. N.; Ames, B. N., *Science*, **1987**, *235*, 1043-1045.

(21) Brüne B.; Ullrich, V., *Mol. Pharmacol.*, **1987**, *32*, 497-504.

(22) Utz, J.; Ullrich, V., *Biochem. Pharmacol.*, **1991**, *41*, 1195-1201.

(23) Wang, R.; Wang, Z.; Wu, L., *Brit. J. Pharmacol.*, **1997**, *121*, 927-934.

(24) Ramos, K. S.; Lin, H.; McGrath, J. J., *Biochem. Pharmacol.*, **1989**, *38*, 1368-1370.

(25) Trischmann, U.; Klockner, U.; Isenberg, G.; Uta, J.; Ullrich, V., *Biochem. Pharmacol.*, **1991**, *41*, 237-241.

(26) Ignarro, L. J. (Nobel Lecture), *Angew. Chem. Int. Ed. Engl.*, **1999**, *38*, 1882-1892.

(27) Ma, X.; Sayed, N.; Beuve, A.; van den Akker, F., *EMBO Journal*, **2007**, *26*, 578-588.

(28) Ghatta, S.; Nimmagadda, D.; Xu, X.; O'Rourke, S. T., *Pharmacol. Therapeut.,* **2006**, *110*, 103-116.

(29) Wu, L.; Wang, Z.; Wang, R., *Can. J. Physiol. Pharmacol.,* **2000**, *78*, 696-707.

(30) (a) Wu, L.; Cao, K.; Lu, Y.; Wang, R., *J. Clin. Invest.*, **2002**, *110*, 691-700. (b) Wang, R.; Wu, L.; Wang, Z., *Pflügers Arch- Eur. J. Physiol.*, **1997**, *434*, 285-291.

(31) Jaggar, J. H.; Li, A.; Parfenova, H.; Liu, J.; Umstot, E. S.; Dopico, A. M.; Leffler, C. W., *Circ. Res.*, **2005**, *97*, 805-812.

(32) Dong, D-L.; Zhang, Y.; Lin, D-H.; Chen, J.; Patschan, S.; Goligorsky, M. S.; Nasjletti, A.; Yang, B-F.; Wang, W-H., *Hypertension*, **2007**, *50*, 643-651.

(33) (a) Piantadosi, C. A., *Free Radical Bio. Med.,* **2008**, 45, 562-569. (b) Gutterman, D. D., *Circ. Res.*, **2005**, *97*, 302-304.

(34) (a) Chin, B. Y.; Jiang, G.; Wegiel, B.; Wang, H. J.; MacDonald, T.; Zhang, X. C.; Gallo, D.; Cszimadia, E.; Bach, F. H.; Lee, P. J.; Otterbein, L. E., *Proc. Natl. Acad. Sci.*, **2007**, *104*, 5109-5114. (b) Chandel, N. S.; McClintock, D. S.; Feliciano, C. E.; Wood, T. M.; Melendez, J. A.; Rodriguez, A. M.; Schumacker, P. T., *J. Biol. Chem.*, **2000**, *275*, 25130-25138.

(35) Kim, H. S.; Loughran, P. A.; Rao, J.; Billiar, T. R.; Zuckerbraun, B. S., *Am. J. Physiol. Gastrointest. Liver Physiol.*, **2008**, *295*, G146-G152.

(36) Vieira, H. L. A.; Queiroga, C. S. F.; Alves, P. M., *J. Neurochem.*, **2008**, *107*, 375-384.

(37) Cargnello, M.; Roux, P. P., *Micobiol. Mol. Biol. Rev.*, **2011**, *75*, 50-83.

(38) Brugger, J.; Schick, M. A.; Brock, R. W.; Baumann, A.; Muellenbach, R. M.; Roewer, N.; Wunder, C., *Microcirculation*, **2010**, *17*, 504-513.

(39) Schwer, C. I.; Mutschler, M.; Stoll, P.; Goebel, U.; Humar, M.; Hoetzel, A.; Schmidt, R., *Mol. Pharmacol.*, **2010**, *77*, 660-669.

(40) Bauer, I.; Pannen, B. H. J., *Crit. Care*, **2009**, *13*, 220.

(41) Nakao, A.; Toyokawa, H.; Abe, M.; Kiyomoto, T.; Nakahira, K.; Choi, A. M. K.; Nalesnik, M. A.; Thomson, A. W.; Murase, N., *Transplantation*, **2006**, *81*, 220-230.

(42) Kaizu, T.; Nakao, A.; Tsung, A.; Toyokawa, H.; Sahai, R.; Geller, D. A.; Murase, N., *Surgery*, **2005**, *138*, 229-235.

(43) Song, R.; Kubo, M.; Morse, D.; Zhou, Z.; Zhang, X.; Dauber, J. H.; Fabisiak J.; Alber, S. M.; Watkins, S. C.; Zuckerbraun, B. S.; Otterbein, L. E.; Ning, W.; Oury, T. D.; Lee, P. J.; McCurry K. R.; Choi, A. M. K., *Am. J. Pathol.*, **2003**, *163*, 231-242.

(44) (a) Guibert, E. E.; Petrenko, A. Y.; Balaban, C. L.; Somov, A. Y; Rodriguez, J. V.; Fuller, B. J., *Transfus. Med. Hemother.*, **2011**, *38*, 125-142. (b) Vardanian, A. J.; Kupiec-Weglinski, J. W., *Curr. Opin. Organ Transplant.*, **2007**, *12*, 135-140.

(45) (a) Martins, P. N. A.; Reutzel-Selke, A.; Jurisch, A.; Denecke, C.; Attrot, K.; Pascher, A.; Kotsch, K.; Pratschke, J.; Neuhaus, P.; Volk, H. D.; Tullius, S. G., *Transplantation*, **2006**, *82*, 938-944. (b) Wang, H.; Lee, S. S.; Gao, W.; Czismadia, E.; McDaid, J.; Öllinger, R.; Soares, M. P.; Yamashita, K.; Bach, F. H., *Diabetes*, **2005**, *54*, 1400-1406.

(46) (a) Song, R.; Mahidhara, R. S.; Zhou, Z.; Hoffman, R. A.; Seol, D. W.; Flavell, R. A.; Billiar, T. R.; Otterbein, L. E.; Choi, A. M. K., *J. Immunol.*, **2004**, *172*, 1220-1226. (b) Morse D.; Pischke, S. E.; Zhou, Z.; Davis, R. J.; Flavell, R. A.; Loop, T.; Otterbein, S. L.; Otterbein, L. E.; Choi, A. M. K., *J. Biol. Chem.*, **2003**, *278 (39)*, 36993-36998. (c) Otterbein, L. E.; Bach, F. H.; Alam, J.; Soares, M.; Lu, H. T.; Wysk, M.; Davis, R. J.; Flavell, R. A.; Choi, A. M. K., *Nat. Med.*, **2000**, *6 (4)*, 422-428.

(47) Sato, K.; Balla, J.; Otterbein, L.; Smith, R. N.; Brouard, S.; Lin, Y.; Csizmadia, E.; Sevigny, J.; Robson, S. C.; Vercellotti, G.; Choi, A. M.; Bach, F. H.; Soares, M. P., *J. Immunol.*, **2001**, *166*, 4185-4194.

(48) Ozaki, K. S.; Kimura, S.; Murase, N., *Transplant. Rev.*, **2012**, *26*, 125-139.

(49) (a) Long, C.; *Top. Organomet. Chem.*, **2010**, *29*, 37-71. (b) Baerends, E. J.; Rosa, A., *Coord. Chem. Rev.*, **1998**, *177*, 97-125.

(50) (a) Beach, N. A.; Gray, H. B., *J. Am. Chem. Soc.*, **1968**, *90*, 5713-5721. (b) Gray, H. B.; Beach, N. A., *J. Am. Chem. Soc.*, **1963**, *85*, 2922-2927.

(51) Kotzian, M.; Rösch, N.; Schröder, H.; Zerner, M. C., *J. Am. Chem. Soc.*, **1989**, *111*, 7687-7696.

(52) Pierloot, K.; Verhulst, J.; Verbeke, P.; Vanquickenborne, L. G., *Inorg. Chem.*, **1989**, *28*, 3059-3063.

(53) (a) Rosa, A.; Baerends, E. J.; van Gisbergen, S. J. A.; van Lenthe, E.; Groeneveld, J. A.; Snijders, J. G., *J. Am. Chem. Soc.*, **1999**, *121*, 10356-11065. (b) Pollak, C.; Rosa, A.; Baerends, E. J.; *J. Am. Chem. Soc.*, **1997**, *119*, 7324-7329.

(54) Pierloot, K.; Tsokos, E.; Vanquickenborne, G., *J. Phys. Chem.*, **1996**, *100*, 16545-16550.

(55) (a) Villaume, S.; Strich, A.; Daniel, C.; Perera, S. A.; Bartlett, R. J., *Phys. Chem. Chem. Phys.*, **2007**, *9*, 6115-6122. (b) Ben Amor, N.; Villaume, S.; Maynau, D.; Daniel, C., *Chem. Phys. Lett.*, **2006**, *421*, 378-382.

(56) Záliš, S.; Busby, M.; Kotrba, T.; Matousek, P.; Towrie, M.; Vlček, Jr., A., *Inorg Chem,* **2004**, *43*, 1723-1734.

(57) Motterlini, R.; Clark, J. E.; Foresti, R.; Sarathchandra, P.; Mann, B. E.; Green, C. J., *Circ. Res.*, **2002**, *90*, e17-e24.

(58) Nayak, S. K.; Farrell, G. J.; Burkey, T. J., *Inorg. Chem*., **1994**, *33*, 2236-2242.

(59) Herrick, R. S.; Brown, T. L., *Inorg. Chem*., **1984**, *23*, 4550-4553.

(60) Johnson, T. R.; Mann, B. E.; Teasdale, I. P.; Adams, H.; Foresti, R.; Green, C. J.; Motterlini, R., *Dalton Trans.*, **2007**, 1500-1508.

(61) Darensbourg, D. J.; Draper, J. D.; Reibenspies, J. H., *Inorg. Chem.*, **1997**, *36*, 3648-3656.

(62) (a) Velásquez, V. P. L.; Jazzazi, T. M. A.; Malassa, A.; Görls, H.; Gessner, G.; Heinemann, S. H.; Westerhausen, M., *Eur. J. Inorg. Chem.,* **2012**, 1072-1078. (b) Zhang, W-Q.; Whitwood, A. C., Fairlamb, I. J. S.; Lynam, J. M., *Inorg. Chem.*, **2010**, *49*, 8941-8952.

(63) (a) Zobi, F.; Blacque, O.; Jacobs, R. A.; Schaub, M. C.; Bogdanova, A. Y.; *Dalton Trans.*, **2012**, *41*, 370-378. (b) Fairlamb, I. J. S.; Duhme-Klair, A-K.; Lynam, J. M.; Moulton, B. E.; O'Brien, C. T.; Sawle, P.; Hammad, J.; Motterlini, R., *Bioorg., Med. Chem. Lett.*, **2006**, *16*, 995-998.

(64) Gonzalez, M. A.; Fry, N. L.; Burt, R.; Davda, R.; Hobbs, A.; Mascharak P. K., *Inorg. Chem.*, **2011**, *50*, 3127- 3134.

(65) Rimmer, R. D.; Richter, H.; Ford, P. C., *Inorg. Chem.*, **2010**, *49*, 1180-1185.

(66) Niesel, J.; Pinto, A.; Peindy N'Dongo, H. W.; Merz, K.; Ott, I.; Gust, R.; Schatzschneider, U., *Chem. Commun.*, **2008**, 1798-1800.

(67) Pfeiffer, H.; Rojas, A.; Niesel, J.; Schatzschneider, U., *Dalton Trans.*, **2009**, 4292.

(68) Dördelmann, G.; Pfeiffer, H.; Birkner, A.; Schatzschneider, U., *Inorg. Chem.*, **2011**, *50*, 4362-4367.

(69) Dördelmann, G.; Meinhardt, T.; Sowik, T.; Krueger, A.; Schatzschneider, U., *Chem. Commun.*, **2012**, *48*, 11528-11530.

(70) Kunz, P. C.; Huber, W.; Rojas, A.; Schatzschneider, U.; Spingler, B., *Eur. J. Inorg. Chem.*, **2009**, 5358-5366.

(71) Huber, W.; Linder, R.; Niesel, J.; Schatzschneider, U.; Spingler, B.; Kunz, P. C., *Eur. J. Inorg. Chem.*, **2012**, 3140-3146.

(72) H. M. Berends and P. Kurz, *Inorg. Chim. Acta*, **2012**, *380*, 141-147.

(73) Mohr, F.; Niesel, J.; Schatzschneider, U.; Lehmann, C. W., *Z. Anorg. Allg. Chem.*, **2012**, *638*, 543-546.

(74) Kretschmer, R.; Gessner, G.; Görls, H.; Heinemann, S. H.; Westerhausen, M., *J. Inorg. Biochem.,* **2011**, *105*, 6-9.

(75) Szakács-Schmidt, A.; Kreisz, J.; Marko, L., *Inorg. Chim. Acta,* **1992**, *198-200*, 401-405.

(76) Jackson, C. S.; Schmitt, S.; Dou, Q. P.; Kodanko, J. J., *Inorg. Chem.*, **2011,** *50*, 5336-5338.

(77) W. Zhang, A. J. Atkin, I. J. S. Fairlamb, A. C. Whitwood, J. M. Lynam, *Organometallics*, **2011***, 30*, 4643-4654.

(78) J. S. Ward, J. M. Lynam, J. W. B. Moir, D. E. Sanin, A. P. Mountford, I. J. S. Fairlamb, *Dalton Trans.*, **2012**, *41*, 10514-10517.

(79) Pierri, A. E.; Pallaoro, A.; Wu, G.; Ford, P. C., *Inorg. Chem.*, **2012**, *134*, 18197-18200.

Chapter 2. Solvent-assisted CO release from Iron Carbonyls Bearing Structurally-Related Pentadentate Ligand Frames

2.1 Background

During the past three decades, three small "toxic" molecules namely nitric oxide (NO), carbon monoxide (CO) and hydrogen sulfide (H_2S) have drawn much attention due to their surprising and unexpected roles in numerous physiological processes.[1] The surge of interest in these "biologically relevant gases" all began with NO. What once was viewed as an environmental pollutant, NO has now been shown to participate in a myriad of physiological and pathological processes including vasodilation,[2] neurotransmission,[3] immune response[4] and cellular apoptosis.[5] More recently, CO and H_2S have also been identified as important signaling molecules.[1,6,7] Among this series of gasotransmitters, NO and CO possess the greatest number of similarities – both known to interact with metalloproteins, particularly those bearing heme moieties.[8] Consequently, the biological relevance of CO, an endogenously produced gaseous molecule, has been emerging at a faster rate during the past few years.[9,10]

To effectively induce the desirable biological effects of CO at a targeted site, controlled site-specific delivery of CO to tissues is required and the resulting CO-donor after CO-release must remain benign. CO is a ubiquitous ligand in organometallic chemistry. Transition metals therefore are incorporated in the syntheses of carbon monoxide releasing molecules (CORMs) to circumvent the inherent toxicity associated with CO inhalation. The early CORMs studied were

commercially available homo and heteroleptic transition metal carbonyls (CO complexes). These included $[Fe(CO)_5]$, $[Mn_2(CO)_{10}]$ and $[\{Ru(CO)_3Cl_2\}]_2$, which exhibited direct biological activities despite poor solubility.[11] These prototypical carbonyls manifested CO delivery to substrates, with the limitation of only being soluble in aprotic solvents, particularly DMSO. $[Ru(glycine)(CO)_3Cl]$, developed by Motterlini and coworkers (and often referred to as CORM-3), was one of the first compounds to be soluble in aqueous media.[12] This CORM effectively mimics the vasorelaxing and cardioprotective properties associated with CO produced endogenously.[12-14] Further efforts in preparing metal carbonyls as therapeutics focused on the incorporation of a biocompatible ligand to facilitate CO delivery. As non-toxic leaving groups, amino acids and amino esters have been utilized as ligands in the preparation of group 6-based CORMs.[15] The involvement of 2-pyrone functionalities in metabolic pathways has also led to the syntheses of Fe and Mo-based CORMs bearing a pyrone moiety.[16]

For several years our lab has developed a series of designed metal nitrosyls (NO complexes of metals such as Fe, Mn and Ru) that rapidly deliver NO upon exposure to lights of a wide range of wavelengths (400-1000 nm).[17-22] We have shown that increase in the extent of conjugation within the ligand frame affords metal nitrosyls exhibiting a significant red shift in their respective photobands and make such complexes more sensitive to low-energy radiation. Our lab has had success in the preparation of photolabile metal nitrosyls bearing the designed pentadentate ligand: *N*,*N*-bis(2-pyridylmethyl)amine-*N*-ethyl-2-pyridine-2-carboxamide ($PaPy_3H$), whose

domains serve to stabilize high and low oxidation states of transition metal ions. Specifically, reaction of $PaPy_3H$ with a Mn(II) center and NO gas generates the photoactive metal nitrosyl: $[Mn(PaPy_3)(NO)]ClO_4$ (λ_{max} = 635 nm) which undergoes NO photorelease upon exposure to visible light energies (λ = 500-600 nm).[18b]

Employing the strategy of adding conjugated moieties to the ligand frame to improve quantum efficiency and NO release capacity, we modified the $PaPy_3H$ ligand to include a quinoline group to isolate the pentadentate ligand, *N*,*N*-bis(2-pyridylmethyl)amine-*N*-ethyl-2-quinoline-2-carboxamide ($PaPy_3QH$). Indeed the corresponding manganese nitrosyl, $[Mn(PaPy_3Q)(NO)]ClO_4$, (λ_{max} = 670 nm) exhibits NO photolability upon illumination with NIR light and has a quantum efficiency (Φ) that is almost double that of the parent $[Mn(PaPy_3)(NO)]ClO_4$ – (0.69 versus 0.38) at 550 nm.[22b]

To explore whether our design principles employed in the preparation of photoactive metal nitrosyls can be extended to the isolation of photolabile CORMs, we have investigated the CO-releasing behavior of three iron carbonyls derived from three designed pentadentate ligands shown in Figure 2.1. As discussed in chapter 1, the incorporation of ligands with low-lying orbitals such as pyridines or diimines facilitates efficient MLCT excitation, which is the first step in governing CO photodissociation. As such, the ligands employed herein not only feature pyridine moieties, but also different trans-labilizing groups to promote CO release.

Although the synthesis and structure of the Fe(II) carbonyl $[(PaPy_3)Fe(CO)]ClO_4$ were reported by us in a previous account,[23] the CO-releasing

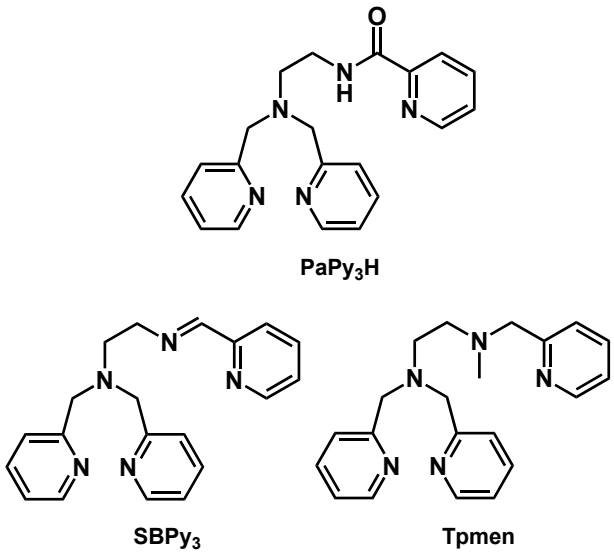

Figure 2.1. Structures of the designed pentadentate ligands, $PaPy_3H$, $SBPy_3$ and Tpmen, used in this study.

property was not studied. We have synthesized and characterized two more Fe(II) carbonyls derived from the related ligands namely *N,N′*-bis(2-pyridylmethyl)amine-N-ethyl-2-pyridine-2-aldimine ($SBPy_3$) and *N*-methyl-*N,N′,N′*-tris(2-pyridylmethyl)ethane-1,2-diamine (Tpmen). In this structurally-related series: $[(PaPy_3)Fe(CO)](ClO_4)$, $[(SBPy_3)Fe(CO)](BF_4)_2$ and $[(Tpmen)Fe(CO)](ClO_4)_2$, the design allowed us to place CO trans to a carboxamido-N (strong σ-donor), an imine-N (moderately π-accepting) and a tertiary amine-N (weak σ-donor) center respectively.

In this chapter, the syntheses, structures and CO-releasing parameters of $[(PaPy_3)Fe(CO)](ClO_4)$, $[(SBPy_3)Fe(CO)](BF_4)_2$ and $[(Tpmen)Fe(CO)](ClO_4)_2$ are described. The utility of these CORMs has been demonstrated in relaxation of mouse aortic smooth muscle tissue in vitro. The possible pathways of CO-mediated relaxation are also highlighted.

2.2. Syntheses and X-ray Structures of Metal Complexes

2.2.1. Characterization of [(SBPy$_3$)Fe(CO)](BF$_4$)$_2$

The excellent affinity of CO for low valent metal centers allowed for the facile formation of $[(L)Fe(CO)]^{n+}$ (where L = pentadentate ligand) under mild conditions. As was previously observed in the synthesis of $[(PaPy_3)Fe(CO)]ClO_4$, the use of methanol as a solvent facilitates metal carbonylation via formation of the solvent-bound species $[(L)Fe(MeOH)]^{2+}$.[23] Subsequent exposure of this solvato species to CO gas affords the desired iron(II) carbonyl in good yield. Similarly when a methanolic

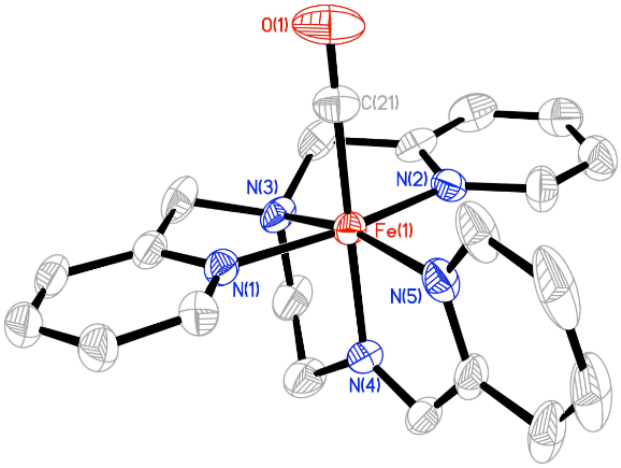

Figure 2.2. ORTEP diagram (30% probability level) of the cation of $[(SBPy_3)Fe(CO)](BF_4)_2$. H-atoms have been omitted for the sake of clarity.

solution of $[Fe(H_2O)_6](BF_4)_2$ was added via cannula to a degassed solution of $SBPy_3$, a deep purple solution was generated, indicating the formation of $[(SBPy_3)Fe(MeOH)]^{2+}$. Replacement of the bound solvent molecule with CO is quite rapid as the color lightens from purple to a deep red hue- with the red-colored solid $[(SBPy_3)Fe(CO)](BF_4)_2$ separating out of solution within minutes. X-ray quality crystals of red blocks were obtained when the MeOH solutions were kept under CO

atmosphere at low temperature. The structure of $[(SBPy_3)Fe(CO)](BF_4)_2$ is shown in Figure 2.2.

The Fe(II) center of $[(SBPy_3)Fe(CO)](BF_4)_2$ is situated in an octahedral environment with the π-accepting imine N moiety trans to CO, while the remaining N donors (three pyridine-N and one tertiary amine-N) are in the equatorial plane. Much like $[(PaPy_3)Fe(CO)]ClO_4$, the Fe-C(O) bond angle at 176.5(3)° is almost linear (Figure 2.3). Similar Fe-C(O) bond angles have been noted with other low-spin Fe(II) carbonyl complexes such as *trans*-$[(DPGH)_2Fe(py)(CO)]$ (178°) (where DPGH = bidentate diphenylglyoximato univalent anion).[24]

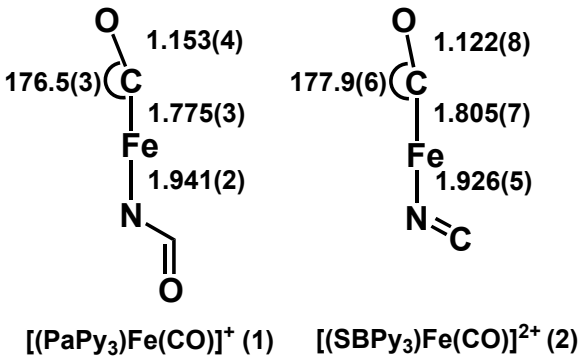

Figure 2.3. Comparison of metric parameters and axial coordination of $[(PaPy_3)Fe(CO)]^+$ and $[(SBPy_3)Fe(CO)]^{2+}$.

2.2.2. Characterization of [(Tpmen)Fe(CO)](ClO₄)₂

To explore the effect a σ-donating moiety trans to a dissociable CO group in this series of structurally related pentadentate ligand frames, the known ligand Tpmen was utilized. The beige solid $[(Tpmen)Fe(CO)](ClO_4)_2$ was isolated when a methanolic solution of $[Fe(MeCN)_4](ClO_4)_2$ was allowed to react with Tpmen followed by immediate passage of CO gas at room temperature. The structure of this carbonyl has

not been fully characterized due to disorder problems in the crystal lattice. Exchange of counterions did not provide any respite. In the *preliminary structure* of the perchlorate salt (Figure 2.4), the connectivity of atoms however is quite clear. The CO is trans to the tertiary amine-N while three pyridyl-Ns and the second tertiary N (with CH_3 group attached to it) are coordinated to the iron center in the equatorial plane. Interestingly, similar difficulties in crystallization were encountered when this same ligand frame was employed in the preparation of the manganese carbonyl, $[Mn(Tpmen)(NO)](ClO_4)_2$.

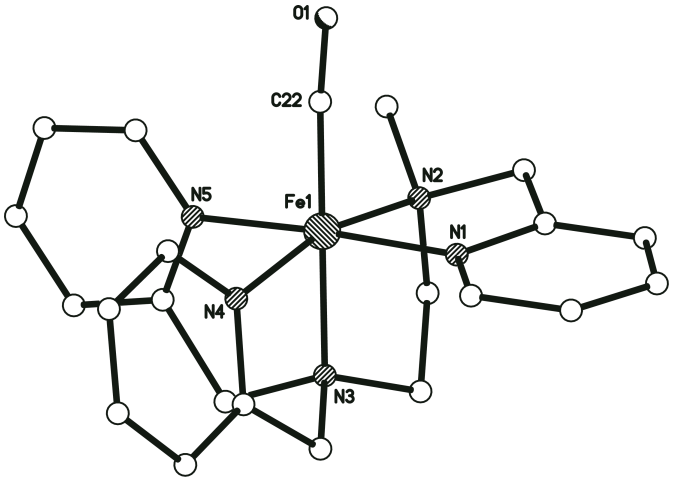

Figure 2.4. Preliminary structure of the cation of $[(Tpmen)Fe(CO)](ClO_4)_2$.

2.3. Comparison of the Properties of Fe(II) carbonyls bearing Structurally-Related Pentadentate Ligand Frames

2.3.1. IR Spectroscopy

A strong CO stretch (ν_{CO}) at 1972 cm^{-1} was noted for $[(PaPy_3)Fe(CO)]ClO_4$ while $[(SBPy_3)Fe(CO)](BF_4)_2$ and $[(Tpmen)Fe(CO)](ClO_4)_2$ exhibit similar CO stretches at 2010 and 2012 cm^{-1} (Figures 2.12 – 2.13) respectively, confirming the

presence of a bound CO ligand in each of the three carbonyls. These ν_{CO} values are within the range noted for other Fe(II) complexes with Fe(II)-CO bonds. For example, *trans*-[(TPP)Fe(1-MeIm)(CO)] (where TPP = 5,10,15,20-tetraphenylporphinate ligand, 1-MeIm = I-methylimidazole)[25] exhibits its ν_{CO} at 1969 cm^{-1} while *trans*-$[(DPGH)_2Fe(py)(CO)]$[24] displays its ν_{CO} at 1996 cm^{-1}. Comparison of the ν_{CO} values of these structurally similar carbonyls reveals an interesting trend. The change from a strong σ-donating and negatively charged carboxamido-N donor in $[(PaPy_3)Fe(CO)]ClO_4$ to a neutral (and moderately π-accepting) imine-N or weak tertiary-N donor (in $[(SBPy_3)Fe(CO)](BF_4)_2$ and $[(Tpmen)Fe(CO)](ClO_4)_2$, respectively) increases the ν_{CO} value from 1972 to 2010-2012 cm^{-1}. In the case of $[(PaPy_3)Fe(CO)]ClO_4$, as more electron density is pushed toward the Fe(II) center by the carboxamido-N moiety, it transfers part of the electron density to the antibonding orbital of the bound CO ligand trans to it thus accounting for the lower observed ν_{CO} stretch. Such transfer strengthens the Fe-C(O) bond in $[(PaPy_3)Fe(CO)]ClO_4$ more than the other two carbonyls and makes it a slow CO-releasing molecule. Conversely, when this negatively charged carboxamido-N donor is replaced by functional groups with greater π-accepting character, the electron density about the metal center is then distributed between the CO ligand and the trans-labilizing group leading to reduced backbonding interactions and a weaker metal-CO bond as noted in the ν_{CO} stretches of $[(SBPy_3)Fe(CO)](BF_4)_2$ and $[(Tpmen)Fe(CO)](ClO_4)_2$.

2.3.2. Electronic Absorption Spectra and CO-release in Solution

The electronic absorption spectra of $[(SBPy_3)Fe(CO)](BF_4)_2$ and $[(Tpmen)Fe(CO)](ClO_4)_2$ have been acquired in MeCN and phosphate buffer (PBS, pH = 7.4) via rapid dissolution and quick data collection. The color of the solutions of all the carbonyls intensifies upon loss of CO and significant changes with distinct isosbestic points are noted in their electronic absorption spectra. For example, $[(SBPy_3)Fe(CO)](BF_4)_2$ exhibits a strong metal-to-ligand charge transfer (MLCT) band with λ_{max} at 455 nm in MeCN, that shifts to 555 nm upon CO release as the color changes from red to deep magenta. Clean isosbestic points are noted at 485, 415, and 340 nm (Figure 2.5). The final spectrum (obtained within 15 min) is identical to that of $[(SBPy_3)Fe(MeCN)](BF_4)_2$, a structurally characterized species reported by us previously.[26] The red shift of the MLCT band upon loss of CO clearly indicates that the electron density from the antibonding π^* orbital of bound CO ligand returns back to the Fe(II) center in $[(SBPy_3)Fe(MeCN)]^{2+}$. With $[(Tpmen)Fe(CO)](ClO_4)_2$, the initial yellow color deepens due to a similar red shift of the MLCT band from 330 nm to 390 nm (isosbestic points at 352 and 242 nm) and the final spectrum of $[(Tpmen)Fe(MeCN)]^{2+}$ appears within ~20 min.

The CO-releasing behavior of $[(PaPy_3)Fe(CO)]ClO_4$ in MeCN (and DMF) depends critically on the presence of dioxygen in solution. A solution of $[(PaPy_3)Fe(CO)]ClO_4$ in degassed MeCN is stable and shows no sign of CO release. Indeed, both the ν_{CO} value (1972 cm^{-1}) and Fe-C(O) distance of $[(PaPy_3)Fe(CO)]ClO_4$ (1.775(3) Å) indicate a stronger Fe-CO bond compared to the other two carbonyls. In

aerated MeCN however, this carbonyl readily loses CO (within ~15 min) much like $[Fe(SBPy_3)(CO)](BF_4)_2$ and $[Fe(Tpmen)(CO)](ClO_4)_2$. Interestingly, the absorption spectrum (λ_{max} at 470 and 390 nm) of $[(PaPy_3)Fe(CO)]ClO_4$ changes to that of the oxo-bridged diiron(III) species $[(PaPy_3)FeOFe(PaPy_3)](ClO_4)_2$ (λ_{max} at 430 and 330 nm, shoulder at 520 nm) upon such CO release (Eq. 1a). It is thus evident that formation of the highly stable oxo-bridged diiron species allows the release of CO from $[(PaPy_3)Fe(CO)]ClO_4$ in aerated MeCN solution.

$$\mathbf{[(PaPy_3)Fe(CO)]^+ \xrightarrow[\text{Degassed MeCN}]{} No\ CO\ loss}$$

$$\mathbf{[(PaPy_3)Fe(CO)]^+ \xrightarrow[\text{MeCN, air}]{} [(PaPy_3)FeOFe(PaPy_3)]^{2+}} \qquad \textbf{(Eq. 1a)}$$

$$\mathbf{[(L)Fe(CO)]^{n+} \xrightarrow[\substack{\text{where L = } SBPy_3\text{ , Tpmen}\\ \text{Solvent (Solv)}\\ \text{MeCN, DMF, } H_2O}]{} [(L)Fe(Solv)]^{n+} + CO} \qquad \textbf{(Eq. 1b)}$$

The stronger tendency of $PaPy_3H$, a ligand with a carboxamide group, toward stabilization of the +3 oxidation state of iron drives the reaction in a completely different pathway in presence of dioxygen and makes this carbonyl an efficient CORM in aerated MeCN (and DMF). Because the other two ligands, namely $SBPy_3$ and Tpmen, are more supportive of the +2 oxidation state of iron, CO release from $[(SBPy_3)Fe(CO)](BF_4)_2$ and $[(Tpmen)Fe(CO)](ClO_4)_2$ gives rise to the solvated Fe(II) product in solution (Eq 1b) under both anaerobic and aerobic conditions.

The CO-releasing properties of these carbonyls have also been studied in aqueous phosphate buffer (PBS, pH 7.4) to assess their utility in biological experiments. As shown in Figure 2.5, smooth release of CO from $[(SBPy_3)Fe(CO)](BF_4)_2$ causes red shift of the 450 nm band to 572 nm with the emergence of a new band with λ_{max} at 400 nm. Clean isosbestic points are also observed at 496 and 430 nm. With $[(Tpmen)Fe(CO)](ClO_4)_2$, a similar red shift of the 330 nm band to 400 nm is noted upon CO release in solution (isosbestic point at 370 nm). The similarities between the final spectra of $[(SBPy_3)Fe(CO)](BF_4)_2$ and $[(Tpmen)Fe(CO)](ClO_4)_2$ in PBS and MeCN suggest that the end products are most possibly the aqua species $[(L)Fe(H_2O)]^{2+}$ (L = $SBPy_3$, Tpmen) in these reactions.

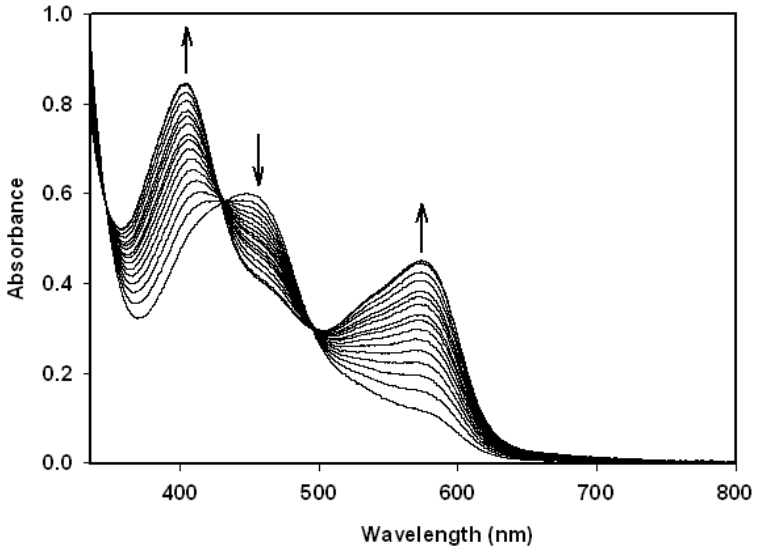

Figure 2.5. Changes in the electronic absorption spectrum of $[(SBPy_3)Fe(CO)](BF_4)_2$ (3.5 mM) upon dissolution (100 mM PBS, pH 7.4).

2.3.3. Delivery of CO to horse heart myoglobin

The designed carbonyls ($[(SBPy_3)Fe(CO)](BF_4)_2$ and $[(Tpmen)Fe(CO)](ClO_4)_2$ readily deliver CO to reduced myoglobin (Mb) under physiological conditions.

Because the carbonyls start CO release immediately upon dissolution, an excess (7-8 fold based on the amount of Mb) of each compound in PBS (pH 7.4) was required to completely convert reduced Mb to carbonyl myoglobin (Mb-CO) with solutions of the CORMs in such reactions. The rapid formation of Mb-CO was apparent within one minute of addition as evidenced by the shift of the Soret band from 435 to 424 nm (Figure 2.6). Mb-CO production levels off after 20 min in the case of $[(SBPy_3)Fe(CO)](BF_4)_2$ and 24 min for $[(Tpmen)Fe(CO)](ClO_4)_2$, with the final absorbance readings taken at 30 min.

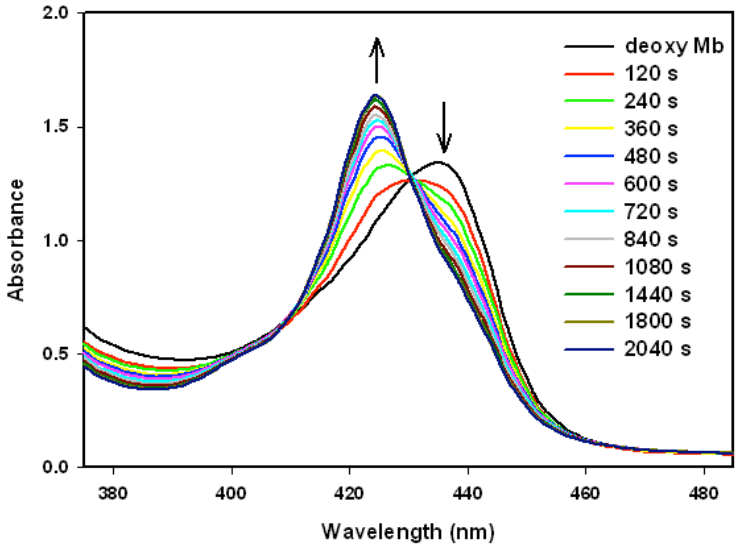

Figure 2.6. Delivery of CO from $[(Tpmen)Fe(CO)](ClO_4)_2$ to reduced Mb (λ_{max} = 435 nm), resulting in Mb-CO adduct (λ_{max} = 424 nm) in PBS pH 7.4.

While kinetic measurements predict a slower rate of CO release for $[(SBPy_3)Fe(CO)](BF_4)_2$ compared to $[(Tpmen)Fe(CO)](ClO_4)_2$, the Mb-based CO release test shows that both carbonyls generate CO at a similar rate over the same period of time. These resulting half-lives, defined as the time during which Mb-CO formation is 50% complete (~ 8 min for both species), are comparable to known

CORMs that release CO when dissolved. For instance, CORM-3 was reported to have a half life of 4-18 min,[12] while some Cr-based CORMs employing amino acids and amino ester ligands have half-lives of 7-9 min.[27]

2.3.4. Kinetic Measurements.

The utility of the metal carbonyls as CORMs depends critically on the apparent rates of CO loss (k_{CO}) under physiological conditions. In our work, we have determined the k_{CO} values of $[(SBPy_3)Fe(CO)](BF_4)_2$ and $[(Tpmen)Fe(CO)](ClO_4)_2$ in PBS (pH 7.4). The CO release from $[(SBPy_3)Fe(CO)](BF_4)_2$ and $[(Tpmen)Fe(CO)](ClO_4)_2$ was followed by recording the electronic spectra of the samples within one minute of dissolution in phosphate buffer and the absorbance values (at 450 nm and 330 nm respectively) were noted vs. time (in seconds). In both cases, CO release obeys a pseudo-first order behavior in aqueous buffer and the corresponding solvato species is generated upon CO dissociation. The kinetic plot of the apparent rate of CO loss by $[(SBPy_3)Fe(CO)](BF_4)_2$ is shown in Figure 2.7. Further decomposition of the solvated species in aqueous media, as noted in the overall decrease of the absorption, occurs at 45 and 30 min, respectively for these two CORMs.

We have compared the k_{CO} values of $[Ru(glycine)(CO)_3Cl]$ (CORM-3),[14] with that of $[(SBPy_3)Fe(CO)](BF_4)_2$ and $[(Tpmen)Fe(CO)](ClO_4)_2$ under similar conditions. The k_{CO} values for $[(SBPy_3)Fe(CO)](BF_4)_2$ and $[(Tpmen)Fe(CO)](ClO_4)_2$ are 7.5×10^{-4} s^{-1} and 3.7×10^{-3} s^{-1}, respectively. Under comparable conditions, CORM-3 affords a k_{CO} value of 1.5×10^{-3} s^{-1}. It thus appears that

$[(SBPy_3)Fe(CO)](BF_4)_2$ releases CO more slowly over a longer period of time compared to CORM-3 while the k_{CO} values of $[(Tpmen)Fe(CO)](ClO_4)_2$ and CORM-3 are quite comparable. The k_{CO} values of $[(SBPy_3)Fe(CO)](BF_4)_2$ and $[(Tpmen)Fe(CO)](ClO_4)_2$ in MeCN (1.3×10^{-3} s^{-1} and 6.3×10^{-3} s^{-1} respectively) are consistently faster than the values in aqueous buffer. This difference could arise from the fact that MeCN is a better donor for the Fe(II) center ligated to the polypyridine ligand.

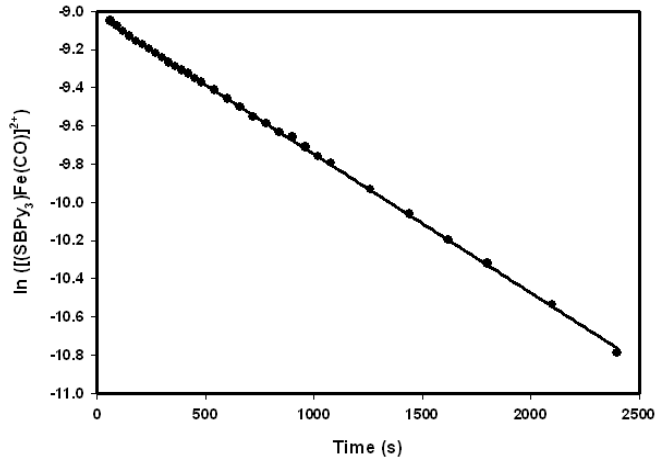

Figure 2.7. Plot of changes in $\ln([(SBPy_3)Fe(CO)]^{2+})$ vs time (s) in 0.1 M PBS, pH 7.4 as monitored by noting the absorbance values at 450 nm.

2.3.5. Vasorelaxation of mouse aorta

The vasorelaxation property of CO has been a subject of debate in relation to its binding and activating to sGC and the concomitant cGMP pathway.[28] Despite the low affinity of CO to sGC, relaxation of smooth muscle by CO via the cGMP pathway has been proposed. We have examined the effect(s) of CO release from the present carbonyls on mouse aorta muscle rings in tissue bath experiments. Both

[$(SBPy_3)Fe(CO)](BF_4)_2$ and [$(Tpmen)Fe(CO)](ClO_4)_2$ (30 nM-300 μM) produced concentration-dependent relaxations with EC_{50} values of 3.4 ± 0.2 μM and 26.2 ± 0.2 μM, respectively (Figure 2.8). These values are superior to values obtained with CORM-3 reported by Motterlini and coworkers.[13] Interestingly, we did not observe much inhibitory effect by 1H-[1,2,4]oxadiazolo[4,3-a]quinoxalin-1-one (ODQ), a common sGC inhibitor (Figure 2.9). In previous work, Motterlini and coworkers have reported initial inhibition by ODQ, which was eventually lost after repeated addition of CORM-3.[13]

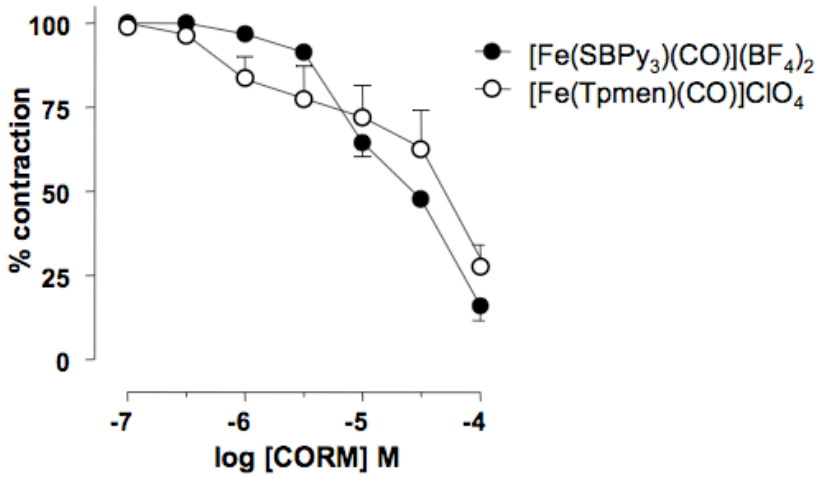

Figure 2.8. Vasorelaxation of mouse aorta muscle ring using [$(SBPy_3)Fe(CO)](BF_4)_2$ and [$(Tpmen)Fe(CO)](ClO_4)_2$ as a function of concentration.

It has been postulated that smooth muscle relaxation by CO could arise from its binding to the channel-bound heme of the large-conductance Ca^{2+}-activated K-channel (BK_{Ca}).[29] To test this hypothesis, we studied the effect of the BK_{Ca} channel blocker iberiotoxin on the inhibition of vasorelaxation by [$(Tpmen)Fe(CO)](ClO_4)_2$. Significant inhibition was indeed observed with this BK_{Ca} channel blocker while no

effect was noted with the K_{ATP} channel blocker glibenclamide or the non-selective K^+-channel blocker TEA (Figures 2.10-2.11). Clearly, more studies are required to determine the origin of vasorelaxation of smooth muscle by these CORMs. Nevertheless, the excellent vasorelaxation effects of merit attention as new CORMs that could be used to deliver CO under physiological conditions. Further studies on the mechanism of vasorelaxation by these CORMs are in progress in this laboratory.

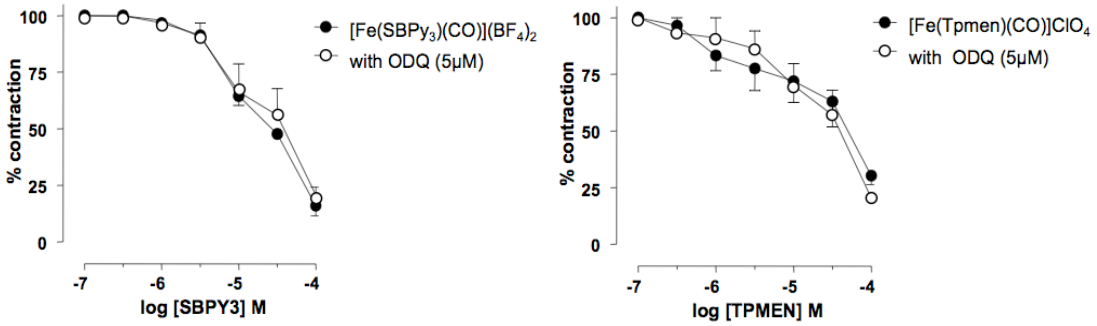

Figure 2.9. Vasorelaxation of mouse aorta muscle rings by $[(SBPy_3)Fe(CO)](BF_4)_2$ (left panel) and $[(Tpmen)Fe(CO)](ClO_4)_2$ (right panel) in the absence and presence of ODQ (5 μM).

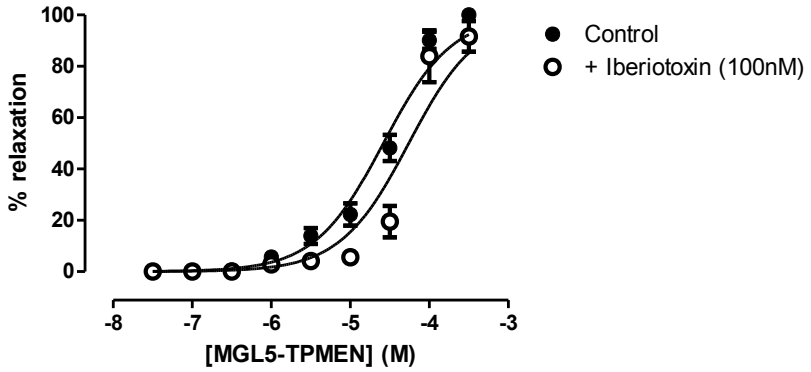

Figure 2.10. Inhibition of vasorelaxation in the presence of Iberiotoxin using $[(Tpmen)Fe(CO)](ClO_4)_2$ as a CO-donor.

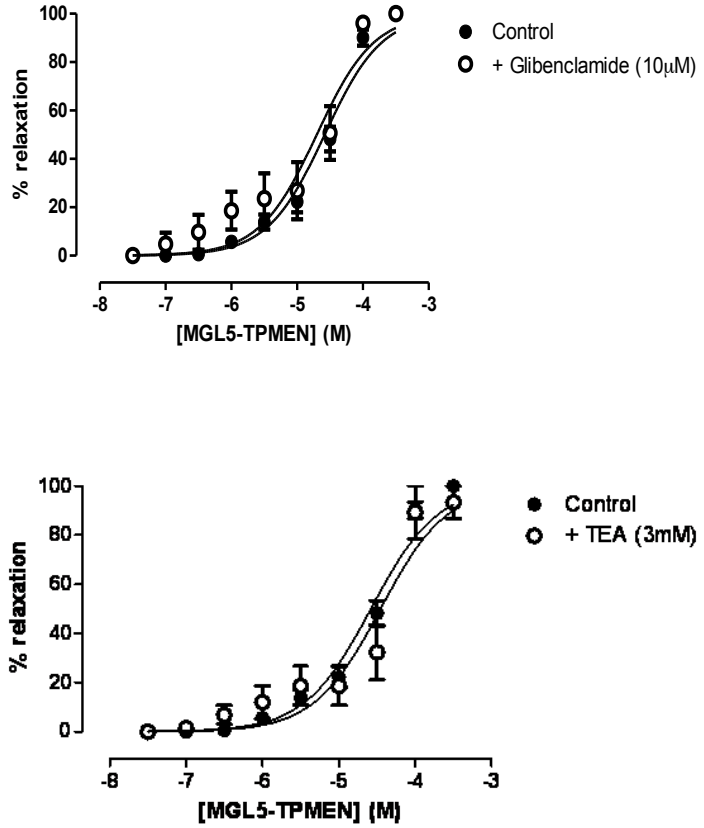

Figure 2.11. Effect of Glibenclamide and TEA on $[(Tpmen)Fe(CO)](ClO_4)_2$ – induced vasorelaxation of mouse aortic rings.

2.4. Experimental Section

Materials. Iron(II) tetrafluoroborate hexahydrate and iron (II) perchlorate hydrate were purchased from Aldrich Chemical Co. and used without further purification. CO gas was procured from Praxair. Horse heart myoglobin (Mb) was purchased from Aldrich and used as received. All solvents were dried by standard techniques and distilled prior to use. The ligands *N,N′*-bis(2-pyridylmethyl)amine-*N*-ethyl-2-pyridine-2-aldimine ($SBPy_3$)[26] and *N*-methyl-*N,N′,N′*-tris(2-pyridylmethyl)ethane-1,2-diamine (Tpmen)[30] were synthesized according to the literature procedures. The

Fe(II) starting salt $[Fe(MeCN)_4](ClO_4)_2$, was also synthesized by following the published procedure.[31]

Caution! Complexes of transition metal perchlorates with organic ligands are hazardous and may explode upon heating. Only small quantities must be handled with the proper protection.

$[(SBPy_3)Fe(CO)](BF_4)_2$. Under dinitrogen, a solution of 0.327 g (0.99 mmol) of $[Fe(H_2O)_6](BF_4)_2$ in 10 mL of MeOH was slowly added to a solution of 0.332 g (0.98 mmol) of $SBPy_3$ ligand in 20 mL MeOH and the deep purple solution was stirred for the next 1 h. Next, CO gas was bubbled through the solution when complex $[(SBPy_3)Fe(CO)](BF_4)_2$ separated out as a red solid within 3-5 min. The red solid thus obtained was filtered, washed with Et_2O and dried in vacuo (0.592 g, 60 % yield). Crystals suitable for X-ray diffraction, were grown by redissolving $[(SBPy_3)Fe(CO)](BF_4)_2$ in MeOH and storing under CO atmosphere at –20°C for 24 h. Anal. Calcd for $C_{21}H_{21}N_5OB_2F_8Fe$: C, 42.83; H, 3.59; N, 11.89. Found: C, 42.80; H 3.48; N, 11.94. Selected IR frequencies (cm^{-1}, KBr disk): 2010 (vs ν_{CO}), 1410 (w), 1053 (vs), 771 (s).

$[(Tpmen)Fe(CO)](ClO_4)_2$. A solution of 0.121 g (0.35 mmol) of Tpmen ligand in 30 mL of MeOH was degassed by freeze-pump-thaw cycles. To the frozen solution of the ligand, a batch of 0.144 g of $[Fe(MeCN)_4](ClO_4)_2$ was added as a solid. The frozen solution was warmed to room temperature in a warm water bath and the clear yellow solution was stirred under dinitrogen at room temperature for 1 h. Next, CO gas was bubbled through the solution when complex $[(Tpmen)Fe(CO)](ClO_4)_2$

separated as a beige solid within 5-10 min. The solid was filtered, washed with Et_2O and dried under vacuo (36% yield). X-ray quality crystals of were grown redissolving $[(Tpmen)Fe(CO)](ClO_4)_2$ in MeOH and storing under CO gas at –20°C for 24 h. Anal. Calcd for $C_{22}H_{25}N_5O_9Cl_2Fe$: C, 41.93; H, 4.00; N, 11.12. Found: C, 41.88; H 4.02; N, 10.77. Selected IR frequencies (cm^{-1}, KBr disk): 2010 (vs ν_{CO}), 1410 (w), 1053 (vs), 771 (s).

Physical Measurements. Electronic absorption spectra were recorded on a Varian Cary 50 Spectrophotometer. Infrared Spectra were obtained by using a Perkin-Elmer 1600 FTIR Spectrophotometer. Room temperature magnetic susceptibility values were measured by using a Johnson Matthey magnetic susceptibility balance. Diffraction data for $[(SBPy_3)Fe(CO)](BF_4)_2$ was collected at 150K on a D3 goniostat equipped with a Bruker APEXII CC detector at Beamline 11.3.1 at the Advanced Light Source (Lawrence Berkeley National Laboratory) using synchrotron radiation tuned to λ = 0.7749Å. The data frames were collected using the program APEX2 v2010.3.0 and processed using the program SAINT v7.60A within APEX2. The data were corrected for absorption and beam corrections based on the multi-scan technique as implemented in SADABS. Diffraction data for $[(Tpmen)Fe(CO)](ClO_4)_2$ was collected at 150 K on a Bruker APEX-II instrument using monochromated Mo-Kα radiation (λ = 0.71073 Å) and corrected for absorption. The structure was solved using direct methods (standard SHELXL-97 package). Due to extensive disorder of the perchlorate counterions and one enantiomer of complex $[(Tpmen)Fe(CO)](ClO_4)_2$ in the lattice, the final refinement of the structure of $[(Tpmen)Fe(CO)](ClO_4)_2$

presented problems. At this time, we have the preliminary structure that clearly depicts the overall connectivity of the atoms.

Measurements on the Apparent CO-release rate in solution. About 0.5-1 mg of $[(SBPy_3)Fe(CO)](BF_4)_2$ or $[(Tpmen)Fe(CO)](ClO_4)_2$ was placed in a quartz cuvette and 1 mL of solvent was added. The mixture was shaken to ensure complete dissolution and absorbance was recorded immediately (within 30 seconds of solvent addition). The rates of CO release of $[(SBPy_3)Fe(CO)](BF_4)_2$ and $[(Tpmen)Fe(CO)](ClO_4)_2$ were determined by monitoring the decrease in absorption at the λ_{max} of each compound in either MeCN or PBS (100mM, pH 7.4). The plots of concentration vs time were fitted to the three parameter exponential equation $C(t) = C_\infty + (C_o - C_\infty) \exp\{-k_{CO}t\}$, where C_o and C_∞ are the initial and final concentrations respectively. The apparent rate of CO loss (k_{CO}) was calculated from the ln(C) vs. time plot for each CORM.

Delivery of CO to Myoglobin. Horse heart myoglobin was dissolved in phosphate buffer (100 mM, pH 7.4) and reduced by adding sodium dithionite. The concentration of the deoxymyoglobin (Mb) generated was calculated from the absorbance of the Soret band at 435 nm (extinction coefficient = 121 $mM^{-1}cm^{-1}$). Based on the Mb concentration, a PBS solution of either $[(SBPy_3)Fe(CO)](BF_4)_2$ or $[(Tpmen)Fe(CO)](ClO_4)_2$ was added to the Mb solution and the initial absorbance was taken within one minute. Carbonmonoxymyoglobin (Mb-CO) production was monitored over time. A shift in λ_{max} from 435 nm to 424 nm was observed in each case due to formation of the Mb-CO. Final concentrations of Mb-CO were assessed at

424 nm (extinction coefficient = 207 $mM^{-1}cm^{-1}$) and compared to the initial Mb present in solution to quantify CO release by each compound.

CO delivery to mouse aorta. Male C57BLK6 mice (25–35 g) were stunned and killed by cervical dislocation. The thoracic aorta was carefully removed, cleaned of connective tissue and cut into three to four ring segments of approximately 4 mm in length. Aortic rings were mounted in 10 mL organ baths containing Krebs-bicarbonate buffer (composition (mM): Na^+ 143; K^+ 5.9; Ca^{2+} 2.5; Mg^{2+} 1.2; Cl^- 128; HCO_3^- 25; HPO_4^{2-} 1.2; SO_4^{2-} 1.2; D-glucose 11) maintained at 37°C and gassed with 95% O_2/5% CO_2. Tension was initially set at 0.3 g and reset at intervals following an equilibration period of 1 h during which time fresh Krebs-bicarbonate buffer was replaced every 15–20 min. After equilibration, the rings were primed with KCl (48 mM), washed and precontracted with phenylephrine (PE, 1 μM) was added. Once this response had stabilized, acetylcholine (ACh, 1μM) was added to the bath to assess the integrity of the endothelium. If the contractions to PE were not maintained, or relaxations greater than 50% of the PE-induced tone to ACh were not observed, the tissues were discarded.

Tissues were then washed for 30 min (by addition of fresh Krebs-bicarbonate buffer at 15 min intervals) after which cumulative concentrations of PE (1nM-1μM) were added to the organ bath. The tissues were then washed over 60 min to restore basal tone before contracting to approximately 80% of the maximum PE-induced response. Once a stable response to PE was achieved, cumulative concentration–

response curves to $[(SBPy_3)Fe(CO)](BF_4)_2$ (30 nM-100 μM) and $[(Tpmen)Fe(CO)](ClO_4)_2$ (30 nM-300 μM) were constructed.

To determine the role of soluble guanylate cyclase (sGC) in the vasorelaxant response to the CO-donors, concentration–response curves to both $[(SBPy_3)Fe(CO)](BF_4)_2$ and $[(Tpmen)Fe(CO)](ClO_4)_2$ were constructed in tissues in the absence or presence of the sGC inhibitor ODQ (1H-[1,2,4]oxadiazolo[4,3-a]quinoxalin-1-one, 5 μM). To investigate the effect of K^+-channel activation in the vasorelaxant response to the CO-donors, concentration–response curves to $[(Tpmen)Fe(CO)](ClO_4)_2$ were constructed in tissues in the absence or presence of the large-conductance calcium-activation K^+-channel (BK_{Ca}) blocker iberiotoxin (100 nM), the K_{ATP} channel blocker glibenclamide (10 μM), and the non-selective K^+-channel blocker tetraethylammonium (TEA; 3 mM) ion.

2.5. Additional Experimental Data: IR Spectra

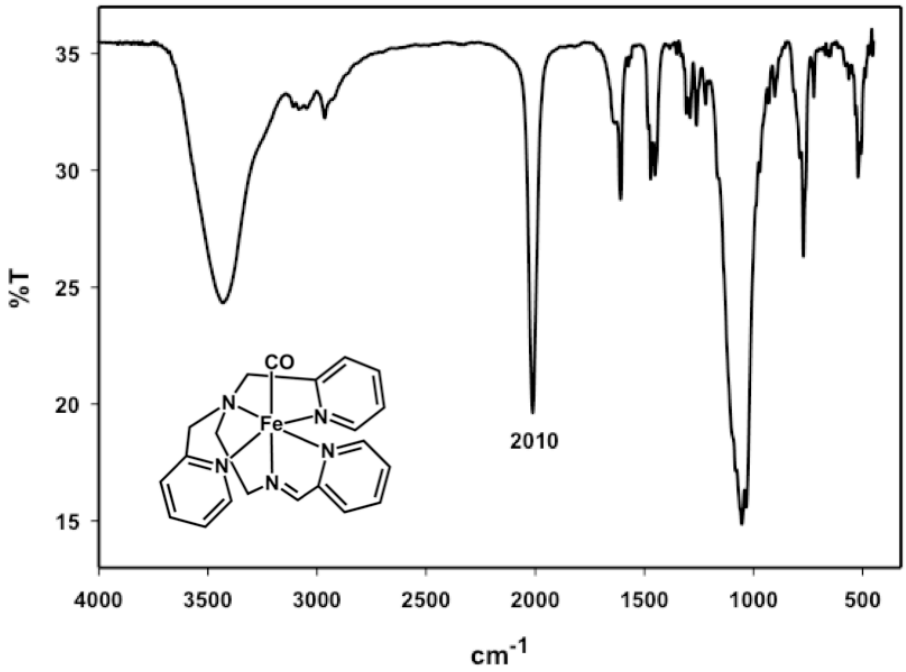

Figure 2.12. IR Spectrum of $[(SBPy_3)Fe(CO)](BF_4)_2$ in KBr pellet.

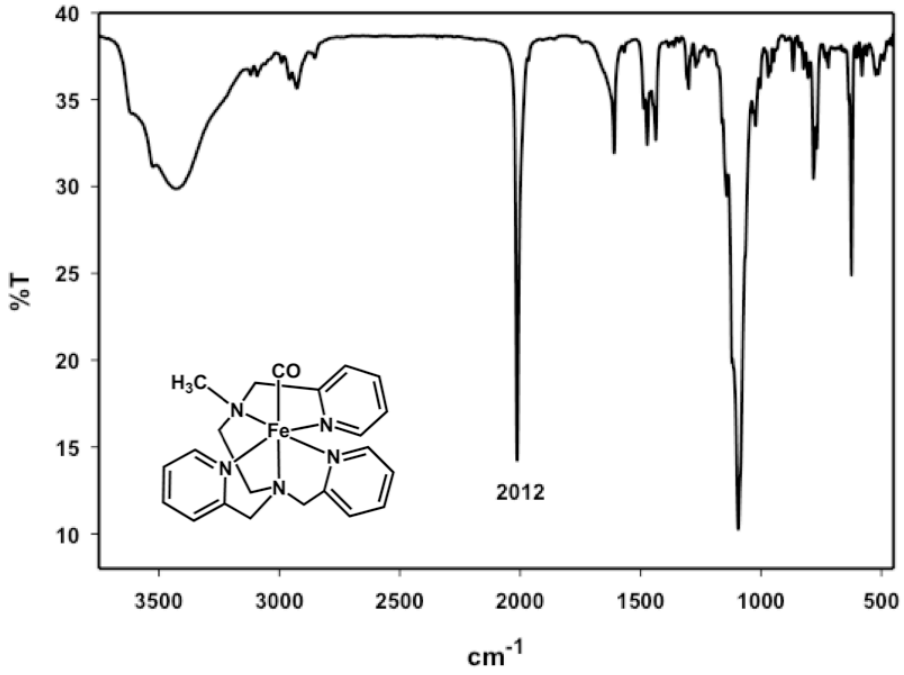

Figure 2.13. IR Spectrum of $[(Tpmen)Fe(CO)](BF_4)_2$ in KBr pellet.

2.6. References

(1) *Signal Transduction and the Gasotransmitters: NO, CO and H_2S in Biology and Medicine*; Wang, R. Humana Press: Totowa: New Jersey, 2004.

(2) Ignarro, L. J. *Nitric Oxide: Biology and Pathobiology*; Academic Press: San Diego, 2000.

(3) *Nitric Oxide Free Radicals in Peripheral Neurotransmission*; Kalsner, S., Ed.; Birkhauser: Boston, 2000.

(4) *Nitric Oxide and Infection*; Fang, F. C., Ed.; Kluwer Academic: New York, 1999.

(5) *Nitric Oxide and Cell: Proliferation, Differentiation and Death*; Moncada, S.; Higgs, E. A.; Bagetta, G., Eds.; Portland Press: London, 1998.

(6) Fukuto, J. M.; Collins, M. D. *Current Pharmaceutical Design* **2007**, *13*, 2952-2978.

(7) Li, L.; Hsu, A.; Moore, P. K. *Pharmacology & Therapeutics* **2009**, *123*, 386-400.

(8) *The Smallest Biomolecules: Diatomics and their Interactions with Heme Proteins*; Ghosh, A., Ed.; Elsevier: Amsterdam, 2008.

(9) (a) Kaczorowski, D. J.; Zuckerbraun, B. S. *Curr. Med. Chem*. **2007**, *14*, 2720-2725. (b) Kim, H. P.; Ryter, S. W.; Choi, A. M. K. *Ann. Rev. Pharmacol. Toxicol*. **2006**, *46*, 411-449.

(10) Hartsfeield, C. L. *Antioxid. Redox Signal*. **2002**, *4*, 301-307.

(11) (a) Johnson, T. R.; Mann, B. E.; Clark, J. E.; Foresti, R.; Green, C. J.; Motterlini, R. *Angew. Chem. Intl. Ed*. **2003**, *42*, 3722-3729. (b) Motterlini, R.; Clark, J. E.; Foresti, R.; Sarathchandra, P.; Mann, B. E.; Green, C. J. *Circ. Res*. **2002**, *90*, e17-e24.

(12) Clark, J. E.; Naughton, P.; Shurey, S.; Green, C. J.; Johnson, T. R.; Mann, B. E.; Foresti, R.; Motterlini, R. *Circ. Res.*, **2003**, *93*, e2-e8.

(13) Foresti, R.; Hammad, J.; Clark, J. E.; Johnson, T. R.; Mann, B. R.; Friebe, A.; Green, C. J.; Motterlini, R. *Brit. J. Pharmacol*. **2004**, *142*, 453-460.

(14) Alberto, R.; Motterlini, R. *Dalton Trans.* **2007**, 1651-1660.

(15) Sawle, P.; Hammad, J.; Fairlamb, I. J. S.; Moulton, B.; O'Brien, C. T.; Lynam, J. M.; Duhme-Klair A. K.; Foresti, R.; Motterlini, R. *J. Pharmacol. Expt. Therap*. **2006**, *318*, 403-410.

(16) Zhang, W. Q.; Atkin, A. J.; Thatcher, R. J.; Whitwood, A. C.; Fairlamb, I. J. S.; Lynam, J. M., *Dalton Trans*., **2009**, *49*, 4351-4358.

(17) (a) Eroy-Reveles, A. A.; Hoffman-Luca, C. G.; Mascharak, P. K. *Dalton Trans.* **2007**, 5268-5274. (b) Patra, A. K.; Rose, M. J.; Olmstead, M. M.; Mascharak, P. K. *J. Am. Chem. Soc*. **2004**, *126*, 4780-4781. (c) Patra, A. K.; Rowland, J. M.; Marlin, D. S.; Bill, E.; Olmstead, M. M.; Mascharak, P. K. *Inorg. Chem*. **2003**, *42*, 6812-6823. (d) Patra, A. K.; Afshar, R.; Olmstead, M. M.; Mascharak, P. K. *Angew. Chem. Int. Ed*. **2002**, *41*, 2512-2515.

(18) (a) Hoffman-Luca, C. G.; Eroy-Reveles, A. A.; Alvarenga, J.; Mascharak, P. K. *Inorg. Chem*. **2009**, *48*, 9104-9111. (b) Ghosh, K.; Eroy-Reveles, A. A.; Holman, T. R.; Olmstead, M. M.; Mascharak, P. K. *Inorg. Chem.* **2004**, *43*, 2988-2997.

(19) (a) Rose, M. J.; Mascharak, P. K. *Coord. Chem. Rev.* **2008**, *252*, 2093-2114. (b) Rose, M. J.; Mascharak, P. K. *Curr. Opin. Chem. Biol*. **2008**, *12*, 238-244.

(20) (a) Rose, M. J.; Patra, A. K.; Olmstead, M. M.; Mascharak, P. K. *Inorg. Chem.* **2007**, *46*, 2328-2338. (b) Patra, A. K.; Rose, M. J.; Murphy, K. A.; Olmstead, M. M.; Mascharak, P. K. *Inorg. Chem*. **2004**, *43*, 4487-4495. (c) Patra, A. K.; Mascharak, P. K. *Inorg. Chem*. **2003**, *42*, 7363-7365.

(21) (a) Rose, M. J.; Mascharak, P. K. *Inorg. Chem.* **2009**, *48*, 6904-6917. (b) Rose, M. J.; Olmstead, M. M.; Mascharak, P. K. *J. Am. Chem. Soc.* **2007**, *129*, 5342-5343.

(22) (a) Eroy-Reveles, A. A.; Mascharak, P. K. *Future Med. Chem*. **2009**, *1(8),* 1497-1507. (b) Eroy-Reveles, A. A.; Leung, Y.; Beavers, C. M.; Olmstead, M. M.; Mascharak, P. K. *J. Am. Chem. Soc*. **2008**, *130*, 4447-4458. (c) Eroy-Reveles, A. A.; Leung, Y.; Mascharak, P. K. *J. Am. Chem. Soc.* **2006**, *128*, 7166-7167.

(23) Afshar, R. K.; Patra, A. K.; Bill, E.; Olmstead, M. M.; Mascharak, P. K. *Inorg. Chem.*, **2006**, *45*, 3374-3781.

(24) Vaska, L.; Yamaji, T. *J. Am. Chem. Soc*. **1971**, *93*, 6673-6674.

(25) Salzmann, R.; Ziegler, C. J.; Godbout, N.; McMahon, M. T.; Suslick, K. S.; Oldfield, E. *J. Am. Chem. Soc*. **1998**, *120*, 11323-11334.

(26) Patra, A. K.; Olmstead, M. M.; Mascharak, P. K., *Inorg. Chem.*, **2002**, *41*, 5403-5409.

(27) Zhang, W. Q.; Whitwood, A. C.; Fairlamb, I. J. S.; Lynam, J. M., *Inorg. Chem.*, **2010**, *49*, 8941-8952.

(28) Wang, R.; Wang, Z.; Wu, L., *Brit. J. Pharmacol.*, **1997**, *121*, 927-934.

(29) (a) Wu, L.; Wang, Z.; Wang, R., *Can. J. Physiol. Pharmacol.,* **2000**, *78*, 696-707. (b) Wu, L.; Cao, K.; Lu, Y.; Wang, R., *J. Clin. Invest.*, **2002**, *110*, 691-700. (c) Wang, R.; Wu, L.; Wang, Z., *Pflügers Arch- Eur. J. Physiol.*, **1997**, *434*, 285-291.

(30) Bernal, I.; Jensen, I. M.; Jensen, K. B.; McKenzie, C. J.; Toftlund, H.; Tuchagues, J.-P. *J. Chem. Soc. Dalton Trans*. **1995**, 3667-3675.

(31) Sugimoto, H.; Sawyer, D. T. *J. Am. Chem. Soc*. **1985**, *107*, 5712-5716.

2.7 Reprint of Publication

(1) Gonzalez, M. A.; Fry, N. L.; Burt, R.; Davda, R.; Hobbs, A. J.; Mascharak, P. K., "Designed Iron Carbonyls as Carbon Monoxide (CO) Releasing Molecules: Rapid CO Release and Delivery to Myoglobin in Aqueous Buffer and Vasorelaxation of Mouse Aorta," *Inorg. Chem.*, **2011**, *50*, 3127-3134.

Reprinted with Permission from the American Chemical Society, Copyright 2011

Inorganic Chemistry

ARTICLE

pubs.acs.org/IC

Designed Iron Carbonyls as Carbon Monoxide (CO) Releasing Molecules: Rapid CO Release and Delivery to Myoglobin in Aqueous Buffer, and Vasorelaxation of Mouse Aorta

Margarita A. Gonzalez,[†] Nicole L. Fry,[†] Richard Burt,[‡] Riddhi Davda,[‡] Adrian Hobbs,[*,‡] and Pradip K. Mascharak[*,†]

[†]Department of Chemistry and Biochemistry, University of California, Santa Cruz, California 95064, United States

[‡]Department of Pharmacology, University College, London WC1E 6BT, U.K.

Supporting Information

ABSTRACT: The physiological roles of CO in neurotransmission, vasorelaxation, and cytoprotective activities have raised interest in the design and syntheses of CO-releasing materials (CORMs) that could be employed to modulate such biological pathways. Three iron-based CORMs, namely, $[(PaPy_3)Fe(CO)](ClO_4)$ (**1**), $[(SBPy_3)Fe(CO)](BF_4)_2$ (**2**), and $[(Tpmen)Fe(CO)](ClO_4)_2$ (**3**), derived from designed polypyridyl ligands have been synthesized and characterized by spectroscopy and X-ray crystallography. In these three Fe(II) carbonyls, the CO is trans to a carboxamido-N (in **1**), an imine-N (in **2**), and a tertiary amine-N (in **3**), respectively. This structural feature has been correlated to the strength of the Fe-CO bond. The CO-releasing properties of all three carbonyls have been studied in various solvents under different experimental conditions. Rapid release of CO is observed with **2** and **3** upon dissolution in both aqueous and nonaqueous media in the presence and absence of dioxygen. With **1**, CO release is observed only under aerobic conditions, and the final product is an oxo-bridged diiron species while with **2** and **3**, the solvent bound $[(L)Fe(CO)]^{2+}$ (where L = $SBPy_3$ or Tpmen) results upon loss of CO under both aerobic and anaerobic conditions. The apparent rates of CO loss by these CORMs are comparable to other CORMs such as $[Ru(glycine)(CO)_3Cl]$ reported recently. Facile delivery of CO to reduced myoglobin has been observed with both **2** and **3**. In tissue bath experiments, **2** and **3** exhibit rapid vasorelaxation of mouse aorta muscle rings. Although the relaxation effect is not inhibited by the soluble guanylate cyclase inhibitor ODQ, significant inhibition is observed with the BK_{Ca} channel blocker iberiotoxin.

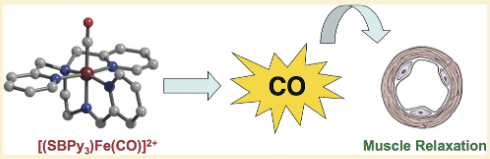

INTRODUCTION

During the past three decades, three small "toxic" molecules namely nitric oxide (NO), carbon monoxide (CO), and hydrogen sulfide (H_2S) have drawn much attention because of their surprising and unexpected roles in numerous physiological processes.[1] The surge of interest in these "biologically relevant gases" all began with NO. What once was viewed as an environmental pollutant, NO, has now been shown to participate in a myriad of physiological and pathological processes including vasodilation,[2] neurotransmission,[3] immune response,[4] and cellular apoptosis.[5] More recently, CO and H_2S have also been identified as important signaling molecules.[1,6,7] While the role of NO in several biological pathways has been established firmly, research on the mechanistic role of H_2S is in its infancy. Among this series of gasotransmitters, NO and CO possess the greatest number of similarities—both known to interact with metalloproteins, particularly those bearing heme moieties.[8] Consequently, the biological relevance of CO, an endogenously produced gaseous molecule, has been emerging at a faster rate during the past few years.[9,10] The bulk of CO in tissues and cells is generated from the catabolism of heme by heme oxygenase (HO)[11] while minor amounts are derived from iron-catalyzed lipid peroxidation. CO, like NO, has been implicated in regulatory functions including neurotransmission, vasorelaxation, and cytoprotective activity. For instance, while NO is known to have a greater binding affinity for soluble guanylyl cyclase (sGC),[12] it has been determined that sGC is able to bind CO thus supporting the notion of CO-mediated vasorelaxation through cGMP attenuation.[9,12] Other pathways for CO-mediated signaling include a cytochrome p450-based monooxygenase system,[13] and modulation of K^+-channels.[14] Perhaps the most interesting feature of CO is its ability to exert cytoprotective action. CO has been found to protect against hyperoxic lung injury,[15] organ transplant rejection,[16] and to promote mitochondrial biogenesis.[17]

To effectively induce the desirable biological effects of CO at a targeted site, controlled site-specific delivery of CO to tissues is

Received: January 13, 2011
Published: March 08, 2011

ACS Publications © 2011 American Chemical Society

required and the product after CO-release must remain benign. CO is a ubiquitous ligand in organometallic chemistry. Not surprisingly, the early CORMs were mostly homo and heteroleptic transition metal carbonyls (CO complexes) such as $[Fe(CO)_5]$, $[Mn_2(CO)_{10}]$, and $[\{Ru(CO)_3Cl_2\}]_2$.[18] The kinetics (and trends) of CO release from metal carbonyls (M = Cr, Mo, W) upon solvation has been studied by Lynam and coworkers.[19] These prototypical carbonyls manifested CO delivery to substrates, with the limitation of only being soluble in aprotic solvents, particularly dimethylsulfoxide (DMSO). [Ru(glycine)$(CO)_3Cl$], developed by Motterlini and co-workers (and often referred to as CORM-3), was one of the first compounds to be found soluble in aqueous media.[20] This CORM effectively mimics the vasorelaxing and cardioprotective properties associated with CO produced endogenously.[20−22] Further efforts in preparing metal carbonyls as therapeutics focused on the incorporation of a biocompatible ligand to facilitate CO delivery. As nontoxic leaving groups, amino acids and amino esters have been utilized as ligands in the preparation of group 6-based CORMs.[23] The involvement of 2-pyrone functionalities in metabolic pathways has also led to the syntheses of Fe and Mo-based CORMs bearing a pyrone moiety.[24] As with all of the previously reported CORMs, these carbonyls release CO rapidly upon dissolution. In a recent account, Schatzschneider and coworkers have reported a tricarbonyl complex $[Mn(CO)_3(tmp)](PF_6)$ [tmp = tris(pyrazolylmethane)] that releases CO upon irradiation with UV light.[25,26] The limited applicability of the reported metal carbonyls in CO delivery to biological targets has, however, kept the search for new water-soluble CORMs with predictable CO-releasing properties ongoing.

Previously, we have reported several designed metal nitrosyls (NO complexes of metals such as Fe, Mn, and Ru) that rapidly deliver NO upon exposure to lights of a wide range of wavelengths (400−1000 nm).[27−32] Such NO donors have been employed to inhibit enzymes,[33] trigger apoptosis in human breast cancer cells,[34] and eradicate pathogenic bacteria[35] under the control of light. To explore whether the design principles could be utilized in synthesizing CORMs, we have now investigated the CO-releasing behavior of three iron carbonyls derived from three pentadentate polypyridine ligands shown in Figure 1. These ligands are expected to stabilize Fe(II) centers and allow CO binding. Although the synthesis and structure of the Fe(II) carbonyl derived from *N*,*N*′-bis(2-pyridyl-methyl)amine-*N*-ethyl-2-pyridine-2-carboxamide ($PaPy_3H$), namely, $[(PaPy_3)Fe(CO)](ClO_4)$ (**1**), were reported by us in a previous account,[36] the CO-releasing property was not studied. In the present work, we have synthesized and characterized two more Fe(II) carbonyls derived from related ligands, namely, *N*,*N*′-bis(2-pyridylmethyl)amine-N-ethyl-2-pyridine-2-aldimine ($SBPy_3$) and *N*-methyl-*N*,*N*′,*N*′-tris(2-pyridylmethyl)ethane-1,2-diamine (Tpmen). In the structurally related series $[(PaPy_3)Fe(CO)](ClO_4)$ (**1**), $[(SBPy_3)Fe(CO)](BF_4)_2$ (**2**), and $[(Tpmen)Fe(CO)](ClO_4)_2$ (**3**), the design allowed us to place CO trans to a carboxamido-N (strong σ-donor), an imine-N (moderately π-accepting) and a tertiary amine-N (weak σ-donor) center, respectively. The structures of **2** and **3** and their spectroscopic properties are reported in this paper. All three carbonyls are soluble in aqueous buffers and rapidly release CO in such solutions. The CO-releasing parameters of **1**−**3** have been carefully evaluated both in acetonitrile (in presence and absence of dioxygen) and in aerated aqueous phosphate buffer. The extent of CO release from **2** and **3** has been assessed using myoglobin assay under physiological conditions. Finally, the utility of these new CORMs has been demonstrated in relaxation of mouse aortic smooth muscle tissue in vitro, and the possible pathways of CO-mediated relaxation are discussed.

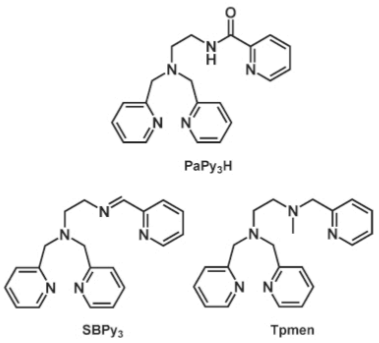

Figure 1. Structures of the designed ligands used in this study.

EXPERIMENTAL SECTION

Materials. Iron(II) tetrafluoroborate hexahydrate and Iron(II) perchlorate hydrate were purchased from Aldrich Chemical Co. and used without further purification. CO was procured from Praxair. Horse heart myoglobin (Mb) was purchased from Aldrich and used as received. All solvents were dried by standard techniques and distilled prior to use. The ligands $SBPy_3$ and Tpmen were synthesized according to the literature procedures.[37,38] The Fe(II) starting salt $[Fe(MeCN)_4](ClO_4)_2$, was also synthesized by following the published procedure.[39]

. ***Caution!*** *Complexes of transition metal perchlorates with organic ligands are hazardous and may explode upon heating. Only small quantities must be handled with the proper protection.*

Syntheses of Compounds. *[(SBPy$_3$)Fe(CO)](BF$_4$)$_2$ (**2**).* Under dinitrogen, a solution of 0.415 g (0.99 mmol) of $[Fe(MeCN)_4](ClO_4)_2$ in 10 mL of MeOH was slowly added to a solution of 0.332 g (0.98 mmol) of $SBPy_3$ ligand in 20 mL of MeOH, and the deep purple solution was stirred for the next 1 h. Next, CO was bubbled through the solution when complex **2** separated out as a red solid within 3−5 min. The red solid thus obtained was filtered, washed with Et_2O, and dried in vacuo (0.592 g, 60% yield). Crystals of $[(SBPy_3)Fe(CO)](BF_4)_2$, suitable for X-ray diffraction, were grown by redissolving **2** in MeOH and storing under CO atmosphere at −20 °C for 24 h. Anal. Calcd for $C_{21}H_{21}N_5OB_2F_8Fe$: C, 42.83; H, 3.59; N, 11.89. Found: C, 42.80; H 3.48; N, 11.94. Selected IR frequencies (cm^{-1}, KBr disk): 2010 (vs ν_{CO}), 1471 (w), 1053 (vs), 771 (s).

*[(Tpmen)Fe(CO)](ClO$_4$)$_2$ (**3**).* A solution of 0.121 g (0.35 mmol) of Tpmen ligand in 30 mL of MeOH was degassed by freeze−pump−thaw cycles. To the frozen solution of the ligand, a batch of 0.144 g (0.35 mmol) of $[Fe(MeCN)_4](ClO_4)_2$ was added as a solid. The frozen solution was warmed to room temperature in a warm water bath, and the clear yellow solution was stirred under dinitrogen at room temperature for 1 h. Next, CO was bubbled through the solution when complex **3** separated as a beige solid within 5−10 min. The solid was filtered, washed with Et_2O, and dried under vacuo (0.083 g, 38% yield). X-ray quality crystals of $[(Tpmen)Fe(CO)](ClO_4)_2$ were grown by redissolving **3** in MeOH and storing under CO at −20 °C for 24 h. Anal. Calcd for $C_{22}H_{25}N_5O_9Cl_2Fe$: C, 41.93; H, 4.00; N, 11.12. Found: C, 41.88; H

Table 1. Summary of Crystal Data, Intensity Collection, and Refinement Parameters for $[(SBPy_3)Fe(CO)](BF_4)_2$ (2)

empirical formula	$C_{21}H_{21}N_5OB_2F_8Fe$
formula weight	588.90
crystal color	red blocks
crystal size (mm^3)	0.04 × 0.03 × 0.03
temperature (K)	150(2)
wavelength (Å)	0.77490
crystal system	orthorhombic
space group	$Pca2_1$
a (Å)	12.9790(5)
b (Å)	12.2232(5)
c (Å)	15.0473(5)
α (deg)	90.00
β (deg)	90.00
γ (deg)	90.00
V ($Å^3$)	2387.18(16)
Z	4
d_{cal} (g/cm^3)	1.639
μ (mm^{-1})	0.852
GOF[a] on F^2	1.036
final R indices	R_1 = 0.0648
$[I > 2\sigma(I)]$	wR_2 = 0.1766
R indices[b]	R_1 = 0.0833
all data[c]	wR_2 = 0.1952

[a] GOF = $[\Sigma[w(F_o^2 - F_c^2)^2]/(N_o - N_v)]^{1/2}$ (N_o = number of observations, N_v = number of variables). [b] $R_1 = \Sigma||F_o| - |F_c||/\Sigma|F_o|$. [c] $wR_2 = [\Sigma w(F_o^2 - F_c^2)^2/\Sigma w(F_o^2)^2]^{1/2}$.

Table 2. Selected Bond Distances (Å) and Angles (deg) for $[(SBPy_3)Fe(CO)](BF_4)_2$ (2)

Fe−C21	1.805(7)
C21−O1	1.122(8)
Fe−N1	1.968(5)
Fe−N2	1.968(5)
Fe−N3	2.003(5)
Fe−N4	1.926(5)
Fe−N5	1.998(5)
Fe−C21−O1	177.9(6)
C21−Fe−N4	176.5(3)

4.02; N, 10.77. Selected IR frequencies (cm^{-1}, KBr disk): 2012 (vs ν_{CO}), 1472 (w), 1093 (vs), 771 (s), 624 (s).

Physical Measurements. Electronic absorption spectra were recorded on a Varian Cary 50 Spectrophotometer. Infrared Spectra were obtained by using a Perkin-Elmer 1600 FTIR Spectrophotometer. Room temperature magnetic susceptibility values were measured by using a Johnson Matthey magnetic susceptibility balance. Diffraction data for **2** was collected at 150 K on a D3 goniostat equipped with a Bruker APEXII CC detector at Beamline 11.3.1 at the Advanced Light Source (Lawrence Berkeley National Laboratory) using synchrotron radiation tuned to λ = 0.7749 Å. The data frames were collected using the program APEX2 v2010.3.0 and processed using the program SAINT v7.60A within APEX2. The data were corrected for absorption and beam corrections based on the multiscan technique as implemented in SADABS. Diffraction data for **3** was collected at 150 K on a Bruker APEX-II instrument using monochromated Mo−Kα radiation (λ = 0.71073 Å) and corrected for absorption. The structure was solved using direct methods (standard SHELXL-97 package). Machine parameters, crystal data, and data collection parameters for **2** are summarized in Table 1 while selected bond distances and angles are listed in Table 2. Complete crystallographic data for **2** have been submitted as Supporting Information. Because of extensive disorder of the perchlorate counterions and one enantiomer of complex **3** in the lattice, the final refinement of the structure of **3** presented problems. At this time, we have the preliminary structure that clearly depicts the overall connectivity of the atoms (see Supporting Information, Figure S1). The final structure will be reported in due time.

Measurements on the Apparent CO-Release Rate in Solution. About 0.5−1 mg of **2** or **3** was placed in a quartz cuvette, and 1 mL of solvent was added. The mixture was shaken to ensure complete dissolution, and absorbance was recorded immediately. The rates of CO release of **2** and **3** were determined by monitoring the decrease in absorption at the λ_{max} of each compound in either MeCN or PBS (100 mM, pH 7.4). The plots were fitted to the three parameter exponential equation $A(t) = A_\infty + (A_o - A_\infty)\exp\{-k_{CO}t\}$, where A_o and A_∞ are the initial and final absorbance values, respectively. The apparent rate of CO loss (k_{CO}) was calculated from the ln(C) versus time plot for each CORM.

Delivery of CO to Myoglobin. Horse heart myoglobin was dissolved in phosphate buffered saline (PBS, 100 mM, pH 7.4) and reduced by adding sodium dithionite. The concentration of the deoxymyoglobin (Mb) generated was calculated from the absorbance of the Soret band at 435 nm (extinction coefficient = 121 mM^{-1} cm^{-1}). On the basis of the Mb concentration, we added a PBS solution of either **2** or **3** to the Mb solution, and the initial absorbance was taken within 1 min. Carbonyl myoglobin (Mb-CO) production was monitored over time. A shift in λ_{max} from 435 to 424 nm was observed in each case because of formation of the Mb-CO. Final concentrations of Mb-CO were assessed at 424 nm (extinction coefficient =207 mM^{-1} cm^{-1}) and compared to the initial Mb present in solution to quantify CO release by each compound.

CO Delivery to Mouse Aorta. Male CS7BLK6 mice (25−35 g) were stunned and killed by cervical dislocation. The thoracic aorta was carefully removed, cleaned of connective tissue, and cut into three to four ring segments of approximately 4 mm in length. Aortic rings were mounted in 10 mL organ baths containing Krebs-bicarbonate buffer (composition (mM): Na^+ 143; K^+ 5.9; Ca^{2+} 2.5; Mg^{2+} 1.2; Cl^- 128; HCO_3^- 25; HPO_4^{2-} 1.2; SO_4^{2-} 1.2; D-glucose 11) maintained at 37 °C and gassed with 95% O_2/5% CO_2. Tension was initially set at 0.3 g and reset at intervals following an equilibration period of 1 h during which time fresh Krebs-bicarbonate buffer was replaced every 15−20 min. After equilibration, the rings were primed with KCl (48 mM), washed, and precontracted phenylephrine (PE, 1 μM) was added. Once this response had stabilized, acetylcholine (ACh, 1 μM) was added to the bath to assess the integrity of the endothelium. If the contractions to PE were not maintained, or relaxations greater than 50% of the PE-induced tone to ACh were not observed, the tissues were discarded.

Tissues were then washed for 30 min (by addition of fresh Krebs-bicarbonate buffer at 15 min intervals) after which cumulative concentrations of PE (1 nM−1 μM) were added to the organ bath. The tissues were then washed over 60 min to restore basal tone before contracting to approximately 80% of the maximum PE-induced response. Once a stable response to PE was achieved, cumulative concentration−response curves to **2** (30 nM−100 μM) and **3** (30 nM−300 μM) were constructed.

To determine the role of soluble guanylate cyclase (sGC) in the vasorelaxant response to the CO-donors, concentration−response curves to both **2** and **3** were constructed in tissues in the absence or presence of the sGC inhibitor ODQ (1H-[1,2,4]oxadiazolo[4,3-a]quinoxalin-1-one, 5 μM). To investigate the effect of K^+-channel activation in the vasorelaxant response to the CO-donors, concentration−response curves to **3** were constructed in tissues in the absence or presence of the large-conductance calcium-activation K^+-channel

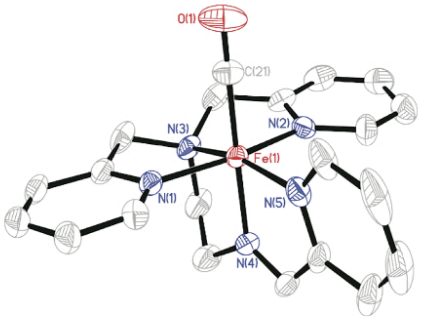

Figure 2. Thermal ellipsoid (probability level 30%) plot of $[(SBPy_3)Fe(CO)]^{2+}$ (cation of **2**) with the atom labeling scheme. H atoms have been omitted for the sake of clarity.

(BK_{Ca}) blocker iberiotoxin (100 nM), the K_{ATP} channel blocker glibenclamide (10 μM), and the nonselective K^+-channel blocker tetraethylammonium (TEA; 3 mM) ion.

RESULTS AND DISCUSSION

Reactions of the pentadentate ligands of Figure 1 with $[Fe(MeCN)_4](ClO_4)_2$ in MeOH results in formation of the solvent-bound species $[(L)Fe(MeOH)]^{n+}$ which upon exposure to CO affords the desired Fe(II) carbonyls **1**−**3**. In case of $PaPy_3H$, the presence of a base (Et_3N) is required for deprotonation of the carboxamide group.[36] The presence of the solvent-bound species in these reactions has been confirmed by the isolation and structural characterization of $[(SBPy_3)Fe(MeCN)](BF_4)_2$ when $SBPy_3$ is allowed to react with $[Fe(MeCN)_4](ClO_4)_2$ in MeCN.[37] Replacement of the bound solvent molecule with CO is quite rapid, and the carbonyls crystallize out of the MeOH solutions when kept under CO atmosphere at low temperature. In solid state, all three carbonyls are indefinitely stable at room temperature.

A strong CO stretch (ν_{CO}) at 1972 (for **1**), 2010 (for **2**), and 2012 (for **3**) cm^{-1} confirms the presence of bound CO ligand in the three carbonyls. These ν_{CO} values are within the range noted for other Fe(II) complexes with Fe(II)-CO bonds. For example, *trans*-[(TPP)Fe(1-MeIm)(CO)] (where TPP = 5,10,15,20-tetraphenylporphinate ligand, 1-MeIm = I-methylimidazole)[40] exhibits its ν_{CO} at 1969 cm^{-1} while *trans*-$[(DPGH)_2Fe(py)(CO)]$ (where DPGH = bidentate diphenylglyoximato univalent anion)[41] displays its ν_{CO} at 1996 cm^{-1}. Comparison of the ν_{CO} values of structurally similar carbonyls **1**−**3** reveals an interesting trend. The change from a strong σ-donating and negatively charged carboxamido-N donor in **1** to a neutral (and moderately π-accepting) imine-N or weak tertiary-N donor (in **2** and **3** respectively), increases the ν_{CO} value from 1972 to 2010−2012 cm^{-1}. This increase in ν_{CO} value clearly demonstrates that as more electron density is pushed toward the Fe(II) center, it transfers part of the electron density to the antibonding orbital of the bound CO ligand trans to it (as is the case in **1**). Such transfer strengthens the Fe−C(O) bond in **1** more than the other two carbonyls and makes it a slow CO-releasing molecule (vide infra).

The low-spin configuration of the Fe(II) center in **1**−**3** has been confirmed by their diamagnetism in solid state. The

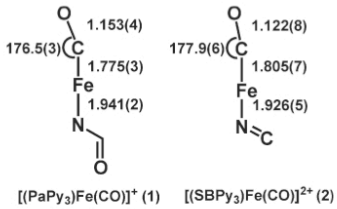

$[(PaPy_3)Fe(CO)]^+$ (**1**) $[(SBPy_3)Fe(CO)]^{2+}$ (**2**)

Figure 3. Comparison of the metric parameters and axial coordination of **1** and **2**.

Mössbauer parameters (δ = 0.15 mm s^{-1}, $|\Delta E_Q|$ = 0.74 mm s^{-1}) of **1** also corroborate this assignment.[36] Out of the three carbonyls, only **1** does not lose CO in degassed aprotic solvents like MeCN. This fact allowed us to acquire a clean ^1H NMR spectrum in CD_3CN in our previous study.[36]

Structures of the Complexes. $[(SBPy_3)Fe(CO)](BF_4)_2$ (2). The structure of $[(SBPy_3)Fe(CO)]^{2+}$, cation of **2**, is shown in Figure 2, and selected metric parameters are listed in Table 2. The Fe(II) center is situated in an octahedral environment with the imine N trans to CO, while the remaining N donors (three pyridine-N and one tertiary amine-N) are in the equatorial plane. Much like **1**, the Fe−C(O) bond angle is almost linear (176.5(3)°). Similar Fe−C(O) bond angles have been noted with other low-spin Fe(II) carbonyl complexes such as *trans*-$[(DPGH)_2Fe(py)(CO)]$ (178°).[41]

Comparison of the structural parameters of **2** with that of **1** reveals interesting similarities and differences (Figure 3). The Fe−C(O) bond distance observed for **2** (1.805(7) Å) is noticeably longer than that observed in **1** (1.775(3) Å). The C−O bond length in **2** (1.122(8) Å) is, however, shorter than that in **1** (1.153(4) Å). The elongated Fe−C(O) and shorter C−O bond distances observed in **2** suggest a reduced degree of π-backbonding in this complex compared to **1**. The Fe−N_{imine} bond length of 1.926(5) Å further supports reduced backbonding character in **2**, as the imine group is able to accept electron density from the metal center. These structural parameters are consistent with the facile CO release observed with **2** (vide infra).

[(Tpmen)Fe(CO)](ClO$_4$)$_2$ (3). As mentioned above, the structure of **3** has not been fully characterized because of disorder problems in the crystal lattice. Exchange of counterions did not provide any respite. In the *preliminary structure* of the perchlorate salt, the connectivity of atoms, however, is quite clear (Supporting Information, Figure S1). The CO is trans to the tertiary amine-N while three pyridyl-Ns and the second tertiary N (with CH_3 group attached to it) are coordinated to the iron center in the equatorial plane.

Electronic Absorption Spectra and CO-Release in Solution. In the present study, the behavior of **1**−**3** in solution has been studied in detail to evaluate their capacity as CORMs. The electronic absorption spectra of **1**−**3** have been acquired in MeCN and phosphate buffer (PBS, pH = 7.4) via rapid dissolution and quick data collection. The color of the solutions of all the carbonyls intensifies upon loss of CO and significant changes with distinct isosbestic points are noted in their electronic absorption spectra. For example, **2** exhibits a strong metal-to-ligand charge transfer (MLCT) band with λ_{max} at 455 nm in MeCN which shifts to 555 nm upon CO release and the color changes from red to deep magenta. Clean isosbestic points are noted at 485, 415, and 340 nm (Supporting Information, Figure S2). The final spectrum (obtained

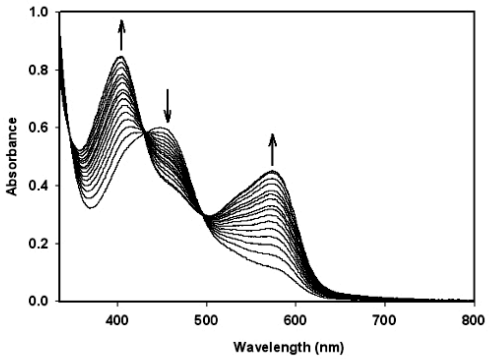

Figure 4. Electronic absorption spectrum of $[(SBPy_3)Fe(CO)](BF_4)_2$ (**2**) in 0.1 M PBS, pH 7.4 (concentration of **2** = 3.5 mM).

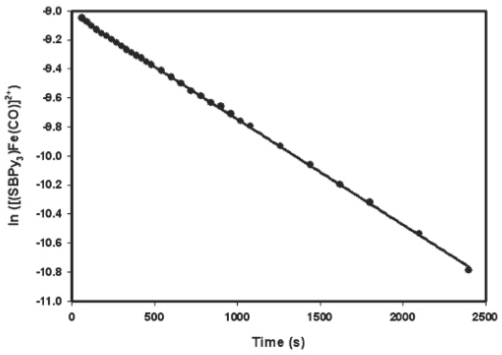

Figure 5. Plot of changes in ln[**2**] versus time(s) in 0.1 M PBS, pH 7.4 as monitored by noting the absorbance values at 450 nm.

within 15 min) is identical to that of $[(SBPy_3)Fe(MeCN)](BF_4)_2$, a structurally characterized species reported by us previously.[37] The red shift of the MLCT band upon loss of CO clearly indicates that the electron density from the antibonding π^* orbital of bound CO ligand returns back to the Fe(II) center in $[(SBPy_3)Fe(MeCN)]^{2+}$. With **3**, the initial yellow color deepens because of similar red shift of the MLCT band from 330 to 390 nm (isosbestic points at 352 and 242 nm) and the final spectrum of $[(Tpmen)Fe(MeCN)]^{2+}$ appears within ~20 min (Supporting Information, Figure S3).

The CO-releasing behavior of **1** in MeCN (and DMF) depends critically on the presence of dioxygen in solution. As mentioned above, **1** does not lose CO in degassed MeCN. Indeed, both the ν_{CO} value (1972 cm^{-1}) and the Fe−C(O) distance of **1** (1.775 (3) Å) indicate a stronger Fe-CO bond compared to that in the other two carbonyls. However, in aerated MeCN, **1** readily loses CO (within ~15 min) much like **2** and **3**. Interestingly, the absorption spectrum (λ_{max} at 470 and 390 nm) of **1** changes to that of the oxo-bridged diiron(III) species $[(PaPy_3)FeOFe(PaPy_3)](ClO_4)_2$ (λ_{max} at 430 and 330 nm, shoulder at 520 nm)[27d] upon such CO release (eq 1a). It is thus evident that formation of the highly stable oxo-bridged diiron species allows the release of CO from **1** in aerated MeCN solution. The stronger tendency of $PaPy_3H$, a ligand with a carboxamide group, toward stabilization of the +3 oxidation state of iron[27,42] drives the reaction in a completely different pathway in presence of dioxygen and makes **1** an efficient CORM in aerated MeCN (and DMF). Since the other two ligands namely $SBPy_3$ and Tpmen, are more supportive of the +2 oxidation state of iron, CO release from **2** and **3** gives rise to the solvated Fe(II) product in solution (eq 1b) both under anaerobic and aerobic conditions.

$$[(PaPy_3)Fe(CO)]^{2+} \xrightarrow[\text{Degassed MeCN}]{} \text{No CO loss} \qquad (1)$$

$$[(PaPy_3)Fe(CO)]^{2+} \xrightarrow[\text{MeCN, air}]{} [(PaPy_3)FeOFe(PaPy_3)]^{2+} \qquad (1a)$$

$$[(L)Fe(CO)]^{n+} \xrightarrow[\text{Solvent (Solv) MeCN, DMF, } H_2O]{L = SBPy_3, \text{ Tpmen}} [(L)Fe(Solv)]^{n+} + CO \qquad (1b)$$

The CO-releasing properties of **1**−**3** have also been studied in aqueous phosphate buffer (PBS, pH 7.4) to assess their utility in biological experiments. As shown in Figure 4, smooth release of CO from **2** causes a red shift of the 450 nm band to 572 nm with the emergence of a new band with λ_{max} at 400 nm. Clean isosbestic points are also observed at 496 and 430 nm. With **3**, a similar red shift of the 330 nm band to 400 nm is noted upon CO release in solution (isosbestic point at 370 nm). The similarities between the final spectra of **2** and **3** in PBS and MeCN suggest that the end products are most possibly the aqua species $[(L)Fe(H_2O)]^{2+}$ (L = $SBPy_3$, Tpmen) in these reactions.

Kinetic Measurements. The utility of the metal carbonyls as CORMs depends critically on the apparent rates of CO loss (k_{CO}) under physiological conditions. In the present work we have determined the k_{CO} values of **1**−**3** in PBS (pH 7.4). The CO release from the carbonyls was followed by recording the electronic spectra of the samples within 1 min of dissolution in phosphate buffer and the absorbance values at specific absorption maximum (405 nm for **1**, 450 nm for **2**, and 330 nm for **3**) were noted versus time (in seconds). For all three carbonyls, CO release obeys a pseudofirst order behavior in aqueous buffer (and MeCN, Supporting Information, Figure S4). The kinetic plot of the apparent rate of CO loss by **2** is shown in Figure 5. Further decomposition of the solvated species in aqueous media, as noted in the overall decrease of the absorption, occurs only after 45−60 min for these CORMs.

To date, a handful of water-soluble CORMs have been reported that act as fast CO donors. We have compared the k_{CO} value of $[Ru(glycine)(CO)_3Cl]$ (CORM-3),[20] with those of **1**−**3** under similar conditions. The k_{CO} values for **1**−**3** are 1.3×10^{-3} s^{-1}, 7.5×10^{-4} s^{-1}, and 3.7×10^{-3} s^{-1}, respectively. Under comparable conditions, CORM-3 affords a k_{CO} value of 1.5×10^{-3} s^{-1}. It thus appears that **2** releases CO more slowly over a longer period of time compared to CORM-3 while the k_{CO} values of **1** and CORM-3 are quite comparable. The k_{CO} values of **2** and **3** in MeCN (1.3×10^{-3} s^{-1} and 6.3×10^{-3} s^{-1} respectively) are consistently faster than the values in aqueous buffer. This difference could arise from the fact that MeCN is a better donor for the Fe(II) center ligated to polypyridine ligand.[36]

Delivery of CO to Myoglobin. The designed carbonyls readily deliver CO to reduced myoglobin (Mb) under physiological conditions. Because the carbonyls start release of CO

immediately upon dissolution, an excess (7−8 fold based on the amount of Mb) of each compound in PBS (pH 7.4) was required to completely convert reduced Mb to carbonyl myoglobin (Mb-CO) with solutions of the CORMs in such reactions. The rapid formation of Mb-CO was apparent within 1 min of addition as evidenced by the shift of the Soret band from 435 to 424 nm (Figure 6). Mb-CO production levels off after 20 min in the case of **2** and 24 min for **3**, with the final absorbance readings taken at 30 min. While kinetic measurements predict a slower rate of CO release for **2** compared to **3**, the Mb-based CO release test shows that both carbonyls generate CO at a similar rate over the same period of time. These resulting half-lives, defined as the time during which Mb-CO formation is 50% complete (~ 8 min for both species), are comparable to known CORMs that release CO when dissolved. For instance, CORM-3 was reported to have a half-life of 4−18 min,[20] while some Cr-based CORMs employing amino acids and amino ester ligands have half-lives of 7−9 min.[24]

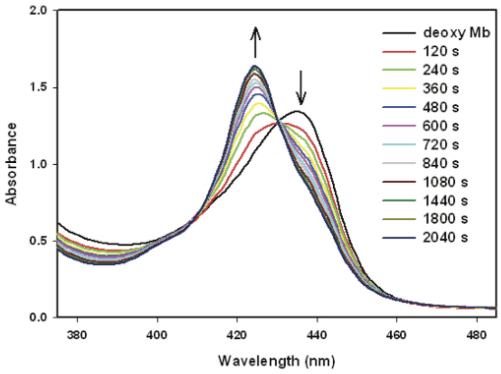

Figure 6. Delivery of CO from **3** to reduced Mb (λ_{max} = 435 nm), resulting in Mb-CO adduct (λ_{max} = 424 nm) in PBS pH 7.4.

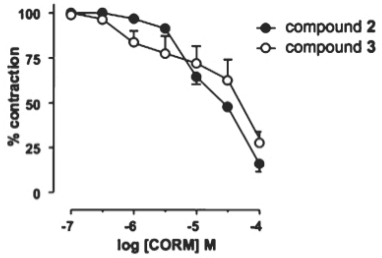

Figure 7. Vasorelaxation of mouse aorta muscle ring using **2** and **3** as a function of concentration.

Vasorelaxation of Mouse Aorta. The vasorelaxation property of CO has been a subject of debate in relation to its binding and activating to sGC and the concomitant cGMP pathway. Despite low affinity of CO to sGC,[12] relaxation of smooth muscle by CO via cGMP pathway has been proposed.[18,21] In the present study, we have examined the effect(s) of CO release from the present carbonyls on mouse aorta muscle rings in tissue bath experiments. Both **2** (30 nM−100 μM) and **3** (30 nM−300 μM) produced concentration-dependent relaxations with EC_{50} values of 3.4 ± 0.2 μM and 26.2 ± 0.2 μM, respectively (Figure 7). These values are superior to values obtained with CORM-3 reported by Motterlini and co-workers.[21] Interestingly, we did not observe much inhibitory effect by ODQ, a common sGC inhibitor (Figure 8). In previous work, Motterlini and co-workers have reported initial inhibition by ODQ which was eventually lost after repeated addition of CORM-3.[21]

It has been postulated that smooth muscle relaxation by CO could arise from its binding to the channel-bound heme of the large-conductance Ca^{2+}-activated K-channel (BK_{Ca}).[14b,43,44] To test this hypothesis, we studied the effect of the BK_{Ca} channel blocker iberiotoxin on the inhibition of vasorelaxation by **3**. Significant inhibition was indeed observed with this BK_{Ca} channel blocker while no effect was noted with the K_{ATP} channel blocker glibenclamide or the nonselective K^+-channel blocker TEA (data not shown). Clearly, more studies are required to determine the origin of vasorelaxation of smooth muscle by these CORMs. Nevertheless, the excellent vasorelaxation effects of **2** and **3** merit attention as new CORMs that could be used to deliver CO under physiological conditions. Further studies on the mechanism of vasorelaxation by these CORMs are in progress in this laboratory.

SUMMARY AND CONCLUSIONS

The following are the summary and conclusions of this work.

(a) Three structurally related Fe(II) carbonyls **1**−**3** have been synthesized from designed polypyridine ligands and characterized by spectroscopy and X-ray crystallography. The structure of **1** has been reported by us in a previous account.[36]

(b) In aqueous and nonaqueous solutions, these carbonyls rapidly release CO and hence can act as potential CORMs.

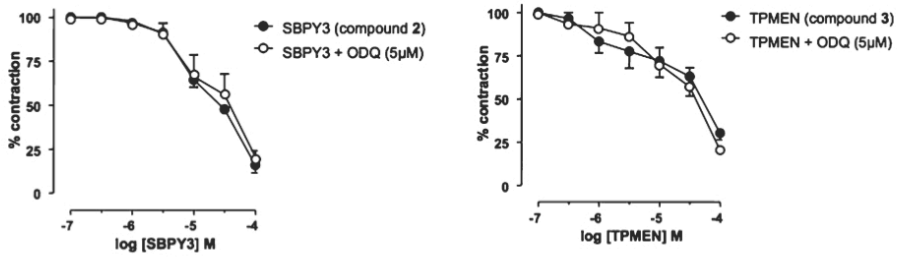

Figure 8. Vasorelaxation of mouse aorta muscle rings by **2** and **3** in the absence and presence of ODQ (5 μM).

(c) Both **2** and **3** have been employed to deliver CO to myoglobin under physiological conditions.

(d) **2** and **3** exhibit excellent vasorelaxation in mouse aorta muscle rings in tissue-bath experiments. The relaxation effect is not inhibited by ODQ, an sGC inhibitor. However, significant inhibition is observed with the BK_{Ca} channel blocker iberiotoxin.

■ ASSOCIATED CONTENT

Supporting Information. X-ray crystallographic data (in CIF format) for $[(SBPy_3)Fe(CO)](BF_4)_2$ (**2**) and preliminary structure of $[(Tpmen)Fe(CO)](ClO_4)_2$ (**3**, Figure S1), changes in the electronic absorption spectra of **2** and **3** in MeCN (Figures S2 and S3), plot of changes in ln(Absorbance) of **2** versus time in MeCN (Figure S4). This material is available free of charge via the Internet at http://pubs.acs.org.

■ AUTHOR INFORMATION

Corresponding Author

*E-mail: pradip@chemistry.ucsc.edu.

■ ACKNOWLEDGMENT

This research was supported by the NSF Grant CHE-0957251. M.G. was supported by the IMSD Grant GM-58903 and the NHGRI Grant HG002371. We thank Drs. Marilyn Olmstead and Allen Oliver for help in crystallographic studies. The ALS is supported by the U.S. Department of Energy, Office of Energy Sciences Materials Sciences Division, under contract DE-AC02-05CH11231.

■ REFERENCES

(1) *Signal Transduction and the Gasotransmitters: NO, CO and H2S in Biology and Medicine*; Wang, R., Ed.; Humana Press: Totowa, NJ, 2004.

(2) Ignarro, L. J. *Nitric Oxide: Biology and Pathobiology*; Academic Press: San Diego, 2000.

(3) *Nitric Oxide Free Radicals in Peripheral Neurotransmission*; Kalsner, S., Ed.; Birkhauser: Boston, 2000.

(4) *Nitric Oxide and Infection*; Fang, F. C., Ed.; Kluwer Academic: New York, 1999.

(5) *Nitric Oxide and Cell: Proliferation, Differentiation and Death*; Moncada, S., Higgs, E. A., Bagetta, G., Eds.; Portland Press: London, 1998.

(6) Fukuto, J. M.; Collins, M. D. *Curr. Pharm. Des.* **2007**, *13*, 2952–2978.

(7) Li, L.; Hsu, A.; Moore, P. K. *Pharmacol. Ther.* **2009**, *123*, 386–400.

(8) *The Smallest Biomolecules: Diatomics and their Interactions with Heme Proteins*; Ghosh, A., Ed.; Elsevier: Amsterdam, 2008.

(9) (a) Kaczorowski, D. J.; Zuckerbraun, B. S. *Curr. Med. Chem.* **2007**, *14*, 2720–2725. (b) Kim, H. P.; Ryter, S. W.; Choi, A. M. K. *Annu. Rev. Pharmacol. Toxicol.* **2006**, *46*, 411–449.

(10) Hartsfeield, C. L. *Antioxid. Redox Signaling* **2002**, *4*, 301–307.

(11) Kikuchi, G.; Yoshida, T.; Noguchi, M. *Biochem. Biophys. Res. Commun.* **2005**, *338*, 558–567.

(12) (a) Ma, X.; Sayed, N.; Beuve, A.; van den Akker, F. *EMBO J.* **2007**, *26*, 578–588. (b) Stone, J. R.; Marletta, M. A. *Biochemistry* **1994**, *33*, 5636–5640.

(13) (a) Wang, R. *Can. J. Physiol. Pharmacol.* **1998**, *76*, 1–15. (b) Coceani, F.; Kelsey, L.; Seidlitz, E. *Br. J. Pharmacol.* **1996**, *118*, 1689–1696.

(14) (a) Dong, D.-L.; Zhang, Y.; Lin, D. -H.; Chen, J.; Patschan, S.; Goligorsky, M. S.; Nasjletti, A.; Yang, B. -F.; Wang, W. -H. *Hypertension* **2007**, *50*, 643–651. (b) Jaggar, J. H.; Li, A.; Parfenova, H.; Liu, J.; Umstot, E. S.; Dopico, A. M.; Leffler, C. W. *Circ. Res.* **2005**, *97* (8), 805–812. (c) Wang, R.; Wu, L. *J. Biol. Chem.* **1997**, *272*, 8222–8226.

(15) Otterbein, L. E.; Mantell, L. L.; Choi, A. M. K. *Am. J. Physiol.* **1999**, *276*, L688–L694.

(16) Otterbein, L. E.; Zuckerbraun, B. S.; Haga, M.; Liu, F.; Song, R.; Usheva, A.; Stachular, C.; Bodyak, N.; Smith, R. N.; Csizmadia, E.; Tyagi, S.; Akamatsu, Y.; Flavell, R. J.; Billiar, T. R.; Tzeng, E.; Bach, F. H.; Choi, A. M. K.; Soares, M. P. *Nat. Med.* **2003**, *9*, 183–190.

(17) Suliman, H. B.; Carraway, M. S.; Tatro, L. G.; Piantadosi, C. A. *J. Cell Sci.* **2007**, *120*, 299–308.

(18) (a) Johnson, T. R.; Mann, B. E.; Clark, J. E.; Foresti, R.; Green, C. J.; Motterlini, R. *Angew. Chem., Int. Ed.* **2003**, *42*, 3722–3729. (b) Motterlini, R.; Clark, J. E.; Foresti, R.; Sarathchandra, P.; Mann, B. E.; Green, C. J. *Circ. Res.* **2002**, *90*, e17–e24.

(19) Zhang, W. Q.; Atkin, A. J.; Thatcher, R. J.; Whitwood, A. C.; Fairlamb, I. J. S.; Lynam, J. M. *Dalton Trans.* **2009**, 4351–4358.

(20) Clark, J. E.; Naughton, P.; Shurey, S.; Green, C. J.; Johnson, T. R.; Mann, B. E.; Foresti, R.; Motterlini, R. *Circ. Res.* **2003**, *93*, e2–e8.

(21) Foresti, R.; Hammad, J.; Clark, J. E.; Johnson, T. R.; Mann, B. R.; Friebe, A.; Green, C. J.; Motterlini, R. *Br. J. Pharmacol.* **2004**, *142*, 453–460.

(22) Alberto, R.; Motterlini, R. *Dalton Trans.* **2007**, 1651–1660.

(23) Zhang, W. Q.; Whitwood, A. C.; Fairlamb, I. J. S.; Lynam, J. M. *Inorg. Chem.* **2010**, *49*, 8941–8952.

(24) Sawle, P.; Hammad, J.; Fairlamb, I. J. S.; Moulton, B.; O'Brien, C. T.; Lynam, J. M.; Duhme-Klair, A. K.; Foresti, R.; Motterlini, R. *J. Pharmacol. Exp. Ther.* **2006**, *318*, 403–410.

(25) Niesel, J.; Pinto, A.; N'Dongo, H. W. P.; Merz, K.; Ott, I.; Gust, R.; Schatzschneider, U. *Chem. Commun.* **2008**, 1798.

(26) Metal carbonyls such as $[Mn_2(CO)_{10}]$[21] and $[Fe(CO)_5]$[22] are known to give off CO through photodissociation. See Zhang, S.; Zhang, H. T.; Brown, T. L. *Organometallics* **1992**, *11*, 3929. Waller, I. M.; Davis, H. F.; Hepburn, J. W. *J. Phys. Chem.* **1987**, *91*, 506.

(27) (a) Eroy-Reveles, A. A.; Hoffman-Luca, C. G.; Mascharak, P. K. *Dalton Trans.* **2007**, 5268–5274. (b) Patra, A. K.; Rose, M. J.; Olmstead, M. M.; Mascharak, P. K. *J. Am. Chem. Soc.* **2004**, *126*, 4780–4781. (c) Patra, A. K.; Rowland, J. M.; Marlin, D. S.; Bill, E.; Olmstead, M. M.; Mascharak, P. K. *Inorg. Chem.* **2003**, *42*, 6812–6823. (d) Patra, A. K.; Afshar, R.; Olmstead, M. M.; Mascharak, P. K. *Angew. Chem., Int. Ed.* **2002**, *41*, 2512–2515.

(28) (a) Hoffman-Luca, C. G.; Eroy-Reveles, A. A.; Alvarenga, J.; Mascharak, P. K. *Inorg. Chem.* **2009**, *48*, 9104–9111. (b) Ghosh, K.; Eroy-Reveles, A. A.; Holman, T. R.; Olmstead, M. M.; Mascharak, P. K. *Inorg. Chem.* **2004**, *43*, 2988–2997.

(29) (a) Rose, M. J.; Mascharak, P. K. *Coord. Chem. Rev.* **2008**, *252*, 2093–2114. (b) Rose, M. J.; Mascharak, P. K. *Curr. Opin. Chem. Biol.* **2008**, *12*, 238–244.

(30) (a) Rose, M. J.; Patra, A. K.; Olmstead, M. M.; Mascharak, P. K. *Inorg. Chem.* **2007**, *46*, 2328–2338. (b) Patra, A. K.; Rose, M. J.; Murphy, K. A.; Olmstead, M. M.; Mascharak, P. K. *Inorg. Chem.* **2004**, *43*, 4487–4495. (c) Patra, A. K.; Mascharak, P. K. *Inorg. Chem.* **2003**, *42*, 7363–7365.

(31) (a) Rose, M. J.; Mascharak, P. K. *Inorg. Chem.* **2009**, *48*, 6904–6917. (b) Rose, M. J.; Olmstead, M. M.; Mascharak, P. K. *J. Am. Chem. Soc.* **2007**, *129*, 5342–5343.

(32) (a) Eroy-Reveles, A. A.; Mascharak, P. K. *Future Med. Chem.* **2009**, *1* (8), 1497–1507. (b) Eroy-Reveles, A. A.; Leung, Y.; Beavers, C. M.; Olmstead, M. M.; Mascharak, P. K. *J. Am. Chem. Soc.* **2008**, *130*, 4447–4458. (c) Eroy-Reveles, A. A.; Leung, Y.; Mascharak, P. K. *J. Am. Chem. Soc.* **2006**, *128*, 7166–7167.

(33) (a) Madhani, M.; Patra, A. K.; Miller, T. W.; Eroy-Reveles, A. A.; Hobbs, A.; Fukuto, J. M.; Mascharak, P. K. *J. Med. Chem.* **2006**, *49*, 7325–7330. (b) Szundi, I.; Rose, M. J.; Sen, I.; Eroy-Reveles, A. A.; Mascharak, P. K.; Einarsdottir, O. *Photochem. Photobiol.* **2006**, *82*, 1377–1384. (c) Afshar, R. K.; Patra, A. K.; Mascharak, P. K. *J. Inorg. Biochem* **2005**, *99*, 1458–1464.

(34) Rose, M. J.; Fry, N. L.; Marlow, R.; Hinck, L.; Mascharak, P. K. *J. Am. Chem. Soc.* **2008**, *130*, 8834–8846.
(35) (a) Halpenny, G. M.; Gandhi, K. R.; Mascharak, P. K. *ACS Med. Chem. Lett.* **2010**, *1*, 180–183. (b) Halpenny, G. M.; Steinhardt, R. C.; Okialda, K. A.; Mascharak, P. K. *J. Mater. Sci: Mater. Med.* **2009**, *20*, 2353–2360.
(36) Afshar, R. K.; Patra, A. K.; Bill, E.; Olmstead, M. M.; Mascharak, P. K. *Inorg. Chem.* **2006**, *45*, 3774–3781.
(37) Patra, A. K.; Olmstead, M. M.; Mascharak, P. K. *Inorg. Chem.* **2002**, *41*, 5403–5409.
(38) Bernal, I.; Jensen, I. M.; Jensen, K. B.; McKenzie, C. J.; Toftlund, H.; Tuchagues, J.-P. *J. Chem. Soc., Dalton Trans.* **1995**, 3667–3675.
(39) Sugimoto, H.; Sawyer, D. T. *J. Am. Chem. Soc.* **1985**, *107*, 5712–5716.
(40) Salzmann, R.; Ziegler, C. J.; Godbout, N.; McMahon, M. T.; Suslick, K. S.; Oldfield, E. *J. Am. Chem. Soc.* **1998**, *120*, 11323–11334.
(41) Vaska, L.; Yamaji, T. *J. Am. Chem. Soc.* **1971**, *93*, 6673–6674.
(42) Marlin, D. S.; Mascharak, P. K. *Chem. Soc. Rev.* **2000**, *29*, 69–74.
(43) Horrigan, F. T.; Heinemann, S. H.; Hoshi, T. *J. Gen. Physiol.* **2005**, *126*, 7–21.
(44) Wang, R.; Wu, L.; Wang, Z. *Pflugers Arch.- Eur. J. Physiol.* **1997**, *434*, 285–291.

Chapter 3. Photoactive d^6 Metal Carbonyl Complexes Bearing Designed Tridentate Ligand Frames

Part I: Photoactive Manganese Carbonyl Complexes bearing Structurally-related Tripodal Ligand Frames: Investigation of Conjugation Effects on CO Photorelease

3.I.1 Introduction

Recent highlights on the biological significance of CO and its parallels with other endogenously produced gases, namely NO, have renewed interest in the design and syntheses of a new generation of metal carbonyl complexes as tunable CO-delivery systems. Strategies for CO release from metal carbonyl complexes include: both thermal[1] and photochemical[2] dissociation. Inclusion of specific ancillary ligands have also been found to promote metal-CO bond homolysis in selected cases.[3]

The inherent photosensitivity of metal carbonyls has made photochemical metal-CO bond labilization the most promising strategy in controlled CO-delivery to biological targets using metal carbonyls. The photoreactivity of metal carbonyls and the related CO ligand displacement mechanisms have been attributed to metal-to-ligand charge transfer (MLCT) excited states, as MLCT electronic transitions are common in organometallic compounds bearing both low valent metal centers and electron-accepting ligand moieties (such as bipyridines, phenanthrolines and polypyridines). Other outcomes of MLCT excitation include: (1) ultrafast ligand dissociation, (2) population of a long-lived, charge-separated triplet MLCT state, (3) thermal population of a more reactive excited state, (4) facilitate electron transfer reactions and (5) decay to the ground state without further reactivity.[4]

It is now firmly established that excitation into an MLCT excited state is the primary step in metal-ligand bond homolysis. It is from this state that other charge transfer excited states become accessible. Because MLCT transitions are spectroscopically allowed, illumination at such charge transfer bands is an efficient way of adding energy. As discussed in the introductory chapter with $Cr(CO)_6$ as a prototypical example, the metal-CO antibonding orbitals lie at relatively high energy, such that metal-CO bond breaking from a ligand field (LF) excited state is unlikely. Irradiation of $Cr(CO)_6$ at 4 eV instead populates a low energy ^{1}MLCT ($d_\pi \rightarrow \pi^*$) state, which then crosses over to an excited ^{1}LF ($d_\pi \rightarrow d_{\sigma^*}$) state at increasing metal-CO bond lengths. It is this mixing of the ^{1}MLCT and ^{1}LF excited states that account the observed CO photodissociation in $Cr(CO)_6$.[4a,5]

Indeed the first set of compounds to be identified as photoCORMs consisted of homoleptic metal carbonyls like $Fe(CO)_5$, $Mn_2(CO)_{10}$, which deliver CO to reduced myoglobin upon irradiation with a cold light source.[6] A drawback in the use of such metal carbonyls as photoCORMs, apart from their limited solubility in biologically relevant media, is the need for high energy light to induce CO photodissociation.[7,8] In order to utilize light of lower energies in triggering CO photorelease, a ligand frame must be designed such that single electron excitation into a ^{1}MLCT excited state requires low energy radiation.

Previous work on group 6 metal carbonyls has shown that the incorporation of functional groups with low-lying orbitals such as diimines, polypyridines, and macrocyclic ligand frames effectively lowers the energies associated with these

charge transfer bands. For instance, carbonyls of the type: $[M(CO)_4(diimine)]$ (where M = Cr, Mo, W) exhibit intense absorption bands in the visible region attributed to HOMO-2 to LUMO electronic transitions, wherein the HOMO-2 is of metal and axial CO ligand bonding character, while the LUMO is almost solely comprised of the diimine moiety.[3] The net effect of irradiation into these MLCT bands is the dissociation of an axial CO group at lower energies.

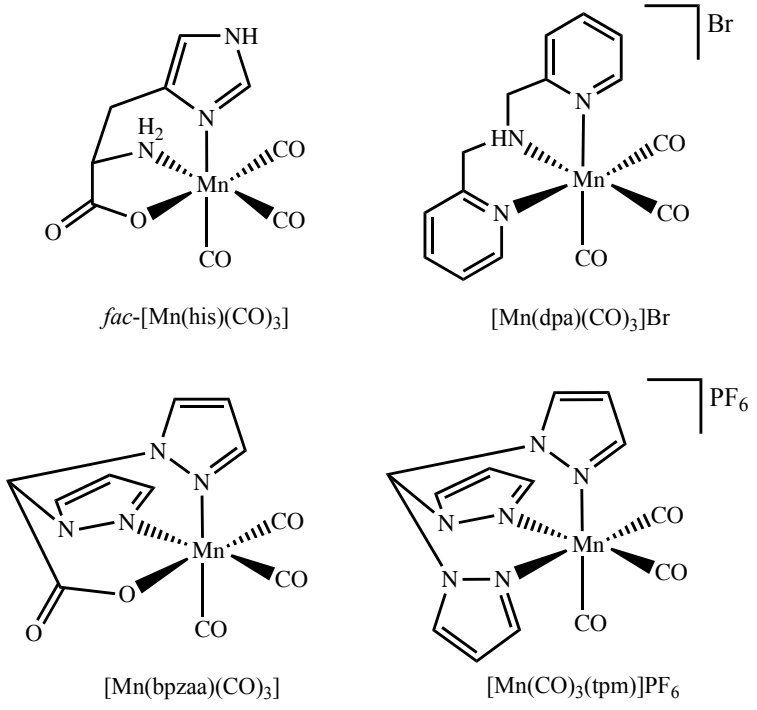

fac-$[Mn(his)(CO)_3]$ $[Mn(dpa)(CO)_3]Br$

$[Mn(bpzaa)(CO)_3]$ $[Mn(CO)_3(tpm)]PF_6$

Figure 3.I.1. Examples of *fac*- Mn(I) tricarbonyl complexes bearing tripodal ligand frames as photoCORMs.

Although the first photoactive Mn-based CORM, $[Mn(CO)_3(tpm)]PF_6$ (tpm = tris(pyrazolyl)methane), was initially prepared by Trofimenko,[9] its potential as a photodynamic therapy (PDT) agent was not explored until several years later by Schatzschneider and co-workers. This compound was found to release CO when activated by 365 nm light and exhibited photoinduced cytotoxicity against the human

colon cancer cell line HT29.[10] It is important to note here that CO release from $[Mn(CO)_3(tpm)]PF_6$ has been mostly applied towards cytotoxic purposes and not in the expected protective assay that CO is known for. Isolation of this photoCORM has set the stage for the preparation of a series of *fac*-Mn(I) tricarbonyl complexes[11] (Figure 3.I.1), all of which exhibit CO photodissociation when irradiated with UV and/or visible light.

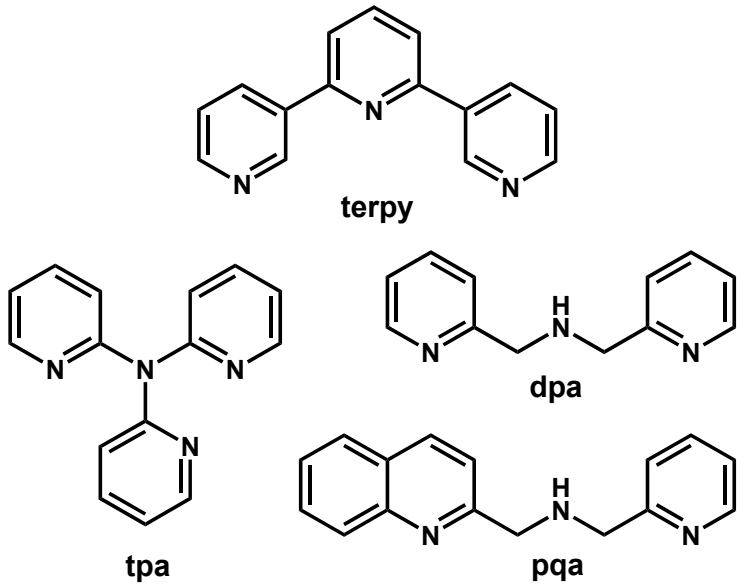

Figure 3.I.2. Structures of the tridentate ligands, terpy, tpa, dpa and pqa utilized in this study.

As part of our research effort in the area of the development of suitable photoCORMs, we have prepared a series of photoactive manganese carbonyls bearing tridentate ligands with varying degrees of conjugation in their frameworks. The structures of the ligands employed are shown in Figure 3.I.2. We intended to find out whether an increase in the number of pyridine N-donors and/or extent of conjugation will cause a shift in the absorption maximum of the resulting carbonyls, thus lowering

the energy required for CO dissociation from the resulting metal carbonyls. This chapter describes the syntheses, characterization, and photoactivity of $[Mn(tpa)(CO)_3]ClO_4$ (where tpa = tris(2-pyridyl)amine, $[Mn(dpa)(CO)_3]Br$ (where dpa = *N,N*-bis(2-pyridylmethyl)amine) and $[Mn(pqa)(CO)_3]ClO_4$ (where pqa = (2-pyridylmethyl)(2-quinolylmethyl)amine). The rates of CO release of these carbonyls upon exposure to UV (305 nm) and visible light ($\lambda > 350$ nm) have been measured to evaluate their utility as photoCORMs for biological studies. The efficacy of CO photorelease from $[Mn(pqa)(CO)_3]ClO_4$ has also been determined on the basis of relaxation of mouse aortic smooth muscle tissue in-vitro.

3.I.2. Syntheses of the Metal Complexes

3.I.2.1. Mn(I) terpyridine carbonyl complexes

We initially selected the known ligand 2,2':6',2"- terpyridine (terpy) (Figure 3.I.2) as a ligand frame in the preparation CORMs as coordination by terpy generates metal complexes with intense absorption and emission spectra characteristic of low lying MLCT states. Numerous reports of Ru(II), Os(II) and Pt(II) complexes of terpy have been prepared to study their enhanced photoluminescence and redox behavior.[12] Enhancement of the excited state lifetimes for Ru-based terpy complexes for instance, has been achieved by direct incorporation of electron-donating or withdrawing groups on the terpy frame, thereby manipulating the energy difference between ^{3}MLCT and ^{3}MC, from which radiative decay to the ground state occurs concurrent with emission.[13] Potential applications of these luminescent Ru(II) complexes include

DNA intercalating agents[14], enzyme inhibitors[15], components of dye-sensitized solar cells[16] and ion-selective sensors.[17]

While the photophysics of ruthenium terpy complexes is well documented, there are only a few examples of manganese based terpy complexes as CO-releasing molecules. Much of the work reported on Mn-based terpy compounds has so far focused on their catalytic efficacy in (1) molecular catalysts in water splitting processes, mimicking of active site of the oxygen-evolving component of photosystem II[18] and (2) hydrogen peroxide activators in the bleaching processes.[19]

Our attempts to synthesize a terpy complex featuring a low valent manganese carbonyl include reactions of 1:1 ratio of terpyridine to $Mn(CO)_5Br$ in THF under reflux conditions. The dark purple solid that separated from solution exhibited two CO stretching frequencies at 1915 and 1847 cm^{-1} (Figure 3.I.14) suggesting a *cis* configuration of the CO groups. Although the crude product with a proposed formula: $[Mn(terpy)(CO)_2Br]$, exhibits excellent solubility in polar protic and aprotic solvents such as methanol, DMF and MeCN, its breakdown within minutes in these solvents under aerobic conditions made its structural characterization challenging. We postulate that oxidation and decarbonylation of $[Mn(terpy)(CO)_2Br]$ occurs at ambient temperature. Such conditions facilitate the formation of the bis-terpyridine complex $[Mn(terpy)_2]^{2+}$, which appears to be a thermodynamic driving force, hindering the isolation of $[Mn(terpy)(CO)_2Br]$. Indeed the electronic absorption spectrum of $[Mn(terpy)(CO)_2Br]$ when kept in acetonitrile under aerobic conditions

show a gradual loss of charge transfer bands in the 600-800 nm region, with final UV-Vis spectrum was consistent with the known complex $[Mn(terpy)_2](ClO_4)_2$.[20]

Interestingly, among the group 7 metals, terpy is known to bind to Re(I) centers in either a bidentate or tridentate fashion. The straightforward preparation of $[Re(terpy)(CO)_2Cl]$ from the reaction of terpy with one equivalent of $[Re(CO)_5Cl]$ was reported some time ago,[21] however the initial set of crystal structures to be obtained from these set of conditions were not those of the expected dicarbonyl complex, but rather $[Re(terpy)(CO)_3Cl]$[22] and $[Re(terpy)(CO)_3Br]$[23] wherein terpy acts as a bidentate ligand. Abel and co-workers have determined the fluxional nature of such Re(I) tricarbonyls in solution, with terpy oscillating between bidentate and tridentate coordination, prevents the isolation of the meridionally-coordinated terpy complex.[23]

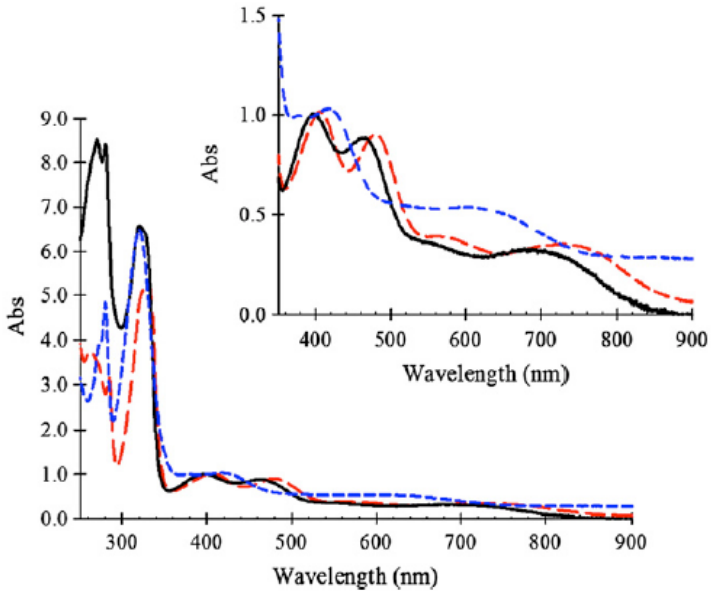

Figure 3.I.3. Absorption spectrum of *mer,cis*-[Re(terpy)$(CO)_2Cl$] in CH_3CN (black, solid line), CH_2Cl_2 (red, dashed line) and H_2O (blue, short dashed line). Inset shows the region between 350 – 900 nm. (Black and Hightower, 2012).[24]

More recent works by Hightower have confirmed that thermal decarbonylation of [Re(terpy)$(CO)_3$Cl] is a synthetic route in the preparation of the dicarbonyl, *mer,cis*-**[**Re(terpy)$(CO)_2$Cl], albeit x-ray quality crystals were not obtained.[24] The electronic absorption spectrum of *mer,cis*-**[**Re(terpy)$(CO)_2$Cl] features absorption bands in the visible region assigned to MLCT transitions (Figure 3.I.3), much like the UV-Vis spectrum of our preliminary Mn species, [Mn(terpy)$(CO)_2$Br] (Figure 3.I.15).

3.I.2.2. Mn carbonyls bearing tripodal ligand frames

The *meridional* configuration of terpyridine would have been ideal in the preparation of a Mn-based CORM, as a planar ligand facilitates MLCT excited states at lower energies giving rise to more photolabile CO donors. However the inherent decarbonylation reactions occurring under ambient conditions for this class of manganese complexes hampers further efforts to characterize Mn photoCORMs featuring the terpyridine ligand frame. To prevent the formation of $[Mn(L)_2]^{2+}$ (where L = tridentate polypyridine ligand), we turned our attention to a series of structurally related polypyridine tripodal ligands that impose *facial* coordination to a Mn(I) center. We have modified our designed ligands such as to investigate the effects of conjugation and/or number of pyridine donors on the CO releasing capacities of the resulting CORMs.

The carbonyl [Mn(tpa)$(CO)_3$]ClO_4 (where tpa = tris(2-pyridyl)amine) was synthesized according to a published procedure[25] with the exception of using chloroform as a solvent in place of acetone under reflux conditions. Reactions of the

tripodal ligands *N,N*-bis(2-pyridylmethyl)amine (dpa) and (2-pyridylmethyl)(2-quinolylmethyl)amine (pqa) with either *fac*-$[Mn(CO)_3(MeCN)_3]ClO_4$ or $[Mn(CO)_5Br]$ as starting salts in THF afforded compounds $[Mn(dpa)(CO)_3]Br$ and $[Mn(pqa)(CO)_3]ClO_4$. All three carbonyls were isolated as yellow solids that are stable under aerobic conditions for an indefinite period of time when kept in the dark. They are soluble in aprotic polar solvents like MeCN and DMSO with limited solubility in $CHCl_3$. Such solutions are stable for several hours if kept in the dark.

3.I.3. Characterization of the Photoactive Mn Complexes

The complexes $[Mn(tpa)(CO)_3]ClO_4$, $[Mn(dpa)(CO)_3]Br$ and $[Mn(pqa)(CO)_3]ClO_4$ were extensively characterized. The IR spectra of these carbonyl complexes exhibit two strong bands in the carbonyl region (Figures 3.I.16 - 3.I.18), one sharp followed by one broad CO stretch (ν_{CO}) pertaining to the axial and equatorial CO ligands, respectively. This pattern is consistent with known Mn carbonyls bearing facially-capping CO groups.[26-28] In the case of $[Mn(tpa)(CO)_3]ClO_4$ and $[Mn(pqa)(CO)_3]ClO_4$, the broad ν_{CO} in the region of 1930-1950 cm^{-1} feature a minor splitting, suggesting a distinction between the two remaining CO ligands bound in the equatorial plane (vide infra), as the ligands tpa and pqa are not completely symmetric. Similar peak splitting has been observed in the IR spectra of some "piano-stool" carbonyls such as $[(C_5H_5)Mn(CO)_3]$.[29] The higher symmetry of the cation in $[Mn(dpa)(CO)_3]Br$ is reflected in two sharp ν_{CO} bands at 2030 and 1930 cm^{-1} (no splitting in the ~1930 cm^{-1} band).

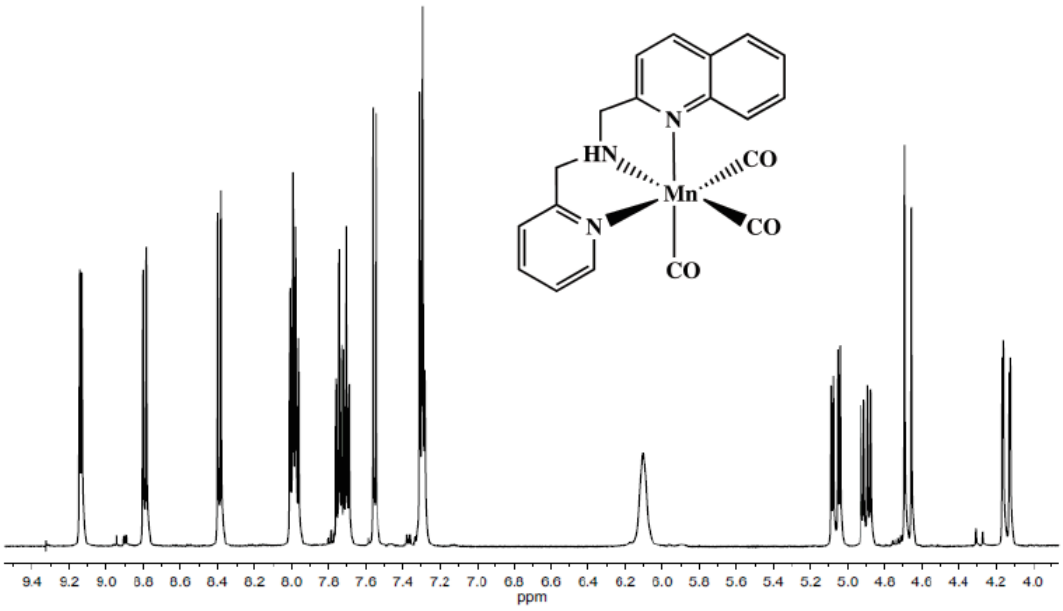

Figure 3.I.4. ^{1}H NMR (500 MHz) spectrum of $[Mn(pqa)(CO)_3]ClO_4$ in CD_3CN (3.5-9.5 ppm range).

The poor diffraction pattern of the crystals of $[Mn(pqa)(CO)_3](ClO_4)$ has so far hindered the determination of its crystal structure. However, the spectral properties of this carbonyl clearly establish the similarities of its structure with those of $[Mn(tpa)(CO)_3]ClO_4$ and $[Mn(dpa)(CO)_3]Br$. For example, $[Mn(pqa)(CO)_3](ClO_4)$ exhibits three ν_{CO} frequencies of 2034, 1942 and 1919 cm^{-1} (Figure 3.I.18) in KBr matrix supporting the facial coordination of the ligand frame. In addition, the clean ^{1}H NMR spectrum confirms its integrity in solution. As shown in Figure 3.I.4, the NH proton shifts from 2.5 ppm to 6.1 ppm upon ligation to the Mn(I) center and the pyridine/quinoline protons spread over the range of 7.3-9.2 ppm. In addition, facial coordination of the ligand to the Mn(I) center leads to diastereomeric methylene

protons that appear as four distinct signals in the range of 4.1-5.1 ppm (in free ligand, these give rise to two singlets at 3.95 and 4.05 ppm).

Both $[Mn(tpa)(CO)_3]ClO_4$ and $[Mn(dpa)(CO)_3]Br$ exhibit diamagnetism in the solid state and in solution as evidenced by clean ^1H NMR spectra in solvents like CD_3CN (Figures 3.I.19-3.I.20).

3.I.3.1. X-ray Structures of $[Mn(tpa)(CO)_3]ClO_4$ and $[Mn(dpa)(CO)_3]Br$

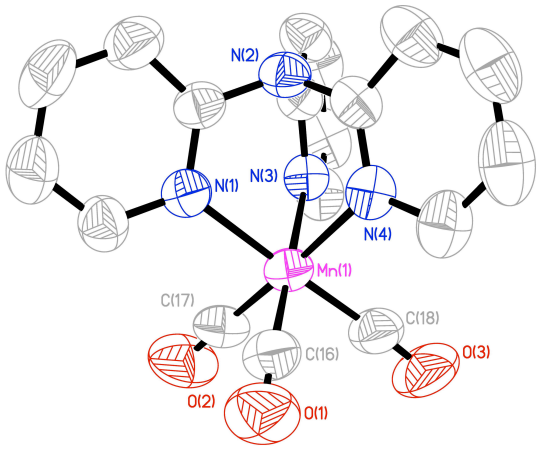

Figure 3.I.5. ORTEP diagram (50% probability level) of the cation of $[Mn(tpa)(CO)_3]ClO_4$ with select atom labeling. H-atoms have been omitted for clarity.

Although $[Mn(tpa)(CO)_3]ClO_4$ was first synthesized by Edwards and coworkers,[25] its solid state structure has not been determined by crystallography. The structure of the cation of $[Mn(tpa)(CO)_3]ClO_4$ is shown in Figure 3.I.5. The octahedral geometry of the complex consists of a facially capping tpa ligand and three CO ligands opposite to each of the pyridine rings resulting in an approximate C_{3v} symmetry. Two of the CO ligands are in an equatorial plane opposite two pyridine moieties, while the remaining CO is positioned axially. Bond distances of the

coordinated ligand, Mn–N(py), range from 2.058 Å to 2.065 Å. On the other hand, the Mn–C(O) bond lengths are more uniform. Two Mn–C(O) bonds are noted at 1.806(5) Å and 1.809(5) Å, while the remaining Mn-C(O) is slightly longer at 1.813(5) Å. The symmetry and Mn–C(O) bond distances observed in $[Mn(tpa)(CO)_3]ClO_4$ are consistent with other complexes such as $[(C_5H_5)Mn(CO)_3]$[29] and $[Mn(bmip)(CO)_3]$ (bmip = 3,3-bis(1-methylimidazole-2-yl)propionic acid).[30]

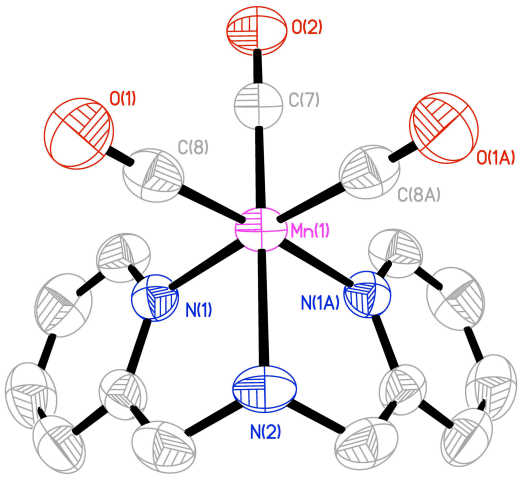

Figure 3.I.6. ORTEP diagram (50% probability level) of the cation of $[Mn(dpa)(CO)_3]Br$ with select atom labeling. H atoms have been omitted for clarity.

The structure of $[Mn(dpa)(CO)_3]^+$ is shown in Figure 3.I.6. Much like $[Mn(tpa)(CO)_3]ClO_4$, this carbonyl possesses an octahedral geometry featuring the tripodal dpa ligand and three CO groups opposite to each of the N-donors. The symmetric nature of the free dpa ligand generates a mirror plane passing through the C7–Mn1–N2 axis in the resulting complex. The Mn–N(py) and Mn–N(amine) distances are almost identical at 2.053(3) Å and 2.063(4) Å, respectively. The Mn-

C(O) bond lengths for $[Mn(dpa)(CO)_3]Br$ are in the same range as that seen in other Mn(I) tricarbonyl complexes.

3.I.3.2. Electronic Absorption Spectra and CO Release in Solution

In MeCN, $[Mn(tpa)(CO)_3]ClO_4$ exhibits a broad absorption band centered at ~330 nm with higher energy bands at 260 and 240 nm. Compounds $[Mn(dpa)(CO)_3]Br$ and $[Mn(pqa)(CO)_3](ClO_4)$ display similar profiles, with a broad shoulder at 350 and 360 nm, respectively (Figure 3.I.7). Comparison of the λ_{max} of $[Mn(dpa)(CO)_3]Br$ and $[Mn(pqa)(CO)_3](ClO_4)$ reveals an incremental shift of the absorption band towards lower energies upon replacement of one of the pyridine rings in $[Mn(dpa)(CO)_3]Br$ with a quinoline moiety in $[Mn(pqa)(CO)_3](ClO_4)$. However, the extinction coefficients of the two bands at 300 and 360 nm increase considerably in case of $[Mn(pqa)(CO)_3](ClO_4)$ with additional conjugation (pyridine vs. quinoline) in the ligand frame (Figure 3.I.7). This result clearly demonstrates that the strategy of adding extended conjugation in the ligand framework does increase the amount of light absorbed by the designed carbonyl in the low-energy range.

Solutions of all three carbonyls in MeCN are stable up to 6 h *if kept in the dark*. However, such solutions steadily lose their yellow color when exposed to light. Experiments with reduced myoglobin (Mb) confirm that such bleaching is associated with photorelease of CO from $[Mn(tpa)(CO)_3]ClO_4$, $[Mn(dpa)(CO)_3]Br$ and $[Mn(pqa)(CO)_3]ClO_4$ (*vide infra*).

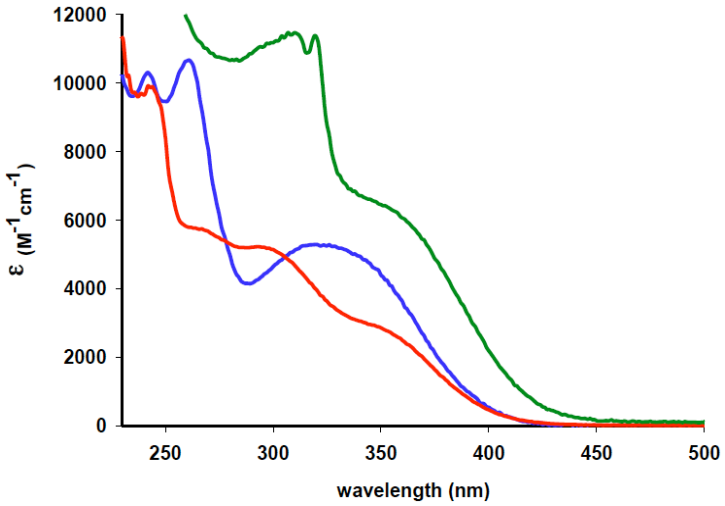

Figure 3.I.7. Electronic absorption spectra of $[Mn(tpa)(CO)_3]ClO_4$ (blue trace), $[Mn(dpa)(CO)_3]Br$ (red trace) and $[Mn(tpa)(CO)_3]ClO_4$ (green trace) in MeCN.

The light-induced CO release of $[Mn(tpa)(CO)_3]ClO_4$, $[Mn(dpa)(CO)_3]Br$ and $[Mn(pqa)(CO)_3]ClO_4$ in solution has been evaluated to assess their utility as photoCORMs. Acetonitrile solutions of the aforementioned were prepared and irradiated with a low intensity light source, equipped with a cut-off filter set at 350 nm. All solutions become clear after irradiation, which is consistent with the loss of charge transfer bands in the ~350 nm region. For instance, the initial absorption spectrum of $[Mn(tpa)(CO)_3]ClO_4$ in MeCN features an MLCT band with a λ_{max} at 320 nm region, which shifts to 295 nm and isosbestic points for were noted at 325 nm and 265 nm (Figure 3.I.8). Similar features have been observed in the photolysis of $[Mn(dpa)(CO)_3]Br$ and $[Mn(pqa)(CO)_3]ClO_4$.

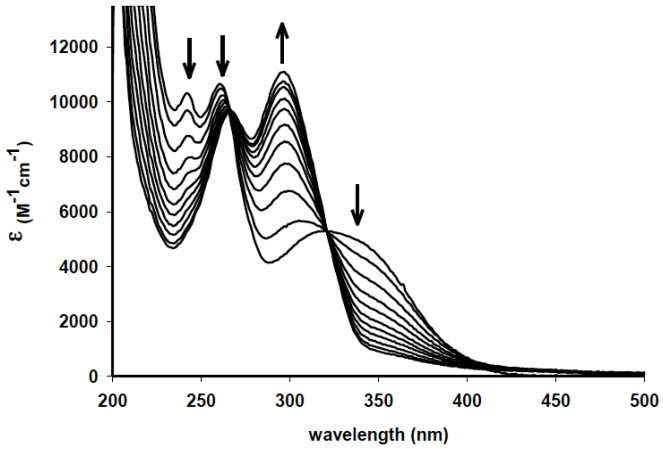

Figure 3.I.8. Changes in the electronic absorption spectrum of $[Mn(tpa)(CO)_3]ClO_4$ in MeCN (concentration = 0.07 mM) upon exposure to light ($\lambda > 350$ nm).

Clean isosbestic points in all three carbonyls strongly suggest that $[Mn(tpa)(CO)_3]ClO_4$, $[Mn(dpa)(CO)_3]Br$ and $[Mn(pqa)(CO)_3]ClO_4$ do not fall apart upon exposure to light to provide CO. However, the presence of multiple CO ligands in these photoCORMs makes it difficult to identify the photoproduct(s) at the end of CO release (viz the final trace in Figure 3.I.8). Photolysis of $[Mn(tpa)(CO)_3]ClO_4$, $[Mn(dpa)(CO)_3]Br$ and $[Mn(pqa)(CO)_3]ClO_4$ in MeCN under anaerobic conditions afforded products that still exhibited weak CO stretching frequencies in the 2050-1950 cm^{-1} region, suggesting that all three CO ligands are not released upon low-power illumination.

3.I.3.3. EPR Spectra

With the intended use of these carbonyls in biological experiments in mind, we have explored the nature of the photoproduct(s) formed under aerobic conditions. Following the photorelease of CO, these carbonyls afford paramagnetic species

(Figure 3.I.9) that display IR spectra indicating the presence of the intact ligands. For example, $[Mn(dpa)(CO)_3]Br$ produces $[Mn(dpa)_2]^{2+}$ as the major product in the solution as evidenced by its final electronic absorption spectrum photolyzed under aerobic conditions (Figure 3.I.9). Similar results have been obtained with $[Mn(pqa)(CO)_3]ClO_4$ as well. Oxidation of the Mn(I) centers possibly occurs during photolysis in air. No further attempt has been made to determine the structures and mechanism(s) of formation of such photoproducts in the present work.

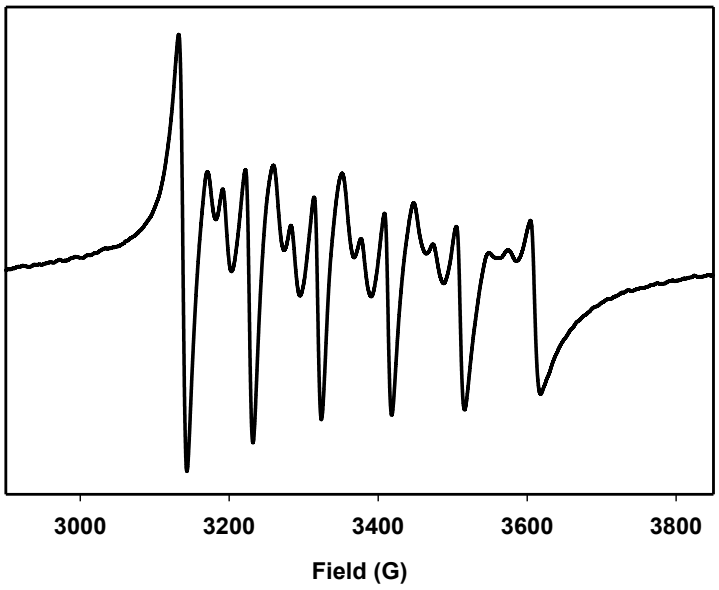

Figure 3.I.9. X-band EPR spectrum of $[Mn(pqa)_2]^{2+}$ in frozen DMF/toluene glass (110K). Instrument settings: microwave frequency, 9.443 GHz; power, 31.7 mW; modulation, 100kHz; modulation amplitude, 2G.

CO loss from the subset of photoCORMs bearing the formula *fac*-$[Mn(L)(CO)_3]^+$ (where L = tripodal ligand) has recently been investigated by Berends and Kurz. Irradiation in coordinating media was proposed to trigger sequential CO release, thereby generating the corresponding Mn(II) solvato species: $[Mn(L)(solvent)_3]^{2+}$.

Further oxidation of the Mn(II) center to Mn(III) occurs concomitant with the formation of a μ-O-Mn^{III} species, which is assigned as the final photoproduct in this generalized scheme.[31] The formation of a bridged μ-O-Mn^{III} species is consistent with observations of complete loss of ν_{CO} bands and an EPR active photoproduct when photoCORMs such as $[Mn(dpa)(CO)_3]$ and $[Mn(pqa)(CO)_3]ClO_4$ are completely photolyzed.

3.I.3.4. CO delivery to Myoglobin

Photoinduced CO release by the carbonyl complexes $[Mn(tpa)(CO)_3]ClO_4$, $[Mn(dpa)(CO)_3]Br$ and $[Mn(pqa)(CO)_3]ClO_4$ has been investigated by the myoglobin (Mb) assay.[32] In a typical experiment, a 10-fold excess of the appropriate photoCORM was added to a solution of reduced-Mb in phosphate buffer (pH 7.4) in the dark. The mixture was then irradiated with a broadband light source fitted with a 350 nm cut-off filter and changes in the Soret band were recorded at defined time intervals. As shown in Figure 3.I.10, smooth release of CO from $[Mn(dpa)(CO)_3]Br$ causes a shift of the 435 nm band to 424 nm confirming the formation of Mb-CO under the experimental conditions. Very similar CO-releasing capacity was observed for all three photoCORMs.

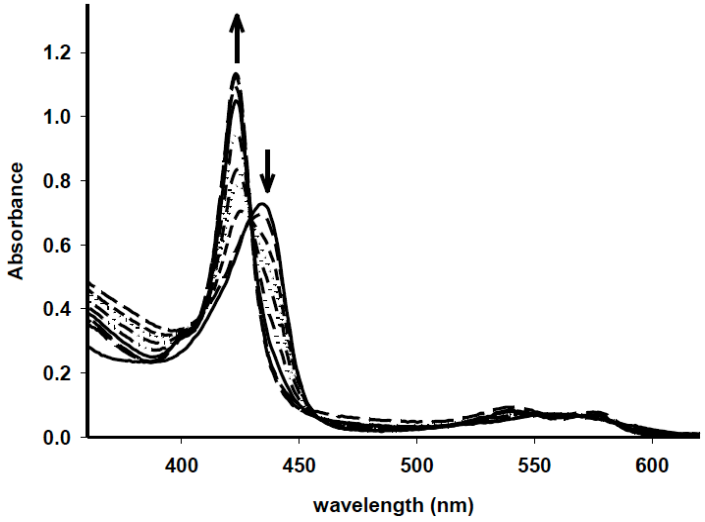

Figure 3.I.10. Conversion of reduced-Mb to Mb-CO in a mixture of $[Mn(dpa)(CO)_3]Br$ and reduced Mb in 100 mM phosphate buffer (pH 7.4) upon exposure to light ($\lambda > 350$ nm).

3.I.3.5. Kinetic and Quantum Yield Measurements

To date, the few studies on photoCORMs have utilized light in the 313-365 nm range to initiate CO release.[10b,33] In MeCN, the present carbonyls exhibit fast rates of CO release upon exposure to UV light. The rates of CO release were determined by recording the changes in electronic spectrum of each compound at specified absorption wavelengths (350 nm for $[Mn(tpa)(CO)_3]ClO_4$, 300 nm for $[Mn(dpa)(CO)_3]Br$, and 360 nm for $[Mn(pqa)(CO)_3]ClO_4$) when irradiated with UV light (307 nm, 7 mW) for defined time intervals. For all three carbonyls, CO release obeys a pseudofirst order behavior in MeCN. The apparent CO-release rate k_{CO} values of $[Mn(tpa)(CO)_3]ClO_4$, $[Mn(dpa)(CO)_3]Br$ and $[Mn(pqa)(CO)_3]ClO_4$ are $9.1\pm0.2 \times 10^{-2}\ s^{-1}$, $11.7\pm0.2 \times 10^{-2}\ s^{-1}$, and $8.1\pm0.2 \times 10^{-2}\ s^{-1}$, respectively under our experimental conditions (*vide supra*). Since our intention has been the use of light of

longer wavelengths, we have also examined the rates of CO release under white light ($\lambda > 350$ nm, 120 mW) with a UV cut-off filter.

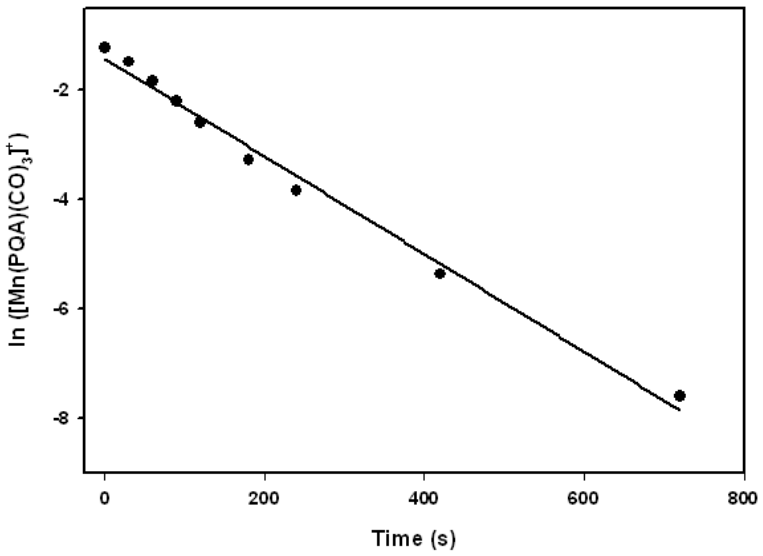

Figure 3.I.11. Plot of changes in ln ($[Mn(pqa)(CO)_3]^+$) versus time (s) in MeCN upon exposure to visible (($\lambda > 350$ nm, 120 mW) light (concentration = 0.13 mM).

Following a similar procedure, solutions of $[Mn(tpa)(CO)_3]ClO_4$, $[Mn(dpa)(CO)_3]Br$ and $[Mn(pqa)(CO)_3]ClO_4$ were irradiated with visible light for selected time intervals and changes were monitored at specified absorption wavelengths (350 nm for $[Mn(tpa)(CO)_3]ClO_4$ and $[Mn(dpa)(CO)_3]Br$, and 360 nm for $[Mn(pqa)(CO)_3]ClO_4$). The apparent CO-release rate k_{CO} values of $[Mn(tpa)(CO)_3]ClO_4$, $[Mn(dpa)(CO)_3]Br$ and $[Mn(pqa)(CO)_3]ClO_4$ are $6.0\pm0.2 \times 10^{-3}$ s^{-1}, $5.2\pm0.2 \times 10^{-3}$ s^{-1}, and $8.3\pm0.2 \times 10^{-3}$ s^{-1}, respectively under visible light. As expected, $[Mn(pqa)(CO)_3]ClO_4$ exhibits the highest rate of CO release under visible light due to strong absorption of light in the 350-360 nm region (Figure 3.I.8). The kinetic plot of the apparent CO loss from $[Mn(pqa)(CO)_3]ClO_4$ is shown in Figure 3.I.11. The photoproduct(s) appear to be

stable in solution, as evidenced by the final electronic absorption spectra of $[Mn(tpa)(CO)_3]ClO_4$, $[Mn(dpa)(CO)_3]Br$ and $[Mn(pqa)(CO)_3]ClO_4$. Taken together, these results confirm that these photoCORMs are effective CO donors ($t_{1/2}$ in the range 1.4-2.2 min) under a wide range of light although the k_{CO} values for all three carboyls are uniformly higher in the UV region.

The apparent quantum yield (ϕ_{358}) values of $[Mn(tpa)(CO)_3]ClO_4$, $[Mn(dpa)(CO)_3]Br$ and $[Mn(pqa)(CO)_3]ClO_4$ in MeCN (0.07 ± 0.01, 0.09 ± 0.01, and 0.06 ± 0.01 respectively) are lower than typical metal carbonyls such as $Na_3[W(CO)_5(TPPTS)]$[33] or $[W(CO)_6]$.[34] Nevertheless, these photoCORMs release CO in a slow yet steady pace for extended periods of time under *low-power (mW)* UV and visible light sources.

3.I.3.6. Vasorelaxation of Mouse Aorta

Activation of sGC upon binding of CO to the active site heme and concomitant relaxation of smooth muscle via the cyclic GMP pathway[35] has been utilized for the assessment of various CO donors such as CORM-3.[36] In the present study, we have examined such relaxation of aortic muscle rings in the presence of $[Mn(tpa)(CO)_3]ClO_4$, $[Mn(dpa)(CO)_3]Br$ and $[Mn(pqa)(CO)_3]ClO_4$ under light and dark conditions. Small loss of CO (over a period of hours) from both $[Mn(tpa)(CO)_3]ClO_4$ and $[Mn(dpa)(CO)_3]Br$ in tissue bath media has added complications in such measurements. However, $[Mn(pqa)(CO)_3]ClO_4$ is very stable in aqueous buffers and shows no loss of CO in the dark. When a mixture of $[Mn(pqa)(CO)_3]ClO_4$ and reduced Mb in PBS is kept in the dark for 4 h, no formation

of Mb-CO is observed. However, $[Mn(pqa)(CO)_3]ClO_4$ releases CO in the presence of light with an apparent CO-release rate k_{CO} value of 5.6 x 10^{-3} s^{-1} in PBS ($t_{1/2}$ = 2 min). Although this rate is less than that observed in MeCN, $[Mn(pqa)(CO)_3]ClO_4$ retains an excellent capacity of CO delivery under illumination in PBS.

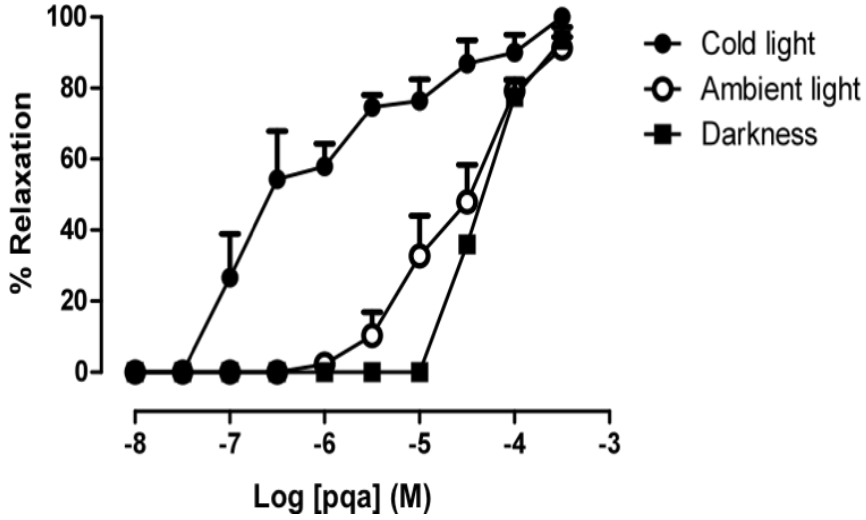

Figure 3.I.12. Vasorelaxation of mouse aorta muscle rings by $[Mn(pqa)(CO)_3]ClO_4$ upon exposure to visible (cold) light and ambient room light.

We have therefore examined the effect of $[Mn(pqa)(CO)_3]ClO_4$ on mouse aorta rings in tissue bath experiments. As shown in Figure 3.I.12, $[Mn(pqa)(CO)_3]ClO_4$ produced a concentration-dependent relaxation (in the 10^{-7} to 10^{-4} M range) under direct light exposure (indicated as cold light), while $[Mn(dpa)(CO)_3]Br$ generated minimal relaxation response at higher concentrations (10^{-5} M to 10^{-4} M range) under the same conditions. $[Mn(tpa)(CO)_3]ClO_4$ on the other hand, failed to trigger any sort of light-induced vasorelaxation response at the concentration range of interest (Figure 3.I.13). When the tissue-bath experiment was performed in a lighted room (no direct light exposure), similar albeit weak response to light was observed (indicated as

ambient light) for the compounds $[Mn(pqa)(CO)_3]ClO_4$ and $[Mn(dpa)(CO)_3]Br$ only. No relaxation was observed in the dark for concentrations below 10^{-5} M. These relaxations were inhibited by the sGC inhibitor ODQ, suggesting that CO-mediated vasorelaxation proceeds via a cGMP pathway.

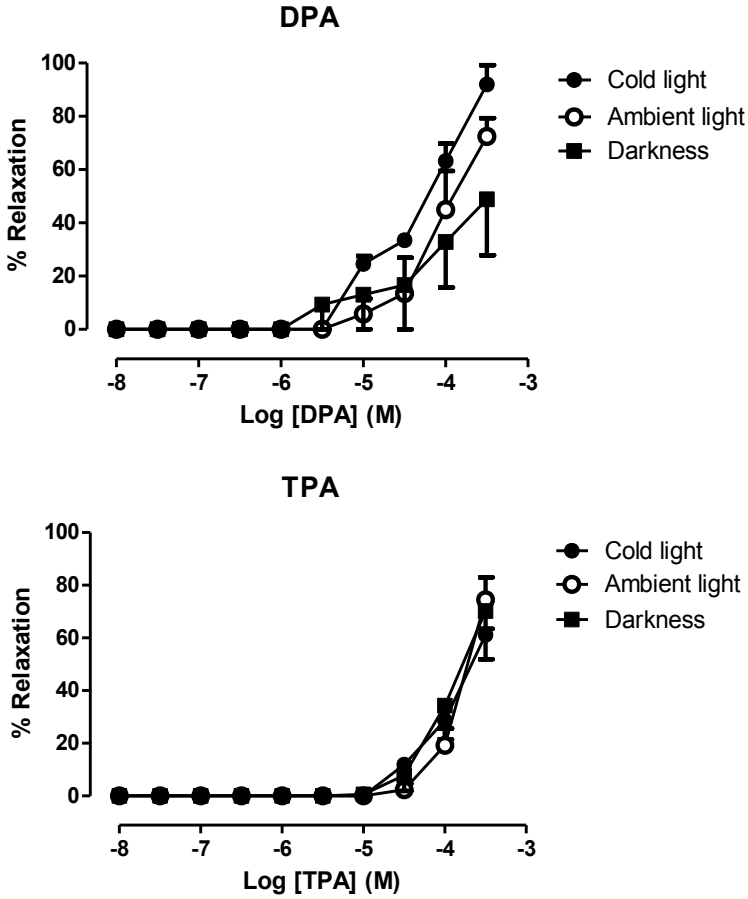

Figure 3.I.13. Vasorelaxation of mouse aorta muscle rings by $[Mn(dpa)(CO)_3]Br$ (top panel) and $[Mn(tpa)(CO)_3]ClO_4$ (bottom panel) upon exposure to visible (cold) light and ambient room light.

Collectively, these findings confirm that $[Mn(pqa)(CO)_3]ClO_4$ is an effective photoCORM that could find use in biological applications. Integrity of the tissues in the presence of the photoCORM when kept in dark also attests the fact that in the

concentration range of 10^{-7} to 10^{-4} M, the compound exhibits minimum toxic effect(s).

3.I.4. Experimental Section

General Procedures. All experimental manipulations were performed under anaerobic conditions using standard Schlenk line techniques. Manganese pentacarbonyl bromide ([$Mn(CO)_5Br$]) was purchased from Alfa Aesar. The ligands tri(2-pyridyl)amine (tpa),[37] *N,N*-bis(2-pyridylmethyl)amine (dpa),[38] (2-pyridylmethyl)(2-quinolylmethyl)amine (pqa)[39] and the starting salt, *fac*-[$Mn(CO)_3(MeCN)_3$](ClO_4)[25] were synthesized following published procedures. Solvents were purified and/or dried by standard techniques prior to use.

[$Mn(tpa)(CO)_3$]ClO_4 (1). A batch of 0.077 g (0.31 mmol) of tpa was dissolved in 20 mL of $CHCl_3$ and degassed. To a frozen solution of the ligand, 0.113 g (0.31 mmol) of *fac*-[$Mn(CO)_3(MeCN)_3$]ClO_4 was added as a solid. Upon thawing, the color of the mixture turned to a clear yellow. The solution was heated to reflux under nitrogen for 24 h with minimal exposure to light, during which some yellow precipitate was observed. The mixture was concentrated to ~ 25% of its original volume and the yellow solid was filtered and dried in vacuo. (0.276 g, 89% yield). X-ray quality crystals of **1** were obtained by diffusion of pentane into a dichloromethane solution of **1**. Anal. Calcd. $C_{18}H_{12}N_4O_7ClMn$: C, 44.42; H, 2.49; N, 11.51. Found: C, 44.39; H, 2.36; N, 11.54. Electronic Absorption Spectrum in MeCN, λ_{max} (nm, ε (M^{-1} cm^{-1})): 240 (10 130), 260 (10 240), 330 (5 270). Selected IR frequencies (KBr disk, cm^{-1}):

2041 (s, ν_{CO}), 1953 (s, ν_{CO}), 1930 (s, ν_{CO}), 1463 (w), 1086 (s, ν_{ClO4}), 767 (m), 624 (w). ^{1}H NMR (CD_3CN, 500 MHz), δ (ppm from TMS): 9.06 (d, 3H), 8.12 (t, 3H), 7.96 (d, 3H), 7.50 (t, 3H).

[Mn(dpa)(CO)$_3$]Br (2). A solution of 0.163 g (0.82 mmol) of dpa in 25 mL THF was degassed by freeze-pump-thaw cycles. To a frozen solution of the ligand, 0.225 g (0.82 mmol) of [$Mn(CO)_5Br$] was added as a solid. A clear orange color developed upon thawing. Under dim light conditions, the solution was heated to reflux under nitrogen for 5 h during which the orange color deepened and some yellow precipitate was observed. The yellow solid thus obtained was filtered and dried in vacuo. (0.382 g, 47% yield). Yellow crystalline needles suitable for X-ray studies were obtained by diffusion of pentane into dichloromethane solution of **2**. Anal. Calcd. for $C_{15}H_{13}N_3O_3BrMn$: C, 43.08; H, 3.13; N, 10.05. Found: C, 43.13; H, 3.10; N, 10.12. Electronic Absorption Spectrum in MeCN, λ_{max} (nm (ε, $M^{-1}cm^{-1}$)): 245 (9 650), 270 (5 680), 300 (5 150), 350 (2 860). Selected IR frequencies (KBr disk, cm^{-1}): 2030 (s, ν_{CO}), 1930 (s, ν_{CO}), 1607 (w), 1486 (w), 1439 (w), 758 (m). ^{1}H NMR (CD_3CN, 500 MHz), δ (ppm from TMS): 8.90 (d, 2H), 7.78 (t, 2H), 7.38 (d, 2H), 7.30 (t, 2H), 4.78 (s, 2H), 4.26 (s, 2H).

[Mn(pqa)(CO)$_3$]ClO$_4$ (3). With minimal exposure to light, a batch of 0.446 g (1.23 mmol) of *fac*-[$Mn(CO)_3(MeCN)_3$]ClO_4 was dissolved in a degassed solution of 0.307 g (1.23 mmol) of pqa in 25 mL of THF. The reaction mixture was heated to reflux

under nitrogen. During the heating process, the color changed from orange to a darker yellow green. The reaction mixture was allowed to reflux for 14 h when the color turned lighter orange and a yellow precipitate appeared. The yellow solid was collected by filtration, washed with diethyl ether and dried in vacuo. (0.30 g, 50% yield). Anal. Calcd for $C_{19}H_{15}N_3O_7ClMn$: C, 46.79; H, 3.10; N, 8.62. Found: C, 46.67; H, 3.13; N, 8.44. Electronic Absorption Spectrum in MeCN, λ_{max} (nm (ε, $M^{-1}cm^{-1}$)): 360 (6 060), 320 (3 220). Selected IR frequencies (KBr disk, cm^{-1}): 2033 (s, ν_{CO}), 1928 (s, ν_{CO}), 1943 (s, ν_{CO}), 1607 (w), 1515 (w), 1441 (w), 1102 (s, ν_{ClO4}), 764 (m), 628 (m). ^{1}H NMR (CD_3CN, 500 MHz), δ (ppm from TMS): 9.14 (d, 1H), 8.80 (d, 1H), 8.40 (d, 1H), 8.00 (q, 2H), 7.68-7.78 (m, 3H), 7.56 (d, 1H), 7.30 (d, 1H), 6.10 (s, 1H), 5.20 (d, 1H), 4.80 (d, 1H), 4.53 (d, 1H), 4.20 (d, 1H).

Physical Measurements. The ^{1}H NMR spectra were recorded at 298 K on a Varian Unity Inova 500 MHz instrument. A Perkin-Elmer Spectrum-One FT-IR was utilized to monitor the IR spectra of the compounds. Electronic absorption spectra were obtained on a Varian Cary 50 Spectrophotometer. Room temperature magnetic susceptibility measurements were performed with a Johnson Matthey magnetic susceptibility balance.

Delivery of CO to Myoglobin. Horse heart myoglobin was dissolved in phosphate buffered saline (PBS, 100 mM, pH 7.4) and reduced by adding sodium dithionite. The concentration of the resulting deoxymyoglobin (Mb) was calculated from the absorbance of the Soret band at 435 nm (extinction coefficient = 121 mM^{-1} cm^{-1}).

Next, aliquots of **1-3** in MeCN were added to Mb and the absorbance was taken after 5 min to ensure that the myoglobin was still reduced. Conversion of Mb to carbonyl myoglobin (Mb-CO) was monitored upon exposure to monochromatic light of 350 nm (40 mW continuous wave diode laser, Intelite Inc.) at defined time intervals. A shift in λ_{max} from 435 nm to 424 nm was noted in each case due to the formation of Mb-CO. Final concentrations of Mb-CO were assessed at 424 nm (extinction coefficient = 207 mM^{-1} cm^{-1}) and compared to the initial Mb present in solution to quantify light induced CO release by each compound.

X-ray Crystallography. Diffraction data for **1** and **2** were collected at 296 K on a Bruker APEX-II instrument using monochromated Mo-K_α radiation (λ = 0.71073 Å). All data were corrected for absorption and the structures were solved by direct methods using SHELXTL (1995-99) software package (Bruker Analytical X-ray Systems Inc.). Additional refinement details are contained in CIF files.

Photochemical Experiments. The quantum yield (ϕ) values of CO release were determined by using a Newport Oriel Apex Illuminator (150W Xenon lamp) equipped with an Oriel 1/8 m Cornerstone monochromator. The source of visible light was an IL 410 Illuminator (measured power 146-150 mW) equipped with a high energy light filter (350 nm cutoff). Standard ferrioxalate actinometry was used to determine the quantum yield values at 358 nm (ϕ_{358}).[38] Solutions of **1-3** in MeCN were prepared under dim light conditions and placed in a 2 x 10 mm quartz cuvette, 2 cm away from the light source. Solutions were prepared to ensure sufficient

absorbance (> 90%) at the irradiation wavelength, and changes in the electronic spectra in the 300-350 nm region (< 10% photolysis) were used to determine the extent of CO release.

The rate of CO release was measured by recording electronic absorption spectrum of **1**-**3** in MeCN (< 2 mM, 1.4 mL) and monitoring the loss of absorbance of samples exposed to a broadband light source (IL 410 Illuminator) at defined time intervals. The plots were fitted to the three parameter exponential equation $A(t) = A_\infty + (A_o - A_\infty) \exp\{-k_{CO}t\}$, where A_o and A_∞ are the initial and final absorbance values, respectively. The apparent rate of CO loss (k_{CO}) was calculated from the ln(C) versus time (T) plot for each CORM.

CO delivery to mouse aorta: Preparation of the tissue rings. Male C57BLK6 mice (25-35 g) were stunned and killed by cervical dislocation. The thoracic aorta was carefully removed, cleaned of connective tissue and cut into three to four ring segments of approximately 4 mm in length. Aortic rings were mounted in 10 mL organ baths containing Krebs-bicarbonate buffer (composition, (mM): Na^+ 143; K^+ 5.9; Ca^{2+} 2.5; Mg^{2+} 1.2; Cl^- 128; HCO_3^- 25; HPO_4^{2-} 1.2; SO_4^{2-} 1.2; D-glucose 11) maintained at 37 °C and gassed with 95% O_2/5% CO_2. Tension was initially set at 0.3 g and reset at intervals following an equilibration period of 1 h during which time fresh Krebs-bicarbonate buffer was replaced every 15-20 min. After equilibration, the rings were primed with KCl (48 mM), washed and precontracted with phenylephrine (PE, 1μM) was added. Once this response had stabilized, acetylcholine (ACh, 1μM) was added to the bath to assess the integrity of the endothelium. If the contractions to

PE were not maintained, or relaxations greater than 50% of the PE-induced tone to ACh were not observed, the tissues were discarded. Tissues were then washed for 30 min (by addition of fresh Krebs-bicarbonate buffer at 15 min intervals) after which cumulative concentrations of PE (1nM-1μM) were added to the organ bath. The tissues were then washed over 60 min to restore basal tone before contracting to approximately 80% of the maximum PE-induced response.

Once a stable response to PE was achieved, cumulative concentration–response curves to **1**-**2** (30 nM-300 μM) were constructed under each of the following three conditions: (a) darkness (tissue baths wrapped in Al foil), (b) ambient light (tissue baths exposed to regular laboratory light), and (c) cold light (tissue baths illuminated by a cold white light source, fiber optic lamp, 150 W, 5 cm distance). To determine the role of soluble guanylate cyclase (sGC) in the vasorelaxant response to the CO-donors, concentration-response curves to both **2** and **3** were constructed in tissues in the absence or presence of the sGC inhibitor ODQ (1H-[1,2,4]oxadiazolo[4,3-a]quinoxalin-1-one, 5 μM).

3.I.5. Additional Experimental Data: IR, ^{1}H NMR and Electronic Absorption Spectra

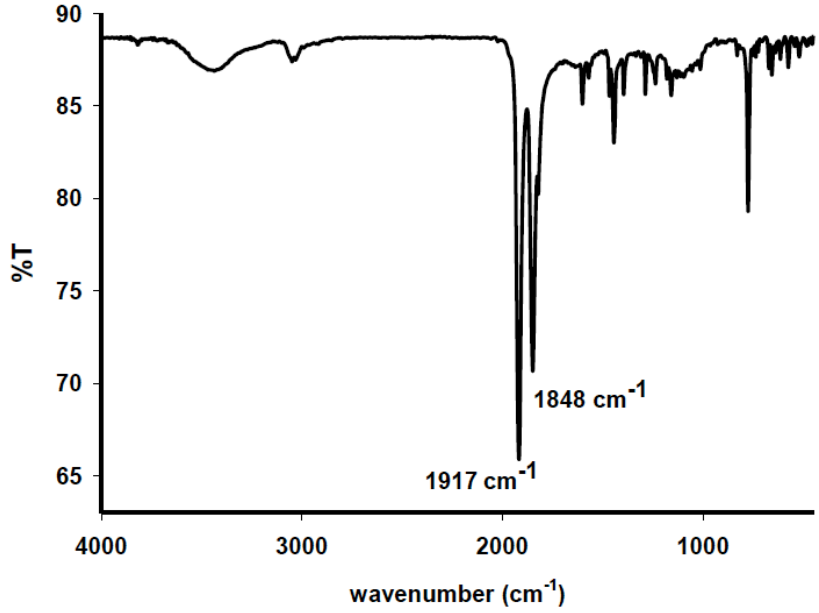

Figure 3.I.14. IR spectrum of [Mn(terpy)(CO)$_2$Br] in KBr pellet.

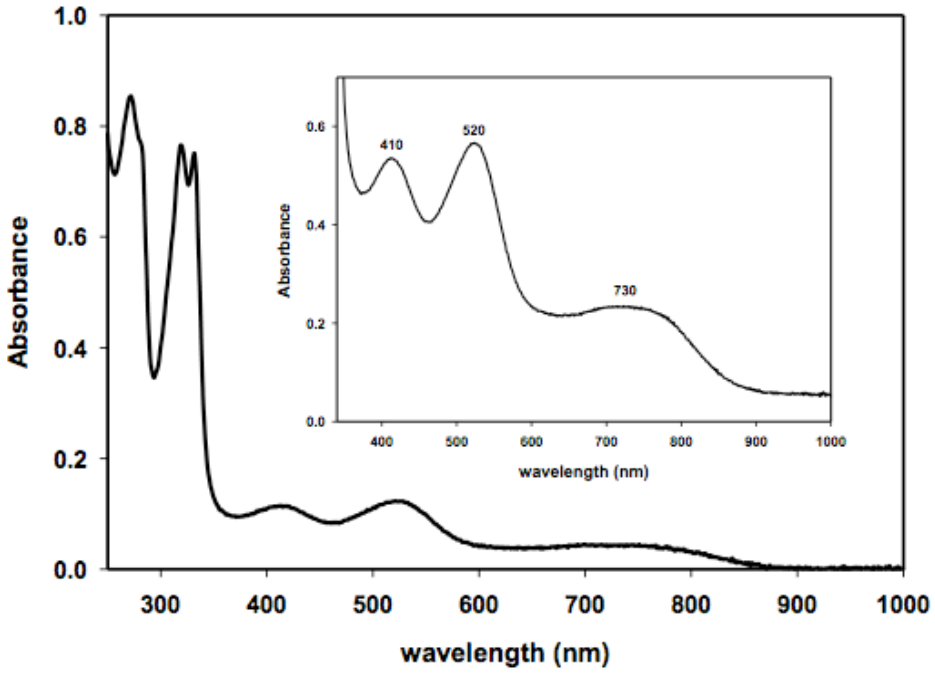

Figure 3.I.15. Electronic absorption spectrum of [Mn(terpy)(CO)$_2$Br] in MeCN (λ_{max} = 730 nm).

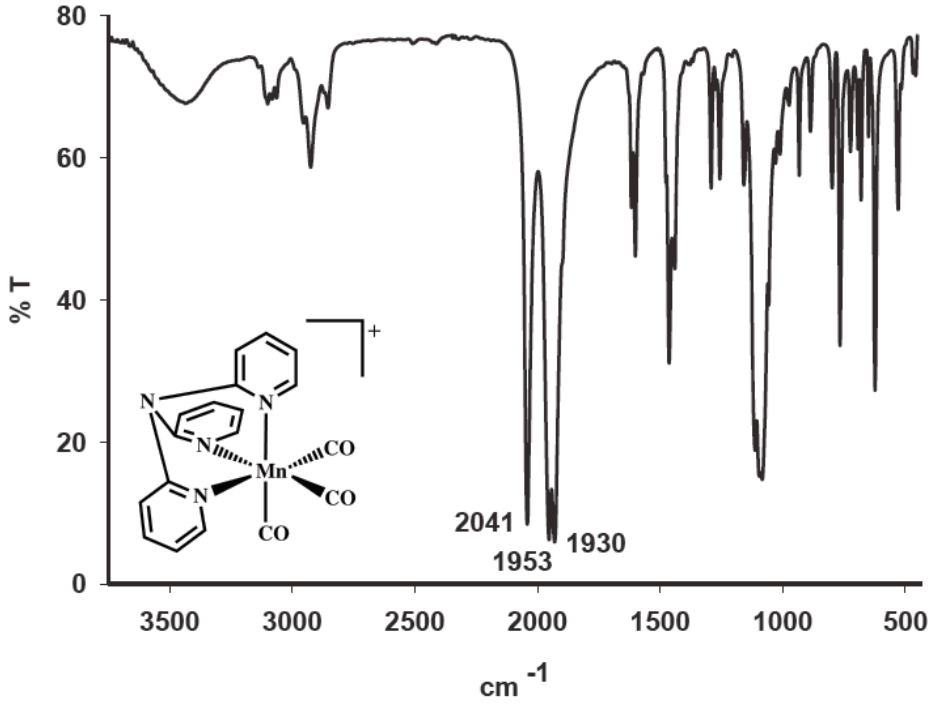

Figure 3.I.16. IR spectrum of $[Mn(tpa)(CO)_3]ClO_4$ in KBr disk.

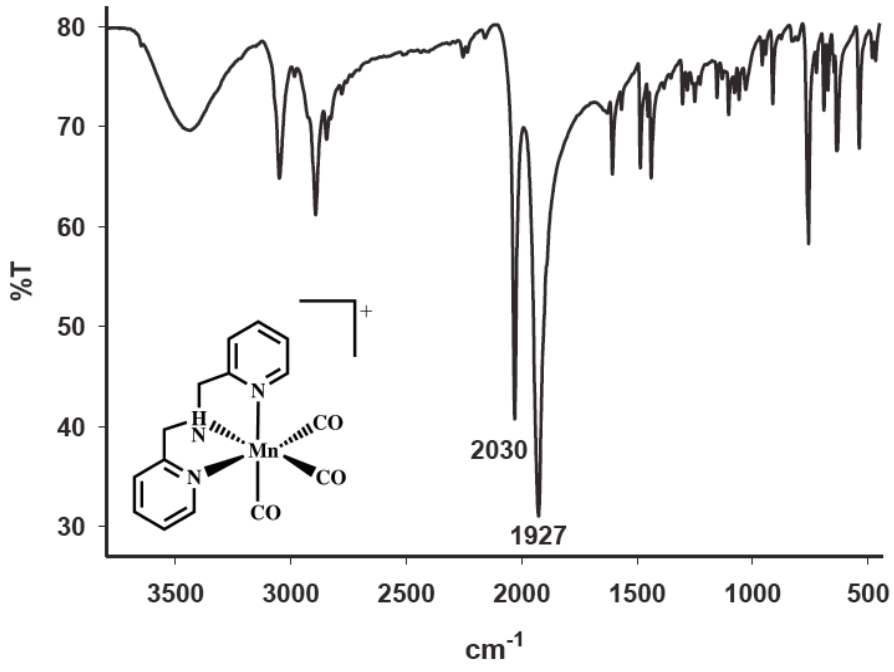

Figure 3.I.17. IR spectrum of $[Mn(dpa)(CO)_3]Br$ in KBr disk.

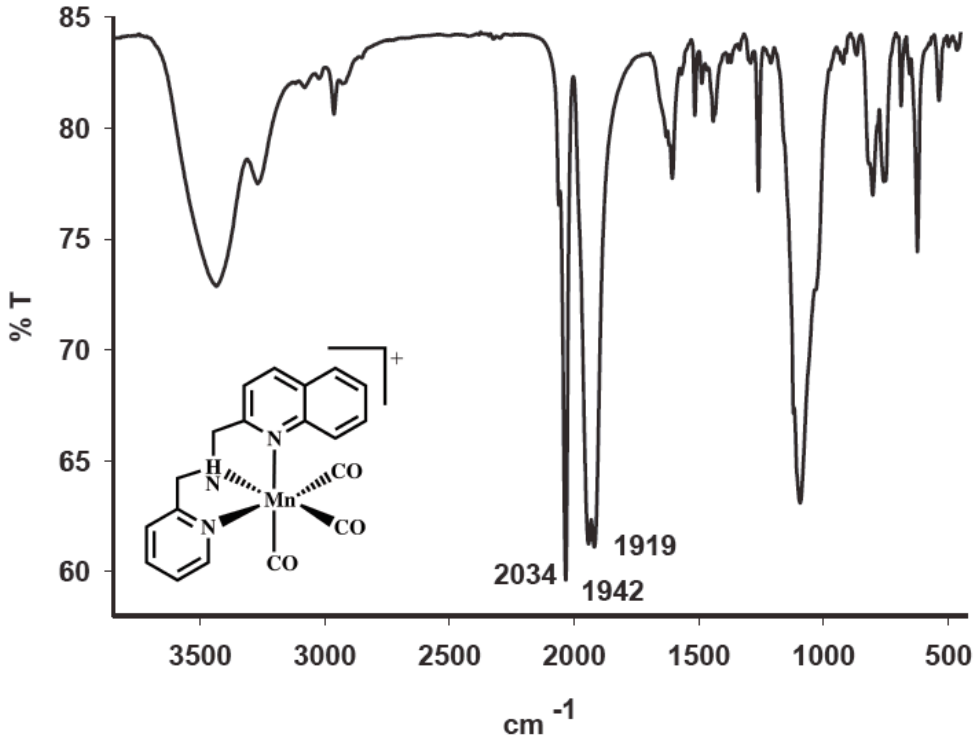

Figure 3.I.18. IR spectrum of $[Mn(pqa)(CO)_3]ClO_4$ in KBr disk.

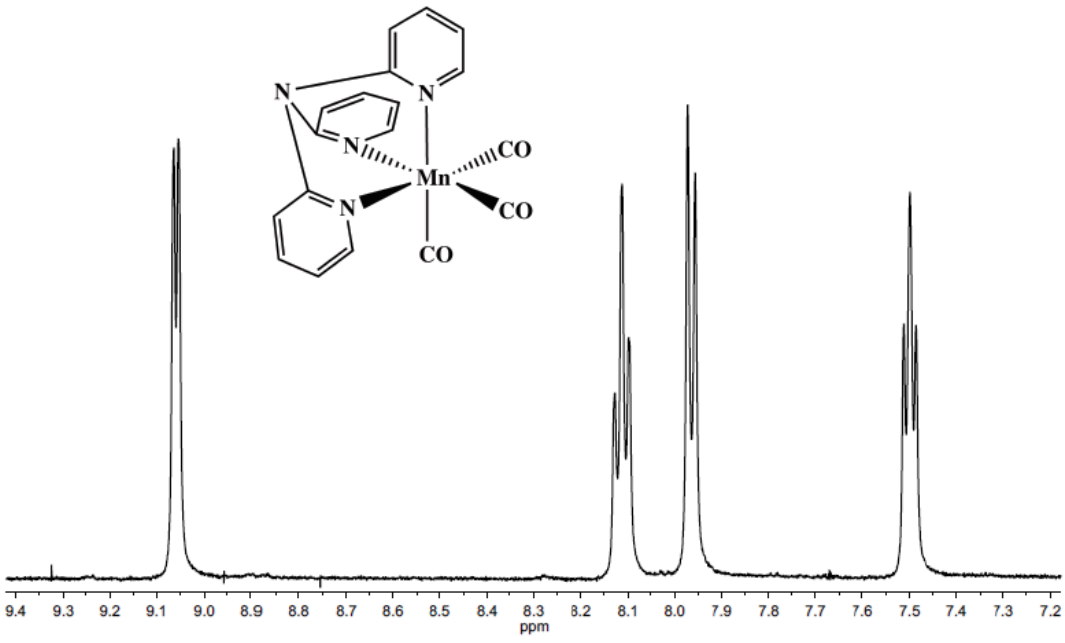

Figure 3.I.19. ^1H NMR Spectrum of $[Mn(tpa)(CO)_3]ClO_4$ in CD_3CN.

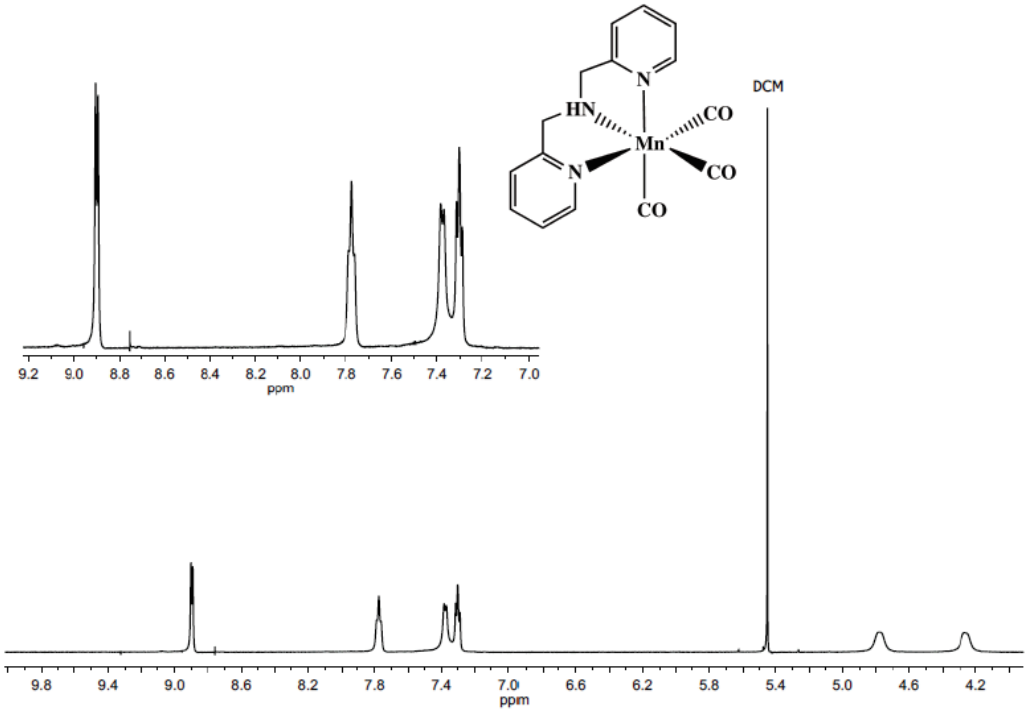

Figure 3.I.20. ^{1}H NMR Spectrum of $[Mn(dpa)(CO)_3]ClO_4$ in CD_3CN.

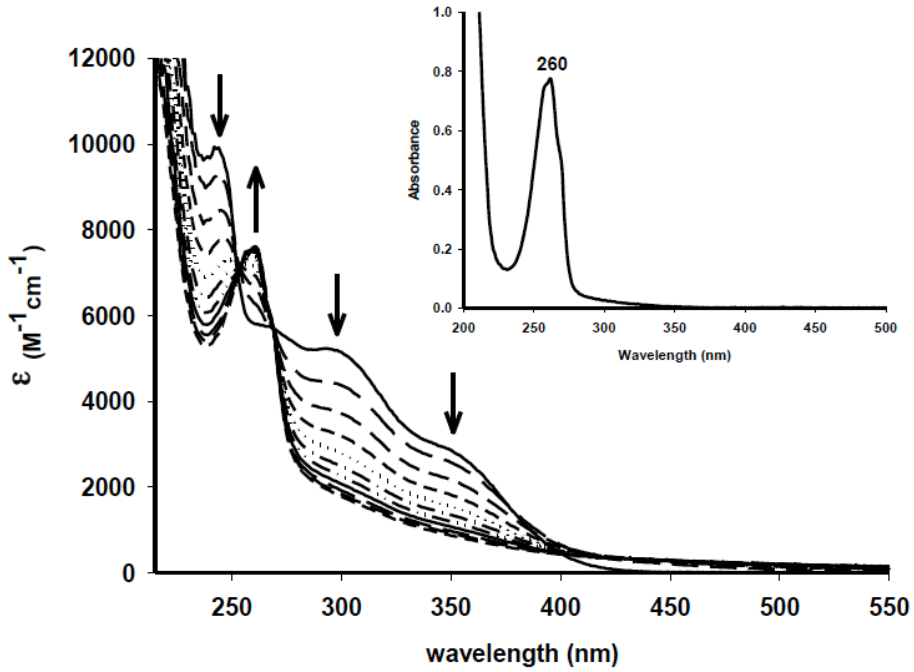

Figure 3.I.21. Electronic absorption spectrum of $[Mn(dpa)(CO)_3]Br$ in MeCN (λ_{max} = 350 nm); Inset: Electronic absorption spectrum of $[Mn(dpa)_2]^{2+}$ in MeCN.

3.I.6. References

(1) (a) Muhammad, S.; Yempally, V.; Anas, M.; Moncho, S.; Kyran, S. J.; Brothers, E. N.; Darensbourg, D. J.; Bengali, A. A., *Inorg. Chem.*, **2012**, *51,* 13041-13049. (b) Darensbourg, D. J, Draper, J. D.; Larkins, D. L.; Frost, B. J.; Reibenspies, J. H., *Inorg. Chem.*, **1998**, *37*, 2538-2546.

(2) (a) Kemnitz, C. R.; Ball, E. S.; McMahon, R. J., *Organometallics*, **2012**, *31*, 70-84. (b) Rimmer, R. D.; Pierri, A. E.; Ford, P. C., *Coord. Chem. Rev.*, **2012**, *256*, 1509-1519. (c) Rimmer, R. D; Richter, H.; Ford, P. C., *Inorg. Chem.*, **2010**, *49*, 1180-1185.

(3) Rossenaar, B. D.; Stufkens, D. J.; Oskam, A.; Fraanje, J.; Goubitz, K., *Inorg. Chim. Acta*, **1996**, *247*, 215-229.

(4) (a) Baerends, E. J.; Rosa, A., *Coord. Chem. Rev.*, **1998**, *177*, 97-125. (b) Vlček, A., *Coord. Chem. Rev.*, **1998**, *177*, 219-256.

(5) (a) Ben Amor, N.; Villaume, S.; Maynau, D.; Daniel, C., *Chem. Phys. Lett.*, **2006**, *421*, 378-382. (b) Rosa, A.; Baerends, E. J.; van Gisbergen, S. J. A.; van Lenthe, E.; Groeneveld, J. A.; Snijders, J. G., *J. Am. Chem. Soc.*, **1999**, *121*, 10356-10365. (c) Pollak, C.; Rosa, A.; Baerends, E. J., *J. Am. Chem. Soc.*, **1997**, *119*, 7324-7329.

(6) Motterlini, R; Clark, J. E.; Foresti, R.; Sarathchandra, P.; Mann, B. E.; Green, C. J., *Circ. Res.*, **2002**, *90*, e17.

(7) Herrick, R. S.; Brown, T. L., *Inorg. Chem*., **1984**, *23*, 4550-4553.

(8) Nayak, S. K.; Farrell, G. J.; Burkey, T. J., *Inorg. Chem.*, **1994,** *33*, 2236-2242.

(9) Trofimenko, S, *J. Am. Chem. Soc.*, **1970,** *92*, 5118-5126.

(10) (a) Schatzschneider, U. *Inorg. Chim. Acta* **2011**, *374*, 19-23. (b) Niesel, J.; Pinto, A.; N'Dongo, H. W. P.; Merz, K.; Ott, I.; Gust, R.; Schatzschneider, U. *Chem. Commun.* **2008**, 1798.

(11) (a) Huber, W.; Linder, R.; Niesel, J.; Schatzschneider, U.; Spingler, B.; Kunz, P. C., *Eur. J. Inorg. Chem.*, **2012**, 3140. (b) Kunz, P. C.; Huber, W.; Rojas, A.; Schatzschneider, U.; Spingler, B., *Eur. J. Inorg. Chem.*, **2009**, 5358-5366.

(12) (a) Bhaumik, C.; Das, S.; Maity, D.; Baitalik, S., *Dalton Trans.*, **2012**, *41*, 2427-2438. (b) Rajalakshmanan, E.; Alexander, V., *Inorg. Chem.*, **2007**, *46*, 6252-6260. (c) Wong, K. M. C.; Yam, V. W. W., *Coord. Chem. Rev.*, **2007**, *251*, 2477-2488.

(13) Medlycott, E. A.; Hanan, G. S., *Chem. Soc. Rev.*, **2005**, *34*, 133-142.

(14) Li, L. Y.; Jia, H. N.; Yu, H. J.; Du, K. J.; Lin, Q. T.; Qiu, K. Q.; Chao, H.; Ji, L. N., *J. Inorg. Biochem.*, **2012**, *113*, 31-39.

(15) Sharma, S.; Singh, S. K.; Pandey, D. S., *Inorg. Chem.*, **2008**, *47*, 1179-1189.

(16) (a) Robson, K. C. D.; Koivisto, B. D.; Yella, A.; Sporinova, B.; Nazeeruddin, M. K.; Baumgartner, T.; Grätzel, M.; Berlinguette, C. P., *Inorg. Chem.*, **2011**, *50*, 5494-5508. (b) Chan, H. T.; Mak, C. S. K.; Djurišič, A. B.; Chan, W. K., *Macromol. Chem. Phys.*, **2011**, *212*, 774-784.

(17) (a) Zheng, Z. B.; Duan, Z. M.; Zhang, J. X.; Wang, K. Z., *Sensor. Actuat. B-Chem.*, **2012**, *169*, 312-319. (b) Pei, L. M.; Lin, Q. T.; Chao, H.; Ji, L. N., *Inorg. Chem. Commun.*, **2012**, *22*, 90-92.

(18) Romain, S.; Duboc, C.; Retegan, M.; Leprêtre, J. C.; Blackman, A. G.; Deronzier, A.; Collomb, M. N., *Inorg. Chim. Acta*, **2011**, *374*, 187-196.

(19) (a) Wieprecht, T.; Xia, J.; Heinz, U.; Dannacher, J.; Schlingloff, G., *J.Mol. Catal. A-Chem*., **2006**, *251*, 159-176. (b) Wieprecht, T.; Heinz, U.; Xia, J.; Schlingloff, G.; Dannacher, J., *J. Surfactants Deterg.,* **2004**, *7*, 59-66.

(20) (a) Walesa-Chorab, M.; Stefankiewicz, A. R.; Ciesielski, D.; Hnatejko, Z.; Kubicki, M.; Klak, J.; Korabik, M. J.; Patroniak, V., *Polyhedron*, **2011**, *30*, 730-737. (b) Baffert, C.; Romero, I.; Pécaut, J.; Llobet, A.; Deronzier, A.; Collomb, M. N., *Inorg. Chim. Acta*, **2004**, *357*, 3430-3436.

(21) Juris, A.; Campagna, S.; Bidd, I.; Lehn, J. M.; Ziessel, R., *Inorg. Chem.*, **1988**, *27,* 4007-4011.

(22) Anderson, P. A.; Keene, F. R.; Horn, E.; Tiekink, E. R. R., *Appl. Organomet. Chem.*, **1990**, *4*, 523-533.

(23) Abel, E. W.; Dimitrov, V. S.; Long, N. J.; Orrell, K. G.; Osborne, A. G.; Pain, H. M.; Šik, V.; Hursthouse, M. B.; Mazid, M. A., *J. Chem. Soc. Dalton Trans.*, **1993**, 597-603.

(24) Black, D. R.; Hightower, S. E., *Inorg. Chem. Commun.*, **2012**, *24*, 16-19.

(25) Edwards, D.; Marshalsea, J. *J. Organomet. Chem.*, **1977**, *131*, 73-91.

(26) Reger, D. L.; Grattan, T. C.; Brown, K. J.; Little, C. A.; Lamba, J. J. S.; Rheingold, A. L.; Sommer, R. D.; *J. Organomet. Chem.*, **2000**, *607*, 120-128.

(27) Carlos, R. M.; Carlos, I. A.; Lima Neto, B. S.; Neumann, M. G., *Inorg. Chim. Acta*, **2000**, *299*, 231-237.

(28) Hyams, I. J.; Bailey, R. T.; Lippincott, E. R., *Spectro. Chim. Acta*, **1967**, *23A*, 273-284.

(29) Berndt, A. F.; Marsh, R. E. *Acta Cryst.* **1963**, *16*, 118-123.

(30) Peters, L.; Hübner, E.; Burzlaff, N. *J. Organomet. Chem*. **2005**, *690*, 2009-2016.

(31) H. M. Berends and P. Kurz, *Inorg. Chim. Acta*, *380*, 141 (2012).

(32) Romberg, R. W.; Kassner, R. J. *Biochemistry* **1979**, *18*, 5387-5392.

(33) Rimmer, R. D.; Richter, H.; Ford, P. C. *Inorg. Chem*. **2010**, *49*, 1180-1185.

(34) Wieland, S.; van Eldik, R. *J. Phys. Chem*. **1990**, *94*, 5865-5870.

(35) Ignarro, L. J. *Nitric Oxide: Biology and Pathology*; Academic Press: San Diego, 2000.

(36) Foresti, R.; Hammad, J.; Clark, J. E.; Johnson, T. R.; Mann, B. E.; Friebe, A.; Green, C. J.; Motterlini, R. *Br. J. Pharmacol*. **2004**, *142*, 453-460.

(37) Nagao, N.; Egashira, K.; Mogi, D., *Bull. Chem. Soc. Jpn.* **2004**, *77*, 1171-1172.

(38) Wong, Y.; Mak, C.; Kwan, H. S.; Lee, H. K. *Inorg. Chim. Acta*, **2010**, *363*, 1246-1253.

(39) Baldeau, S. M.; Slinn, C. H.; Krebs, B.; Rompel, A. *Inorg. Chim. Acta*, **2004**, *357*, 3295-3303.

3.I.7. Reprint of Publication

(1) Gonzalez, M. A.; Yim, M. A.; Cheng, S.; Moyes, A,; Hobbs, A. J.; Mascharak, P. K., "Manganese Carbonyls Bearing Tripodal Polypyridine Ligands as Photoactive Carbon Monoxide-Releasing Molecules," *Inorg. Chem.* **2012**, *51*, 601-608.

Reprinted with Permission from the American Chemical Society, Copyright 2012

Inorganic Chemistry

Article

pubs.acs.org/IC

Manganese Carbonyls Bearing Tripodal Polypyridine Ligands as Photoactive Carbon Monoxide-Releasing Molecules

Margarita A. Gonzalez,[†] Melanie A. Yim,[†] Stephanie Cheng,[‡] Amie Moyes,[‡] Adrian J. Hobbs,[‡] and Pradip K. Mascharak*[,†]

[†]Department of Chemistry and Biochemistry, University of California, Santa Cruz, California 95064, United States

[‡]Department of Pharmacology, University College, London WC1E 6BT, U.K.

Supporting Information

ABSTRACT: The recently discovered cytoprotective action of CO has raised interest in exogenous CO-releasing materials (CORMs) such as metal carbonyls (CO complexes of transition metals). To achieve control on CO delivery with metal carbonyls, we synthesized and characterized three Mn(I) carbonyls, namely, $[Mn(tpa)(CO)_3]ClO_4$ [**1**, where tpa = tris(2-pyridyl)amine], $[Mn(dpa)(CO)_3]Br$ [**2**, where dpa = *N*,*N*-bis(2-pyridylmethyl)amine], and $[Mn(pqa)(CO)_3]ClO_4$ [**3**, where pqa = (2-pyridylmethyl)(2-quinolylmethyl)amine], by crystallography and various spectroscopic techniques. All three carbonyls are sensitive to light and release CO when illuminated with low-power UV (5−10 mW) and visible (λ > 350 nm, ∼100 mW) light. The sensitivity of **1**−**3** to light has been assessed with respect to the number of pyridine groups in their ligand frames. When a pyridine ring is replaced with quinoline, extended conjugation in the ligand frame increases the absorptivity and makes the resulting carbonyl **3** more sensitive to visible light. These photosensitive CORMs (photoCORMs) have been employed to deliver CO to myoglobin under the control of light. The superior stability of **3** in aqueous media makes it a photoCORM suitable for inducing vasorelaxation in mouse aortic muscle rings.

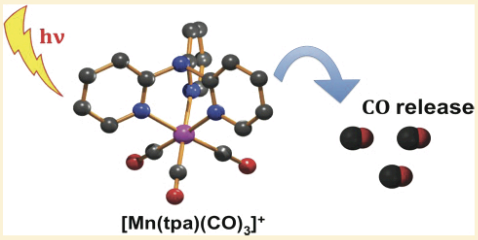

■ INTRODUCTION

In recent years, the biochemistry of carbon monoxide (CO) has been explored for its physiological significance and potential as a therapeutic.[1] This extremely toxic molecule is generated in the human body at a basal rate of 500 μmol/day.[2a] The major source of CO in mammalian cells is the result of degradation of heme by the enzyme heme oxygenases (HO).[3] This family of enzymes not only function in the normal breakdown of aged or damaged erythrocytes but also are upregulated in the presence of external stress, which includes exposure to heavy metals, arsenite, nitric oxide, and ultraviolet-A radiation.[2b] Increased CO levels fostered by HO have been correlated with long-term organ transplant survival,[4] anti-inflammatory action,[5] and anti-apoptotic outcomes.[6] Because the upregulation of HO is initiated in the wake of cellular stress, the endogenous production of CO has been equated with cytoprotective action.

Initial studies in this area focused on the utility of exogenously applied CO gas in the prevention of hyperoxic lung injury,[7] promotion of antioxidant activity,[8] and reversal of induced hypertension.[9] Even though most animal models yield promising results when CO is administered, its high affinity for hemoglobin poses a risk of hypoxic injury to human subjects. Strategic delivery of this noxious gas to the intended tissues is thus crucial in simulating some of the desirable effects of CO. The affinity of CO for low-valent metal centers has been the basis for the application of metal carbonyls (CO complexes of transition metals) as exogenous carbon monoxide-releasing molecules (CORMs) in recent attempts along this direction. Transition metal carbonyls can indeed serve as benign vehicles for CO transport, thus circumventing the inherent toxicity associated with CO inhalation. $[Ru(glycinate)(CO)_3Cl]$, developed by Motterlini and co-workers (often termed CORM-3), was one of the first compounds to be soluble in aqueous media that exhibited promising results.[10] As benign leaving groups, amino acids and amino esters have been incorporated in the preparation of group 6-based CORMs.[11] The involvement of pyrone groups in known metabolic pathways prompted the syntheses of some Fe- and Mo-based CORMs.[12] Other solvent-labile CORMs analyzed for biological applications include Ir(III), Re(II), and Co(0) carbonyls.[13−15] The aforementioned compounds all undergo solvent-assisted CO release, which may be desirable in some applications. A better handle for triggering CO release is, however, necessary to accurately administer this potentially toxic agent.

Metal carbonyls have also been known to release CO via photodissociation. The release of CO from the homoleptic carbonyls $[Mn_2(CO)_{10}]$[16] and $[Fe(CO)_5]$,[17] for example, has been assessed using laser flash photolysis. It is not thus not surprising that these compounds were employed as CORMs in

Received: September 30, 2011
Published: December 9, 2011

ACS Publications © 2011 American Chemical Society

the earlier CO-mediated biological assays.[18] As is typical of homoleptic metal carbonyls, these compounds exhibit poor solubility in protic solvents and require a high-power light source to achieve photolysis. Schatzschneider and co-workers have recently reported some improvement with a tricarbonyl complex $[Mn(CO)_3(tmp)](PF_6)$ [tmp = tris-(pyrazolylmethane)] that releases CO upon irradiation with UV light.[19] Ford and co-workers have also reported autoxidation of the tungsten center of $[W(CO)_5(TPPTS)]^{3-}$ [TPPTS = tris(sulfonatophenyl)phosphine trianion] with subsequent CO release upon irradiation with near-UV light.[20] The latter group has introduced the term "photoCORM" to describe this class of compounds. In a recent account, an Fe-based carbonyl bearing cysteamine ligands (termed CORM-S1) has been shown to deliver CO upon irradiation with visible light (λ > 400 nm).[21]

During the past few decades, the role of another endogenously produced diatomic molecule, namely, nitric oxide (NO), in vascular relaxation,[22] neurotransmission,[23] immune response,[24] and apoptotic pathways[25] has been firmly established. As part of our research in the area of exogenous NO donors, we have been involved in the syntheses of designed metal nitrosyls [nitric oxide (NO) complexes of metals such as Fe, Mn, and Ru] that rapidly deliver NO upon exposure to light of a wide range of wavelengths (400−1000 nm).[26−31] The efficacy of these compounds in delivering NO to biological targets such as cellular enzymes, breast cancer cells, and bacteria has been demonstrated.[32] Recent findings about the role of endogenously produced CO in cell signaling and cytoprotective activity appear to complement that of NO.[2a] The parallels in the biological relevance and synthetic chemistry of these two diatomic ligands prompted us to extend our design principles in the preparation of light-activated CORMs (photoCORMs). Our initial efforts to prepare CORMs based on previously designed ligand frames resulted in a series of structurally related solvent-labile iron carbonyls that steadily give off CO under physiological conditions.[33] However, these CORMs did not require light for CO release.

As part of our quest for suitable photoCORMs, we herein report a series of photoactive manganese carbonyls bearing tridentate ligands with varying degrees of conjugation in their frameworks. The structures of the ligands employed are shown in Figure 1. We intended to determine whether an increase in the number of pyridine N donors and/or extent of conjugation will cause a shift in the absorption maximum of the resulting carbonyls, thus lowering the energy required for dissociation of CO from the resulting metal carbonyls. The syntheses, characterization, and photoactivity of $[Mn(tpa)(CO)_3]ClO_4$ [**1**, where tpa = tris(2-pyridyl)amine], $[Mn(dpa)(CO)_3]Br$ [**2**, where dpa = *N*,*N*-bis(2-pyridylmethyl)amine], and $[Mn(pqa)(CO)_3]ClO_4$ [**3**, where pqa = (2-pyridylmethyl)(2-quinolylmethyl)amine] are described in this paper. The rates of release of CO from **1**−**3** upon exposure to UV (305 nm) and visible light (λ > 350 nm) have been determined to evaluate their efficacy as photoCORMs for biological studies. The efficacy of photorelease of CO from **3** has also been evaluated on the basis of relaxation of mouse aortic smooth muscle tissue in vitro.

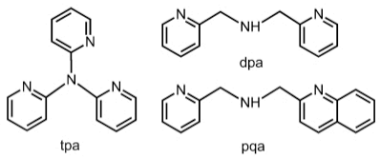

Figure 1. Structures of the ligands used in this study.

EXPERIMENTAL SECTION

General Procedures. All experimental manipulations were performed under anaerobic conditions using standard Schlenk line techniques. Manganese pentacarbonyl bromide {$[Mn(CO)_5Br]$} was purchased from Alfa Aesar. The ligands tris(2-pyridyl)amine (tpa),[34] *N*,*N*-bis(2-pyridylmethyl)amine (dpa),[35] and (2-pyridylmethyl)(2-quinolylmethyl)amine (pqa)[36] and the starting salt *fac*-$[Mn(CO)_3(MeCN)_3](ClO_4)$[37] were synthesized following published procedures. Solvents were purified and/or dried by standard techniques prior to being used.

Caution! *Transition metal perchlorates should be prepared in small quantities and handled with great caution as metal perchlorates may explode upon heating.*

$[Mn(tpa)(CO)_3]ClO_4$ (1). A batch of 0.077 g (0.31 mmol) of tpa was dissolved in 20 mL of $CHCl_3$ and degassed. To a frozen solution of the ligand was added 0.113 g (0.31 mmol) of *fac*-$[Mn(CO)_3(MeCN)_3]ClO_4$ as a solid. When the mixture thawed, its color turned to a clear yellow. The solution was heated to reflux under nitrogen for 24 h with minimal exposure to light, during which time some yellow precipitate was observed. The mixture was concentrated to ∼25% of its original volume, and the yellow solid was filtered and dried in vacuo (0.276 g, 89% yield). X-ray quality crystals of **1** were obtained by diffusion of pentane into a dichloromethane solution of **1**. Anal. Calcd for $C_{18}H_{12}N_4O_7ClMn$: C, 44.42; H, 2.49; N, 11.51. Found: C, 44.39; H, 2.36; N, 11.54. Electronic absorption spectrum in MeCN, λ_{max} (nm) [ε (M^{-1} cm^{-1})]: 240 (10130), 260 (10240), 330 (5270). Selected IR frequencies (KBr disk, cm^{-1}): 2041 (s, ν_{CO}), 1953 (s, ν_{CO}), 1930 (s, ν_{CO}), 1463 (w), 1086 (s, ν_{ClO_4}), 767 (m), 624 (w). ^1H NMR (CD_3CN, 500 MHz), δ (from TMS): 9.06 (d, 3H), 8.12 (t, 3H), 7.96 (d, 3H), 7.50 (t, 3H).

$[Mn(dpa)(CO)_3]Br$ (2). A solution of 0.163 g (0.82 mmol) of dpa in 25 mL of THF was degassed by freeze−pump−thaw cycles. To a frozen solution of the ligand was added 0.225 g (0.82 mmol) of $[Mn(CO)_5Br]$ as a solid. A clear orange color developed when the sample thawed. Under dim light conditions, the solution was heated to reflux under nitrogen for 5 h, during which time the orange color deepened and some yellow precipitate was observed. The yellow solid thus obtained was filtered and dried in vacuo (0.382 g, 47% yield). Yellow crystalline needles suitable for X-ray studies were obtained by diffusion of pentane into a dichloromethane solution of **2**. Anal. Calcd for $C_{15}H_{13}N_3O_3BrMn$: C, 43.08; H, 3.13; N, 10.05. Found: C, 43.13; H, 3.10; N, 10.12. Electronic absorption spectrum in MeCN, λ_{max} (nm) [ε (M^{-1} cm^{-1})]: 245 (9650), 270 (5680), 300 (5150), 350 (2860). Selected IR frequencies (KBr disk, cm^{-1}): 2030 (s, ν_{CO}), 1930 (s, ν_{CO}), 1607 (w), 1486 (w), 1439 (w), 758 (m). ^1H NMR (CD_3CN, 500 MHz), δ (from TMS): 8.90 (d, 2H), 7.78 (t, 2H), 7.38 (d, 2H), 7.30 (t, 2H), 4.78 (s, 2H), 4.26 (s, 2H).

$[Mn(pqa)(CO)_3]ClO_4$ (3). With minimal exposure to light, a batch of 0.446 g (1.23 mmol) of *fac*-$[Mn(CO)_3(MeCN)_3]ClO_4$ was dissolved in a degassed solution of 0.307 g (1.23 mmol) of pqa in 25 mL of THF. The reaction mixture was heated to reflux under nitrogen. During the heating process, the color changed from orange to a darker yellow green. The reaction mixture was allowed to reflux for 14 h, during which time the color turned lighter orange and a yellow precipitate appeared. The yellow solid was collected by filtration, washed with diethyl ether, and dried in vacuo (0.30 g, 50% yield). Anal. Calcd for $C_{19}H_{15}N_3O_7ClMn$: C, 46.79; H, 3.10; N, 8.62. Found: C, 46.67; H, 3.13; N, 8.44. Electronic absorption spectrum in MeCN, λ_{max} (nm) [ε (M^{-1} cm^{-1})]: 360 (6060), 320 (3220). Selected IR frequencies (KBr disk, cm^{-1}): 2033 (s, ν_{CO}), 1928 (s, ν_{CO}), 1943 (s, ν_{CO}), 1607 (w), 1515 (w), 1441 (w), 1102 (s, ν_{ClO_4}), 764 (m), 628

(m). ^{1}H NMR (CD_3CN, 500 MHz), δ (from TMS): 9.14 (d, 1H), 8.80 (d, 1H), 8.40 (d, 1H), 8.00 (q, 2H), 7.68−7.78 (m, 3H), 7.56 (d, 1H), 7.30 (d, 1H), 6.10 (s, 1H), 5.20 (d, 1H), 4.80 (d, 1H), 4.53 (d, 1H), 4.20 (d, 1H).

Physical Measurements. The ^{1}H NMR spectra were recorded at 298 K on a Varian Unity Inova 500 MHz instrument. A Perkin-Elmer Spectrum-One FT-IR instrument was utilized to monitor the IR spectra of the compounds. Electronic absorption spectra were recorded on a Varian Cary 50 spectrophotometer. Room-temperature magnetic susceptibility measurements were performed with a Johnson Matthey magnetic susceptibility balance.

Delivery of CO to Myoglobin. Horse heart myoglobin was dissolved in phosphate-buffered saline (PBS, 100 mM, pH 7.4) and reduced by addition of sodium dithionite. The concentration of the resulting deoxymyoglobin (Mb) was calculated from the absorbance of the Soret band at 435 nm (extinction coefficient of 121 mM^{-1} cm^{-1}). Next, aliquots of **1**−**3** in MeCN were added to Mb, and the absorbance was taken after 5 min to ensure that the myoglobin was still reduced. Conversion of Mb to carbonyl myoglobin (Mb-CO) was monitored upon exposure to monochromatic 350 nm light (40 mW continuous wave diode laser, Intelite Inc.) at defined time intervals. A shift in λ_{max} from 435 to 424 nm was noted in each case because of the formation of Mb-CO. Final concentrations of Mb-CO were assessed at 424 nm (extinction coefficient of 207 mM^{-1} cm^{-1}) and compared to the that of initial Mb present in solution to quantify light-induced CO release by each compound.

X-ray Crystallography. Diffraction data for **1** and **2** were collected at 296 K on a Bruker APEX-II instrument using monochromated Mo Kα radiation (λ = 0.71073 Å). The fact that the perchlorate anion and the solvent (CH_2Cl_2) molecule in the structure of **1** were disordered is reflected in the high R_w value as listed in Table 1. All data were corrected for absorption, and the structures were determined by direct methods using the SHELXTL (1995−99) software package (Bruker Analytical X-ray Systems Inc.). Additional refinement details are contained in CIF files (Supporting Information). Crystal data and instrument and data collection parameters are summarized in Table 1. Selected bond distances and angles are listed in Table 2.

Table 1. Summary of Crystal Data and Intensity Collection and Refinement Parameters for $[Mn(tpa)(CO)_3]ClO_4 \cdot CH_2Cl_2$ ($1 \cdot CH_2Cl_2$) and $[Mn(dpa)(CO)_3]Br$ (2)

	1	2
empirical formula	$C_{19}H_{14}N_4O_7Cl_3Mn$	$C_{15}H_{13}N_3O_3BrMn$
formula weight	571.63	418.13
crystal color	yellow blade	colorless plate
crystal size (mm^3)	0.10 × 0.08 × 0.06	0.105 × 0.095 × 0.090
temperature (K)	296(2)	296(2)
wavelength (Å)	0.71073	0.71073
crystal system	monoclinic	orthorhombic
space group	C2/c	*Pnma*
a (Å)	19.9291(18)	11.4036(13)
b (Å)	18.0036(16)	15.0946(17)
c (Å)	13.5731(12)	9.6955(11)
α (deg)	90	90.00
β (deg)	94.0860(10)	90.00
γ (deg)	90	90.00
V ($Å^3$)	4857.6(8)	1668.9(3)
Z	8	4
d_{cal} (g/cm^3)	1.563	1.664
μ (mm^{-1})	0.920	3.201
goodness of fit[a] on F^2	1.050	1.063
final R indices	R_1 = 0.0809	R_1 = 0.0359
$[I > 2\sigma(I)]$	wR_2 = 0.2484	wR_2 = 0.0891
R indices[b]	R_1 = 0.1005	R_1 = 0.0504
all data[c]	wR_2 = 0.2724	wR_2 = 0.0992

[a]Goodness of fit = $[\sum w(|F_o|^2 - |F_c|^2)^2/(N_o - N_v)]^{1/2}$, where N_o is the number of observations and N_v the number of variables. [b]$R_1 = \sum||F_o| - |F_c||/\sum|F_o|$. [c]$wR_2 = [\sum w(|F_o|^2 - |F_c|^2)^2/\sum w|F_o|^2]^{1/2}$.

Table 2. Selected Bond Distances (angstroms) and Angles (degrees) of 1 and 2

Complex 1			
Mn−N1	2.058(4)	Mn−N3	2.065(4)
Mn−N4	2.059(4)	Mn−C16	1.813(5)
Mn−C17	1.806(5)	Mn−C18	1.809(5)
C16−O1	1.143(7)	C17−O2	1.141(6)
C18−O3	1.121(6)		
C16−Mn−N1	92.4(2)	C16−Mn−N3	176.22(19)
C16−Mn−N4	92.6(2)	C17−Mn−N1	91.9(2)
C17−Mn−N3	92.83(19)	C17−Mn−N4	176.78(18)
C18−Mn−N1	178.06(19)	C18−Mn−N3	92.9(2)
C18−Mn−N4	92.6(2)	N1−Mn−N3	85.34(14)
N1−Mn−N4	86.48(14)	N3−Mn−N4	84.29(14)
C17−Mn−C16	90.3(2)	C17−Mn−18	89.0(3)
C18−Mn−C16	89.3(2)	Mn−C16−O1	178.3(6)
Mn−C17−O2	178.6(6)	Mn−C18−O3	176.7(5)
Complex 2			
Mn−N1	2.053(3)	Mn−N2	2.063(4)
Mn−C7	1.794(5)	Mn−C8	1.805(4)
C7−O2	1.144(6)	C8−O1	1.145(4)
C7−Mn−N1	95.53(14)	C7−Mn−N1A	95.52(14)
C7−Mn−N2	174.87(19)	C7−Mn−C8A	87.90(16)
C7−Mn−C8	87.90(16)	C8A−Mn−C7	87.90(16)
C8−Mn−N1	92.10(13)	C8−Mn−N1A	176.07(14)
C8A−Mn−N1	176.07(14)	C8A−Mn−N1A	92.10(13)
C8−Mn−N2	95.72(14)	C8A−Mn−N2	95.72(14)
C8−Mn−C8A	90.0(2)		

Photochemical Experiments. The quantum yield (ϕ) values of CO release were determined by using a Newport Oriel Apex Illuminator (150 W xenon lamp) equipped with an Oriel 1/8 m Cornerstone monochromator. The source of visible light was an IL 410 illuminator (measured power of 146−150 mW) equipped with a high-energy light filter (350 nm cutoff). Standard ferrioxalate actinometry was used to determine the quantum yields at 358 nm (ϕ_{358}).[38] Solutions of **1**−**3** in MeCN were prepared under dim light conditions and placed in a 2 mm × 10 mm quartz cuvette, 2 cm from the light source. Solutions were prepared to ensure sufficient absorbance (>90%) at the irradiation wavelength, and changes in the electronic spectra in the 300−350 nm region (<10% photolysis) were used to determine the extent of CO release.

The rate of CO release was measured by recording electronic absorption spectra of **1**−**3** in MeCN (<2 mM, 1.4 mL) and monitoring the loss of absorbance of samples exposed to a broadband light source (IL 410 illuminator) at defined time intervals. The plots were fitted to the three-parameter exponential equation $A(t) = A_\infty + (A_o - A_\infty)\exp(-k_{CO}t)$, where A_o and A_∞ are the initial and final absorbance values, respectively. The apparent rate of CO loss (k_{CO}) was calculated from the ln(C) versus time (T) plot for each CORM.

Delivery of CO to Mouse Aorta: Preparation of the Tissue Rings. Male C57BLK6 mice (25−35 g) were stunned and killed by cervical dislocation. The thoracic aorta was carefully removed, cleaned of connective tissue, and cut into three to four ring segments approximately 4 mm in length. Aortic rings were mounted in 10 mL organ baths containing Krebs-bicarbonate buffer (143 mM Na^+, 5.9

dx.doi.org/10.1021/ic2021287 | Inorg. Chem. 2012, 51, 601−608

mM K^+, 2.5 mM Ca^{2+}, 1.2 mM Mg^{2+}, 128 mM Cl^-, 25 mM HCO_3^-, 1.2 mM HPO_4^{2-}, 1.2 mM SO_4^{2-}, and 11 mM D-glucose) maintained at 37 °C and gassed with a 95% O_2/5% CO_2 mixture. Tension was initially set at 0.3 g and reset at intervals following an equilibration period of 1 h, during which time fresh Krebs-bicarbonate buffer was replaced every 15−20 min. After equilibration, the rings were primed with KCl (48 mM), washed, and precontracted with phenylephrine (PE, 1 μM). Once this response had stabilized, acetylcholine (ACh, 1 μM) was added to the bath to assess the integrity of the endothelium. If the contractions to PE were not maintained or relaxations greater than 50% of the PE-induced tone to ACh were not observed, the tissues were discarded. Tissues were then washed for 30 min (by addition of fresh Krebs-bicarbonate buffer at 15 min intervals), after which time cumulative concentrations of PE (1 nM to 1 μM) were added to the organ bath. The tissues were then washed over 60 min to restore basal tone before contracting to approximately 80% of the maximal PE-induced response.

Once a stable response to PE was achieved, cumulative concentration−response curves to **1** and **2** (30 nM to 300 μM) were constructed under each of the following three conditions: (a) darkness (tissue baths wrapped in Al foil), (b) ambient light (tissue baths exposed to regular laboratory light), and (c) cold light (tissue baths illuminated by a cold white light source, fiber optic lamp, 150 W, 5 cm distance). To determine the role of soluble guanylate cyclase (sGC) in the vasorelaxant response to the CO donors, concentration−response curves to both **2** and **3** were constructed in tissues in the absence or presence of the sGC inhibitor ODQ (1*H*-[1,2,4]-oxadiazolo[4,3-*a*]quinoxalin-1-one, 5 μM).

RESULTS AND DISCUSSION

To incorporate photolability in designed CORMs for biological applications, we have utilized a series of tridentate polypyridine ligands with varying degrees of conjugation in this work. In previous syntheses of the structurally related photoactive manganese nitrosyls with polypyridine ligands, we discovered that incorporation of conjugated ring systems leads to a significant lowering of the energies of the "photoband" of the resulting NO complexes.[27a,28b] We tested this hypothesis in the design of our photoactive metal carbonyls. Our goal was to isolate photoCORMs that could deliver CO upon exposure to light of longer wavelengths (350−650 nm) that are not harmful to biological targets.

The carbonyl $[Mn(tpa)(CO)_3]ClO_4$ (**1**) was synthesized according to a published procedure[37] with the exception of using chloroform as a solvent in place of acetone under refluxing conditions. Reactions of the tripodal ligands *N*,*N*-bis(2-pyridylmethyl)amine (dpa) and (2-pyridylmethyl)(2-quinolylmethyl)amine (pqa) with either *fac*-$[Mn(CO)_3(MeCN)_3]ClO_4$ or $[Mn(CO)_5Br]$ as starting salts in THF afforded compounds **2** and **3**, respectively. All three carbonyls were isolated as yellow solids that are stable under aerobic conditions for an indefinite period of time when kept in the dark. They are soluble in aprotic polar solvents like MeCN and DMSO with limited solubility in $CHCl_3$. Such solutions are stable for several hours if kept in the dark.

The IR spectra of carbonyls **1**−**3** exhibit two strong bands in the carbonyl region (Figure 2), a pattern consistent with known Mn carbonyls bearing facially capping CO groups.[39−42] One sharp CO stretch (ν_{CO}) is observed at 2041 cm^{-1} in the case of **1** and at ∼2030 cm^{-1} for **2** and **3**. The second broad CO stretching frequency in the region of 1930−1950 cm^{-1} for **1** and **3** displays a minor splitting, suggesting a distinction between the two remaining CO ligands bound in the equatorial plane (vide infra). Peak splitting of a broad ν_{CO} stretch has been observed in some "piano-stool" carbonyls such as

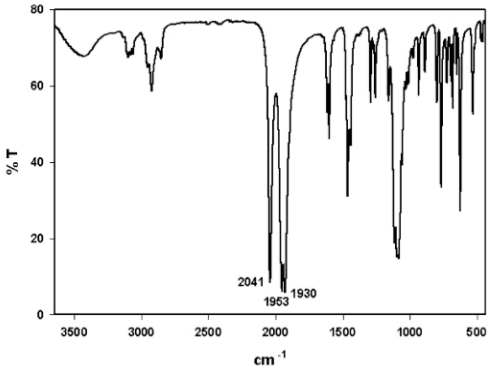

Figure 2. IR spectrum of $[Mn(tpa)(CO)_3]ClO_4$ (**1**) in a KBr disk.

$[(C_5H_5)Mn(CO)_3]$.[39] In the case of **2**, the higher symmetry of the cation is reflected in two sharp ν_{CO} bands at 2030 and 1930 cm^{-1} (no splitting in the ∼1930 cm^{-1} band). Carbonyls **1**−**3** are diamagnetic in the solid state and in solution as evidenced by clean ^1H NMR spectra in solvents like CD_3CN (Figure 5 and Figures S1 and S2 of the Supporting Information).

Structures of the Complexes. Although $[Mn(tpa)(CO)_3]ClO_4$ (**1**) was first synthesized by Edwards and coworkers,[37] its solid state structure has not been determined by crystallography. The structure of the cation of **1** is shown in Figure 3, and selected metric parameters are listed in Table 2.

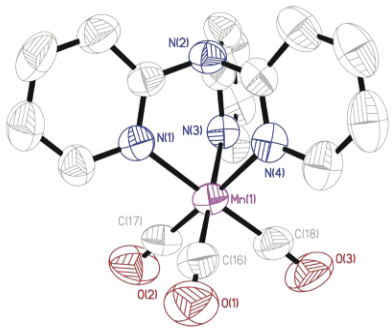

Figure 3. Thermal ellipsoid (50% probability level) plot of $[Mn(tpa)(CO)_3]^+$ (cation of **1**) with select atom labeling. H atoms have been omitted for the sake of clarity.

The octahedral geometry of the complex consists of a facially capping tpa ligand and three CO ligands opposite to each of the pyridine rings, resulting in an approximate C_{3v} symmetry. Two of the CO ligands are in an equatorial plane opposite two pyridine moieties, while the remaining CO is positioned axially. Bond distances of the coordinated ligand, Mn−N(py), range from 2.058 to 2.065 Å. On the other hand, the Mn−C(O) bond lengths are more uniform. Two Mn−C(O) bonds with lengths of 1.806 and 1.809 Å are noted, while the remaining Mn−C(O) bond is slightly longer (1.813 Å). The symmetry and Mn−C(O) bond distances observed in **1** are consistent

dx.doi.org/10.1021/ic2021287 | *Inorg. Chem.* 2012, 51, 601−608

with other complexes such as $[(C_5H_5)Mn(CO)_3]$[43] and $[Mn(bmip)(CO)_3]$ [bmip = 3,3-bis(1-methylimidazol-2-yl)-propionic acid].[44]

The structure of $[Mn(dpa)(CO)_3]^+$ (cation of **2**) is shown in Figure 4. Much like **1**, carbonyl **2** possesses an octahedral

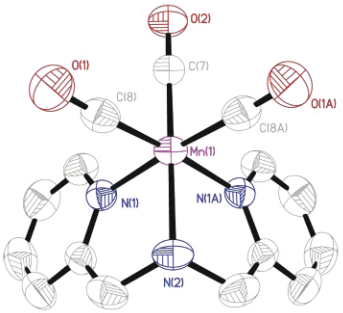

Figure 4. Thermal ellipsoid (50% probability level) plot of $[Mn(dpa)(CO)_3]^+$ (cation of **2**) with select atom labeling. H atoms have been omitted for the sake of clarity.

geometry featuring the tripodal dpa ligand and three CO groups opposite each of the N donors. The symmetric nature of the free dpa ligand generates a mirror plane passing through the C7−Mn1−N2 axis in the resulting complex **2**. The Mn−N(py) and Mn−N(amine) distances are almost identical (2.05 and 2.06 Å, respectively). Much like **1**, the Mn−C(O) bond lengths for **2** are in the same range as that seen in other Mn(I) tricarbonyl complexes. The symmetry of the structure is reflected in the recorded IR spectrum in which only two CO stretching frequencies are observed: one ν_{CO} corresponds to the CO trans to the N(amine) moiety, and the other ν_{CO} is due to the CO groups opposite the pyridine moieties of the dpa ligand.

The poor diffraction pattern of the crystals of $[Mn(pqa)(CO)_3](ClO_4)$ (**3**) has so far hindered the determination of its crystal structure. However, the spectral properties of this carbonyl clearly establish the similarities of its structure with those of **1** and **2**. For example, **3** exhibits three ν_{CO} frequencies of 2034, 1942, and 1919 cm^{-1} in a KBr matrix, supporting the facial coordination of the ligand frame. In addition, the clean ^1H NMR spectrum confirms its integrity in solution. As shown in Figure 5, the NH proton shifts from 2.5 to 6.1 ppm upon ligation to the Mn(I) center and the pyridine/quinoline protons spread over the range of 7.3−9.2 ppm. In addition, facial coordination of the ligand to the Mn(I) center leads to diastereomeric methylene protons that appear as four distinct signals in the range of 4.1−5.1 ppm (in free ligand, these give rise to two singlets at 3.95 and 4.05 ppm).

Electronic Absorption Spectra and CO Release in Solution. In MeCN, **1** exhibits a broad absorption band centered at ∼330 nm with higher-energy bands at 260 and 240 nm. Compounds **2** and **3** display similar profiles, with broad shoulders at 350 and 360 nm, respectively (Figure 6).

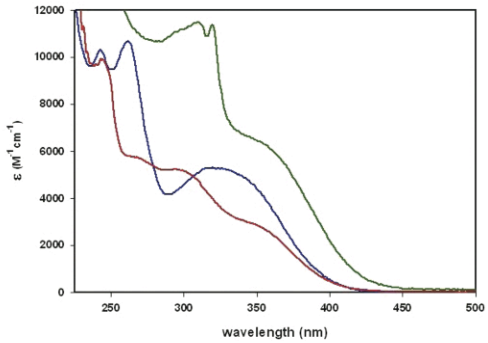

Figure 6. Electronic absorption spectra of $[Mn(tpa)(CO)_3]ClO_4$ (**1**, blue trace), $[Mn(dpa)(CO)_3]Br$ (**2**, red trace), and $[Mn(tpa)(CO)_3]ClO_4$ (**3**, green trace) in MeCN.

Comparison of the λ_{max} values of **2** and **3** reveals an incremental shift of the absorption band toward lower energies upon replacement of one of the pyridine rings in **2** with a quinoline moiety in **3**. However, the extinction coefficients of the two bands at 300 and 360 nm increase considerably in the case of **3** with additional conjugation (pyridine vs quinoline) in the ligand frame (Figure 6). This result clearly demonstrates that the strategy of adding extended conjugation in the ligand framework does increase the amount of light absorbed by the designed carbonyl in the low-energy range. Solutions of **1**−**3** in MeCN are stable for up to 6 h if kept in the dark. However,

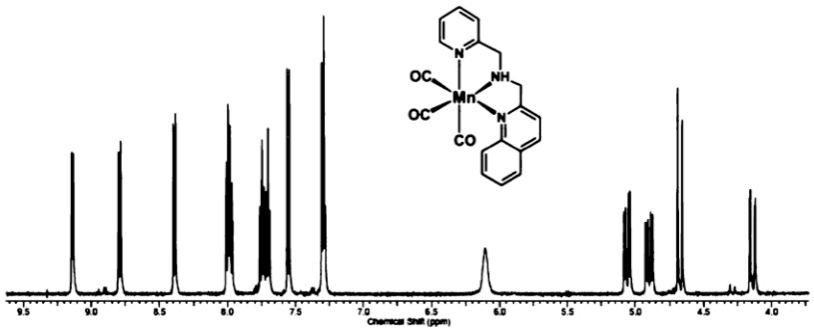

Figure 5. ^1H NMR (500 MHz) spectrum of $[Mn(pqa)(CO)_3](ClO_4)$ (**3**) in CD_3CN (3.5−9.5 ppm range).

dx.doi.org/10.1021/ic2021287 | Inorg. Chem. 2012, 51, 601−608

immediately upon dissolution, an excess (7−8 fold based on the amount of Mb) of each compound in PBS (pH 7.4) was required to completely convert reduced Mb to carbonyl myoglobin (Mb-CO) with solutions of the CORMs in such reactions. The rapid formation of Mb-CO was apparent within 1 min of addition as evidenced by the shift of the Soret band from 435 to 424 nm (Figure 6). Mb-CO production levels off after 20 min in the case of **2** and 24 min for **3**, with the final absorbance readings taken at 30 min. While kinetic measurements predict a slower rate of CO release for **2** compared to **3**, the Mb-based CO release test shows that both carbonyls generate CO at a similar rate over the same period of time. These resulting half-lives, defined as the time during which Mb-CO formation is 50% complete (∼ 8 min for both species), are comparable to known CORMs that release CO when dissolved. For instance, CORM-3 was reported to have a half-life of 4−18 min,[20] while some Cr-based CORMs employing amino acids and amino ester ligands have half-lives of 7−9 min.[24]

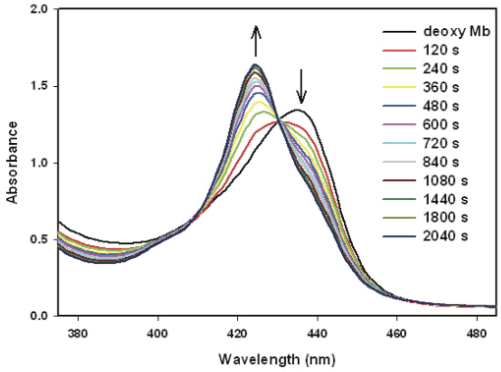

Figure 6. Delivery of CO from **3** to reduced Mb (λ_{max} = 435 nm), resulting in Mb-CO adduct (λ_{max} = 424 nm) in PBS pH 7.4.

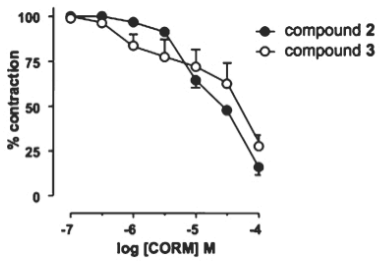

Figure 7. Vasorelaxation of mouse aorta muscle ring using **2** and **3** as a function of concentration.

Vasorelaxation of Mouse Aorta. The vasorelaxation property of CO has been a subject of debate in relation to its binding and activating to sGC and the concomitant cGMP pathway. Despite low affinity of CO to sGC,[12] relaxation of smooth muscle by CO via cGMP pathway has been proposed.[18,21] In the present study, we have examined the effect(s) of CO release from the present carbonyls on mouse aorta muscle rings in tissue bath experiments. Both **2** (30 nM−100 μM) and **3** (30 nM−300 μM) produced concentration-dependent relaxations with EC_{50} values of 3.4 ± 0.2 μM and 26.2 ± 0.2 μM, respectively (Figure 7). These values are superior to values obtained with CORM-3 reported by Motterlini and co-workers.[21] Interestingly, we did not observe much inhibitory effect by ODQ, a common sGC inhibitor (Figure 8). In previous work, Motterlini and co-workers have reported initial inhibition by ODQ which was eventually lost after repeated addition of CORM-3.[21]

It has been postulated that smooth muscle relaxation by CO could arise from its binding to the channel-bound heme of the large-conductance Ca^{2+}-activated K-channel (BK_{Ca}).[14b,43,44] To test this hypothesis, we studied the effect of the BK_{Ca} channel blocker iberiotoxin on the inhibition of vasorelaxation by **3**. Significant inhibition was indeed observed with this BK_{Ca} channel blocker while no effect was noted with the K_{ATP} channel blocker glibenclamide or the nonselective K^+-channel blocker TEA (data not shown). Clearly, more studies are required to determine the origin of vasorelaxation of smooth muscle by these CORMs. Nevertheless, the excellent vasorelaxation effects of **2** and **3** merit attention as new CORMs that could be used to deliver CO under physiological conditions. Further studies on the mechanism of vasorelaxation by these CORMs are in progress in this laboratory.

SUMMARY AND CONCLUSIONS

The following are the summary and conclusions of this work.

(a) Three structurally related Fe(II) carbonyls **1**−**3** have been synthesized from designed polypyridine ligands and characterized by spectroscopy and X-ray crystallography. The structure of **1** has been reported by us in a previous account.[36]

(b) In aqueous and nonaqueous solutions, these carbonyls rapidly release CO and hence can act as potential CORMs.

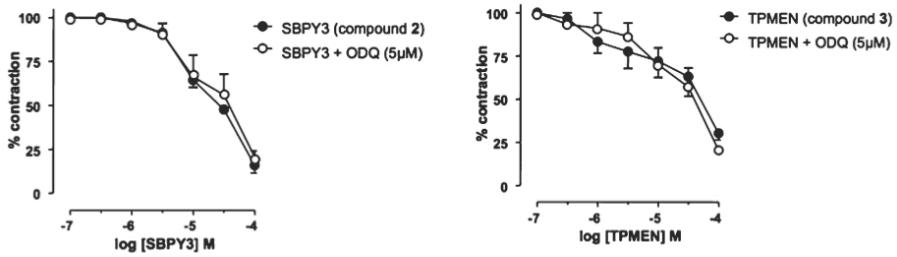

Figure 8. Vasorelaxation of mouse aorta muscle rings by **2** and **3** in the absence and presence of ODQ (5 μM).

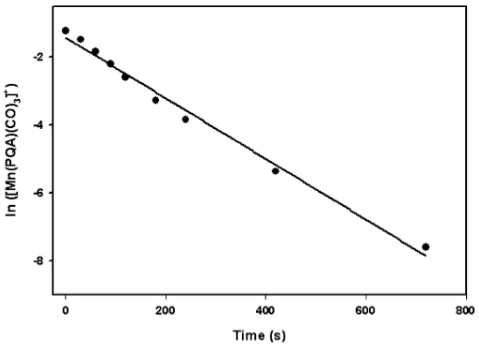

Figure 9. Plot of changes in ln[**3**] vs time in MeCN upon exposure to visible (λ > 350 nm, 120 mW) light (0.13 mM **3**).

Figures S5 and S6, respectively, of the Supporting Information). As expected, **3** exhibits the highest rate of CO release under visible light because of the strong absorption of light in the 350−360 nm region (Figure 5). The photoproducts appear to be stable in solution, as evidenced by the final electronic absorption spectra of **1**−**3**. Taken together, these results confirm that these photoCORMs are effective CO donors ($t_{1/2}$ in the range of 1.4−2.2 min) under a wide range of light, although the k_{CO} values for all three carboyls are uniformly higher in the UV region.

The quantum yield (ϕ_{358}) values of **1**−**3** in MeCN (0.07 ± 0.01, 0.09 ± 0.01, and 0.06 ± 0.01, respectively) are lower than those of typical metal carbonyls such as $[W(CO)_6]$[46] or $Na_3[W(CO)_5(TPPTS)]$.[20] Nevertheless, these photoCORMs release CO at a slow yet steady pace for extended periods of time under low-power (milliwatt) UV and visible light sources.

Vasorelaxation of Mouse Aorta. Activation of sGC upon binding of CO to the active site heme and concomitant relaxation of smooth muscle via the cyclic GMP pathway[22] has been utilized for the assessment of various CO donors such as CORM-3.[47] In this study, we have examined such relaxation of aortic muscle rings in the presence of **1**−**3** under light and dark conditions. Small loss of CO (over h) from both **1** and **2** in tissue bath media has added complications to such measurements. However, **3** is very stable in aqueous buffers and shows no loss of CO in the dark. The latter fact is confirmed by the fact that when a mixture of **3** and reduced Mb in PBS is kept in the dark for 4 h, no formation of Mb-CO is observed. However, **3** releases CO in the presence of light with an apparent CO release rate k_{CO} value of 5.6×10^{-3} s^{-1} in PBS ($t_{1/2}$ = 2 min). Although this rate is lower than that observed in MeCN, **3** retains an excellent capacity of CO delivery under illumination in PBS. We have therefore examined the effect of **3** on mouse aorta rings in tissue bath experiments. As shown in Figure 10, **3** produced a concentration-dependent relaxation (in the 10^{-7} to 10^{-4} M range) under direct light exposure (indicated as cold light). When the tissue bath experiment was performed in a lighted room (no direct light exposure), a similar albeit weak response to light was observed (indicated as ambient light). The relaxations were inhibited by the sGC inhibitor ODQ. No relaxation was observed in the dark for concentrations of $<10^{-5}$ M. Collectively, these findings confirm that **3** is an effective photoCORM that could find use in biological applications. The

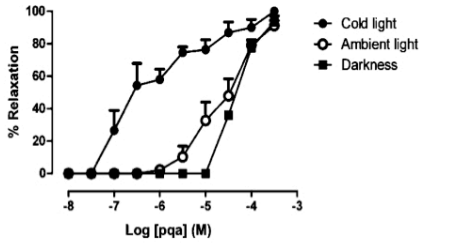

Figure 10. Vasorelaxation of mouse aorta muscle rings by $[Mn(pqa)(CO)_3]ClO_4$ (**3**) upon exposure to visible (cold) light and ambient room light (see the text for details).

integrity of the tissues in the presence of the photoCORM when kept in the dark also attests to the fact that in the concentration range of 10^{-7} to 10^{-4} M, the compound exhibits minimal toxic effect(s).

SUMMARY AND CONCLUSIONS

Research to date has indicated that metal carbonyls could act as exogenous CO donors that can elicit a typical physiological response as with endogenously produced CO. However, controlled delivery of CO at biological targets demands isolation and/or identification of new metal carbonyls that could be triggered to deliver CO when needed. The results of this work demonstrate that it is possible to synthesize metal carbonyls derived from designed ligands (such as pqa) that could be triggered by light to release CO. Carbonyls **1**−**3** add to the small list of photoCORMs reported so far.[19−21,48,49] Studies of the stability and reliability of these photoCORMs in various cytoprotective assays are in progress at this time, and results will be repoted in due time.

ASSOCIATED CONTENT

Supporting Information

X-ray crystallographic data (in CIF format) for $[Mn(tpa)(CO)_3]ClO_4 \cdot CH_2Cl_2$ (**1**·CH_2Cl_2) and $[Mn(dpa)(CO)_3]Br$ (**2**), ^1H NMR spectra (500 MHz) of **1** and **2** in CD_3CN (Figures S1 and S2, respectively), X-band EPR spectrum of the photolyzed solution of **3** at 100 K (Figure S3), changes in the electronic absorption spectrum of **2** in MeCN under aerobic conditions {and the spectrum of $[Mn(dpa)_2]^{2+}$ as an inset} (Figure S4), and kinetic plots of release of CO from **1** and **2** (Figures S5 and S6, respectively). This material is available free of charge via the Internet at http://pubs.acs.org.

AUTHOR INFORMATION

Corresponding Author

*E-mail: pradip@ucsc.edu.

ACKNOWLEDGMENTS

Financial support from National Science Foundation Grant CHE-0957251 is gratefully acknowledged. M.A.G. received support from the Initiative for Maximizing Student Development Grant GM-58903.

REFERENCES

(1) Wang, R., Ed. *Signal Transduction and the Gasotransmitters: NO, CO and H_2S in Biology and Medicine*; Humana Press: Totowa, NJ, 2004.

(2) (a) Hartsfield, C. L. *Antioxid. Redox Signaling* **2002**, *4*, 301−307. (b) Ryter, S.; Alam, J.; Choi, A. *Physiol. Rev.* **2006**, *86*, 583−650.
(3) Kikuchi, G.; Yoshida, T.; Noguchi, M. *Biochem. Biophys. Res. Commun.* **2005**, *338*, 558−567.
(4) Nakao, A.; Choi, A. M. K.; Murase, N. *J. Cell. Mol. Med.* **2006**, *10*, 650−671.
(5) Morse, D.; Pischke, S. E.; Zhou, Z.; Davis, R. J.; Flavell, R. A.; Loop, T.; Otterbein, S. L.; Otterbein, L. E.; Choi, A. M. K. *J. Biol. Chem.* **2003**, *278*, 36993−36998.
(6) Brouard, S.; Otterbein, L. E.; Anrather, J.; Tobiasch, E.; Bach, F. H.; Choi, A. M.; Soares, M. P. *J. Exp. Med.* **2000**, *192*, 1015−1026.
(7) Otterbein, L. E.; Mantell, L. L.; Choi, A. M. K. *Am. J. Physiol.* **1999**, *276*, 688−694.
(8) Kobayashi, A.; Ishikawa, K.; Matsumoto, H.; Kimura, S.; Kamiyama, Y.; Maruyama, Y. *Hypertension* **2007**, *50*, 1040−1048.
(9) Zuckerbraun, B. S.; Chin, B. Y.; Wegiel, B.; Billiar, T. R.; Czsimadia, E.; Rao, J.; Shimoda, L.; Ifedigbo, E.; Kanno, S.; Otterbein, L. E. *J. Exp. Med.* **2006**, *203*, 2109−2119.
(10) Clark, J. E.; Naughton, P.; Shurey, S.; Green, C. J.; Johnson, T. R.; Mann, B. E.; Foresti, R.; Motterlini, R. *Circ. Res.* **2003**, *93*, e2−e8.
(11) Zhang, W. Q.; Whitwood, A. C.; Fairlamb, I. J. S.; Lynam, J. M. *Inorg. Chem.* **2010**, *49*, 8941−8952.
(12) (a) Fairlamb, I. J. S.; Lynam, J. M.; Moulton, B. E.; Taylor, I. E.; Duhme-Klair, A. K.; Sawle, P. S.; Motterlini, R. *Dalton Trans.* **2007**, 3603−3605. (b) Fairlamb, I. J. S.; Duhme-Klair, A. K.; Lynam, J. M.; Moulton, B. E.; O'Brien, C. T.; Sawle, P.; Hammad, J.; Motterlini, R. *Bioorg. Med. Chem. Lett.* **2006**, *16*, 995−998.
(13) Bikiel, D. E.; González Solveyra, E.; Di Salvo, F.; Milagre, H. M. S.; Eberlin, M. N.; Corrêa, R. S.; Ellena, J.; Estrin, D. A.; Doctorovich, F. *Inorg. Chem.* **2011**, *50*, 2334−2345.
(14) Zobi, F.; Degonda, A.; Schaub, M. C.; Bogdanova, A. Y. *Inorg. Chem.* **2010**, *49*, 7313−7322.
(15) Atkin, A. J.; Williams, S.; Sawle, P.; Motterlini, R.; Lynam, J. M.; Fairlamb, I. J. S. *Dalton Trans.* **2009**, 3653−3656.
(16) Herrick, R. S.; Brown, T. L. *Inorg. Chem.* **1984**, *23*, 4550−4553.
(17) Engelking, P. C.; Lineberger, W. C. *J. Am. Chem. Soc.* **1979**, *101*, 5569−5573.
(18) Motterlini, R.; Clark, J. E.; Foresti, R.; Sarathchandra, P.; Mann, B. E.; Green, C. J. *Circ. Res.* **2002**, *90*, e17−e24.
(19) (a) Schatzschneider, U. *Inorg. Chim. Acta* **2011**, *374*, 19−23. (b) Niesel, J.; Pinto, A.; N'Dongo, H. W. P.; Merz, K.; Ott, I.; Gust, R.; Schatzschneider, U. *Chem. Commun.* **2008**, 1798.
(20) Rimmer, R. D.; Richter, H.; Ford, P. C. *Inorg. Chem.* **2010**, *49*, 1180−1185.
(21) Kretschmer, R.; Gessner, G.; Görls, H.; Heinemann, S. H.; Westerhausen, M. *J. Inorg. Biochem.* **2011**, *105*, 6−9.
(22) Ignarro, L. J. *Nitric Oxide: Biology and Pathology*; Academic Press: San Diego, 2000.
(23) Kalsner, S., Ed. *Nitric Oxide Free Radicals in Peripheral Neurotransmission*; Birkhauser: Boston, 2000.
(24) Fang, F. C., Ed. *Nitric Oxide and Infection*; Kluwer Academic/Plenum Publishers: New York, 1999.
(25) Moncada, S., Higgs, E. A., Bagetta, G., Eds. *Nitric Oxide & the Cell: Proliferation, Differentiation and Death*; Portland Press: London, 1998.
(26) (a) Eroy-Reveles, A. A.; Hoffman-Luca, C. G.; Mascharak, P. K. *Dalton Trans.* **2007**, 5268−5274. (b) Patra, A. K.; Rowland, J. M.; Marlin, D. S.; Bill, E.; Olmstead, M. M.; Mascharak, P. K. *Inorg. Chem.* **2003**, *42*, 6812−6823. (c) Patra, A. K.; Afshar, R.; Olmstead, M. M.; Mascharak, P. K. *Angew. Chem., Int. Ed.* **2002**, *41*, 2512−2515.
(27) (a) Hoffman-Luca, C. G.; Eroy-Reveles, A. A.; Alvarenga, J.; Mascharak, P. K. *Inorg. Chem.* **2009**, *48*, 9104−9111. (b) Ghosh, K.; Eroy-Reveles, A. A.; Holman, T. R.; Olmstead, M. M.; Mascharak, P. K. *Inorg. Chem.* **2004**, *43*, 2988−2997.
(28) (a) Eroy-Reveles, A. A.; Mascharak, P. K. *Future Med. Chem.* **2009**, *1* (8), 1497−1507. (b) Eroy-Reveles, A. A.; Leung, Y.; Beavers, C. M.; Olmstead, M. M.; Mascharak, P. K. *J. Am. Chem. Soc.* **2008**, *130*, 4447−4458.
(29) (a) Rose, M. J.; Mascharak, P. K. *Coord. Chem. Rev.* **2008**, *252*, 2093−2114. (b) Rose, M. J.; Mascharak, P. K. *Curr. Opin. Chem. Biol.* **2008**, *12*, 238−244.
(30) (a) Rose, M. J.; Patra, A. K.; Olmstead, M. M.; Mascharak, P. K. *Inorg. Chem.* **2007**, *46*, 2328−2338. (b) Patra, A. K.; Rose, M. J.; Murphy, K. A.; Olmstead, M. M.; Mascharak, P. K. *Inorg. Chem.* **2004**, *43*, 4487−4495. (c) Patra, A. K.; Mascharak, P. K. *Inorg. Chem.* **2003**, *42*, 7363−7365.
(31) (a) Rose, M. J.; Mascharak, P. K. *Inorg. Chem.* **2009**, *48*, 6904−6917. (b) Rose, M. J.; Olmstead, M. M.; Mascharak, P. K. *J. Am. Chem. Soc.* **2007**, *129*, 5342−5343.
(32) (a) Halpenny, G. M.; Mascharak, P. K. *Anti-Infect. Agents Med. Chem.* **2010**, *9*, 187−197. (b) Rose, M. J.; Fry, N. L.; Marlow, R.; Hinck, L.; Mascharak, P. K. *J. Am. Chem. Soc.* **2008**, *130*, 8834−8846. (c) Madhani, M.; Patra, A. K.; Miller, T. W.; Eroy-Reveles, A. A.; Hobbs, A.; Fukuto, J. M.; Mascharak, P. K. *J. Med. Chem.* **2006**, *49*, 7325−7330. (d) Szundi, I.; Rose, M. J.; Sen, I.; Eroy-Reveles, A. A.; Mascharak, P. K.; Einarsdottir, O. *Photochem. Photobiol.* **2006**, *82*, 1377−1384. (e) Afshar, R. K.; Patra, A. K.; Mascharak, P. K. *J. Inorg. Biochem* **2005**, *99*, 1458−1464.
(33) Gonzalez, M. A.; Fry, N. L.; Burt, R.; Davda, R.; Hobbs, A. J.; Mascharak, P. K. *Inorg. Chem.* **2011**, *50*, 3127−3134.
(34) Nagao, N.; Egashira, K.; Mogi, D. *Bull. Chem. Soc. Jpn.* **2004**, *77*, 1171−1172.
(35) Wong, Y.; Mak, C.; Kwan, H. S.; Lee, H. K. *Inorg. Chim. Acta* **2010**, *363*, 1246−1253.
(36) Baldeau, S. M.; Slinn, C. H.; Krebs, B.; Rompel, A. *Inorg. Chim. Acta* **2004**, *357*, 3295−3303.
(37) Edwards, D. A.; Marshalsea, J. *J. Organomet. Chem.* **1977**, *131*, 73−91.
(38) Montalti, M.; Credi, A.; Prodi, L.; Gandolfi, M. T. *Handbook of Photochemistry*, 3rd ed.; CRC Press: Boca Raton, FL, 2006.
(39) Kunz, P. C.; Huber, W.; Rojas, A.; Schatzschneider, U.; Spingler, B. *Eur. J. Inorg. Chem.* **2009**, 5358−5366.
(40) Reger, D. L.; Grattan, T. C.; Brown, K. J.; Little, C. A.; Lamba, J. J. S.; Rheingold, A. L.; Sommer, R. D. *J. Organomet. Chem.* **2000**, *607*, 120−128.
(41) Carlos, R. M.; Carlos, I. A.; Lima Neto, B. S.; Neumann, M. G. *Inorg. Chim. Acta* **2000**, *299*, 231−237.
(42) Hyams, I. J.; Bailey, R. T.; Lippincott, E. R. *Spectrochim. Acta* **1967**, *23A*, 273−284.
(43) Berndt, A. F.; Marsh, R. E. *Acta Crystallogr.* **1963**, *16*, 118−123.
(44) Peters, L.; Hübner, E.; Burzlaff, N. *J. Organomet. Chem.* **2005**, *690*, 2009−2016.
(45) Romberg, R. W.; Kassner, R. J. *Biochemistry* **1979**, *18*, 5387−5392.
(46) Wieland, S.; van Eldik, R. *J. Phys. Chem.* **1990**, *94*, 5865−5870.
(47) Foresti, R.; Hammad, J.; Clark, J. E.; Johnson, T. R.; Mann, B. E.; Friebe, A.; Green, C. J.; Motterlini, R. *Br. J. Pharmacol.* **2004**, *142*, 453−460.
(48) Jackson, C. S.; Schmitt, S.; Dou, Q. P.; Kodanko, J. J. *Inorg. Chem.* **2011**, *50*, 5336−5338.
(49) Zhang, W.-Q.; Atkin, A. J.; Fairlamb, I. J. S.; Whitwood, A. C.; Lynam, J. M. *Organometallics* **2011**, *30*, 4643−4654.

Chapter 3. Photoactive d^6 Metal Carbonyl Complexes Bearing Designed Tridentate Ligand Frames

Part II: Ruthenium Carbonyls of the Tridentate NNS ligand qmtpm: Investigation of Auxiliary Ligand Effects on CO Photorelease

3.II.1. Background

The photophysical and photochemical properties of ruthenium(II)-polypyridine complexes are largely attributed to electronic transitions originating from metal to ligand charge transfer (MLCT) excited states. Such Ru(II) compounds typically feature an intense absorption band in the visible region owing to transitions originating from a metal centered Ru^{II} (d_π) orbital into the lowest π^* orbitals of the polypyridine ligand(s). As evident in the case of $[Ru(bpy)_3]^{2+}$ (where bpy = bipyridine), the initial singlet MLCT excited state obtained with visible light absorption undergoes rapid intersystem crossing to generate a long-lived triplet MLCT state. With extended lifetimes on the order of microseconds, this triplet MLCT excited state facilitates a wide range of energy and electron transfer processes.[1] Indeed Ru(II) polypyridine complexes have been extensively investigated for their potential use as chromophores for light harvesting reactions, artificial photosynthesis, and as active components in dye-sensitized solar cells.[2-4]

When carbon monoxide (CO) ligands are incorporated in these Ru(II) polypyridine complexes, photosubstitution reactions can occur which result in the breaking of metal-CO bonds. In the case of *trans(Cl,Cl)*-$[Ru(Cl)_2(CO)_2(bpy)]$ in coordinating solvents like CH_3CN or CH_3OH that irradiation into the lowest

absorption band leads to CO photodissociation.[5] Decarbonylation occurs in a stepwise process that begins with loss of a CO group followed by a shift of the halide ligand from an axial to the equatorial position, generating the *cis(Cl,Cl)*-$[Ru(Cl)_2(CO)(solv)(bpy)]$ adduct. With prolonged irradiation, further CO loss is observed, as is noted in the near-unity quantum yield values.[5,6] This established photosensitivity of Ru(II) polypyridine carbonyl complexes and the decarbonylation processes associated with MLCT excited states make this class of compounds a viable platform in the development of Ru-based photoactive carbon monoxide releasing molecules (photoCORMs).

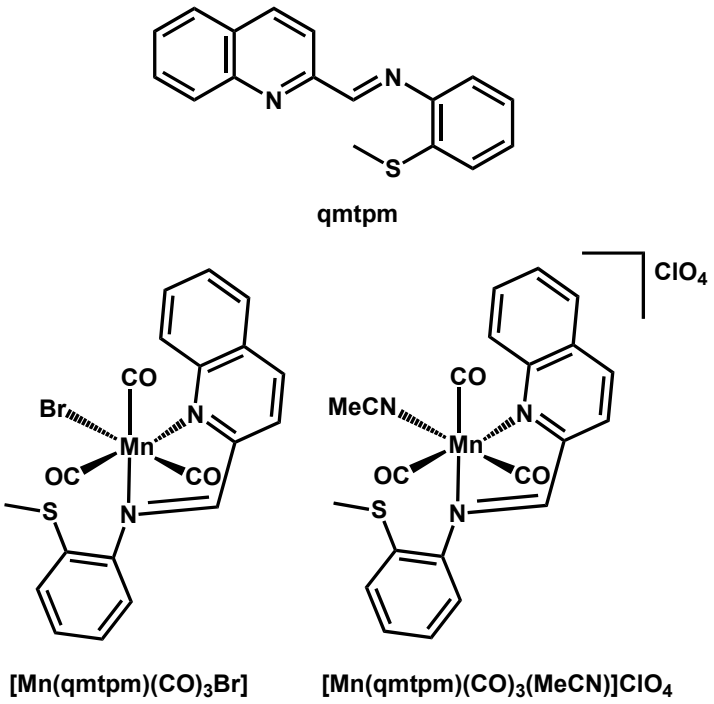

Figure 3.II.1. Structures of the qmtpm ligand and the corresponding *fac*-Mn(I) tricarbonyl complexes, $[Mn(qmtpm)(CO)_3Br]$ and $[Mn(qmtpm)(CO)_3(MeCN)]ClO_4$.

Using the principles of photoreactivity of polypyridine metal carbonyl complexes as the basis in our design of photoCORMs, we have synthesized a series of Ru(II) carbonyl complexes bearing the asymmetric ligand frame [2-quinoline-*N*-(2'-methylthiophenyl) methyleneimine] (qmtpm). This tridentate ligand is comprised of a quinoline, an imine and a thioether moiety (Figure 3.II.1) and is expected to stabilize metal centers in both high and low oxidation states. Inclusion of a quinoline group increases conjugation in the chromophore, thereby facilitating electron delocalization necessary in MLCT processes. While both imine and thioether groups are classified as π-acceptors, the thioether unit is unique in that it is also capable of both π and σ-donation.[7]

We previously employed the qmtpm ligand in the preparation of a series of manganese carbonyl complexes. Although potentially tridentate, reaction of qmtpm with Mn(I) starting salts namely $Mn(CO)_5Br$ and $[Mn(CO)_3(MeCN)_3]ClO_4$, yielded the corresponding *fac*-Mn(I) tricarbonyl complexes $[Mn(qmtpm)(CO)_3Br]$ and $[Mn(qmtpm)(CO)_3(MeCN)]ClO_4$ (Figure 3.II.1), in which only the N-donors are bound to the metal center.[8] The failure of the $–SCH_3$ end of the qmtpm ligand to bind presumably arises from its weak affinity for Mn(I) centers.

In an effort to make qmtpm bind as a tridentate ligand, we turned our attention to a different metal center, Ru(II), whose d^6 configuration makes it isoelectronic with both Mn(I) yet with a higher charge. This chapter discusses the syntheses, structures and photochemical properties of the two stable Ru(II) carbonyl complexes derived from qmtpm in which qmtpm serves as a tridentate ligand. In all of the compounds

isolated, qmtpm binds in a meridional fashion. In addition, we have investigated the effects of increasing CO groups on the photosensitivity of such ruthenium carbonyl complexes bearing the qmtpm ligand frame.

3.II.2. Syntheses of the Metal Complexes

3.II.2.1 Characterization of [Ru(Cl)$_2$(qmtpm)(PPh$_3$)]

Reaction of [Ru(PPh$_3$)$_3$(Cl)$_2$][9] with 2-quinoline-*N*-(2'-methylthiophenyl) methyleneimine (qmtpm)[10] in refluxing toluene afforded [Ru(Cl)$_2$(qmtpm)(PPh$_3$)] as a deep blue solid. The composition of this complex was established with the aid of microanalytical data and its ^{1}H NMR spectrum in $CDCl_3$. The singlet observed at 3.11 ppm confirms S-ligation of qmtpm to the Ru(II) center in [Ru(Cl)$_2$(qmtpm)(PPh$_3$)] (Figure 3.II.13). In free qmtpm, the −SMe signal is noted at 2.52 ppm in CD_3CN (Figure 3.II.11). Integration of the proton resonances indicates the presence of one PPh_3 ligand while the remaining two coordination positions are occupied by the two Cl^- ligands. We have tentatively assigned a *cis* disposition of the two Cl^- ligands in [Ru(Cl)$_2$(qmtpm)(PPh$_3$)] on the basis of the crystal structure of the related complex [Ru(pmtpm)(PPh$_3$)(Cl)$_2$] (where pmtpm = 2-pyridyl-*N*-(2'-methylthiophenyl)methyleneimine).[11]

In the present work, complex [Ru(Cl)$_2$(qmtpm)(PPh$_3$)] was synthesized for its potential use as the starting material for mono- and bis-carbonyl species. However, attempts to replace the Cl^- ligands of [Ru(Cl)$_2$(qmtpm)(PPh$_3$)] with CO leads to very different results depending on the solvent. For example in acetonitrile, addition of one equiv of $AgBF_4$ to [Ru(Cl)$_2$(qmtpm)(PPh$_3$)] generates the magenta complex

$[Ru(Cl)(MeCN)(qmtpm)(PPh_3)]BF_4$ (Scheme 3.II.1). Further addition of one equiv of $AgBF_4$ affords the red complex $[Ru(MeCN)_2(qmtpm)(PPh_3)]^{2+}$ (Scheme 3.II.1) which has been structurally characterized as the perchlorate salt. Bubbling of CO gas to such solutions does *not* yield either the monocarbonyl complex $[Ru(Cl)(CO)(qmtpm)(PPh_3)]BF_4$ or $[Ru(CO)_2(qmtpm)(PPh_3)]^{2+}$, the expected dicarbonyl species. It appears that the affinity of MeCN groups to Ru(II) centers hinders CO ligation.

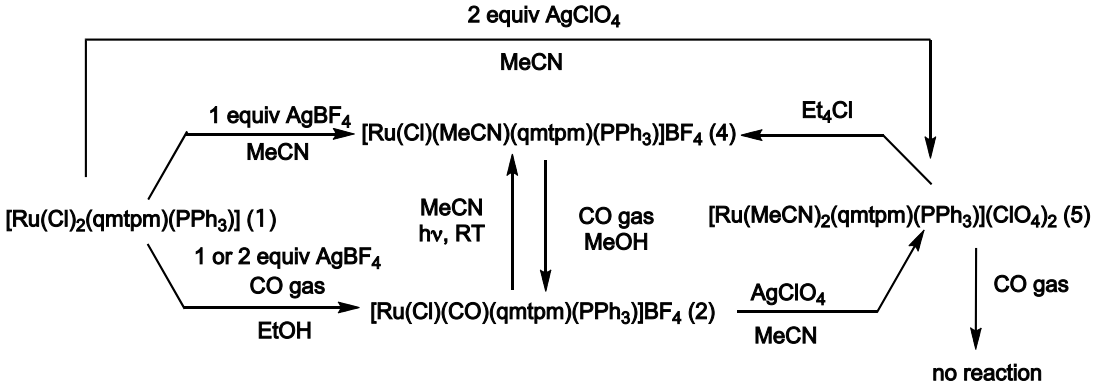

Scheme 3.II.1. Syntheses and Interconversions of Ru(II) qmtpm complexes.

3.II.2.2 Characterization and X-ray Structure of $[Ru(Cl)(CO)(qmtpm)(PPh_3)]BF_4$

Treatment of $[Ru(Cl)_2(qmtpm)(PPh_3)]$ with one equivalent of Ag^+ salt in ethanol followed by passage of a steady stream of CO gas at room temperature, leads to replacement of one Cl^- as evidenced by the formation of the orange-yellow monocarbonyl complex $[Ru(Cl)(CO)(qmtpm)(PPh_3)]BF_4$ (Scheme 3.II.1). It is important to note that even when two equivalents of Ag^+ salt in ethanol are added, only one Cl^- can be exchanged with CO. As will be noted in the crystal structure of $[Ru(Cl)(CO)(qmtpm)(PPh_3)]BF_4$ (vide infra), only the Cl^- ligand trans to PPh_3 is

abstracted by Ag^+ and subsequently replaced by CO, indicating the influence of both the ligand frame and ancillary ligands on these substitution reactions. Collectively, these reactions indicate that acetonitrile is a better donor for the Ru(II) center and any replacement of the Cl^- ligand of $[Ru(Cl)_2(qmtpm)(PPh_3)]$ with CO is possible only in ethanol. The affinity of the Ru(II) center toward acetonitrile is further indicated by the quantitative formation of $[Ru(MeCN)_2(qmtpm)(PPh_3)]ClO_4$ upon reaction of $[Ru(Cl)(CO)(qmtpm)(PPh_3)]BF_4$ with one equiv of Ag^+ salt ($AgClO_4$ or $AgBF_4$) in acetonitrile (Scheme 3.II.1).

The carbonyl complex $[Ru(Cl)(CO)(qmtpm)(PPh_3)]BF_4$ features a sharp ν_{CO} band at 2028 cm^{-1} (Figure 3.II.15) similar to that in $[Ru(Cl)(CO)(terpy)(PPh_3)]PF_6$ (2008 cm^{-1}).[12] $[Ru(Cl)(CO)(qmtpm)(PPh_3)]BF_4$ is indefinitely stable in chlorinated solvents, which allowed for the isolation of x-ray quality crystals of this compound via vapor diffusion of pentane into a dichloromethane solution of $[Ru(Cl)(CO)(qmtpm)(PPh_3)]BF_4$.

The structure of the cation of $[Ru(Cl)(CO)(qmtpm)(PPh_3)]BF_4$ is shown in Figure 3.II.2. The ruthenium center in this complex resides in an octahedral environment with the qmtpm ligand coordinated in a meridional fashion. The bulky π-accepting triphenylphosphine group is axially positioned trans to the CO ligand, while Cl^- occupies the remaining site, in the same plane as qmtpm. This particular orientation of ancillary ligands in $[Ru(Cl)(CO)(qmtpm)(PPh_3)]BF_4$ is not common as Ru(II) carbonyl complexes that incorporate both a PPh_3 and a CO group typically have these two π-acceptors in a *cis* disposition.[13] To our knowledge, two carbonyl complexes,

$[Ru(tpy)(PR_3)(CO)Cl]PF_6$ (where tpy = 2,2':6',2" – terpyridine; R = phenyl or *p*-tolyl) are the only other structurally-characterized ruthenium complexes wherein PPh_3 is situated trans to CO.[12]

The Ru–P bond length of 2.4719(7) Å in $[Ru(Cl)(CO)(qmtpm)(PPh_3)]BF_4$ is slightly longer compared to other Ru(II)-phosphine carbonyl complexes with cis PPh_3 and CO ligands such $[Ru(Cl)(CO)(PPh_3)(H\text{-pybox})]BF_4$, (where H-pybox = 2,6-bis(dihydrooxazolin-2'-yl)pyridine)[13a] and [RuCl(CO)(NN'N)(PPh_3)]OTf (where NN'N = 2,6-bis[(dimethylamino)methyl] pyridine).[13b] Both the short the Ru-C(O) bond distance (1.923(2) Å) and the almost linear Ru–C(O) bond angle of $[Ru(Cl)(CO)(qmtpm)(PPh_3)]BF_4$ are typical of Ru(II)-phosphine monocarbonyl complexes.[14]

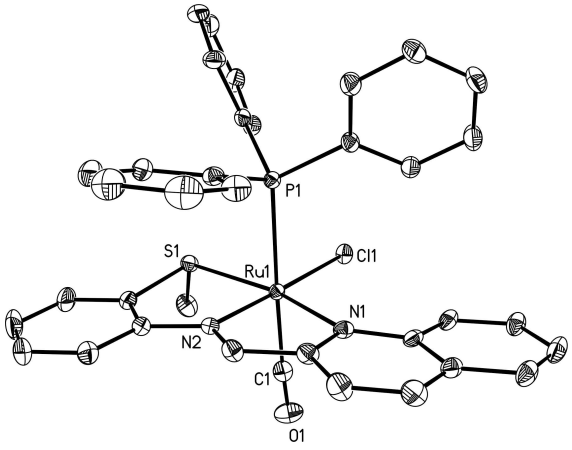

Figure 3.II.2. ORTEP diagram (50% probability level) of the cation of $[Ru(Cl)(CO)(qmtpm)(PPh_3)]BF_4$.

3.II.2.3. Characterization and X-ray Structure of $[Ru(Cl)_2(CO)_2(qmtpm)]ClO_4$

Initial efforts to prepare the corresponding dicarbonyl, $[Ru(CO)_2(qmtpm)(PPh_3)]^{2+}$, were performed by heating to reflux a 1:1 (equivalent)

mixture of qmtpm ligand to *cis*-$[RuCl_2(PPh_3)_2(CO)_2]$[10] in various solvents which included

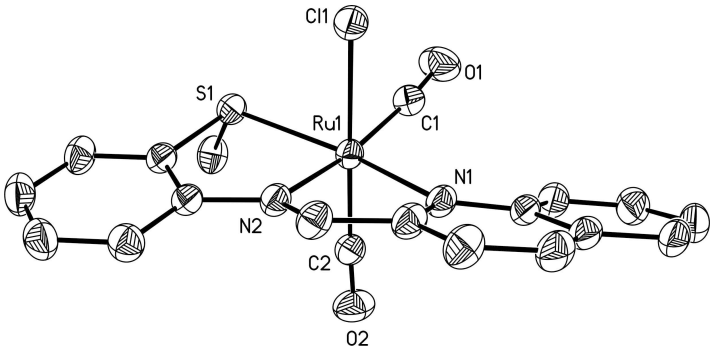

Figure 3.II.3. ORTEP diagram (50% probability level) of the cation of $[Ru(Cl)(CO)_2(qmtpm)]ClO_4$.

methanol, ethanol, chloroform and toluene. Qmtpm ligand coordination to the Ru(II) center under these conditions was not observed and only the starting salt, *cis*-$[RuCl_2(PPh_3)_2(CO)_2]$ remained in the reaction mixture. A different route to the preparation of a dicarbonyl complex bearing the qmtpm ligand frame was employed.

We selected the Ru(II) dimer, $[Ru(CO)_3Cl_2]_2$ as a starting salt as it is known to undergo breakdown into its monomeric components under refluxing conditions in alcoholic media.[15] Indeed, addition of a methanolic solution of qmtpm and to a heated solution of $[Ru(CO)_3Cl_2]_2$ in methanol followed by anion exchange with $NaClO_4$ affords the perchlorate salt of the dicarbonyl complex $[Ru(Cl)(CO)_2(qmtpm)]ClO_4$ in excellent yield. As expected, $[Ru(Cl)(CO)_2(qmtpm)]ClO_4$ displays two strong ν_{CO} bands at 2086 and 2038 cm^{-1} (Figure 3.II.20). Vapor diffusion of toluene into an acetonitrile solution of $[Ru(Cl)(CO)_2(qmtpm)]ClO_4$ afforded crystals suitable for x-ray diffraction.

The structure of the cation of $[Ru(Cl)(CO)_2(qmtpm)]ClO_4$ is shown in Figure 3.II.3. This unit exhibits an octahedral geometry around the ruthenium atom that is coordinated to the sulfur and nitrogen atoms of the qmtpm ligand frame. Two CO groups are *cis*, while one Cl^- donor occupies an axial site in the coordination sphere. The Ru–Cl bond distances in $[Ru(Cl)(CO)(qmtpm)(PPh_3)]BF_4$ and $[Ru(Cl)(CO)_2(qmtpm)]ClO_4$ are similar (2.4352(6) Å vs. 2.4176(7) Å) regardless of the Cl^- ligand's orientation with respect to the imine-N of qmtpm. The Ru–C(O) bond distances in $[Ru(Cl)(CO)_2(qmtpm)]ClO_4$ are almost identical (1.903(3) and 1.890(3) Å), suggesting a uniform extent of back bonding between the two CO ligands and the metal center. Such Ru–C(O) bond lengths and the linearity of the corresponding bond angles (∠O(2)–C(2)–Ru(1): 175.6°) have been observed in other *cis* Ru(II) dicarbonyl complexes such as $[Ru(CO)_2(mnt\text{-}\kappa^2\ SS')(terpy\text{-}\kappa^2 NN')]$, (where mnt-$\kappa^2$ *SS'* = maleonitriledithiolate and terpy-κ^2*NN'* = 2,2':6',2" – terpyridine).[16]

3.II.2.4. Characterization of $[Ru(Cl)(MeCN)(qmtpm)(PPh_3)]BF_4$

The solvato species $[Ru(Cl)(MeCN)(qmtpm)(PPh_3)]BF_4$ was initially obtained when the monocarbonyl complex, $[Ru(Cl)(CO)(qmtpm)(PPh_3)]BF_4$, was dissolved in MeCN and left in the dark for several hours under aerobic conditions (Scheme 3.II.1). The orange-yellow solution of $[Ru(Cl)(CO)(qmtpm)(PPh_3)]BF_4$ became a deep magenta upon standing. Using a combination of spectroscopic techniques, we identified this final magenta species as $[Ru(Cl)(MeCN)(qmtpm)(PPh_3)]BF_4$. The strong CO stretch (ν_{CO}) originally noted at 2028 cm^{-1} for

$[Ru(Cl)(CO)(qmtpm)(PPh_3)]BF_4$ (Figure 3.II.15) is absent in the IR spectrum of $[Ru(Cl)(MeCN)(qmtpm)(PPh_3)]BF_4$ and the final electronic absorption spectrum in acetonitrile exhibits a shift in the absorption maximum from 465 nm to 535 nm suggesting solvent-assisted CO loss (Figure 3.II.14).

The facile substitution of the CO ligand in $[Ru(Cl)(CO)(qmtpm)(PPh_3)]BF_4$ by acetonitrile is attributed to (1) the trans-labilizing effect of a π-acidic PPh_3 ligand in $[Ru(Cl)(CO)(qmtpm)(PPh_3)]BF_4$ (Figure 3.II.2) and (2) the enhanced affinity of acetonitrile for Ru(II) centers. Indeed both FTIR and UV-Vis spectra of $[Ru(Cl)(MeCN)(qmtpm)(PPh_3)]BF_4$ confirm CO loss. It is important to note that the λ_{max} of $[Ru(Cl)(MeCN)(qmtpm)(PPh_3)]BF_4$ at 535 nm is distinct from that of $[Ru(MeCN)_2(qmtpm)(PPh_3)]^{2+}$ (λ_{max} = 490 nm) which has two MeCN ligands. Such solvent-promoted CO dissociation by acetonitrile been documented for other Ru(II) carbonyl complexes such as $[Ru(tpy)(PPh_3)(CO)Cl]PF_6$ (where tpy = 2,2':6',2" – terpyridine).[12]

3.II.2.3. Synthesis and X-ray structure of $[Ru(MeCN)_2(qmtpm)(PPh_3)]ClO_4$

The cation of $[Ru(MeCN)_2(qmtpm)(PPh_3)]ClO_4$ is shown in Figure 3.II.4. The solid state structure confirms the meridional binding of qmtpm to the ruthenium center, much like that observed in the previous complexes $[Ru(Cl)(CO)(qmtpm)(PPh_3)]BF_4$ and $[Ru(Cl)(CO)_2(qmtpm)]ClO_4$. Within this octahedral geometry, the triphenylphosphine group is oriented perpendicular to the

qmtpm plane, while two MeCN ligands are bound in a *cis* disposition. The Ru–P bond length at 2.3485(19) Å

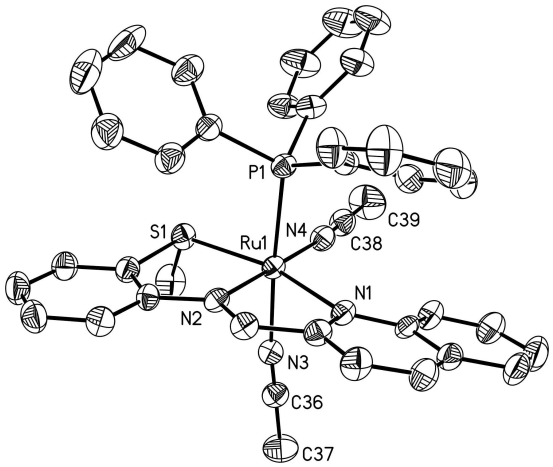

Figure 3.II.4. ORTEP diagram (50% probability level) of the cation of $[Ru(MeCN)_2(qmtpm)(PPh_3)]ClO_4$.

falls in the range of known ruthenium(II) triphenylphosphine complexes.[12,14] Interstingly, the $Ru–N_{MeCN}$ bond lengths at 2.056(6) and 2.087(6) Å are slightly longer than that seen in other ruthenium bis-acetonitrile complexes such as $[Ru(L)(PPh_3)(CH_3CN)_2Cl]Cl$, (where L = 2-(2-pyridyl)benzothiazole), whose measured $Ru–N_{MeCN}$ bond distances are 1.97(13) Å and 2.01(12) Å.[17]

3.II.3. Spectroscopic Properties of Ru(II) qmtpm complexes

3.II.3.1. ^{1}H NMR Spectra

All ruthenium complexes synthesized herein are diamagnetic in the solid state and in solution as evidenced by their clean ^{1}H NMR spectra. As predicted, coordination of the thioether moiety of qmtpm to Ru(II) centers leads to a downfield shift of the singlet resonance from 2.47 ppm (in CD_3CN, Figure 3.II.10) in the free ligand to 3.11

and 3.08 ppm in $[Ru(Cl)_2(qmtpm)(PPh_3)]$ and $[Ru(Cl)(CO)(qmtpm)(PPh_3)]BF_4$, respectively (Figures 3.II.13 and 3.II.17). In $[Ru(Cl)(CO)(qmtpm)(PPh_3)]BF_4$, the signals in the 7.4 -10.0 ppm region are assigned to the qmtpm ligand frame, while the resonances of PPh_3 group are in the 7.0-7.3 region. Similarly in the acetonitrile-bound complex, $[Ru(MeCN)_2(qmtpm)(PPh_3)]ClO_4$ (Figure 3.II.19) a slight downfield shift of the $–SCH_3$ group is observed at 2.90 ppm from 2.47 in the free ligand, with an additional singlet noted at 2.69 is due to the bound acetonitrile ligands.

Interestingly in the case of $[Ru(Cl)(CO)_2(qmtpm)]ClO_4$, the same $–SCH_3$ group coordinated to the metal center appears as two distinct singlets at 3.02 and 3.13 ppm (Figure 3.II.5). Scrutiny of the crystal structure of this dicarbonyl complex suggests that although the $–SCH_3$ segment of qmtpm in $[Ru(Cl)(CO)_2(qmtpm)]ClO_4$ is bound, it could undergo fluxional behavior in solution because of the open structure of $[Ru(Cl)(CO)_2(qmtpm)]ClO_4$. The thioether moiety can be situated either above or below the qmtpm plane in $[Ru(Cl)(CO)_2(qmtpm)]ClO_4$ (Figure 3.II.3) when in solution because of a smaller Cl^- occupying the axial site. Such fluxional behavior is not observed in the related monocarbonyl complex $[Ru(Cl)(CO)(qmtpm)(PPh_3)]BF_4$ due to the steric interactions imposed by bulky PPh_3 group.

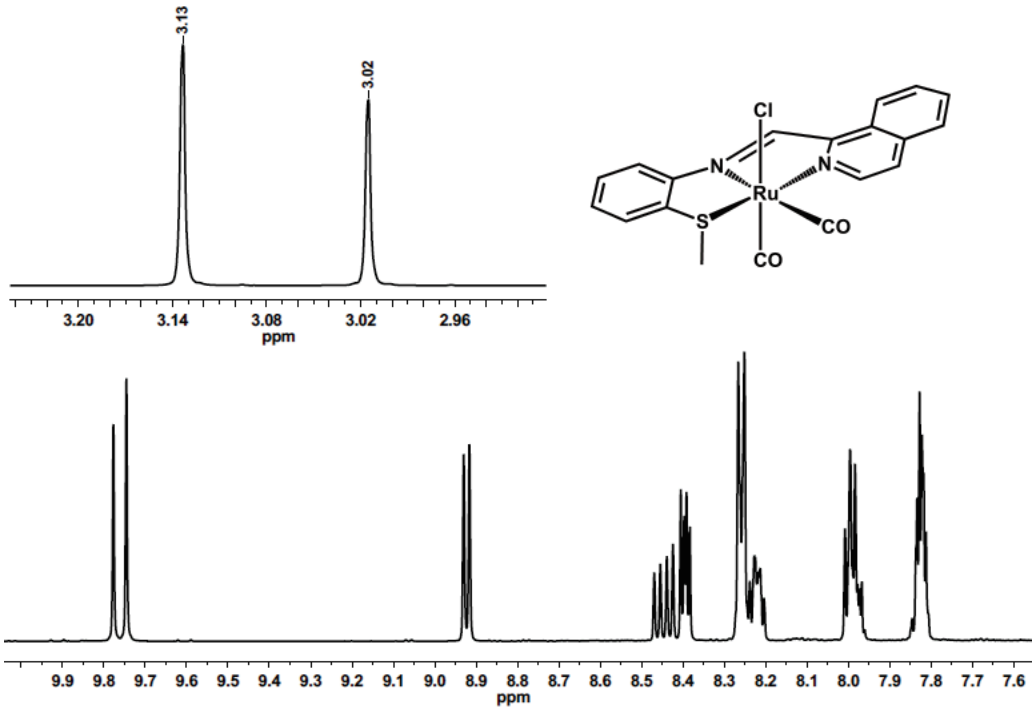

Figure 3.II.5. ^{1}H NMR Spectrum of $[Ru(Cl)(CO)_2(qmtpm)]ClO_4$ in CD_3CN.

3.II.3.2. Electronic Absorption Spectra

The electronic spectra of complexes $[Ru(Cl)_2(qmtpm)(PPh_3)]$, $[Ru(Cl)(CO)(qmtpm)(PPh_3)]BF_4$, $[Ru(Cl)(MeCN)(qmtpm)(PPh_3)]BF_4$ and $[Ru(MeCN)_2(qmtpm)(PPh_3)]ClO_4$ have been recorded in various solvents such as chloroform, ethanol and acetonitrile. Each Ru(II) qmtpm complex features one MLCT band in the visible (400-650 nm) region (Figure 3.II.6) that can also be utilized to identify the products of the interconversions outlined in Scheme 3.II.1. For instance, when the starting salt $[Ru(Cl)_2(qmtpm)(PPh_3)]$ is treated with two equivalents of $AgClO_4$ in acetonitrile, a shift in the MLCT band from 615 nm to 495 nm is observed suggesting the formation of $[Ru(MeCN)_2(qmtpm)(PPh_3)]ClO_4$ via Cl^-

abstraction. Solvent-assisted CO loss from $[Ru(Cl)(CO)(qmtpm)(PPh_3)]BF_4$ in acetonitrile is monitored with the gradual shift of the λ_{max} from 465 nm to 535 nm, following the formation of $[Ru(Cl)(MeCN)(qmtpm)(PPh_3)]BF_4$. Similarly when $[Ru(Cl)(CO)(qmtpm)(PPh_3)]BF_4$ is heated in the presence of 2 equivalents of $AgClO_4$ in acetonitrile, the formation of $[Ru(MeCN)_2(qmtpm)(PPh_3)]ClO_4$ is evident from the shift in the absorption maximum of the 465 nm band to 495 nm.

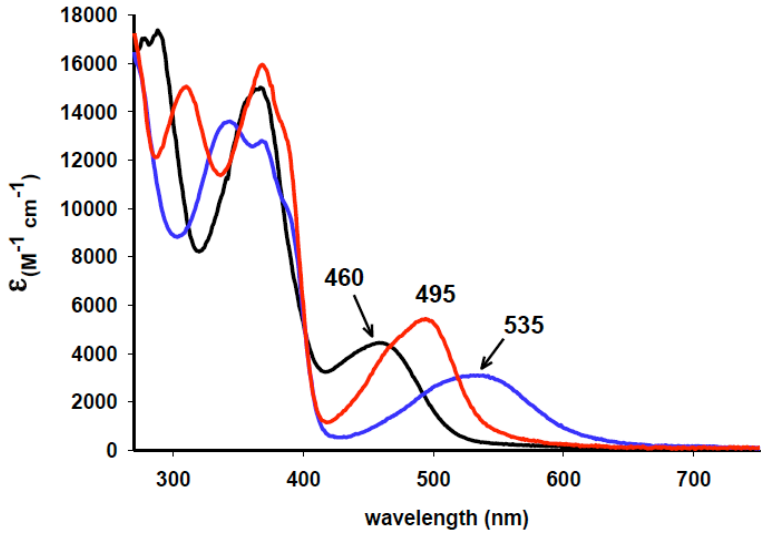

Figure 3.II.6. Electronic absorption spectra of $[Ru(Cl)(CO)(qmtpm)(PPh_3)]BF_4$ (black trace), $[Ru(Cl)(MeCN)(qmtpm)(PPh_3)]BF_4$ (blue trace) and $[Ru(MeCN)_2(qmtpm)(PPh_3)]ClO_4$ (red trace) in acetonitrile.

It is interesting to note that the intense colors for these Ru(II) complexes are lost upon coordination of one or two CO groups, while the absorptivity of the most red-shifted bands remain in the range of ~3000-5000 $M^{-1}cm^{-1}$. For instance, the deep blue color (for $[Ru(Cl)_2(qmtpm)(PPh_3)]$) or magenta (for $[Ru(Cl)(MeCN)(qmtpm)(PPh_3)]BF_4$ become orange-yellow in the isolation of $[Ru(Cl)(CO)(qmtpm)(PPh_3)]BF_4$. Incorporation of two CO groups yields the pale

yellow dicarbonyl complex: $[Ru(Cl)(CO)_2(qmtpm)]ClO_4$, whose absorption maxima is centered at 385 nm (Figure 3.II.7). Such color changes suggest the role of ancillary ligands in modulating the energy levels of the MLCT transitions and in facilitating CO photorelease (vide infra).

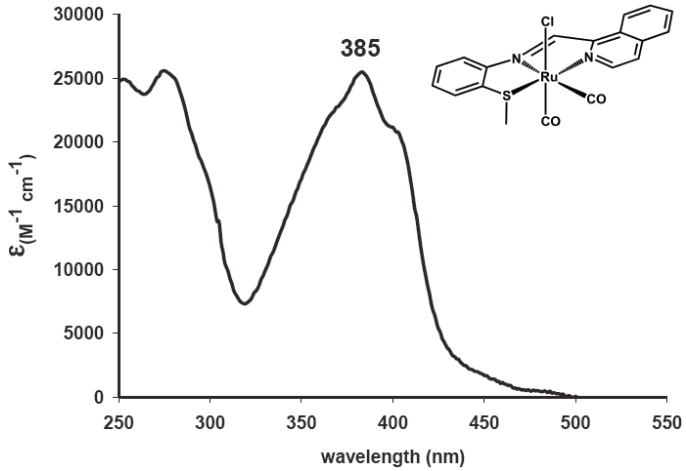

Figure 3.II.7. Electronic Absorption Spectrum of $[Ru(Cl)(CO)_2(qmtpm)]ClO_4$ in acetonitrile.

3.II.3.3. CO Photorelease in Solution

When a solution of $[Ru(Cl)(CO)(qmtpm)(PPh_3)]BF_4$ in ethanol or chloroform is kept in the dark, no change is noted with time. However, solutions of $[Ru(Cl)(CO)(qmtpm)(PPh_3)]BF_4$ in acetonitrile show small changes in its absorption spectrum over hours due to slow replacement of CO with acetonitrile. The strong affinity of acetonitrile toward Ru(II) centers as well as the strong trans-labilizing effect of the PPh_3 ligand promote such CO loss. This behavior has also been reported for $[Ru(Cl)(CO)(terpy)(PPh_3)]PF_6$ under similar conditions.[12] As expected, $[Ru(Cl)(CO)_2(qmtpm)]ClO_4$ with no PPh_3 ligand is indefinitely stable in acetonitrile.

Quite in contrast to these behaviors, exposure to light brings about rapid changes

in the absorption spectra of $[Ru(Cl)(CO)(qmtpm)(PPh_3)]BF_4$ and $[Ru(Cl)(CO)_2(qmtpm)]ClO_4$. When solutions of $[Ru(Cl)(CO)(qmtpm)(PPh_3)]BF_4$ or $[Ru(Cl)(CO)_2(qmtpm)]ClO_4$ in ethanol or acetonitrile are exposed to 350-500 nm light, the absorption spectrum undergoes rapid changes due to photorelease of CO as evidenced by reduced myoglobin assay. Changes in the absorption spectrum of $[Ru(Cl)(CO)(qmtpm)(PPh_3)]BF_4$ in acetonitrile upon exposure to 365 nm light are shown in Figure 3.II.8. Careful inspection of the spectra reveals that $[Ru(Cl)(CO)(qmtpm)(PPh_3)]BF_4$ is quantitatively converted to $[Ru(Cl)(MeCN)(qmtpm)(PPh_3)]BF_4$ (eq. 2) within 60 min with no apparent

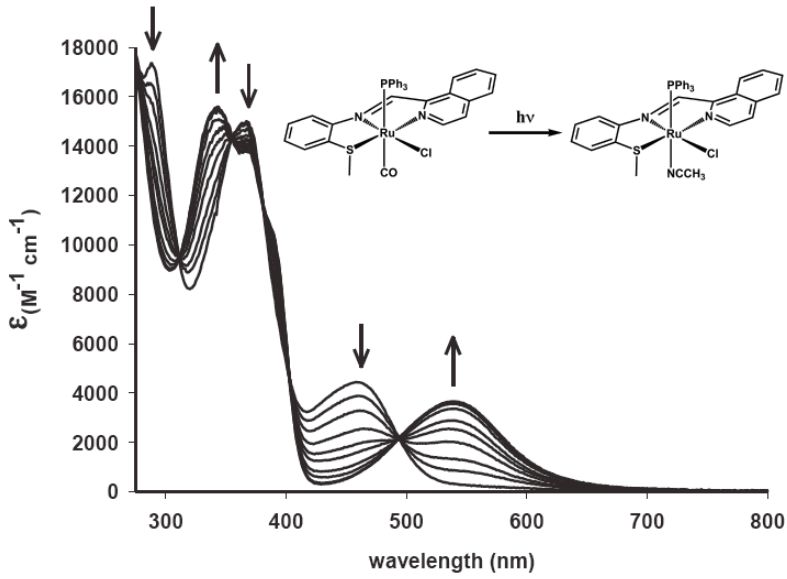

Figure 3.II.8. Changes in the electronic absorption spectrum of $[Ru(Cl)(CO)(qmtpm)(PPh_3)]BF_4$ (0.25 mM) in acetonitrile with UV light irradiation (power = 5-10 mW/cm^2 ; λ = 310 nm).

decomposition as evidenced by clean isosbestic points at 490, 400, 380 and 355 nm (Figure 3.II.8). Data from myoglobin assay confirm that $[Ru(Cl)(CO)(qmtpm)(PPh_3)]BF_4$ delivers one equiv of CO under such illumination.

The apparent first-order rate constant of CO release k_{CO} from $[Ru(Cl)(CO)(qmtpm)(PPh_3)]BF_4$ is faster in acetonitrile than that in ethanol and the k_{CO} values changes with the wavelength of the light. For example, in acetonitrile $[Ru(Cl)(CO)(qmtpm)(PPh_3)]BF_4$ exhibits k_{CO} values of 0.065±0.001 min^{-1} and 0.0063±0.0002 $min^{-1}$with visible light (power = 15 mW/cm^2) with cut-off filters at $\lambda \geq 380$ nm and $\lambda \geq 440$ nm, respectively. In ethanol, the k_{CO} values drops to 0.0032±0.0001 min^{-1} when illuminated with the same light sources. Notable acceleration in CO photorelease from $[Ru(Cl)(CO)(qmtpm)(PPh_3)]BF_4$ is observed with low-power (5-10 mW/cm^2) UV light. For example, in ethanol a k_{CO} value of 0.81±0.01 min^{-1} is obtained under 310 nm illumination.

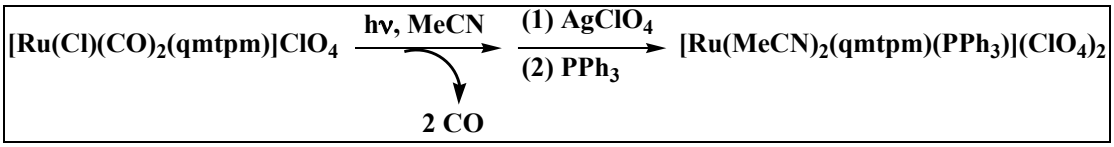

Scheme 3.II.1. Conversion of $[Ru(Cl)(CO)_2(qmtpm)]ClO_4$ to $[Ru(MeCN)_2(qmtpm)(PPh_3)]ClO_4$ after irradiation and subsequent CO release.

Yellow solutions of $[Ru(Cl)(CO)_2(qmtpm)]ClO_4$ in ethanol and acetonitrile release CO upon exposure to light in the 300-360 nm range. For example, when exposed to a narrow-width UV light source with λ_{max} at 310 nm (power = 7 mW/cm^2), $[Ru(Cl)(CO)_2(qmtpm)]ClO_4$ exhibits rapid changes in its electronic absorption spectrum in acetonitrile with isosbestic points at 480, 365, and 300 nm (Figure 3.II.9), and affords a k_{CO} value of 0.22±0.01 min^{-1}. Since exhaustive photolysis of $[Ru(Cl)(CO)_2(qmtpm)]ClO_4$ followed by replacement of the Cl^- ligand with PPh_3

affords $[Ru(MeCN)_2(qmtpm)(PPh_3)]ClO_4$ quantitatively (eq. 3), it is evident that $[Ru(Cl)(CO)_2(qmtpm)]ClO_4$ delivers two equivalents of CO under exposure to 310 nm light. When the λ_{max} of the light source is shifted to 325 nm, the value of k_{CO} drops to 0.08±0.01 min^{-1}, again showing the dependence of k_{CO} on the wavelength of light.

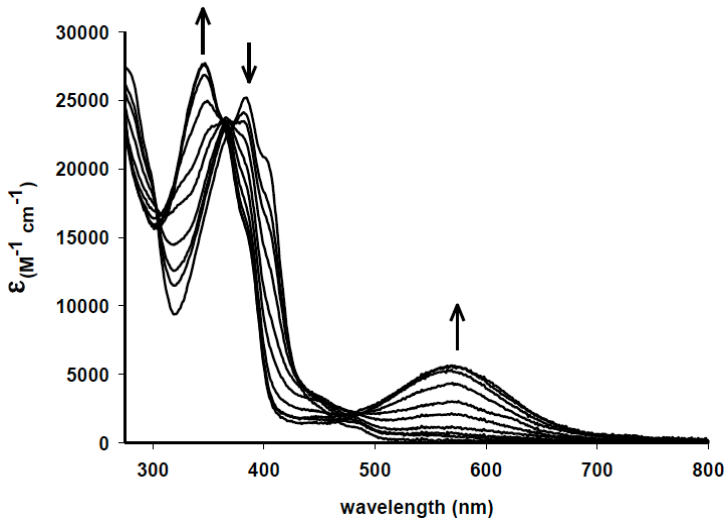

Figure 3.II.9. Changes in the electronic absorption spectrum of $[Ru(Cl)(CO)_2(qmtpm)]ClO_4$ (0.25 mM) in acetonitrile with UV light irradiation (power = 5-10 mW/cm^2 ; λ = 310 nm).

3.II.4. Conclusions

We have shown that the qmtpm ligand frame which features an NNS donor set coordinates readily to Ru(II) centers in a meridional fashion. This mode of ligation was not achieved in the case of isoelectronic Mn(I) or Re(I) centers. Employing the newly characterized starting salt, $[Ru(Cl)_2(qmtpm)(PPh_3)]$, we isolated the monocarbonyl complex, $[Ru(Cl)(CO)(qmtpm)(PPh_3)]BF_4$, which exhibits both solvent-assisted CO release and accelerated CO dissociation upon illumination in

coordinating solvents such as acetonitrile. This reactivity is attributed to the trans-labilizing effect of the PPh_3 ligand in $[Ru(Cl)(CO)(qmtpm)(PPh_3)]BF_4$ and the solid state structure of $[Ru(MeCN)_2(qmtpm)(PPh_3)]ClO_4$ confirms such CO release mechanisms. The related dicarbonyl complex, $[Ru(Cl)(CO)_2(qmtpm)]ClO_4$, shows a much slower CO release rate compared to $[Ru(Cl)(CO)(qmtpm)(PPh_3)]BF_4$. The placement of a σ-donating Cl^- trans to a CO group and the inclusion of a second CO ligand in the coordination sphere of $[Ru(Cl)(CO)_2(qmtpm)]ClO_4$ appears to enhance π-backbonding interactions in this compound, thus accounting for its reduced CO-releasing capacity. Collectively, these findings confirm that in addition to the incorporation of designed ligand frames, the strategic placement of ancillary ligands can modulate the CO-releasing behavior of the resulting photoCORMs.

3.II.5. Experimental Section

Materials and Reagents. $[Ru(Cl)_2(CO)_3]_2$ was purchased from Sigma Aldrich and used as received. The other starting salt $[Ru(Cl)_2(PPh_3)_3]$[9] and the ligand 2-quinoline-*N*-(2'-methylthiophenyl)methyleneimine (qmtpm)[10] were synthesized following literature procedure. Solvents were purified and/or dried by standard techniques prior to use.

$[Ru(Cl)_2(qmtpm)(PPh_3)]$. A batch of 0.741 g (0.77 mmol) of $[Ru(Cl)_2(PPh_3)_3]$ was added to 20 mL of degassed toluene and the red-brown slurry was heated to reflux for 4 h. The solution turned blue and a deep blue solid separated out of the solution. The solid was filtered and washed several times with diethyl ether. After

thorough drying, this procedure afforded $[Ru(Cl)_2(qmtpm)(PPh_3)]$ in analytically pure form (also confirmed by its IR, NMR and electronic spectra). Yield: 510 mg (93%). Selected IR frequencies (KBr disk, cm^1): 1615 (w), 1593 (w), 1519 (m), 1481 (m), 1434 (m), 1090 (m), 827 (w), 787 (w), 753 (m), 697 (s), 525 (s). Electronic Absorption Spectrum in CH_2Cl_2, λ_{max} (nm, ε (M^{-1} cm^{-1})): 280 (19 226), 355 (17 630), 615 (4 235). ^1H NMR ($CDCl_3$, 500 MHz), δ (ppm from TMS): 10.50 (d, 1H), 9.37 (s, 1H), 7.80 (t, 1H), 7.61 (t, 1H), 7.51 (d, 1H), 7.44 (t, 3H), 7.15-7.24 (m, 8H), 7.02 (t, 3H), 6.88 (t, 6H), 6.54 (t, 1H), 3.11 (s, 3H).

$[Ru(Cl)(CO)(qmtpm)(PPh_3)]BF_4$. A slurry of 0.122 g **(**0.17 mmol) of $[Ru(Cl)_2(qmtpm)(PPh_3)]$ in 15 mL of ethanol was treated with 2 equiv of $AgBF_4$ (0.067g, 0.35 mmol) to obtain a magenta solution which was degassed by freeze-pump-thaw technique. The reaction mixture was allowed to stir for 12 h at room temperature and subsequently heated to reflux under nitrogen for 1 h. The resulting purple reaction mixture was filtered through a Celite pad. A steady stream of CO gas was bubbled through the filtrate for 15 min during which the color changed from purple to brown and an orange-yellow solid precipitated out of solution. The solid was collected by filtration and washed several times with diethyl ether. Yield: 80 mg (59%). X-ray quality crystals of yellow blocks were grown by diffusion of pentane into a dilute solution of the complex in dichloromethane. Selected IR frequencies (KBr disk, cm^{-1}): 2028 (vs, ν_{CO}), 1637 (w), 1516 (w), 1480 (w), 1436 (m), 1084 (s, ν_{BF4}), 839 (w), 759 (m), 748 (m), 698 (m), 520 (m). Electronic Absorption Spectrum

in CH_2Cl_2, λ_{max} (nm, ε (M^{-1} cm^{-1})): 292 (15 905), 370 (14 350), 465 (5 310). ^{1}H NMR ($CDCl_3$, 500 MHz), δ (ppm from TMS): 9.92 (d, 1H), 9.61 (s, 1H), 8.52 (d, 1H), 8.34 (d, 1H), 8.14 (t, 1H) 7.96 (t, 1H), 7.80 (m, 2H), 7.47 (s, 1H), 7.28 (t, 7H), 7.20 (t, 3H), 7.04 (t, 5H), 3.08 (s, 3H).

$[Ru(Cl)(CO)_2(qmtpm)]ClO_4$. A batch of 0.167 g (0.326 mmol) of $[Ru(Cl)_2(CO)_3]_2$ was heated to reflux in 7 mL of methanol to generate a pale yellow solution. Separately, a slurry of 0.183 g (0.656 mmol) of qmtpm ligand in 10 mL of methanol was added to the hot solution of $[Ru(Cl)_2(CO)_3]_2$. The resulting red-orange solution was heated to reflux under N_2 atmosphere for 5 h. Next, the volume was reduced to 5 mL under reduced pressure and the orange solid that separated from the solution was filtered. To the filtrate was added 1 equiv of $NaClO_4$ (0.043 g, 0.348 mmol) and the mixture was stirred at room temperature for 30 min when complex $[Ru(Cl)(CO)_2(qmtpm)]ClO_4$ precipitated from the solution as a yellow solid. Yield: 112 mg (60%). X-ray quality crystals of yellow blocks were obtained by diffusion of toluene into an acetonitrile solution of $[Ru(Cl)(CO)_2(qmtpm)]ClO_4$. Selected IR frequencies (KBr disk, cm^{-1}): 2086 (s, ν_{CO}), 2038 (s, ν_{CO}), 1634 (w), 1514 (w), 1434 (w), 1296 (w), 1121 (m), 1083 (s, ν_{ClO4}), 825 (w), 759 (w), 623 (w), 505 (w). Electronic Absorption Spectrum in acetonitrile, λ_{max} (nm, ε (M^{-1} cm^{-1})): 252 (25 350), 275 (25 705), 385 (25 130), 402 (20 770), 485 (2 480). ^{1}H NMR (CD_3CN, 500 MHz), δ (ppm from TMS): 9.76 (d, 1H), 8.92 (d, 1H), 8.42-8.47 (q, 1H), 8.40 (t, 1H), 8.26 (d, 2H) 8.22 (t, 1H), 7.96-8.01 (m, 2H), 7.82 (t, 1H), 3.13 (s, 2H), 3.02 (s, 1H).

[Ru(MeCN)$_2$(qmtpm)(PPh$_3$)](ClO$_4$)$_2$. To a batch of 0.051 g (0.71 mmol) of **1** in 8 mL of acetonitrile was treated with 2 equiv of $AgClO_4$ (0.031 g, 0.150 mmol) dissolved in 7 mL of acetonitrile. The resulting magenta solution was degassed and stirred at room temperature for 12 h, during which a deep red color developed. The solution was filtered through a Celite pad and the filtrate was allowed to evaporate slowly to obtain red blocks of $[Ru(MeCN)_2(qmtpm)(PPh_3)](ClO_4)_2$ suitable for x-ray diffraction. Yield: 40 mg (61%). Selected IR frequencies (KBr disk, cm^1): 1618 (w), 1592 (w), 1435 (w), 1094 (s, ν_{ClO4}), 757 (w), 698 (w), 623 (m), 530 (m). Electronic Absorption Spectrum in CH_3CN, λ_{max} (nm, ε (M^{-1} cm^{-1})): 270 (17 125), 310 (14 240), 368 (15 500), 495 (5 400). ^{1}H NMR (CD_3CN, 500 MHz), δ (ppm from TMS): 9.56 (s, 1H), 8.60 (d, 1H), 8.55 (d, 1H), 8.13 (d, 1H), 8.01 (d, 1H), 7.95 (t, 1H), 7.85 (m, 2H), 7.61 (d, 1H), 7.47-7.52 (m, 2H), 7.22 (m, 3H), 7.06 (m, 15H), 2.90 (s, 3H), 2.69 (s, 3H).

3.II.6. Experimental Data: IR, ^{1}H NMR and Electronic Absorption Spectra

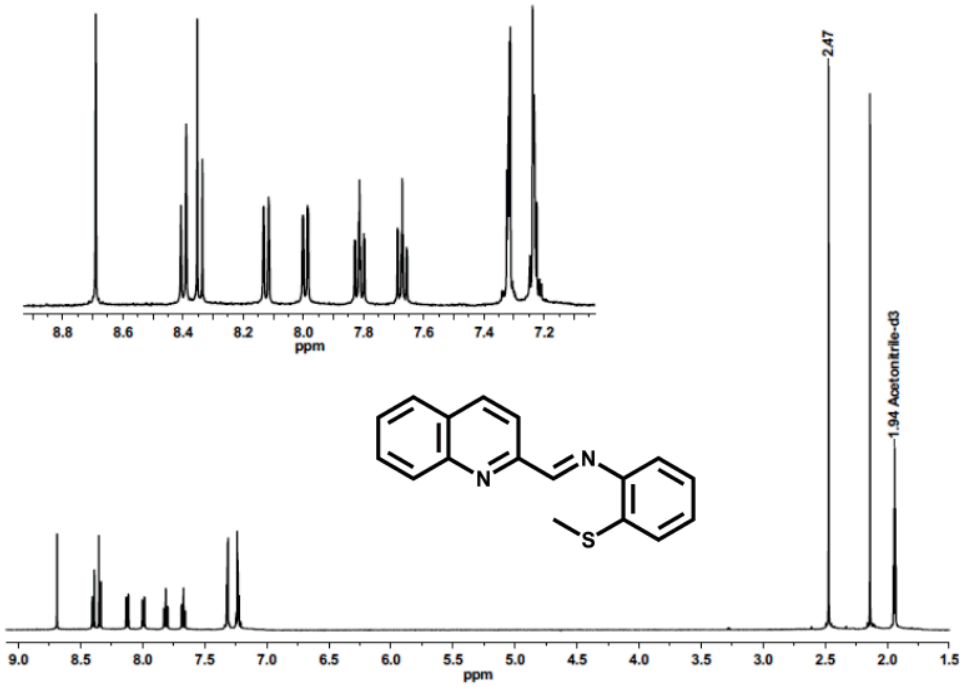

Figure 3.II.10. ^{1}H NMR Spectrum of (1.50-8.75 ppm) of qmtpm in CD_3CN.

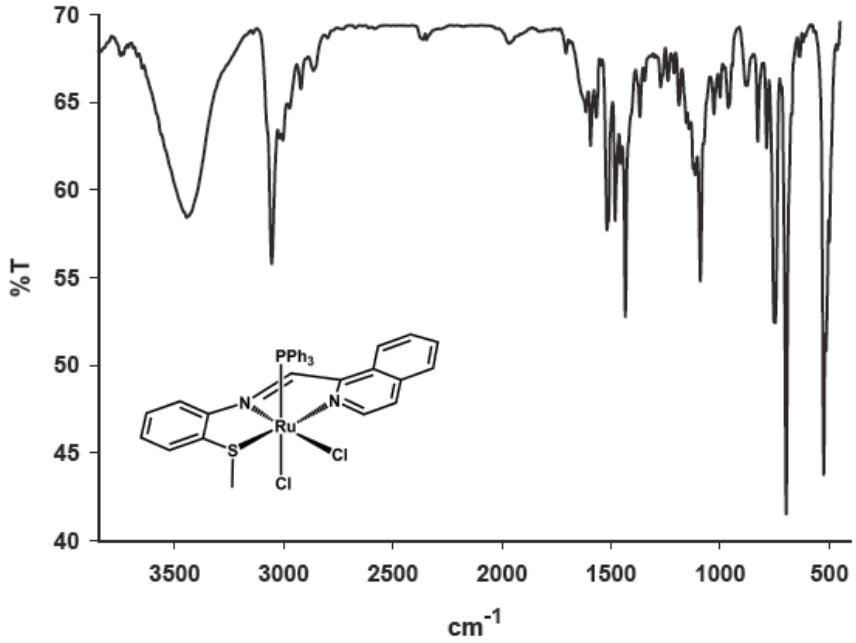

Figure 3.II.11. IR Spectrum of $[Ru(Cl)_2(qmtpm)(PPh_3)]$ in KBr disk.

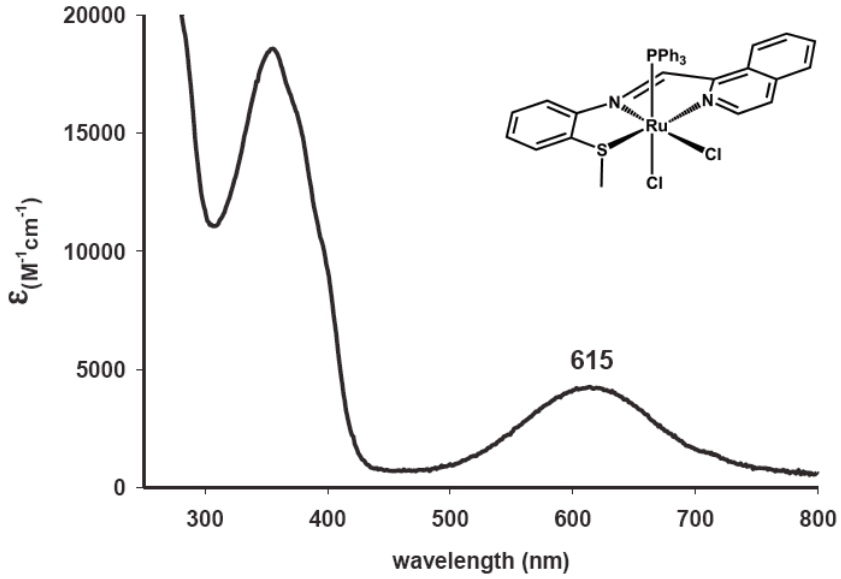

Figure 3.II.12. Electronic Absorption Spectrum of $[Ru(Cl)_2(qmtpm)(PPh_3)]$ in CH_2Cl_2.

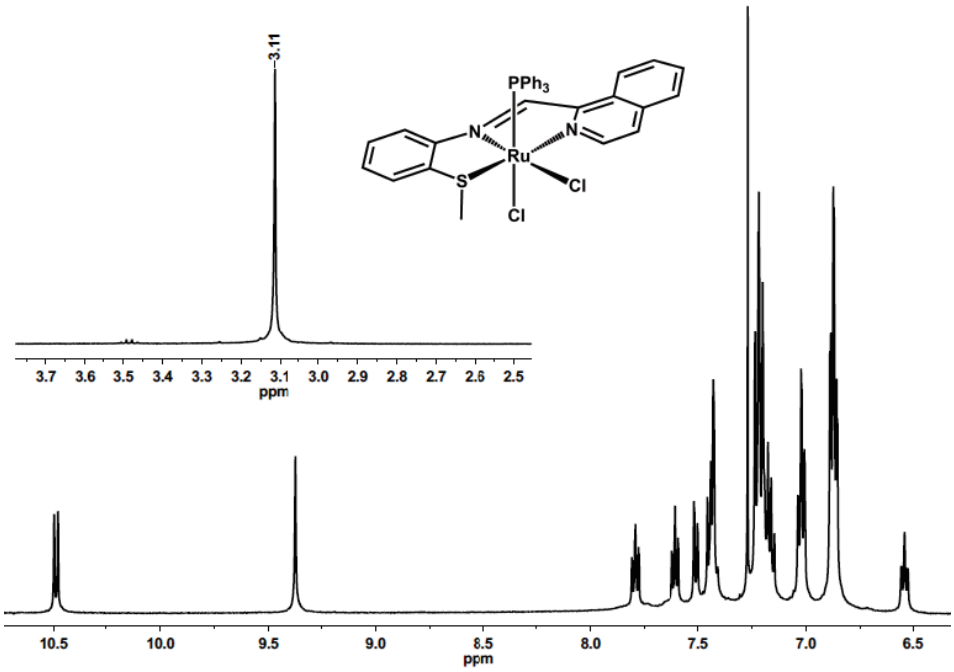

Figure 3.II.13. ^1H NMR Spectrum (6.50-10.50 ppm) of $[Ru(Cl)_2(qmtpm)(PPh_3)]$ in $CDCl_3$. Inset: Thioether resonance at 3.11 ppm.

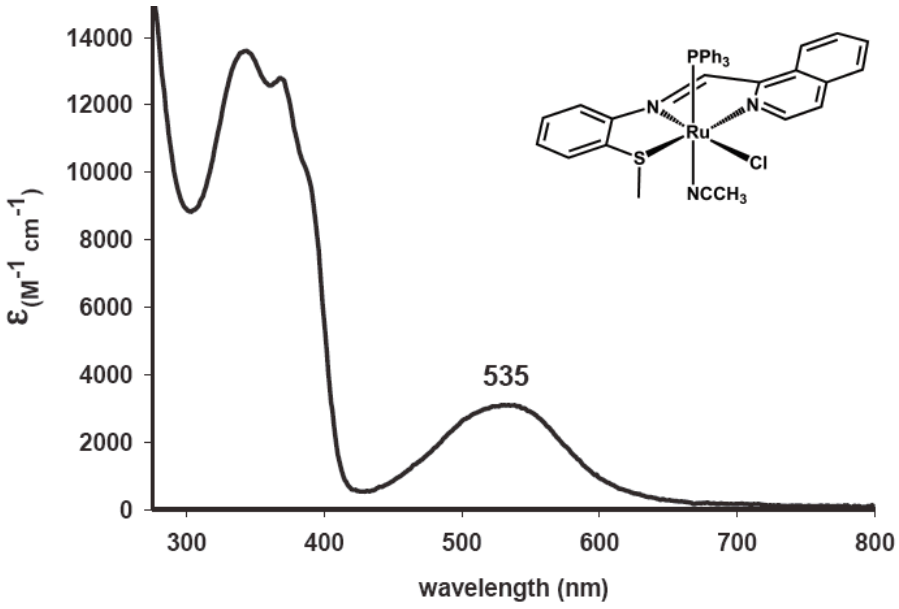

Figure 3.II.14. Electronic Absorption Spectrum of $[Ru(Cl)(MeCN)(qmtpm)(PPh_3)]BF_4$ in CH_3CN.

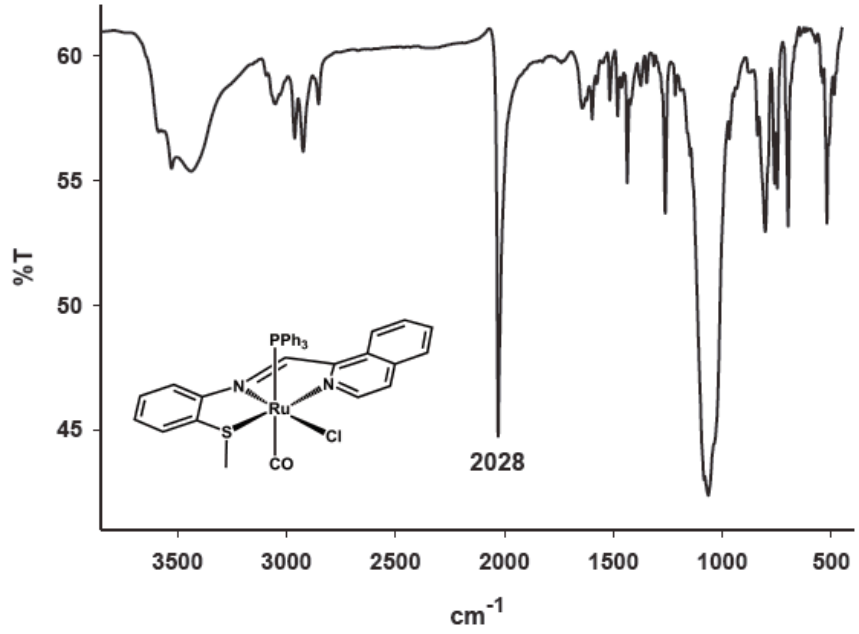

Figure 3.II.15. IR Spectrum of $[Ru(Cl)(CO)(qmtpm)(PPh_3)]BF_4$ in KBr disk.

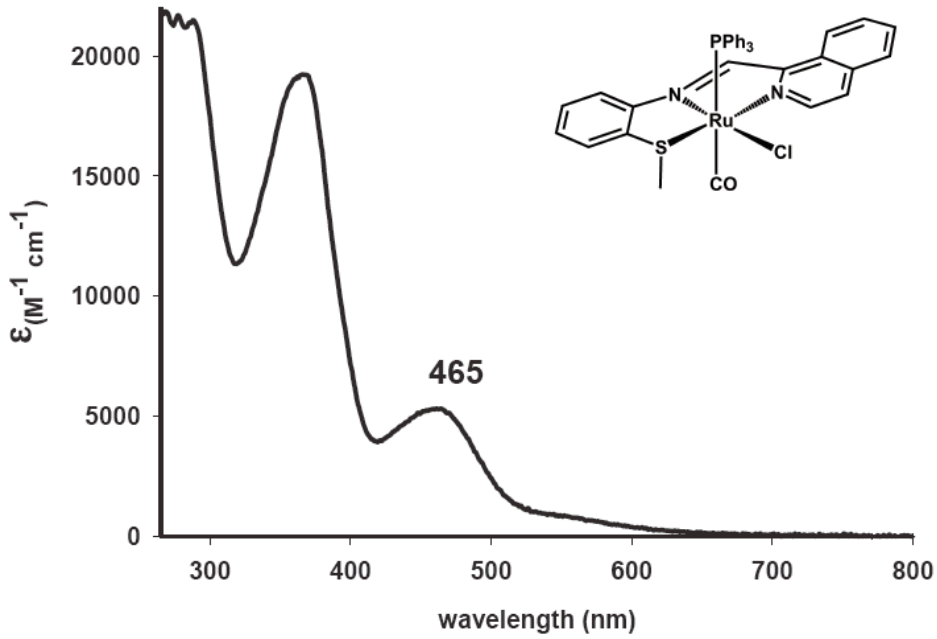

Figure 3.II.16. Electronic Absorption Spectrum of $[Ru(Cl)(CO)(qmtpm)(PPh_3)]BF_4$ in CH_2Cl_2.

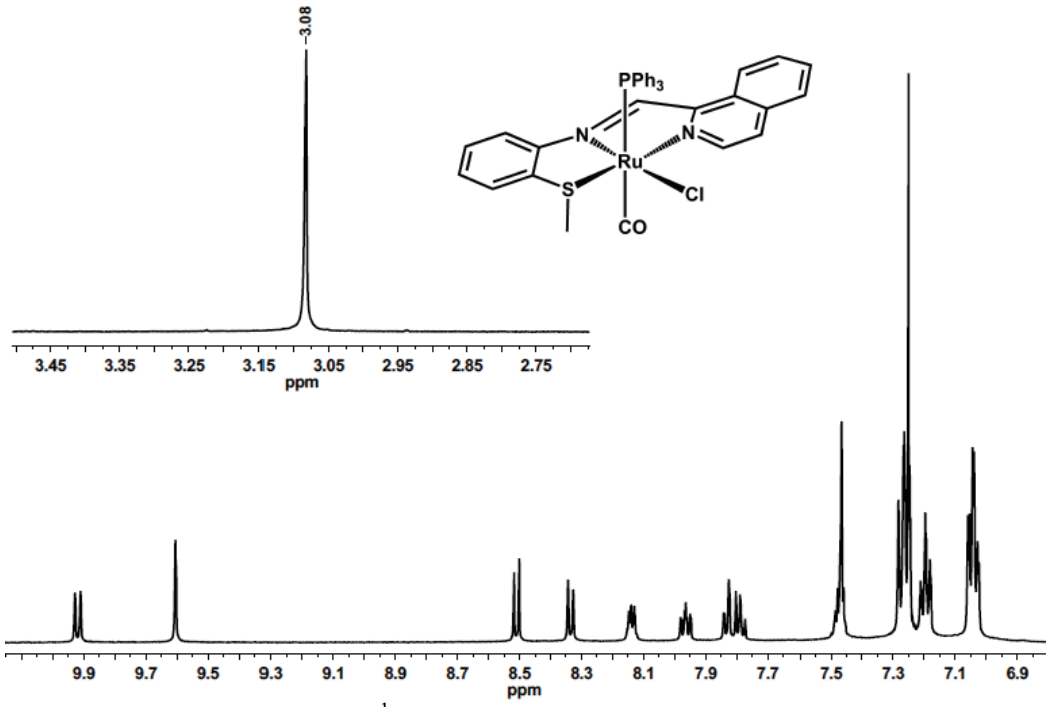

Figure 3.II.17. ^1H NMR Spectrum (7.00-9.90 ppm) of $[Ru(Cl)(CO)(qmtpm)(PPh_3)]BF_4$ in $CDCl_3$. Inset: Thioether resonance at 3.08 ppm.

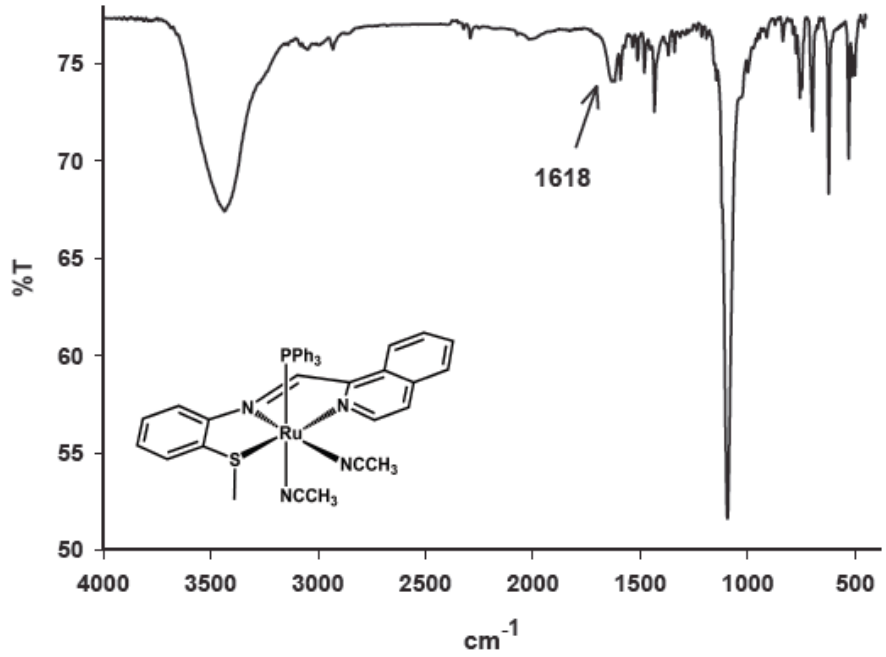

Figure 3.II.18. IR Spectrum of $[Ru(MeCN)_2(qmtpm)(PPh_3)]ClO_4$ in KBr disk.

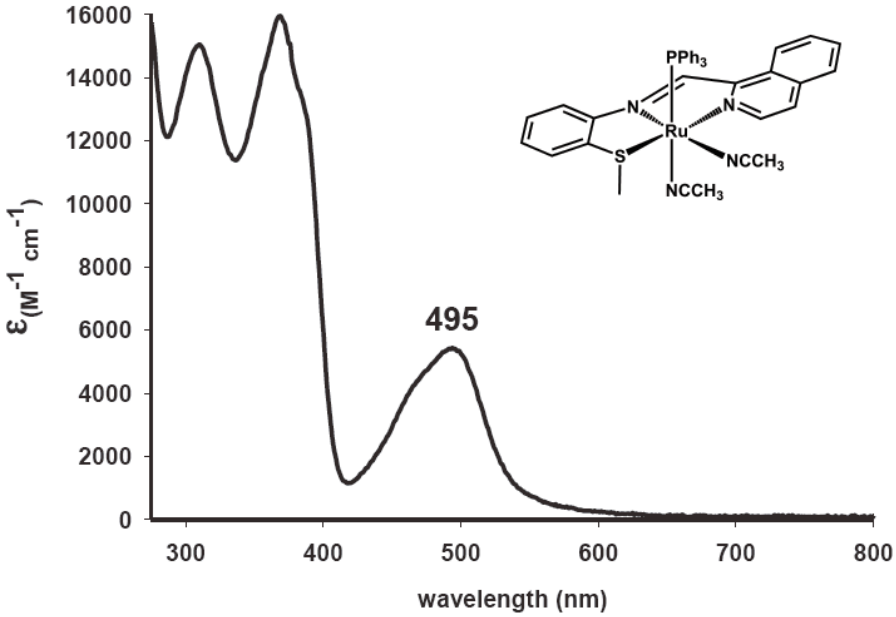

Figure 3.II.19. Electronic Absorption Spectrum of $[Ru(MeCN)_2(qmtpm)(PPh_3)]ClO_4$ in CH_3CN.

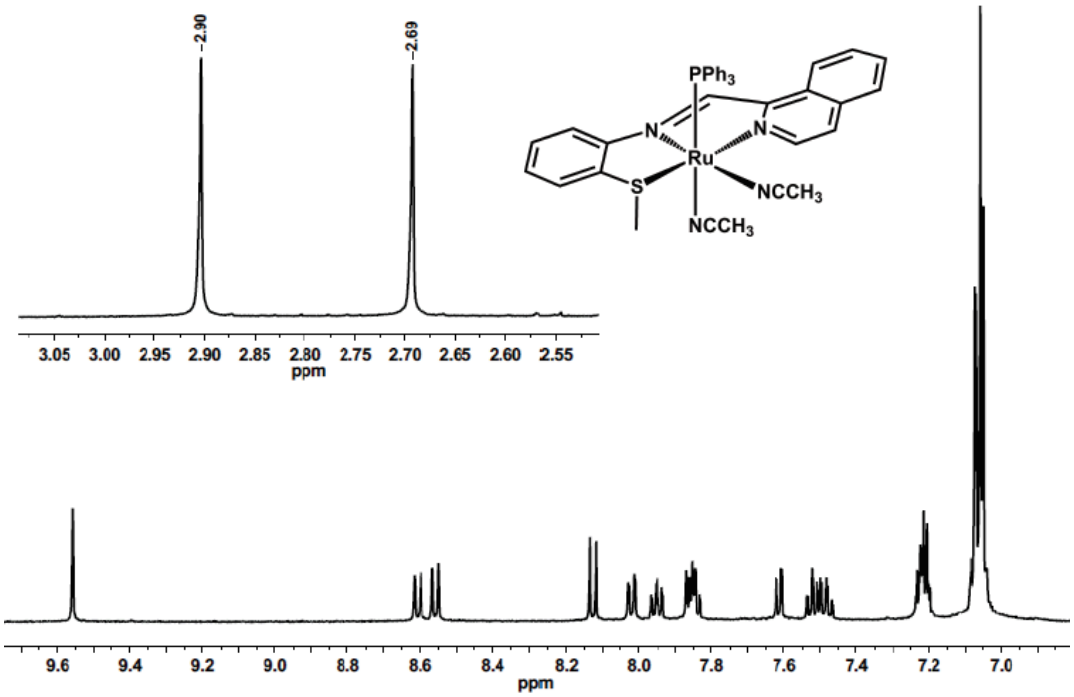

Figure 3.II.20. ^{1}H NMR Spectrum (7.00-9.60 ppm) of $[Ru(MeCN)_2(qmtpm)(PPh_3)]ClO_4$ in $CDCl_3$. Inset: Thioether resonance at 2.90 ppm and an additional singlet noted at 2.69 is due to the bound acetonitrile ligands.

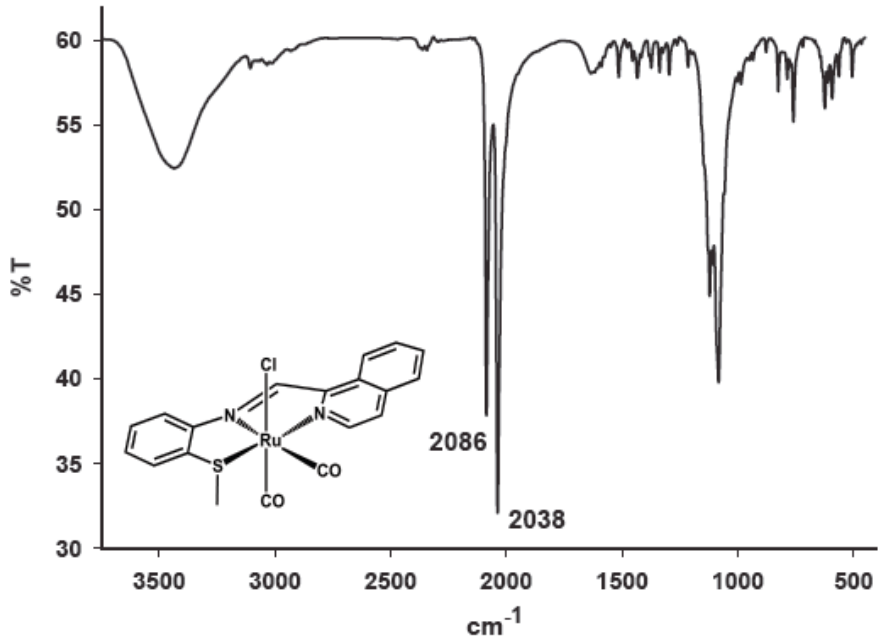

Figure 3.II.21. IR Spectrum of $[Ru(Cl)(CO)_2(qmtpm)]ClO_4$ in KBr disk.

3.II.7. References

(1) (a) Campagna, S.; Puntoriero, F., *Top. Curr. Chem.* **2007**, *280*, 117-214. (b) Roundhill, D. M. *Photochemistry and Photophysics of Metal Complexes;* Plenum Press: New York, 1994.

(2) (a) Sun, Y.; Chen, Z.; Puodziukynaite, E.; Jenkins, D. M.; Reynolds, J. R.; Schanze, K. S., *Macromolecules*, **2012**, *45*, 2632-2642. (b) Gu, J.; Chen, J.; Schmehl, R. H., *J. Am. Chem. Soc.*, **2010**, *132*, 7338-7346.

(3) Meyer, T. J., *Acc. Chem. Res.*, **1989**, *22*, 163-170.

(4) (a) Adeloye A. O.; Olomola, T. O.; Adebayo, A. I.; Ajibade, P. A., *Int. J. Mol. Sci.,* **2012***, 13*, 3511-3526. (b) Zhao, H. C.; Harney, J. P.; Huang, Y-T.; Yum, J-H.; Nazeeruddin, M. K.; Grätzel, M.; Tsai, M-K.; Rochford, J., *Inorg. Chem.*, **2012**, *51,* 1-3. (c) Kisserwan, H.; Ghadar, T. H., *Inorg. Chim. Acta*, **2010,** *363*, 2409-2415.

(5) (a) Gabrielsson, A.; Záliš, S.; Matousek, P.; Towrie, M.; Vlček, A., Jr., *Inorg. Chem.,* **2004**, *43*, 7380-7388. (b) Eskelinen, E.; Kinnunen, T.-J. J.; Haukka, M.; Pakkanen, T. A., *Eur. J. Inorg. Chem.*, **2002**, 1169-1173. (c) Eskelinen, E.; Haukka, M.; Venäläinen, T.; Pakkanen, T. A.; Wasberg, M.; Chardon-Noblat, S.; Deronzier, A., *Organometallics*, **2000**, *19*, 163-169.

(6) Collomb-Dunand-Sauthier, M. N.; Deronzier, A.; Ziessel, R., *J. Organomet. Chem.*, **1993**, *444*, 191-198.

(7) Sellmann, D.; Sutter, J., *Acc. Chem. Res.*, **1997**, *30*, 460-469.

(8) Gonzalez, M. A.; Carrington, S. J.; Fry, N. L.; Martinez, J. L.; Mascharak, P. K., *Inorg. Chem*., **2012**, *51*, 11930-11940.

(9) Stephenson, T. A.; Wilkinson, G., *J. Inorg. Nucl. Chem.*, **1966**, *28*, 945-956.

(10) Castro, A. G.; Costa, J. S.; Pievo, R.; Massera, C.; Mutikainen I.; Turpeinen, U.; Gamez, P.; Reedijk J. *Z. Anorg. Allg. Chem.* **2008**, *634*, 2477-2482.

(11) Hossain, M.; Maji, M.; Chattopadhyay, S. K.; Ghosh, S.; Blake, A. J., *Polyhedron*, **1998**, *17*, 1897-1906.

(12) Ooyama, D.; Saito, M., *Inorg. Chim. Acta*, **2006**, *359,* 800-806.

(13) (a) Cuervo, D.; Ménendez-Pedregal, E.; Díez, J.; Gamasa, M. P., *J. Organomet. Chem.*, **2011**, *696*, 1861-1867. (b) Abbenhuis, R. A. T. M.; del Rio, I.; Bergshoef, M. M.; Boersma, J.; Veldman, N.; Spek, A. L.; van Koten, G., *Inorg. Chem.*, **1998**, *37*, 1749-1758.

(14) Singh, S. K.; Sharma, S.; Dwivedi, S. D.; Zou, R-Q.; Xu, Q.; Pandey, D. S., *Inorg. Chem.*, **2008**, *47*, 11942-11949.

(15) Moreno, M. A.; Haukka, M.; Kallinen, M.; Pakkanen, T. A., *Appl. Organometal. Chem.*, **2006**, *20*, 51-69.

(16) Sugimoto, H.; Tsuge, K.; Tanaka, K., *J. Chem. Soc. Dalton Trans.*, **2001**, 57-63.

(17) Maji, M.; Sengupta, P.; Chattopadhyay, S. K.; Mostafa, G.; Schwalbe, C. H.; Ghosh, S., *J. Coord. Chem.*, **2001**, *54*, 13-24.

Chapter 4. Density Functional Theory Studies to elucidate origin of CO Photolability in d^6 Metal Carbonyls bearing the tridentate NNS ligand qmtpm

Part I: DFT and TDDFT Studies of Manganese qmtpm Carbonyl Complexes

4.I.1. Background

The unusual role of carbon monoxide (CO) as a signaling molecule in several physiological pathways has spurred research in the area of synthesizing new metal carbonyl complexes as photoactive carbon monoxide releasing molecules (photoCORMs). The use of light on these exogenous CO donors provides a better handle and ensures controlled CO delivery. However, the strong affinity of CO for low valent metal centers due to π-backbonding interactions necessitates the use of UV light energies (or higher) in inducing metal-CO bond homolysis and subsequent CO dissociation. Indeed prototypical photoCORMs such as $Mn_2(CO)_{10}$ and $Fe(CO)_5$ have demonstrated the efficacy of CO photorelease in biologically-relevant studies under UV light illumination.[1] These preliminary findings have prompted research in exploring photoCORM design principles that could provide ligands suitable in generating more photosensitive CO-delivery agents.

To date, only a few density functional theory (DFT) calculations have been performed on known photoCORMs that shed light on factors contributing to CO photorelease. A theoretical investigation by Leszczynski and co-workers highlights the role of M—CO bond energies in the observed CO dissociation of $Mn_2(CO)_{10}$ and [Ru(glycinate)$(CO)_3$Cl] (CORM-3), whose calculated bond energies are 46.76 and 42.71 kcal/mol, respectively. In the case of $Mn_2(CO)_{10}$, the bonding is characterized

by a strong Mn($3d_{xy}$) + (C + O)($2p_y$) nature, while for CORM-3 a weaker π-type [Ru($4d_{xz}$) - C($2p_x$) - O($2p_x$)] is reported. In the presence of physiologically relevant ions such as Cl^- and HPO_4^{2-}, the rate of CO dissociation in the case of CORM-3 is enhanced, further supporting the observed facile CO release from this compound.[2]

On a similar note, Cavalli and co-workers recently reported results of their DFT calculations on a series of manganese carbonyl complexes bearing thiolate and bipyridine ligands (Figure 4.I.1). A key feature of their account is the use of natural bond order (NBO) analysis to probe the nature of the Mn—CO bond. Because π-backbonding is a specific type of donor-acceptor stabilizing interaction between metal d-orbital lone pairs and vacant CO π^* orbitals, this group examined the relevant donor and acceptor interactions (i.e. contributions of the axial and equatorial CO groups) which collectively result in the observed stabilization energies. Based on NBO calculations, charge transfer interactions appear to be a major source of Mn—CO bond stabilization.[3] Fine-tuning of charge transfer interactions therefore is key in the design of photoCORMs with greater sensitivity to visible light.

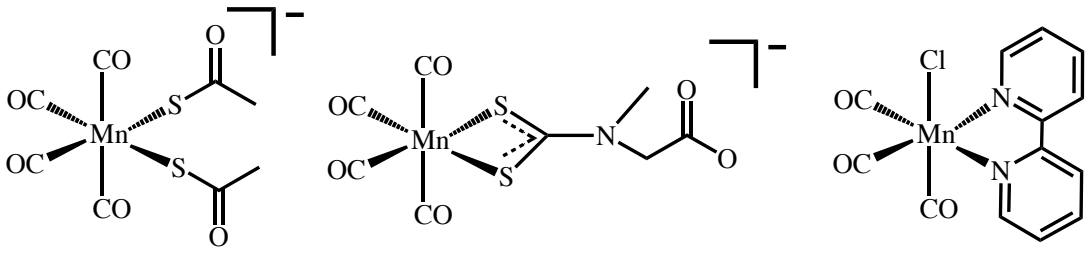

CORM-371 **CORM-401** **CORM-313**

Figure 4.I.1. Manganese-based CORMs bearing thiolate and bipyridine ligands. (adapted from ref. 3)

From previous work reported in part 1 of Chapter 3, we discovered that increased conjugation in the ligand frame results in a systematic increase in absorptivity of the corresponding compounds in the longer wavelength region. The carbonyl complex $[Mn(pqa)(CO)_3]ClO_4$ (where pqa = (2-pyridylmethyl)(2-quinolylmethyl)amine) which features both a pyridine and quinoline moiety (Figure 4.I.1), exhibits a strong absorption band with λ_{max} at 360 nm. This is a notable red-shift in the absorption maximum when compared to the related carbonyl $[Mn(tpa)(CO)_3]ClO_4$ (where tpa = tri(2-pyridyl)amine, λ_{max} = 330 nm) which comprises only pyridine donors in the otherwise similar ligand frame (Figure 4.I.1). Since the affinity of CO toward metals in low oxidation state arises predominantly from backbonding of electrons from the metal center to the π^* level of CO, we hypothesized that *metal-to-ligand charge transfer (MLCT) transitions would reduce CO affinity of the metal center and result in CO photorelease.* Indeed, increased CO photolability of $[Mn(pqa)(CO)_3]ClO_4$ compared to $[Mn(tpa)(CO)_3]ClO_4$ indicates that facilitation of CO photorelease could arise from such transition(s).

To explore the validity of our hypothesis further, we have now designed a series of manganese(I) carbonyls featuring bidentate and potentially tridentate ligands that incorporate both conjugated aromatic nitrogen donors and an imine functionality (in place of the amine nitrogen) in the ligand framework. To probe the effects of ancillary ligands, a Br^- ligand has also been incorporated in the coordination sphere. Finally, a thioether moiety has been added to the ligand frame to compete for a coordination site and promote additional CO release. The structures of the ligands

employed in the present work are shown in Figure 4.I.2. We herein report the syntheses, structures and photochemical parameters of $[Mn(pimq)(CO)_3(MeCN)]ClO_4$ (where pimq = (2-phenyliminomethyl)quinoline),

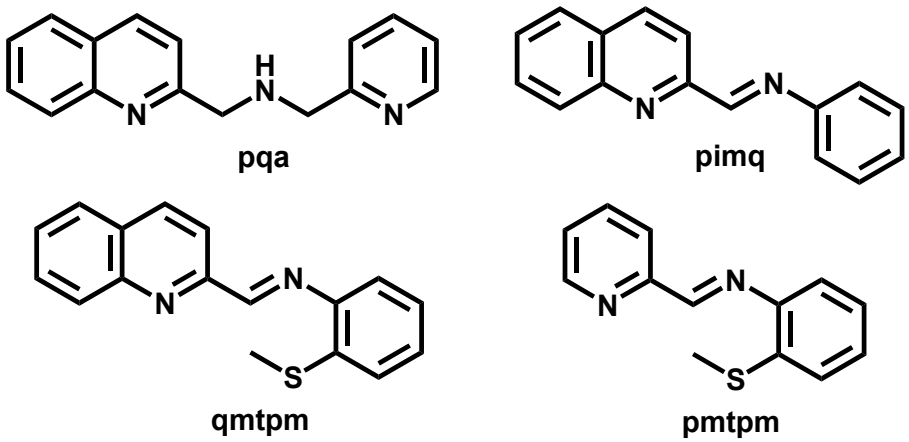

Figure 4.I.2. Structures of the bidentate (pimq) and potentially tridentate ligands (pmtpm and qmtpm) used in this study.

$[Mn(qmtpm)(CO)_3(MeCN)]ClO_4$ (where qmtpm = 2-quinoline-*N*-(2'-methylthiophenyl) methyleneimine), $[Mn(qmtpm)(CO)_3Br]$, $[Mn(pmtpm)(CO)_3(MeCN)]ClO_4$ (where pmtpm = 2-pyridyl-*N*-(2'-methylthiophenyl)methyleneimine), and $[Mn(pmtpm)(CO)_3Br]$. The systematic changes in the ligand frame has afforded progressive red shift of the absorption band maximum from 390 nm (for $[Mn(pmtpm)(CO)_3(MeCN)]ClO_4$) to 535 nm (for $[Mn(qmtpm)(CO)_3Br]$) in this set of photoCORMs. We have also attempted to correlate the CO photolability of these photoCORMs with the results of density functional theory (DFT) and time dependent DFT (TDDFT) calculations and confirm the nature of the MLCT associated with CO release.

4.I.2. Syntheses of the Metal Complexes

In order to promote CO photorelease from our designed photoCORMs through metal-to-ligand charge transfer (MLCT) transitions, we have introduced conjugated ring systems in addition to the imine functionality in the ligand frames of the present work. Out of this set of Mn(I) tricarbonyls, $[Mn(pimq)(CO)_3(MeCN)]ClO_4$ contains the ligand pimq (Figure 4.I.2) in which a phenyl ring is bonded to a quinoline donor through an imine linker. This bidentate ligand provides a significant extent of conjugation. The next subset comprising of $[Mn(qmtpm)(CO)_3(MeCN)]ClO_4$ and $[Mn(pmtpm)(CO)_3(MeCN)]ClO_4$, is derived from the potentially tridentate ligands qmtpm[4] and pmtpm[5] which includes a thioether moiety on the phenyl part of the ligand. The reasons for this inclusion are two-fold. First, it is expected to add electron density to the π-frame of the ligand and second, it could bind to the Mn(I) center[6] and promote further CO release upon illumination. In addition, a pyridine donor in pmtpm (in complex $[Mn(pmtpm)(CO)_3(MeCN)]ClO_4$) has been replaced with a more-conjugated quinoline donor in qmtpm (in complex $[Mn(qmtpm)(CO)_3(MeCN)]ClO_4$) for enhanced absorptions in the visible range.

Finally, in the subset consisting of $[Mn(qmtpm)(CO)_3Br]$ and $[Mn(pmtpm)(CO)_3Br]$, a Br^- ligand replaces the acetonitrile ligand. Introduction of this donor is intended to provide electron density to the Mn(I) center via σ-donation and modulate the MLCT transitions of the resulting carbonyls. In this subset, exchange of the pyridine donor with a quinoline donor has also been applied to correlate the CO photolability of the resulting carbonyls.

Treatment of *fac*-$[Mn(CO)_3(MeCN)_3]ClO_4$ with pimq or qmtpm in $CHCl_3$ under refluxing conditions afforded the cationic species $[Mn(L)(CO)_3(MeCN)]^+$, where L = pimq or qmtpm ($[Mn(pimq)(CO)_3(MeCN)]ClO_4$ or $[Mn(qmtpm)(CO)_3(MeCN)]ClO_4$). While qmtpm has potentially three coordination sites, only the nitrogen atoms of the ligand were found to bind to the metal center as evidenced by crystallographic data (vide infra). The use of a more suitable starting salt such as $Mn(CO)_5Br$ under similar conditions also did not lead to the desired metal-sulfur binding and instead generated the neutral carbonyl $[Mn(qmtpm)(CO)_3Br]$. A similar trend was also observed with the less conjugated ligand pmtpm, wherein reaction with *fac*-$[Mn(CO)_3(MeCN)_3]ClO_4$ or $Mn(CO)_5Br$ generated compounds $[Mn(pmtpm)(CO)_3(MeCN)]ClO_4$ and $[Mn(pmtpm)(CO)_3Br]$, respectively. This outcome was somewhat surprising since scrutiny of the literature revealed a few low valent manganese carbonyls in which multiple thioether groups are coordinated to the metal center in the presence of π-acceptor ligands.[7] We suspect that the rigid framework of the conjugated ligands of Figure 4.I.2 does not allow binding in the *facial* orientation and hence replacement of the MeCN or Br^- ligand was not achieved. The utility of the −SMe moiety is however evident in the enhancement of the CO photorelease from these species thus indicating its electronic effect(s) on the overall CO- donating capacity of these photoCORMs (vide infra). All five carbonyls complexes dissolve in organic solvents such as MeCN, DMSO and $CHCl_3$ and in polar aprotic solvents such as MeOH. Such solutions are stable for hours when kept in the dark.

4.I.3. Spectroscopic Properties

The IR spectra of carbonyls exhibit two strong bands in the carbonyl region, a pattern consistent with known *fac*-Mn(I) tricarbonyl complexes.[8] In the case of the MeCN-adducts $[Mn(pimq)(CO)_3(MeCN)]ClO_4$, $[Mn(qmtpm)(CO)_3(MeCN)]ClO_4$ and $[Mn(pmtpm)(CO)_3(MeCN)]ClO_4$, the first ν_{CO} stretch appears as a sharp peak at 2042-2044 cm^{-1} pertaining to the axial CO ligand (Figures 4.I.16, 4.I.19 and 4.I.23). The second broad ν_{CO} band noted at ~1942-1947 cm^{-1} features a minor splitting pattern which suggests a distinction between the remaining CO groups in the equatorial plane. For the neutral compounds $[Mn(qmtpm)(CO)_3Br]$ and $[Mn(pmtpm)(CO)_3Br]$, a similar pattern is observed, albeit slight shift to lower frequencies. The first sharp ν_{CO} stretch appears at 2020 cm^{-1} followed by the broad ν_{CO} stretch at 1920-1934 cm^{-1}.

All Mn(I) tricarbonyl complexes in this section are diamagnetic in the solid state and in solutions. The S = 0 state of the compounds is readily evidenced by their clean NMR spectra (Figures 4.I.15, 4.I.18, 4.I.20, and 4.I.23). An example is shown in Figure 4.I.3. In this spectrum of $[Mn(qmtpm)(CO)_3(MeCN)]ClO_4$, ligation of the qmtpm ligand to the Mn(I) center is indicated by the downfield shift of the imine proton (see Figure 4.I.22 for ^1H NMR of qmtpm ligand in CD_3CN) to 8.97 ppm. The aromatic protons spread over 7.30-9.00 ppm while the -SMe resonance of qmtpm appears at 2.85 ppm.

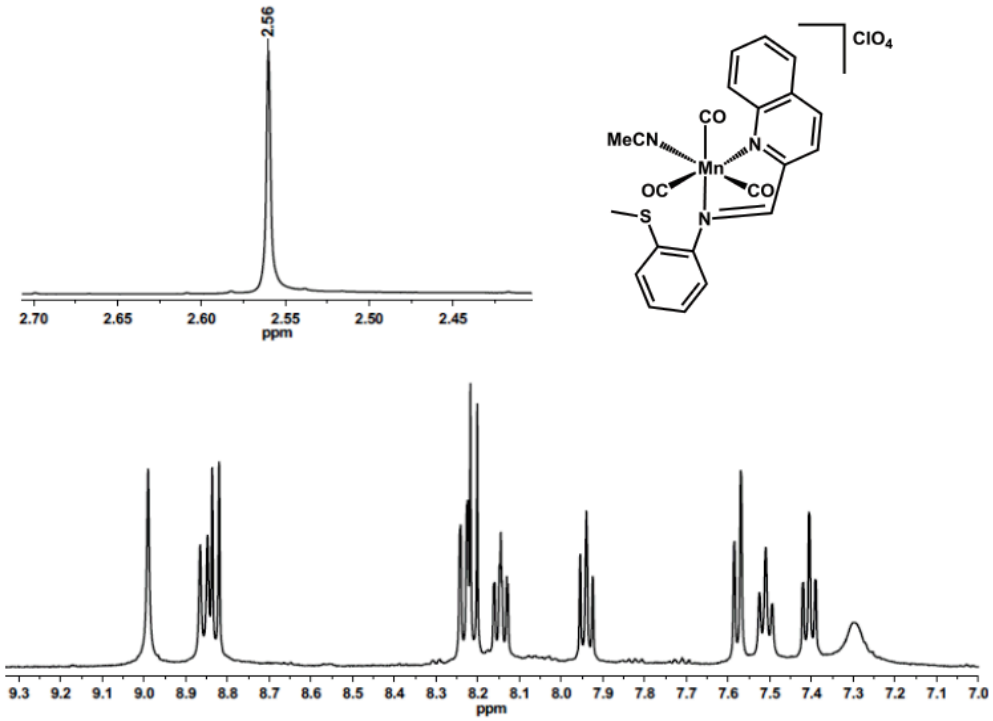

Figure 4.I.3. ^{1}H NMR (500 MHz) spectrum of [Mn(qmtpm)(CO)$_3$(MeCN)]ClO$_4$ in CD$_3$CN (7.40-9.40 ppm range). Inset: Resonance Signal of unbound -SMe group at 2.56 ppm.

4.I.4. Structures of the Metal Complexes.

The cations of the MeCN-bound cationic carbonyls all adopt a similar motif wherein the designed ligands pimq, qmtpm and pmtpm are coordinated in a bidentate fashion. The structures of [Mn(pimq)(CO)$_3$(MeCN)]ClO$_4$, [Mn(qmtpm)(CO)$_3$(MeCN)]ClO$_4$ and [Mn(pmtpm)(CO)$_3$(MeCN)]ClO$_4$ are shown in Figures 4.I.4 – 4.I.6. Three facially coordinated CO ligands force the bidentate ligands and MeCN to occupy different planes in a slightly distorted octahedral geometry.

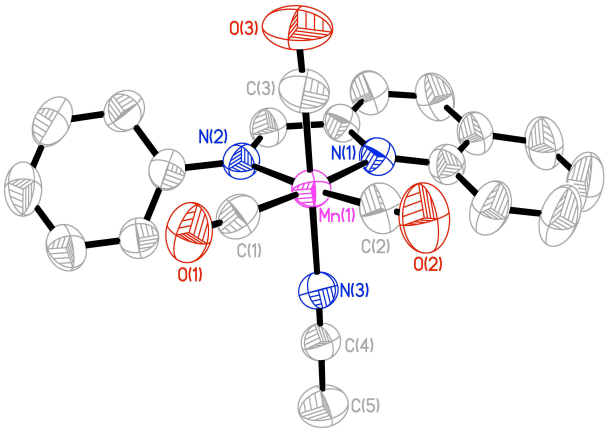

Figure 4.I.4. ORTEP diagram (50% probability level) of the cation of $[Mn(pimq)(CO)_3(MeCN)]ClO_4$. H-atoms have been omitted for clarity.

The Mn(I)-N_{imine} bond distances of $[Mn(pimq)(CO)_3(MeCN)]ClO_4$ and $[Mn(qmtpm)(CO)_3(MeCN)]ClO_4$ (2.053(2) and 2.063(3) Å respectively) are similar to such distances noted in other Mn(I) tricarbonyls featuring bidentate diimine ligands.[9] Also, the Mn(I)-$N_{quinoline}$ bond lengths for $[Mn(pimq)(CO)_3(MeCN)]ClO_4$ and $[Mn(qmtpm)(CO)_3(MeCN)]ClO_4$ (2.126(2) and 2.120(2) Å) compare well with Mn(I) complexes derived from quinoline-containing ligands.[10] These distances are however longer than the Mn(I)-N_{py} bond distance in $[Mn(pmtpm)(CO)_3(MeCN)]ClO_4$ (2.054(2) Å) and confirm the superior coordinating ability of the pyridine N of the pmtpm ligand. In $[Mn(qmtpm)(CO)_3(MeCN)]ClO_4$ and $[Mn(pmtpm)(CO)_3(MeCN)]ClO_4$, the thioether moiety is not coordinated despite the possibility of binding the metal center through displacement of a proximal CO (Figures 4.I.5 and 4.I.6). This presumably arises from the relatively low π-accepting capacity of the thioether S donor compared to CO.

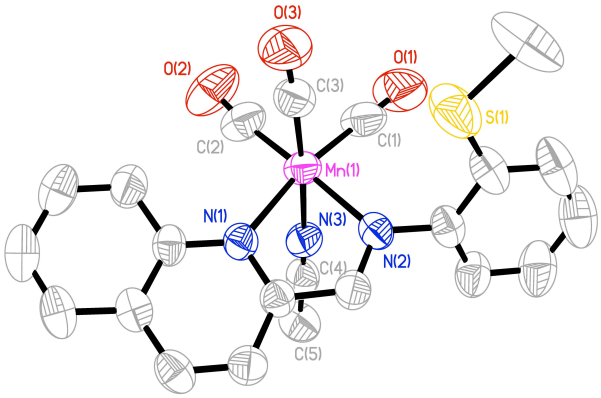

Figure 4.I.5. ORTEP diagram (50% probability level) of the cation of $[Mn(qmtpm)(CO)_3(MeCN)]ClO_4$. H-atoms have been omitted for clarity.

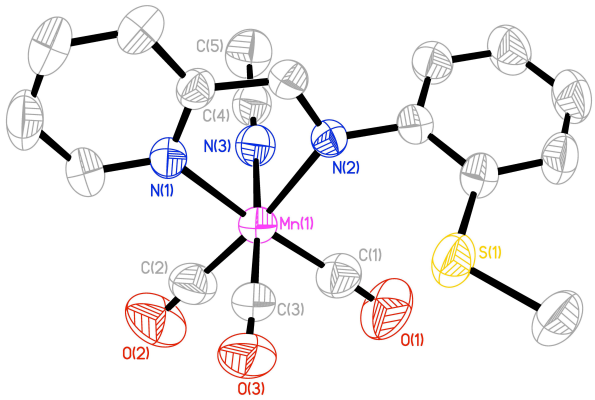

Figure 4.I.6. ORTEP diagram (50% probability level) of the cation of $[Mn(pmtpm)(CO)_3(MeCN)]ClO_4$. H-atoms have been omitted for clarity.

The structure of the neutral carbonyl $[Mn(qmtpm)(CO)_3Br]$ (shown in Figure 4.I.7) is very similar to that of $[Mn(qmtpm)(CO)_3(MeCN)]ClO_4$ except for the replacement of the MeCN ligand with Br^-. The three CO ligands are coordinated in the same facial configuration and the thioether moiety is not coordinated. In $[Mn(qmtpm)(CO)_3Br]$, the Mn(I)-Br distance is 2.5366(6) Å, a value well within the range of Mn(I)-Br distances noted in compounds such as $[BrMn(CO)_2(N,N,N\text{-dapa})]$

[N,N,N-dapa = 2,6-diacetylpyridine-bis(aniline)].[11] The structure of the analogous neutral carbonyl [Mn(pmtpm)(CO)$_3$Br] is shown in Figure 4.I.8.

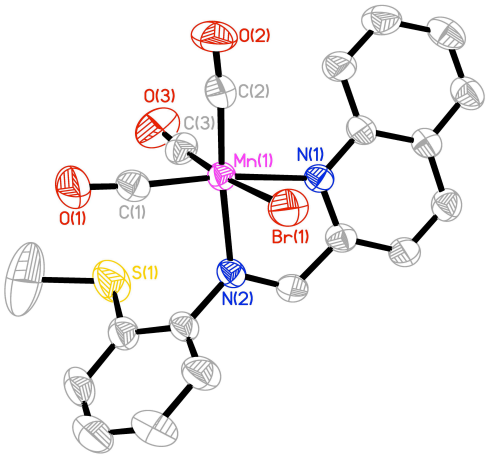

Figure 4.I.7. ORTEP diagram (50% probability level) of [Mn(qmtpm)(CO)$_3$Br]. H-atoms have been omitted for clarity.

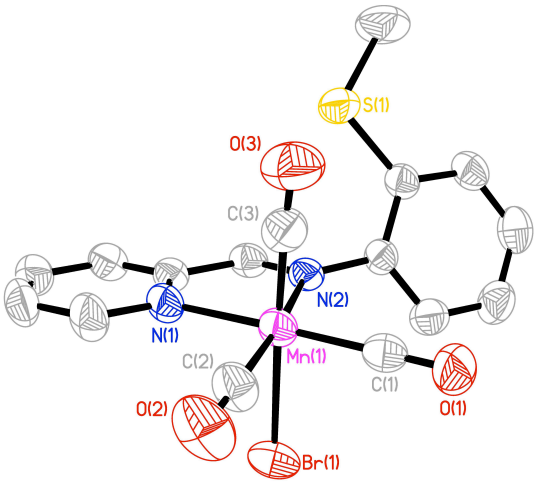

Figure 4.I.8. ORTEP diagram (50% probability level) of [Mn(pmtpm)(CO)$_3$Br]. H-atoms have been omitted for clarity.

4.I.5. Electronic Absorption Spectra and CO Release in Solution

The electronic absorption spectra of all Mn(I) tricarbonyl complexes have been recorded in MeCN, THF and $CHCl_3$. A plot of the respective absorption maxima

(solution in $CHCl_3$) of $Mn(qmtpm)(CO)_3(MeCN)]ClO_4$, $[Mn(qmtpm)(CO)_3Br]$, $[Mn(pmtpm)(CO)_3(MeCN)]ClO_4$ and $[Mn(pmtpm)(CO)_3Br]$ in the visible region is shown in Figure 4.I.9. All absorption spectra were measured in the absence of room light since these carbonyls exhibit facile CO release (vide infra) upon illumination. The effect of increased conjugation in the ligand frame is readily indicated by the *red shift* of the absorption maximum of $Mn(qmtpm)(CO)_3(MeCN)]ClO_4$ (435 nm) compared to that of $[Mn(pmtpm)(CO)_3(MeCN)]ClO_4$ (390 nm). Replacement of the MeCN ligand with the σ–donating Br^- ligand results in *further red shift* of λ_{max} of $[Mn(qmtpm)(CO)_3Br]$ and $[Mn(pmtpm)(CO)_3Br]$ to 535 nm and 500 nm, respectively. Carbonyl complexes $[Mn(pimq)(CO)_3(MeCN)]ClO_4$ and $[Mn(qmtpm)(CO)_3(MeCN)]ClO_4$ exhibit similar absorption profiles with bands

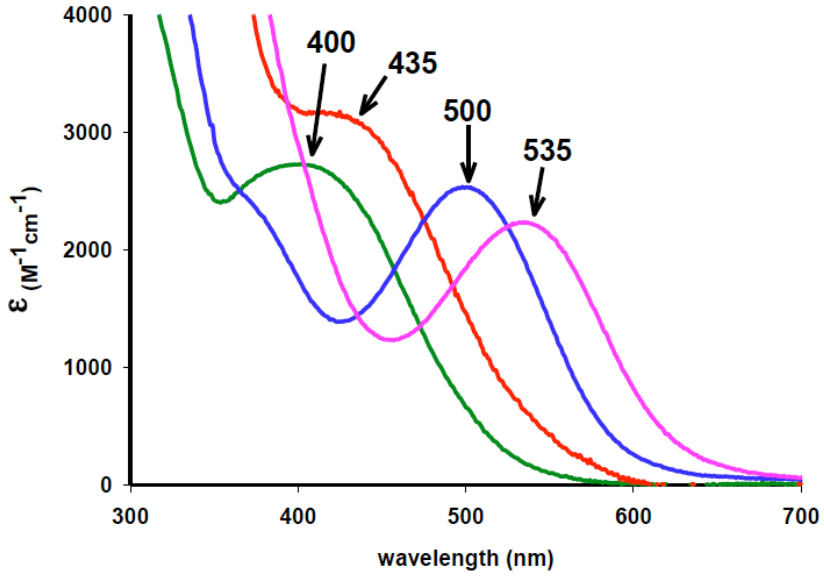

Figure 4.I.9. Electronic absorption spectra of $[Mn(qmtpm)(CO)_3(MeCN)]ClO_4$ (red trace), $[Mn(qmtpm)(CO)_3Br]$ (pink trace), $[Mn(pmtpm)(CO)_3(MeCN)]ClO_4$ (green trace) and $[Mn(pmtpm)(CO)_3Br]$ (blue trace) in $CHCl_3$.

centered at ~ 435, 335 and 265 nm. However, the addition of the –SMe group on the ligand frame leads to a moderate increase in the extinction coefficient of $[Mn(qmtpm)(CO)_3(MeCN)]ClO_4$ compared to $[Mn(pimq)(CO)_3(MeCN)]ClO_4$ (Figure 4.I.10). The high extinction coefficient values for these bands in the 400-600 nm region confirm that they arise from charge transfer transition. Also, the red shift of these bands with more conjugation in the ligand frame (and/or electron-rich ligands or groups in the coordination sphere) readily identifies them as MLCT transition and results of theoretical calculations corroborate this assignment (vide infra).

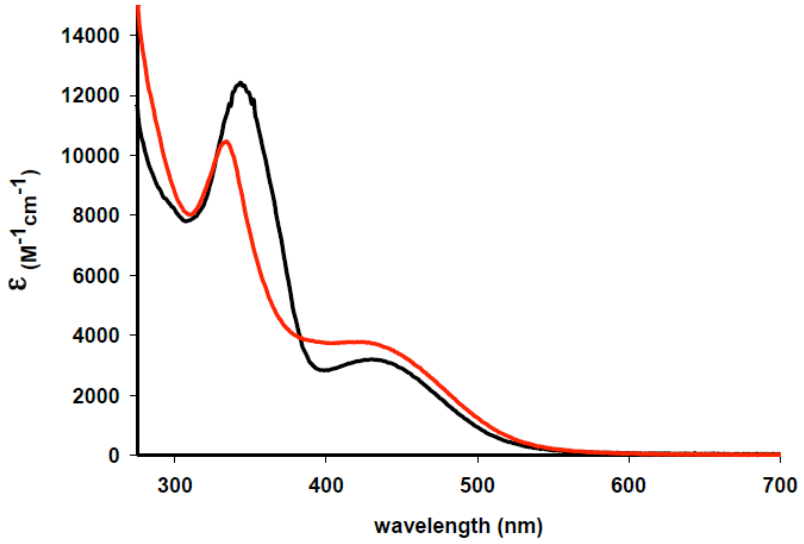

Figure 4.1.10. Electronic absorption spectra of $[Mn(pimq)(CO)_3(MeCN)]ClO_4$ (black trace) and $[Mn(qmtpm)(CO)_3(MeCN)]ClO_4$ (red trace) in MeCN.

Although solutions of $[Mn(pimq)(CO)_3(MeCN)]ClO_4$, $[Mn(qmtpm)(CO)_3(MeCN)]ClO_4$ and $[Mn(pmtpm)(CO)_3(MeCN)]ClO_4$ in MeCN or MeOH are stable for several hours in the dark, exposure of such solutions to low power visible light leads to dramatic changes associated with CO release. Changes in the absorption spectrum of $[Mn(qmtpm)(CO)_3(MeCN)]ClO_4$ upon illumination with

509 nm monochromatic light (5mW) are shown in Figure 4.I.11. Clean isosbestic points 500, 400 and 335 nm confirm that CO loss does not proceed via decomposition. Likewise, THF solutions of [Mn(qmtpm)$(CO)_3$Br] and [Mn(pmtpm)$(CO)_3$Br] exhibit stability in the dark and CO release is only triggered upon illumination with 509 nm light. Isosbestic points for [Mn(qmtpm)$(CO)_3$Br] were noted at 415 nm and 290 nm.

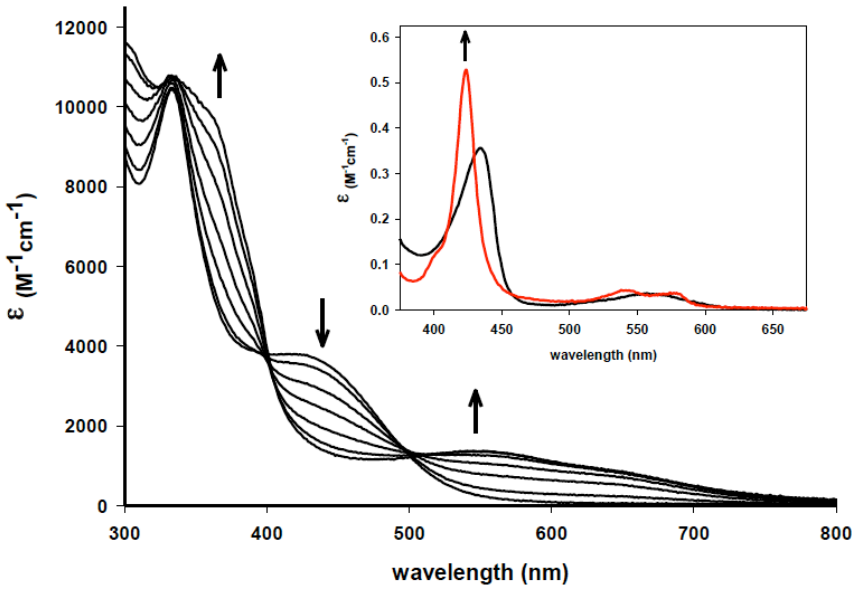

Figure 4.I.11. Changes in the electronic absorption spectrum of [Mn(qmtpm)$(CO)_3$(MeCN)]ClO_4 in MeCN upon exposure to monochromatic light (λ= 509 nm, 5mW). Inset: Formation of CO-Mb with light induced CO release from [Mn(qmtpm)$(CO)_3$(MeCN)]ClO_4 in 100 mM phosphate buffer (pH 7.4).

Light-induced CO release of these Mn(I) tricarbonyl complexes has been investigated by a modified myoglobin assay. In a typical experiment, MeCN or THF solutions of the selected Mn(I) carbonyl complex were degassed and subsequently irradiated with a broadband light source fitted with a 400 nm cut-off filter. The resulting solution was flushed with N_2 gas and the photogenerated CO was transferred

via a cannula into a cuvette containing reduced myoglobin (Mb) in phosphate buffer (pH 7.4). In this method the possibility of carbonyl reduction by dithionite is eliminated.[12] In all cases, a shift in the Soret band from 435 nm to 424 nm confirmed the formation of CO-Mb under anaerobic conditions (Figure 4.I.11 Inset). Because CO release takes place only upon light irradiation it is evident that these compounds comprise *an effective set of Mn-based photoCORMs*.

Although the present carbonyls contain three CO ligands, we have not determined the exact number of CO molecules lost from each photoCORM under illumination. Ford and coworkers have commented on this issue in their work with the photoCORM $Na_3[W(CO)_5(TPPTS)]$. Exhaustive photolysis of this carbonyl afforded product(s) that still exhibited CO-related IR bands in its spectrum.[13] In our work, we have also noted that the exact amount of CO release from the photoCORMs upon illumination is quite difficult to quantify due to subsequent secondary reaction(s) of the initial photoproduct(s) with the oxygen, solvent and other species in solution. Under strict anaerobic conditions, prolonged photolysis of the present carbonyls in solvents like MeCN and THF afford products that exhibit weak CO stretching frequencies in the 2050-1950 cm^{-1} region. NMR measurements on these products indicated the presence of the intact ligand frames. When the photolysis experiments were performed with solutions in open vials, the final photoproducts exhibited strong EPR signals indicating formation of Mn(II) species. In a recent account, Kurt and Berends have reported the formation of both Mn(II) and Mn(III) species in photolysis of the photoCORM *fac*-$[Mn(CO)_3(tpm)]PF_6$ (tpm = tris(pyrazolyl)methane) under

aerobic conditions.[14] Clearly, CO release from CORMs bearing multiple CO ligands follow complicated pathways leading to multiple photoproducts and hence we have not attempted to characterize the photoproducts from all Mn carbonyl complexes in the present study.

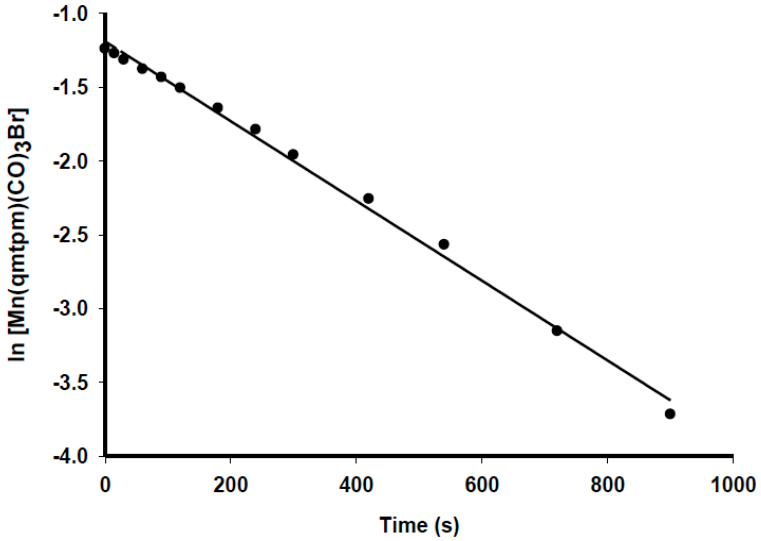

Figure 4.I.12. Plot of changes in ln[Mn(qmtpm)$(CO)_3$Br] vs. time (in s) in THF (concentration of Mn(qmtpm)$(CO)_3$Br = 1.1 mM).

The CO release capacities of [Mn(pimq)$(CO)_3$(MeCN)]ClO_4, [Mn(qmtpm)$(CO)_3$(MeCN)]ClO_4, [Mn(qmtpm)$(CO)_3$Br], [Mn(pmtpm)$(CO)_3$(MeCN)]ClO_4 and [Mn(pmtpm)$(CO)_3$Br] under illumination with visible light have been determined in the present study to correlate the CO-releasing parameters with the features of the ligand (such as conjugation) and the nature of the sixth ligand (MeCN vs. Br^-). For all these carbonyls, the rates of CO release obey a pseudo-first-order behavior (Figure 4.I.12). The apparent rates of CO photorelease (k_{CO}) and the quantum yield values at 509 nm (ϕ_{509}) are shown in Table 4.I.1. The k_{CO} values of [Mn(pimq)$(CO)_3$(MeCN)]ClO_4, [Mn(qmtpm)$(CO)_3$(MeCN)]ClO_4 and

$[Mn(pmtpm)(CO)_3(MeCN)]ClO_4$ were measured in CH_3CN, while those of $[Mn(qmtpm)(CO)_3Br]$ and $[Mn(pmtpm)(CO)_3Br]$ were obtained with THF solutions due to differences in solubility. As evident from Table 4.I.1, with increased conjugation in the ligand frame (going from $[Mn(pmtpm)(CO)_3(MeCN)]ClO_4$ to $[Mn(qmtpm)(CO)_3(MeCN)]ClO_4$), the k_{CO} value increases from 1.1 x 10^{-3} ± 0.1 to 2.0 x 10^{-3} ± 0.1 s^{-1}. In addition, replacement of MeCN with Br^- (going from $[Mn(qmtpm)(CO)_3(MeCN)]ClO_4$ to $[Mn(qmtpm)(CO)_3Br]$) leads to a significant increase in the k_{CO} value (from 2.0 x 10^{-3} ± 0.1 to 2.6 x 10^{-3} ± 0.1 s^{-1}). The effect(s) of incorporating the –SMe group on the ligand frame is evident in the k_{CO} and ϕ_{509} values of $[Mn(pimq)(CO)_3(MeCN)]ClO_4$ and $[Mn(qmtpm)(CO)_3(MeCN)]ClO_4$. The electron-rich S center enhances the ϕ_{509} value of $[Mn(qmtpm)(CO)_3(MeCN)]ClO_4$ (0.208 ± 0.010) compared to $[Mn(pimq)(CO)_3(MeCN)]ClO_4$ (0.130 ± 0.010) to a noticeable extent. Collectively, these correlations support our previous finding related to increased CO photolability with greater conjugation in the ligand frame.[15] In addition, the present results suggest that the ancillary ligands (like Br^-) can also influence the extent of CO photorelease. Since the –SMe donor is not coordinated to the Mn(I) center in $Mn(qmtpm)(CO)_3(MeCN)]ClO_4$, $[Mn(qmtpm)(CO)_3Br]$, $[Mn(pmtpm)(CO)_3(MeCN)]ClO_4$ and $[Mn(pmtpm)(CO)_3Br]$, it is not immediately evident why such modification of the ligand frames (as shown in Figure 4.I.2) affects the CO photolability of these photoCORMs. The results of DFT and TDDFT calculations, as described below, however provide valuable insight into the origins of such enhancement of CO photorelease in $[Mn(qmtpm)(CO)_3(MeCN)]ClO_4$,

[Mn(qmtpm)(CO)$_3$Br], [Mn(pmtpm)(CO)$_3$(MeCN)]ClO$_4$ and [Mn(pmtpm)(CO)$_3$Br] (compared to [Mn(pimq)(CO)$_3$(MeCN)]ClO$_4$).

Table 4.I.1. Apparent Rates of CO release (k_{CO}) and associated quantum yield values at 509 nm (ϕ_{509}) of [Mn(pimq)(CO)$_3$(MeCN)]ClO$_4$, [Mn(qmtpm)(CO)$_3$(MeCN)]ClO$_4$, [Mn(qmtpm)(CO)$_3$Br], [Mn(pmtpm)(CO)$_3$(MeCN)]ClO$_4$ and [Mn(pmtpm)(CO)$_3$Br].

Compound	**Apparent Rate (s^{-1})** (concentration = 1.10 mM)	**Quantum Yield**
[Mn(pimq)(CO)$_3$(MeCN)]ClO$_4$ (solv: MeCN)	1.4 x 10^{-3} ± 0.1	0.130 ± 0.010
[Mn(qmtpm)(CO)$_3$(MeCN)]ClO$_4$ (solv: MeCN)	2.0 x 10^{-3} ± 0.1	0.208 ± 0.010
[Mn(qmtpm)(CO)$_3$Br] (solv: THF)	2.6 x 10^{-3} ± 0.1	0.370 ± 0.010
[Mn(pmtpm)(CO)$_3$(MeCN)]ClO$_4$ (solv: MeCN)	1.1 x 10^{-3} ± 0.1	0.116 ± 0.010
[Mn(pmtpm)(CO)$_3$Br] (solv: THF)	2.1 x 10^{-3} ± 0.1	0.340 ± 0.010

4.I.6. DFT and TDDFT Calculations.

In order to understand how the structural features of these photoCORMs correlate with their capacities for CO photorelease, Samantha Carrington, a graduate student in our group performed DFT and TDDFT calculations. With the crystal structures at hand, the optimized geometries, molecular orbital electron densities, and calculated electronic transitions for [Mn(pimq)(CO)$_3$(MeCN)]ClO$_4$,

$[Mn(qmtpm)(CO)_3(MeCN)]ClO_4$, $[Mn(qmtpm)(CO)_3Br]$, $[Mn(pmtpm)(CO)_3(MeCN)]ClO_4$ and $[Mn(pmtpm)(CO)_3Br]$ were obtained with the use of the hybrid functional B3LYP. All the DFT optimized structures show good agreement with the bond lengths and bond angles observed in the corresponding crystal structure of each complex. A comparison of the X-ray versus DFT optimized bond distances and angles for $[Mn(qmtpm)(CO)_3(MeCN)]ClO_4$ and $[Mn(qmtpm)(CO)_3Br]$ are listed in Table 4.I.2 as an example. The agreement supports the theoretical treatment of the molecules and allowed us to continue on with the TDDFT calculations.

The calculated electronic transitions with oscillator strengths above 0.004 were collected and those with energies falling within the range of the lowest energy experimental absorption band of each complex are presented in Table 4.I.3. For $[Mn(pimq)(CO)_3(MeCN)]ClO_4$, transitions of interest are the HOMO→LUMO (431 nm), HOMO-1→LUMO (406 nm), and HOMO-2→LUMO (388 nm). These correlate to the broad band observed at 430 nm for $[Mn(pimq)(CO)_3(MeCN)]ClO_4$. In case of $[Mn(qmtpm)(CO)_3(MeCN)]ClO_4$, HOMO→LUMO (533 nm), HOMO-1→LUMO (459 nm), combination orbital HOMO-2/HOMO-3→LUMO (432 nm) and HOMO-3→LUMO (417 nm) all fall under the experimental band at 435 nm. Similarly, the theoretical transitions HOMO→LUMO (520 nm), HOMO-1→LUMO (484 nm), HOMO-2→LUMO (460 nm) correlate to the 535 nm band observed experimentally for $[Mn(qmtpm)(CO)_3Br]$ while the 390 nm experimental band of $[Mn(pmtpm)(CO)_3(MeCN)]ClO_4$ corresponds to HOMO→LUMO (484 nm), HOMO-

2→LUMO (372 nm), and HOMO-4→LUMO (346 nm) transitions. And finally, the experimental band at 500 nm of [Mn(pmtpm)$(CO)_3$Br] includes the theoretical transitions HOMO→LUMO (491 nm) and HOMO-2→LUMO (446 nm). Because these calculated transitions fall within the region of wavelengths that was employed to determine the capacity of CO photolability (as described above), we have examined the electron densities of the molecular orbitals that comprise these levels and check whether these transitions do labilize CO ligand(s) from these designed carbonyls.

Table 4.I.2. Selected bond distances (Å) and angles (deg) of [Mn(qmtpm)$(CO)_3$(MeCN)] ClO_4 and [Mn(qmtpm)$(CO)_3$Br] along with optimized DFT bond distances and bond angles for comparison.

	[Mn(qmtpm)$(CO)_3$(MeCN)] ClO_4		[Mn(qmtpm)$(CO)_3$Br]	
	X-ray	**DFT**	**X-ray**	**DFT**
Mn-N1	2.120(2)	2.163	2.106(2)	2.166
Mn-N2	2.063(3)	2.093	2.059(2)	2.088
Mn-N3	2.013(3)	2.045	—	—
Mn-Br	—	—	2.536(6)	2.586
Mn-C1	1.810(4)	1.831	1.800(4)	1.820
Mn-C2	1.831(4)	1.823	1.804(3)	1.824
Mn-C3	1.803(4)	1.852	1.790(4)	1.804
C1-Mn-C2	86.82(18)	89.07	86.11(14)	88.12
C1-Mn-C3	91.09(17)	97.25	89.42(15)	92.47
C1-Mn-N2	91.75(15)	92.05	94.18(12)	93.25
C1-Mn-N3	91.68(15)	90.05	—	—
C2-Mn-C3	87.95(18)	96.14	89.48(14)	92.81
C2-Mn-N1	102.79(14)	99.21	101.07(12)	100.18
C2-Mn-N3	89.43(14)	85.77	—	—
C3-Mn-N1	92.62(13)	84.85	91.68(12)	91.04
C3-Mn-N2	98.73(14)	94.14	100.17(12)	100.16
C1-Mn-Br	—	—	91.31(11)	89.97
C2-Mn-Br	—	—	84.81(10)	82.30

Table 4.I.3. Energies (E, nm) and oscillator strengths (*f*) of the calculated (TDDFT) electronic transitions with the molecular orbitals involved with each transition.[a] Only transitions with energies corresponding to the lowest energy absorption band observed experimentally for each complex are shown.

Energy (nm)	**Oscillator Strength (f)**	**Transitions**
		[Mn(pimq)(CO)$_3$(MeCN)]ClO$_4$
431.98	0.0259762	π(Q)- π(Ph)- π(MnCO)→ π(Q)- π(SB)[HOMO→LUMO]
406.74	0.0573702	π(Q)- π(Ph)-d_{xz}(Mn)→ π(Q)- π(SB)[HOMO-1→LUMO]
388.95	0.0307494	π(MnCO)- π(Ph)→ π(Q)- π(SB)[HOMO-2→LUMO]
		[Mn(qmtpm)(CO)$_3$(MeCN)]ClO$_4$
533.21	0.0450962	π(PhS) →π(Q)-π(SB)[HOMO→LUMO]
459.29	0.0122483	π(MnCO)-π(Q)→π(Q)-π(SB)[HOMO-1→LUMO]
432.41	0.0189162	π(MnCO)-π(Q)→π(Q)-π(SB)[HOMO-2/HOMO-3→LUMO]
417.86	0.0334093	π(MnCO)-π(Q)→π(Q)-π(SB)[HOMO-2→LUMO]
		[Mn(qmtpm)(CO)$_3$Br]
520.47	0.0046467	π(PhS)→ π(Q)- π(SB)[HOMO→LUMO]
484.31	0.0166749	p(Br)- π(MnCO)→ π(Q)- π(SB)[HOMO-1→LUMO]
460.92	0.0533586	p(Br)- π (MnCO)→ π(Q)- π(SB)[HOMO-2→LUMO]
		[Mn(pmtpm)(CO)$_3$(MeCN)]
484.60	0.0301023	π(PhS)→π(Pyr)−π(SB)[HOMO→LUMO]
372.72	0.0491039	π(MnCO)→π(Pyr)−π(SB)[HOMO-2→LUMO]
346.30	0.0606618	π(MnCO)-π(PhS)→π(Pyr)−π(SB)[HOMO-4→LUMO]

	[Mn(pmtpm)(CO)$_3$Br]	
491.25	0.0061503	π(PhS)→ π(Pyr)- π(SB)[HOMO→LUMO]
446.20	0.0241548	π(MnCO)-p(Br)→ π(Pyr)- π(SB)[HOMO-2→LUMO]

[a] Orbitals with greater contributions listed first

The molecular orbital (MO) energy diagram, shown in Figure 4.I.13, displays the compositions of the three lowest occupied MOs and the LUMO of [Mn(pimq)(CO)$_3$(MeCN)]ClO$_4$, [Mn(pmtpm)(CO)$_3$Br], [Mn(qmtpm)(CO)$_3$Br], and [Mn(qmtpm)(CO)$_3$(MeCN)]ClO$_4$. The first and foremost point to note is that in each photoCORM, the lowest energy band corresponds to transitions that promote electron density from HOMO-2 (predominantly Mn-CO bonding character) to the LUMO mostly comprised of the imine functionality and pyridine or quinoline ring. These MLCT transitions therefore shift electron density from the metal center to the ligand π frame, an event that is expected to curb the affinity of the Mn center toward CO (due to loss of π-backdonation from the metal). The CO photolability of the present photoCORMs observed at ~500 nm strongly suggests that these MLCT transitions are responsible for the observed CO photolability.

As one goes from [Mn(pmtpm)(CO)$_3$Br] to [Mn(qmtpm)(CO)$_3$Br], the change of the pyridine ring to more conjugated quinoline lowers the LUMO level and moves the λ_{max} from 500 to 535 nm. It is therefore evident that enhanced conjugation in the ligand frame sensitizes the resulting photoCORM more to the visible light. Inclusion of the electron-rich Br^- ligand raises both the HOMO-1 and HOMO-2 levels of

[Mn(qmtpm)$(CO)_3$Br] and [Mn(pmtpm)$(CO)_3$Br] (both these MOs include contribution from Br^-, Table 4.I.3) compared to the MeCN-bound carbonyls. As a consequence, the MLCT transitions in the visible range are all red shifted (Figure 4.1.13). This finding explains the red shift of these two photoCORMs (535 and 500 nm respectively) compared to [Mn(pimq)$(CO)_3$(MeCN)]ClO_4 (430 nm), [Mn(qmtpm)$(CO)_3$(MeCN)]ClO_4 (435 nm) and [Mn(pmtpm)$(CO)_3$(MeCN)]ClO_4 (390 nm).

Although the –SMe group on the ligand frame does not participate in coordination in [Mn(qmtpm)$(CO)_3$(MeCN)]ClO_4, [Mn(pmtpm)$(CO)_3$(MeCN)]ClO_4, [Mn(qmtpm)$(CO)_3$Br], and [Mn(pmtpm)$(CO)_3$Br], the HOMO of each of these carbonyls is comprised of orbitals belonging to the phenyl ring and the sulfur atom (Figure 4.I.13 and Table 4.I.3). Thus the HOMO→LUMO transition is an intra-ligand charge transfer that promotes electron density from the phenyl thioether moiety of the ligand frame to a MO associated mostly with the imine and the corresponding pyridine or quinoline functionality. A close scrutiny of the energy diagram however reveals that the absence of –SMe unit in [Mn(pimq)$(CO)_3$(MeCN)]ClO_4 lowers the energy of the HOMO (consisting mostly of π(Ph) and π(Q) character) and leads to a slight blue shift of the low energy band (430 nm) compared to the analogous carbonyl [Mn(qmtpm)$(CO)_3$(MeCN)]ClO_4 with –SMe unit on the ligand frame (435 nm).

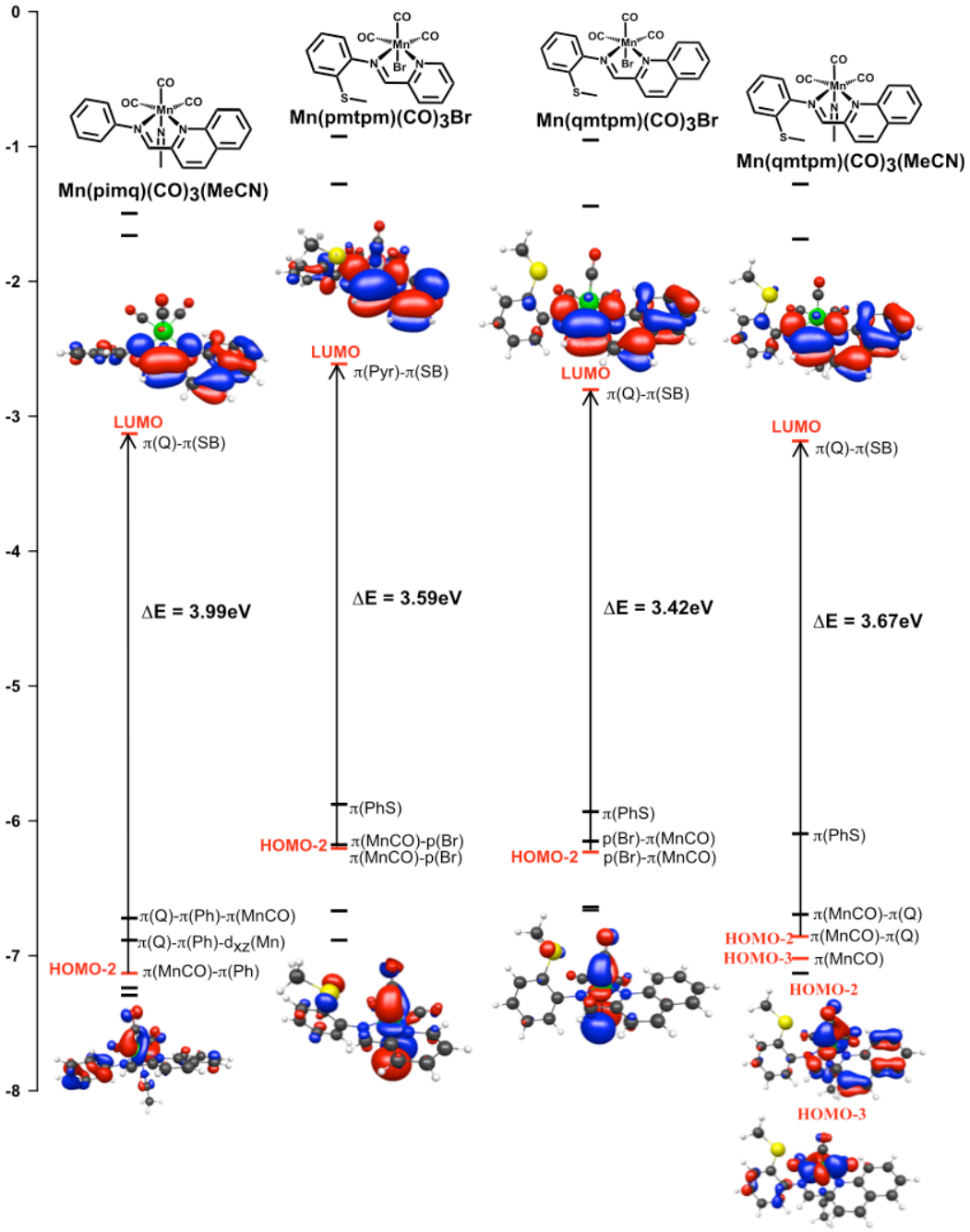

Figure 4.I.13. Calculated HOMO/LUMO energy diagram of complexes $[Mn(pimq)(CO)_3(MeCN)]ClO_4$, $[Mn(pmtpm)(CO)_3Br]$, $[Mn(qmtpm)(CO)_3Br]$, and $[Mn(qmtpm)(CO)_3(MeCN)]ClO_4$ (from left to right). The most prominent MOs involved with transitions under the low energy band and their diagrams are shown. Transitions discussed in the text are shown in red (all other orbitals in TDDFT calculations are labeled in black).

In addition, inclusion of the –SMe unit on the ligand frame enhances both the apparent rate of CO release and the ϕ_{509} value of $[Mn(qmtpm)(CO)_3(MeCN)]ClO_4$ compared to $[Mn(pimq)(CO)_3(MeCN)]ClO_4$ (Table 4.I.1). Since in all the present carbonyls the HOMO→LUMO transition contributes to the low energy band, it appears that the –SMe group enhances the overall CO photolability of $[Mn(qmtpm)(CO)_3(MeCN)]ClO_4$, $[Mn(pmtpm)(CO)_3(MeCN)]ClO_4$, $[Mn(qmtpm)(CO)_3Br]$, and $[Mn(pmtpm)(CO)_3Br]$ presumably through higher absorption of light in the visible region.

Taken together, the results of the theoretical calculations support the hypotheses that guided our design principles. For example, it is evident that low energy MLCT transitions arising from MOs with metal-CO bonding character to MOs associated with the π-frame of the ligand could lead to scission of the Mn-CO bond(s) in the present photoCORMs upon exposure to visible light. Increase in the CO photolability with more conjugated ligand frames further corroborates this conclusion. Baerends and Rosa have discussed the role of ligand-field and charge-transfer excited states in the photochemical dissociation of metal-CO bonds in metal carbonyls derived from α-diimine ligands.[16] The low energy MLCTs in such carbonyls also play key roles in the CO dissociation pathways. The results of the present work further indicate that inclusion of electron-rich functionality on ligands could enhance the CO photolability. In addition, ancillary ligands such as Br^- significantly augment the sensitivity of the designed photoCORMs toward the visible light. More rigorous

theoretical studies to establish the details of the mechanism of CO dissociation arising from the MLCT transition(s) are in progress in this laboratory.

4.I.7. Experimental Section

General Procedures. All experimental manipulations were performed under anaerobic conditions using standard Schlenk techniques and under limited light conditions. Manganese pentacarbonyl bromide ($[Mn(CO)_5Br]$) was purchased from Alfa Aesar. The ligands 2-pyridyl-*N*-(2'-methylthiophenyl)methyleneimine (pmtpm)[5] and 2-quinoline-*N*-(2'-methylthiophenyl) methyleneimine (qmtpm)[4] and the starting salt, *fac*-$[Mn(CO)_3(MeCN)_3](ClO_4)$[17] were synthesized following published procedures. Solvents were purified and/or dried by standard techniques prior to use.

Caution! Transition metal perchlorates should be prepared in small quantities and handled with great caution as metal perchlorates may explode upon heating.

2-(phenyliminomethyl)quinoline (**pimq**). The synthesis and purification of pimq were modified to some extent compared to the procedure reported by Hamer.[18] Aniline (0.80 g, 8.60 mmol) was dissolved in 15 mL of MeOH followed by the addition of quinoline-2-carboxaldehyde (1.23 g, 7.81 mmol) in 15 mL of MeOH. The mixture was heated to reflux for 12 h, after which the solvent was removed under reduced pressure to obtain an orange-red oil. Upon addition of 30 mL of Et_2O and rapid scratching, the product separated as an orange powder. The solid was filtered and dried in vacuo (0.69 g, 60% yield). ^1H NMR (CD_3CN, 500 MHz), δ (ppm from

TMS): 8.74 (s, 1H), 8.37 (d, 1H), 8.30 (d, 1H), 8.12 (d, 1H), 7.98 (d, 1H), 7.80 (t, 1H), 7.66 (t, 1H), 7.47 (t, 2H), 7.38 (d, 2H), 7.33 (t, 1H).

[Mn(pimq)(CO)$_3$(MeCN)]ClO$_4$. A batch of [Mn(CO)$_3$(MeCN)$_3$]ClO$_4$ (0.378 g, 0.97 mmol) was added to a degassed solution of pimq (0.225 g, 0.97 mmol) in 25 mL of $CHCl_3$. The clear yellow orange color of the solution deepened to red brown upon reflux under N_2 atmosphere. After 6 h, the solvent was removed under reduced pressure and the residue was triturated three times with Et_2O to obtain a red orange powder (0.364 g, 90% yield). Slow diffusion of pentane into a dichloromethane solution of [Mn(pimq)(CO)$_3$(MeCN)]ClO$_4$ afforded red blade-like crystals suitable for X-ray studies. Anal. Calcd. for $C_{21}H_{15}ClMnN_3O_7$: C, 49.28; H, 2.93; N, 8.21. Found: C, 49.26; H, 2.87; N, 8.27. Electronic absorption spectrum in MeCN, λ_{max} (nm) [(ε ($M^{-1}cm^{-1}$)]: 430 (3200), 345 (12 760), 260 (27 330). Selected IR frequencies (KBr disk, cm^{-1}): 2044 (s, ν_{CO}), 1970 (s, ν_{CO}), 1947 (s, ν_{CO}), 1593 (m), 1515 (m), 1374 (w), 1092 (s, ν_{ClO4}), 837 (w), 750 (m), 623 (s), 529 (w). ^{1}H NMR (CD_3CN, 500 MHz), δ (ppm from TMS): 9.00 (s, 1H), 8.82 (dd, 2H), 8.20 (dd, 2H), 8.12 (t, 1H), 7.92 (t, 1H), 7.62 (t, 2H), 7.56 (t, 3H).

[Mn(qmtpm)(CO)$_3$(MeCN)]ClO$_4$. To a degassed solution of qmtpm (0.153 g, 0.55 mmol) in 25 mL of $CHCl_3$ was added a batch of [Mn(CO)$_3$(MeCN)$_3$]ClO$_4$ (0.200 g, 0.55 mmol) and the solution was heated to reflux under N_2 for 6 h. Solvent removal and subsequent trituration with Et_2O afforded [Mn(qmtpm)(CO)$_3$(MeCN)]ClO$_4$ as a brick red solid. (0.269 g, 88% yield). X-ray quality crystals (red orange plates) were grown by via diffusion of pentane into a CH_2Cl_2 solution of

[Mn(qmtpm)$(CO)_3$(MeCN)]ClO_4. Anal. Calcd. for $C_{22}H_{17}ClMnN_3O_7S$: C, 47.37; H, 3.07; N, 7.53. Found: C, 47.26; H, 3.10; N, 7.57. Electronic Absorption Spectrum in MeCN, λ_{max} (nm) [ε ($M^{-1}cm^{-1}$)]: 435 (3 680), 335 (10 400), 260 (33 670). Selected IR frequencies (KBr disk, cm^{-1}): 2046 (s, ν_{CO}), 1943 (s, ν_{CO}), 1516 (w), 1438 (w), 1094 (s, ν_{ClO4}), 822 (w), 750 (w), 623 (m). ^{1}H NMR (CD_3CN, 500 MHz), δ (ppm from TMS): 8.97 (s, 1H), 8.82 (t, 2H), 8.20 (t, 2H), 8.12 (t, 1H), 7.91 (t, 1H), 7.55 (d, 1H), 7.49 (t, 1H), 7.38 (t, 1H), 7.27 (s, 1H), 2.52 (s, 3H).

[Mn(qmtpm)$(CO)_3$Br]. A batch of [Mn$(CO)_5$Br] (0.112 g, 0.41 mmol) was added to a degassed solution of qmtpm (0.113 g, 0.41 mmol) in 20 mL of $CHCl_3$. The solution developed a deep reddish purple hue upon reflux under N_2 atmosphere. After 4 h, the solvent was removed in vacuo and the residue was triturated three times with Et_2O to obtain a red purple powder (0.219 g, 80% yield). Slow diffusion of pentane into a CH_2Cl_2 solution of [Mn(qmtpm)$(CO)_3$Br] afforded red plates suitable for X-ray studies Anal. Calcd. for $C_{20}H_{14}BrMnN_2O_3S$: C, 48.31; H, 2.84; N, 5.63. Found: C, 48.24; H, 2.87; N, 5.52. Electronic Absorption Spectrum in $CHCl_3$, λ_{max} (nm) [ε ($M^{-1}cm^{-1}$)]: 535 (2 235), 335 (9 050), 255 (26 710). Selected IR frequencies (KBr disk, cm^{-1}): 2022 (s, ν_{CO}), 1920 (s, ν_{CO}), 1514 (w), 1434 (w), 1262 (s, ν_{ClO4}), 828 (w), 752 (w), 680 (w).

[Mn(pmtpm)$(CO)_3$(MeCN)]ClO_4. This complex was synthesized by following the procedure that afforded [Mn(qmtpm)$(CO)_3$(MeCN)]ClO_4 (as described above). A batch of 0.148 g of pmtpm (0.65 mmol) and 0.236 g (0.65 mmol) of

$[Mn(CO)_3(MeCN)_3]ClO_4$ afforded 0.269 g (82% yield) of the product as a yellow orange powder. Orange blades suitable for X-ray studies were grown by diffusion of pentane into a CH_2Cl_2 solution of $[Mn(pmtpm)(CO)_3(MeCN)]ClO_4$. Anal. Calcd. for $C_{18}H_{12}ClMnN_3O_7S$: C, 42.83; H, 2.40; N, 8.32. Found: C, 42.80; H, 2.46; N, 8.25. Electronic Absorption Spectrum in MeCN, λ_{max} (nm) [ε ($M^{-1}cm^{-1}$)]: 390 (3 620), 270 (17 000). Selected IR frequencies (KBr disk, cm^{-1}): 2042 (s, ν_{CO}), 1945 (s, ν_{CO}), 1592 (w), 1470 (w), 1437 (w), 1307 (w), 1091 (s ν_{ClO4}), 768 (m) 623 (m). ^1H NMR (CD_3CN, 500 MHz), δ (ppm from TMS): 9.18 (d, 1H), 8.72 (s, 1H), 8.27 (t, 1H), 8.20 (d, 1H), 7.86 (t, 1H), 7.56 (d, 1H), 7.48 (t, 1H), 7.38 (t, 1H), 7.24 (s, 1H), 2.55 (s, 3H).

[Mn(pmtpm)(CO)$_3$Br]. This complex was synthesized by following the procedure that afforded $[Mn(qmtpm)(CO)_3Br]$ (as described above). A batch of 0.151 g (0.55 mmol) of $[Mn(CO)_5Br]$ and 0.125 g (0.55 mmol) of pmtpm afforded 0.257 g (47% yield) of $[Mn(pmtpm)(CO)_3Br]$ as an orange powder. Slow diffusion of pentane into a CH_2Cl_2 solution of $[Mn(pmtpm)(CO)_3Br]$ afforded red orange plates suitable for X-ray studies. Anal. Calcd. for $C_{16}H_{12}BrMnN_2O_3S$: C, 42.97; H, 2.70; N, 6.26. Found: C, 43.00; H, 2.66; N, 6.20. Electronic Absorption Spectrum in $CHCl_3$, λ_{max} (nm) [ε ($M^{-1}cm^{-1}$)]: 500 (2 530), 380 (2 280), 315 (5 800), 285 (11 260). Selected IR frequencies (KBr disk, cm^{-1}): 2023 (s, ν_{CO}), 1934 (s, ν_{CO}), 1607 (w), 1468 (w), 1303 (w), 775 (w) 680 (w), 627 (w) 514 (w).

Physical Measurements. The ^{1}H NMR spectra were recorded at 298 K on a Varian Unity Inova 500 MHz instrument. A Perkin-Elmer Spectrum-One FT-IR was employed to monitor the FTIR spectra of the compounds. Electronic absorption spectra were obtained with a Varian Cary 50 Spectrophotometer. Room temperature magnetic susceptibility measurements were performed with the aid of a Johnson Matthey magnetic susceptibility balance.

Photolysis Experiments. For continuous wave photolysis experiments, a Newport Oriel Apex Illuminator (150W Xenon lamp) equipped with an Oriel 1/8 m Cornerstone monochromator (measured power 146-150 mW) was used as the light source. Standard ferrioxalate actinometry was performed to calibrate the light source at 509 nm (ϕ_{509}).[20] Samples of were prepared under dim light conditions and placed in 2 x 10 mm quartz cuvettes positioned 2 cm away from the light source.

Due to differences in solubilities, the quantum yields (ϕ) of CO release for $[Mn(pimq)(CO)_3(MeCN)]ClO_4$ (430 nm), $[Mn(qmtpm)(CO)_3(MeCN)]ClO_4$ and $[Mn(pmtpm)(CO)_3(MeCN)]ClO_4$ were measured in MeCN (1.10 mM), while that of $[Mn(qmtpm)(CO)_3Br]$, $[Mn(pmtpm)(CO)_3Br]$ were measured in THF (1.10 mM). Solutions were prepared to ensure sufficient absorbance (> 90%) at the irradiation wavelength (509 nm) and changes in the electronic spectra in the 350-550 nm region (< 10% photolysis) were used to determine the extent of CO release. Each sample was irradiated with the monochromatic light (power: 5 mW) at defined time intervals. Changes in the respective charge transfer bands of all complexes were monitored along the 2 mm path.

The apparent rates of photolysis were monitored at an appropriate wavelength for each carbonyl and the absorbance versus time plots were fitted to a three parameter exponential equation $A(t) = A_\infty + (A_o - A_\infty) \exp\{-k_{CO}t\}$, where A_o and A_∞ are the initial and final absorbance values, respectively. The apparent rate of CO loss (k_{CO}) was calculated from the ln(C) versus time (T) plot for each carbonyl.

X-ray Crystallography. Diffraction data for all complexes were collected at 296 K on a Bruker APEX-II instrument using monochromated Mo-K_α radiation (λ = 0.71073 Å). All data were corrected for absorption and the structures were solved by direct methods using SHELXTL (1995-99) software package (Bruker Analytical X-ray Systems Inc.).

DFT and TDDFT Calculations. Density functional theory (DFT) and time dependent density functional theory (TDDFT) studies were executed with PC-GAMESS program[22] using the hybrid functional B3LYP. Optimizations for the Mn atom were performed by employing the LANL2DZ basis set and effective core potential (ECP). The Pople 6-311G* split-valence triple-ζ basis set with polarization was used for Br while for all other atoms, the 6-31G* basis set was employed with Valence Double-ζ polarization (VDZP). The X-ray crystal structure coordinates of the manganese tricarbonyl complexes were used as a starting point for the gas-phase geometry optimization of the low spin (S = 0) ground states. Electronic transition energies and oscillator strengths were then calculated for all compounds at their B3YLP-optimized geometries using TDDFT. For these calculations the 40 lowest energy electronic excitations were calculated for each compound and solvent effects

were added using the Polarized Continuum Model (PCM)[19] using EtOH and THF as the solvents for the cationic and neutral species, respectively. The calculated molecular orbitals were visualized using MacMolPlt.

4.I.8. Experimental Data: ^{1}H NMR and IR Spectra

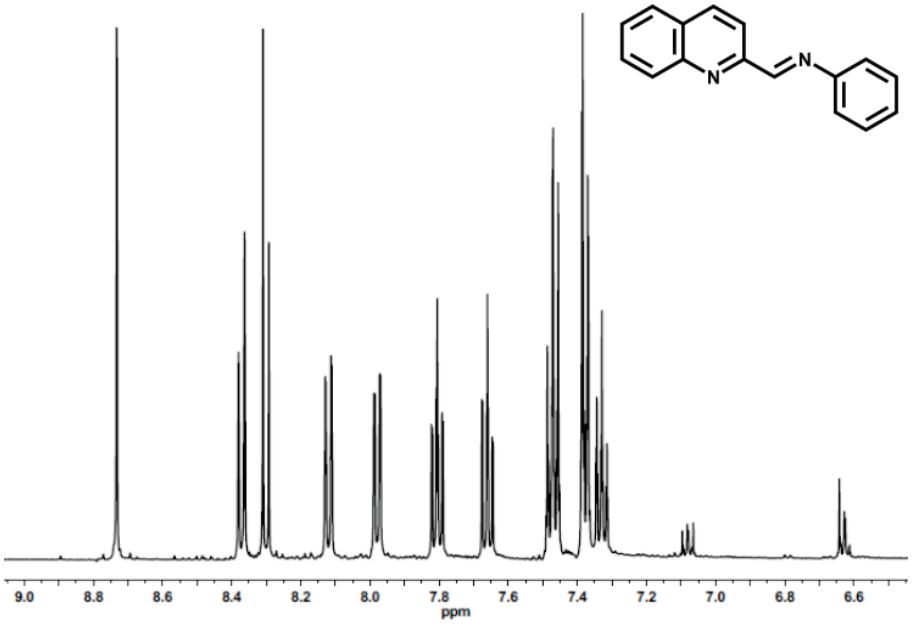

Figure 4.I.14. ^{1}H NMR Spectrum of (6.50-8.90 ppm) of pimq in CD_3CN.

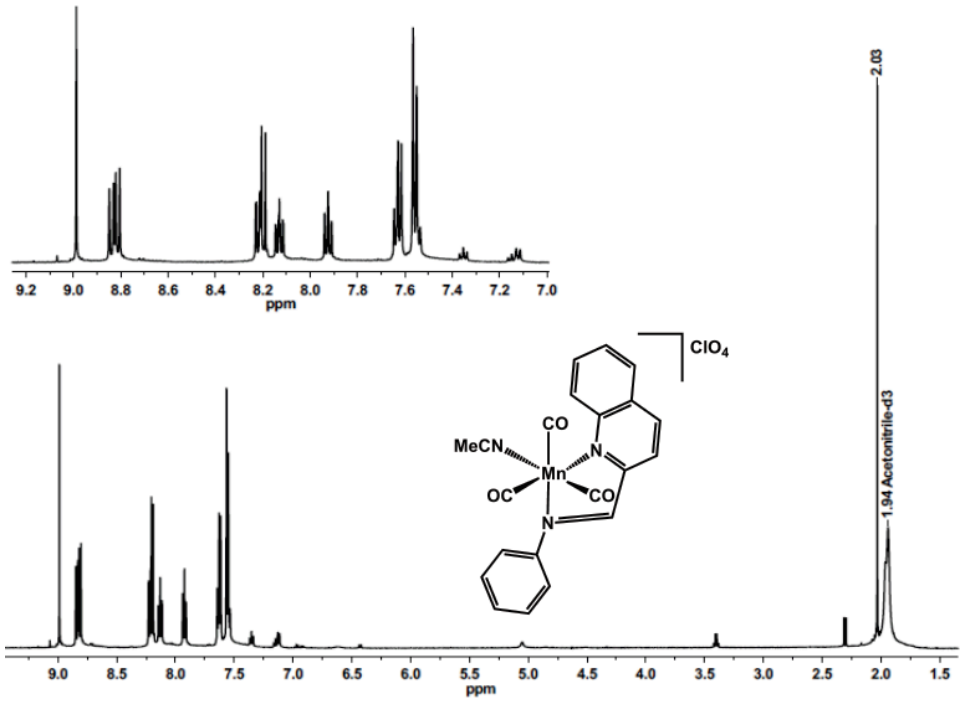

Figure 4.I.15. ^{1}H NMR Spectrum of (1.50-9.00 ppm) of $[Mn(pimq)(CO)_3(MeCN)]ClO_4$ in CD_3CN.

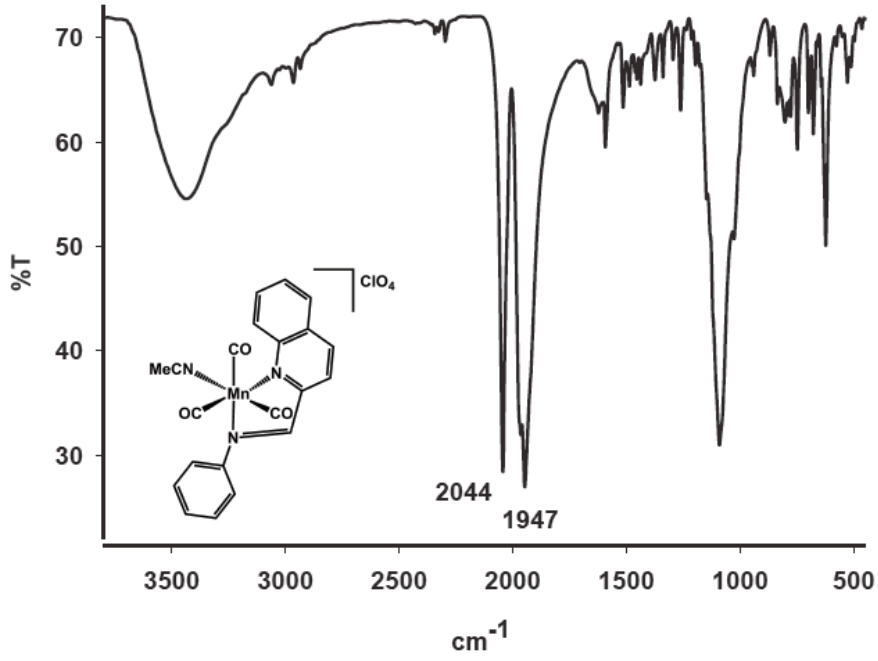

Figure 4.I.16. IR Spectrum of $[Mn(pimq)(CO)_3(MeCN)]ClO_4$ in KBr pellet.

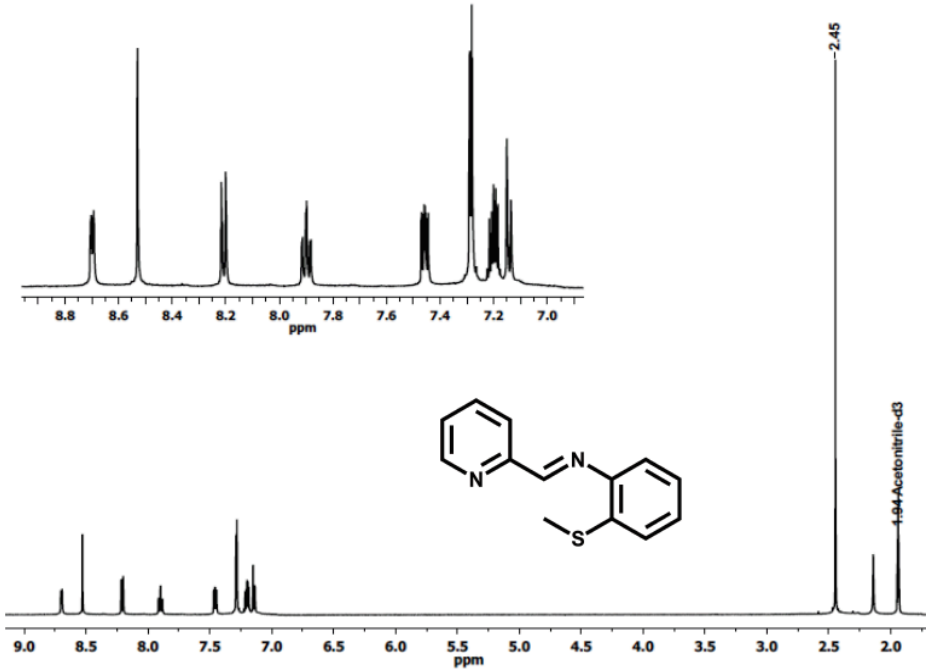

Figure 4.I.17. ^{1}H NMR Spectrum of (1.90-8.90 ppm) of pmtpm in CD_3CN.

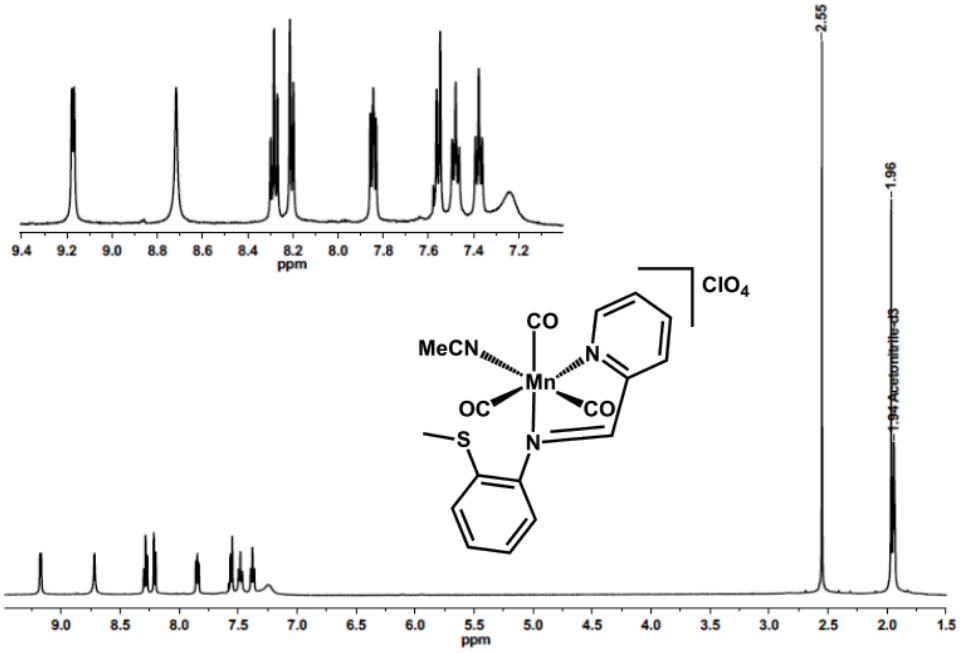

Figure 4.I.18. ^{1}H NMR Spectrum of (1.50-9.75 ppm) of $[Mn(pmtpm)(CO)_3(MeCN)]ClO_4$ in CD_3CN.

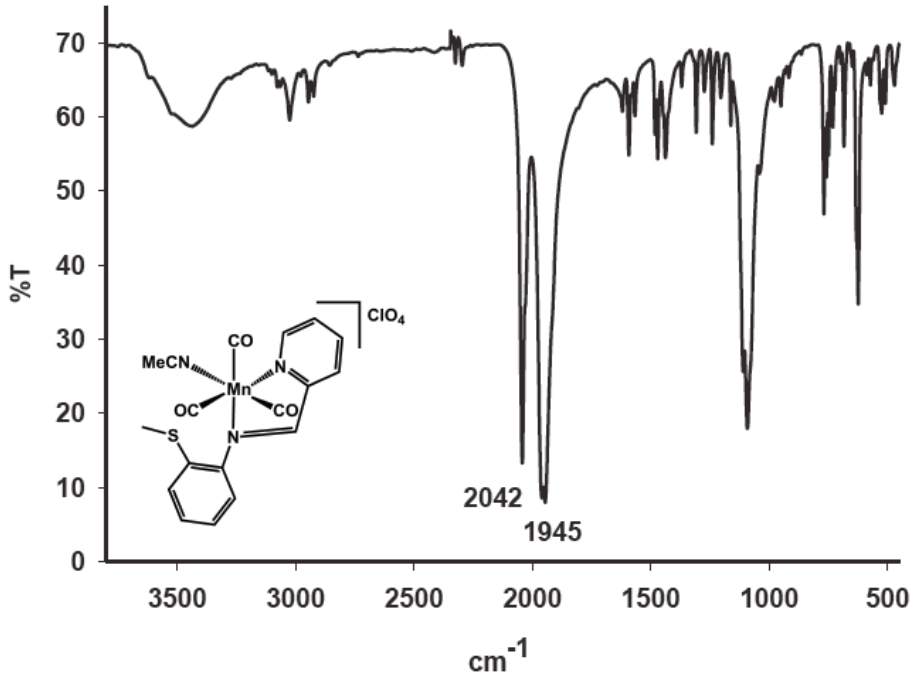

Figure 4.I.19. IR Spectrum of $[Mn(pmtpm)(CO)_3(MeCN)]ClO_4$ in KBr pellet.

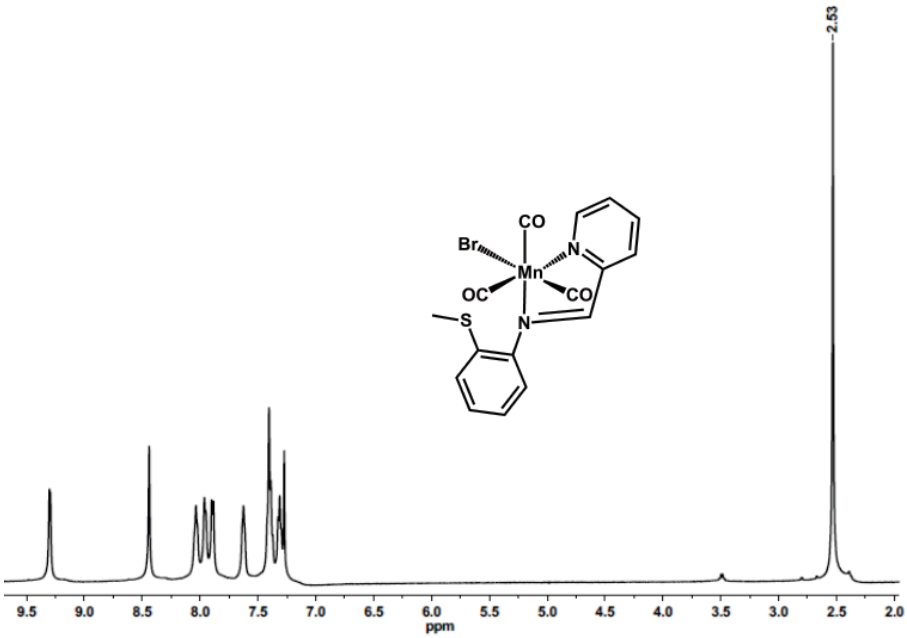

Figure 4.I.20. ^1H NMR Spectrum of (2.00-9.50 ppm) of $[Mn(pmtpm)(CO)_3Br]$ in CD_3CN.

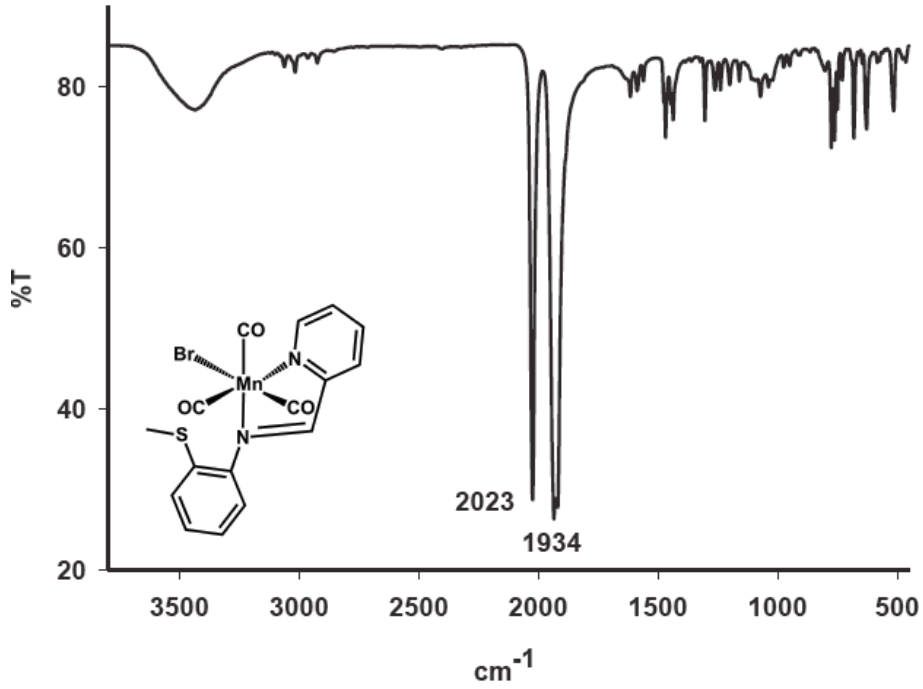

Figure 4.I.21. IR Spectrum of of [Mn(pmtpm)$(CO)_3$Br] in KBr pellet.

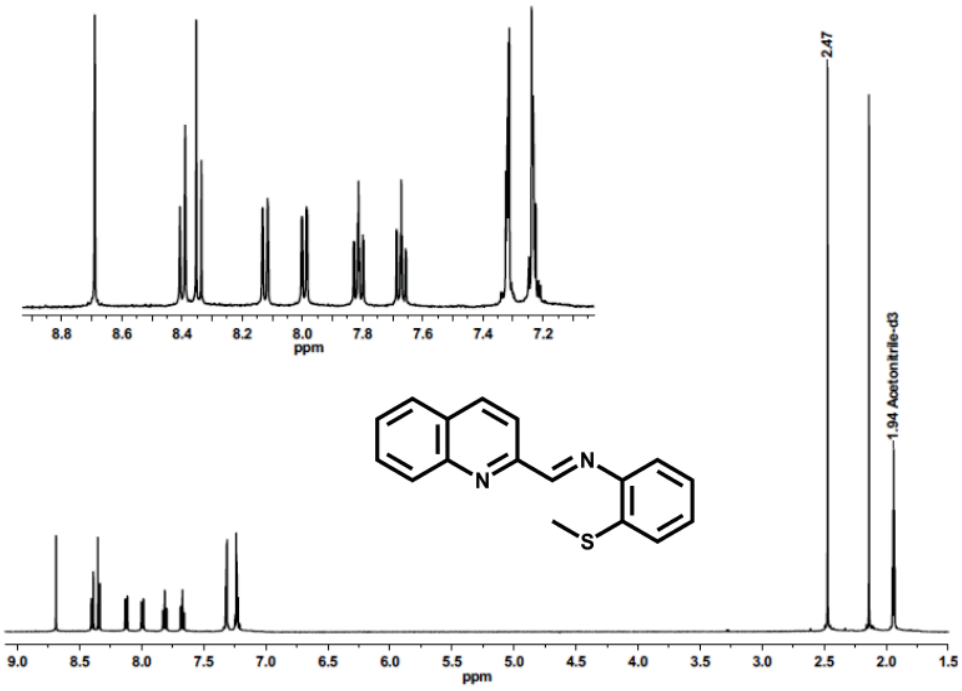

Figure 4.I.22. ^{1}H NMR Spectrum of (1.50-8.75 ppm) of qmtpm in CD_3CN.

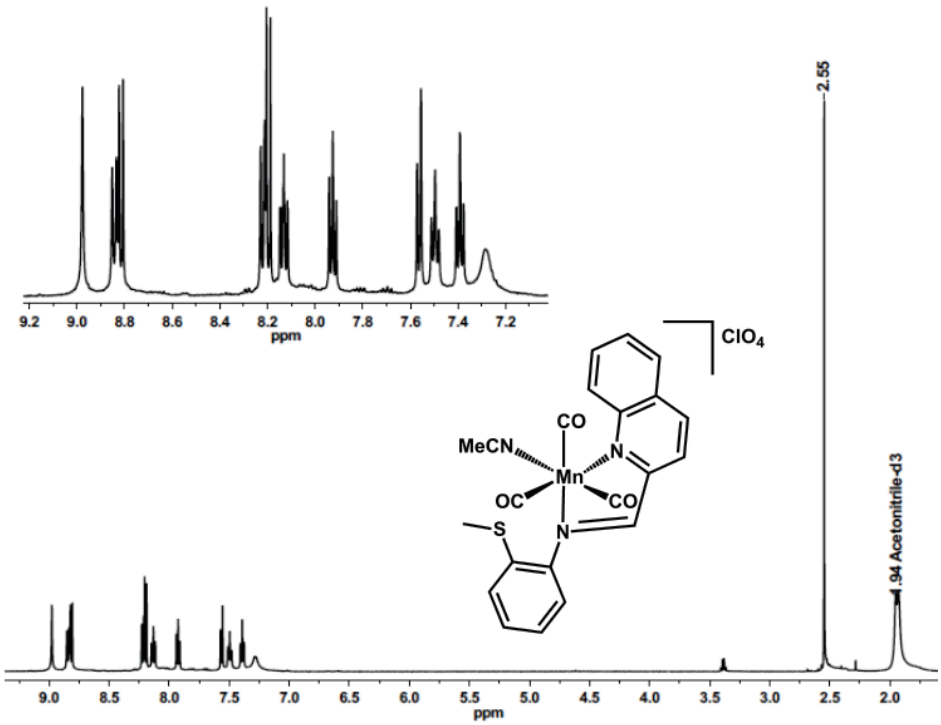

Figure 4.I.23. ^{1}H NMR Spectrum of (1.50-9.00 ppm) of $[Mn(qmtpm)(CO)_3(MeCN)]ClO_4$ in CD_3CN.

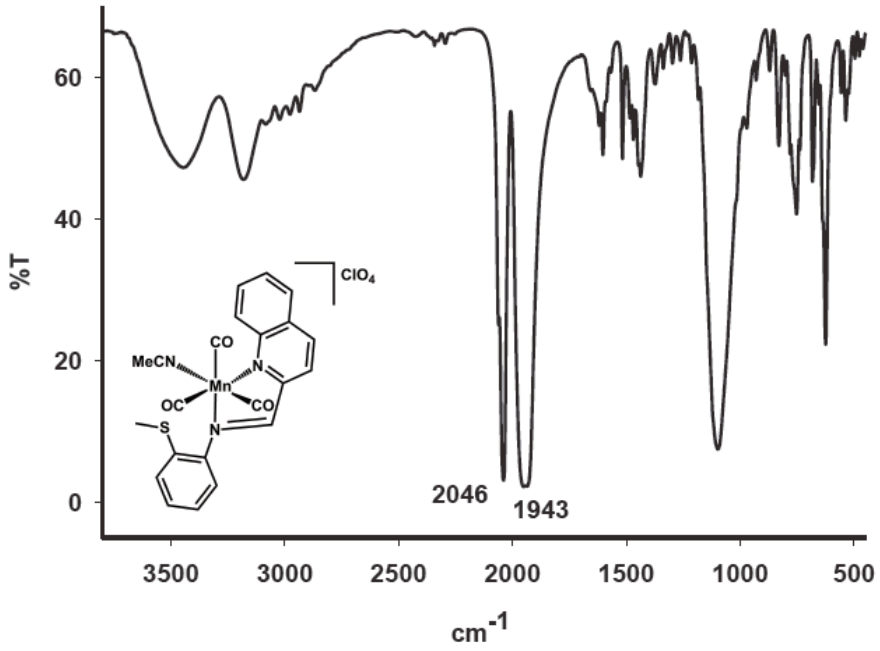

Figure 4.I.24. IR Spectrum of $[Mn(qmtpm)(CO)_3(MeCN)]ClO_4$ in KBr pellet.

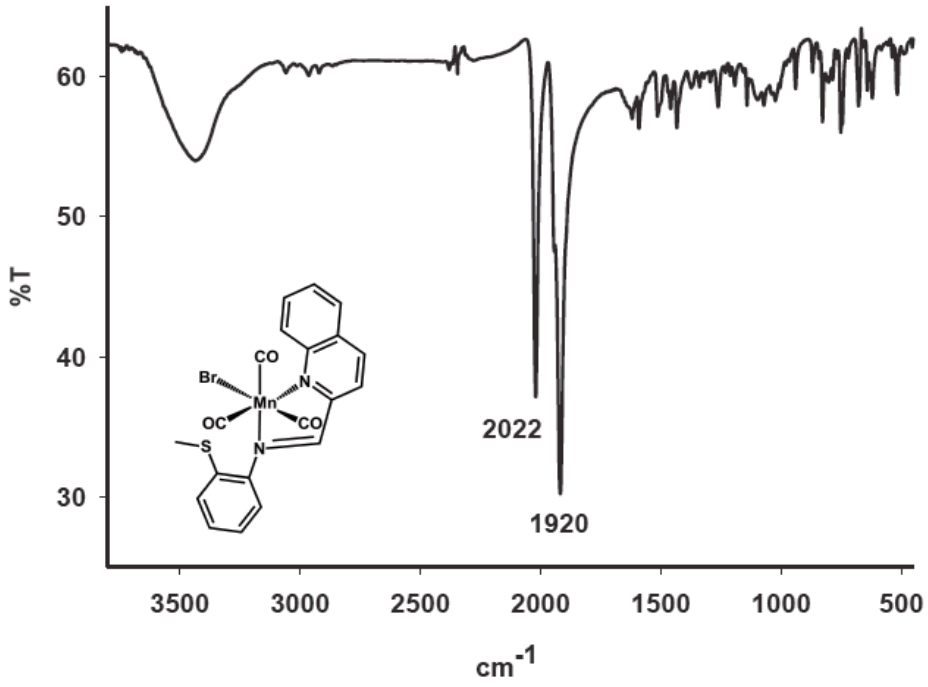

4.I.25. IR Spectrum of of [Mn(qmtpm)$(CO)_3$Br] in KBr pellet.

4.I.9. References

(1) Motterlini, R.; Clark, J. E.; Foresti, R.; Sarathchandra, P.; Mann, B. E.; Green, C. J., *Circ. Res.*, **2002**, *90*, e17-e24.

(2) Pathak, B.; Majumdar, D.; Leszczynski, J., *Int. J. Quantum Chem.*, **2009**, *109*, 2263-2272.

(3) Vummaleti, S. V. C.; Branduardi, D.; Masetti, M.; De Vivo, M.; Motterlini, R.; Cavalli, A., *Chem. Eur. J.*, **2012**, *18*, 9267-9275.

(4) Castro, A. G.; Costa, J. S.; Pievo, R.; Massera, C.; Mutikainen I.; Turpeinen, U.; Gamez, P.; Reedijk J. *Z. Anorg. Allg. Chem.* **2008**, *634*, 2477-2482.

(5) Roy, S.; Mitra, P.; Patra, A. K. *Inorg. Chim. Acta*, **2011**, *370*, 247-253.

(6) (a) Patel, B.; Reid, G. *J. Chem. Soc. Dalton Trans.*, **2000**, 1303-1307. (b) Connolly, J.; Genge, A. R. J.; Levason, W.; Orchard, S. D.; Pope, S. J. A.; Reid, G., *J. Chem. Soc. Dalton Trans.*, **1999**, 2343-2351. (c) Connolly, J.; Goodban, G. W.; Reid, G.; Slawin, A. M. Z. *J. Chem. Soc. Dalton Trans.*, **1998**, 2225-2231.

(7) Nemukhin, A. V.; Grigorenko, B. L.; Granovsky, A. A. *Moscow Univ. Chem. Bull.* **2004**, *45*, 75-102.

(8) (a) Kunz, P. C.; Huber, W.; Rojas, A.; Schatzschneider, U.; Spingler, B. *Eur. J. Inorg, Chem.*, **2009**, 5358-5366. (b) Carlos, R. M.; Carlos, I. A.; Lima Neto, B. S.; Neumann, M. G. *Inorg. Chim. Acta*, **2000**, *299*, 231-237. (c) Reger, D. L.; Grattan, T. C.; Brown, K. J.; Little, C. A.; Lamba, J. J. S.; Rheingold, A. L.; Sommer, R. D. *J. Organomet. Chem.*, **2000**, *607*, 120-128. (d) Hyams, I. J.; Bailey, R. T.; Lippincott, E. R. *Spectro. Chim. Acta*, **1967**, *23A*, 273-284.

(9) (a) García-Escudero, L. A.; Miguel, D.; Turiel, J. A. *J. Organomet. Chem.*, **2006**, *691*, 3434-3444. (b) Valín, M. L.; Moreiras, D.; Solans, X.; Font-Altaba, M.; García-Alonso, F. J. *Acta Crystallogr. C.*, **1986**, *42*, 417-418.

(10) Zhang, J. A.; Pan, M.; Jiang, J. J.; She, Z. G.; Fan, Z. J.; Su, C. Y. *Inorg. Chim. Acta*, **2011**, *374*, 269-277.

(11) Stor, G. J.; van der Vis, M.; Stufkens, D. J.; Oskam, A. *J. Organomet. Chem.*, **1994**, *482*, 15-29.

(12) McLean, S.; Mann, B. E.; Poole, R. K. *Anal. Biochem.* **2012**, *427*, 36-40.

(13) Rimmer, R. D.; Richter, H.; Ford, P. C. *Inorg. Chem*. **2010**, *49*, 1180-1185.

(14) Berends, H.-M.; Kurz, P. *Inorg. Chim. Acta* **2012**, *380*, 141-147.

(15) Gonzalez, M. A.; Yim, M. A.; Cheng, S.; Moyes, A.; Hobbs, A. J.; Mascharak, P. K. *Inorg. Chem.* **2012**, *51*, 601-608.

(16) Baerends, E. J.; Rosa, A. *Coord. Chem. Rev*. **1998**, *177*, 97-125.

(17) Edwards, D. A.; Marshalsea, J., *J. Organomet. Chem*, **1977**, *131*, 73-91.

(18) Hamer, F. M., *J. Chem. Soc.*, **1952**, 3197-3211.

(19) Miertus, S.; Scrocco, E.; Tomasi, *J. Chem. Phys.*, **1981**, *55*, 117-120.

(20) Montalti, M.; Credi, A.; Prodi, L.; Gandolfi, M. T., *Handbook of Photochemistry*, 3rd ed.; CRC Press: Boca Raton, FL, 2006.

(21) Engelking, P. C.; Lineberger, W. C., *J. Am. Chem. Soc.*, **1979***, 101*, 5569-5573.

(22) Nemukhin, A.V.; Grigorenko, B. L.; Granovsky, A. A., *Moscow Univ. Chem. Bull.*, **2004**, *45*, 75-102.

4.I.10. Reprint of Publication

(1) Gonzalez, M. A.; Carrington, S. J.; Fry, N. L.; Martinez, J. L.; Mascharak, P. K., "Syntheses, Structures and Properties of New Manganese Carbonyls as photoactive CO-releasing Molecules (photoCORMs): Design Strategies that Lead to CO Photolability in the Visible Region," *Inorg. Chem.*, 2012, *51*, 11930-11940.

Reprinted with Permission from the American Chemical Society, Copyright 2012

Inorganic Chemistry

Article

pubs.acs.org/IC

Syntheses, Structures, and Properties of New Manganese Carbonyls as Photoactive CO-Releasing Molecules: Design Strategies That Lead to CO Photolability in the Visible Region

Margarita A. Gonzalez, Samantha J. Carrington, Nicole L. Fry, Jose L. Martinez, and Pradip K. Mascharak*

Department of Chemistry and Biochemistry, University of California, Santa Cruz, California 95064, United States

Supporting Information

ABSTRACT: The unusual role of CO as a signaling molecule in several physiological pathways has spurred research in the area of synthesizing new CO-releasing molecules (CORMs) as exogenous CO donors. Auxiliary control on CO delivery can be achieved if CO can be released under the control of light. To synthesize such photoactive CORMs (photoCORMs) with the aid of smart design, a series of manganese carbonyls have been synthesized with ligands that contain extended conjugation and electron-rich donors on their frames. Five such photoCORMs, namely, $[Mn(pimq)(CO)_3(MeCN)]ClO_4$ (**1**, where pimq = (2-phenyliminomethyl)quinoline), $[Mn(qmtpm)(CO)_3(MeCN)]ClO_4$ (**2**, where qmtpm = 2-quinoline-*N*-(2′-methylthiophenyl) methyleneimine), $[Mn(qmtpm)(CO)_3Br]$ (**3**) $[Mn(pmtpm)(CO)_3(MeCN)]ClO_4$ (**4**, where pmtpm = 2-pyridyl-*N*-(2′-methylthiophenyl)methyleneimine), and $[Mn(pmtpm)(CO)_3Br]$ (**5**), have been synthesized and structurally characterized. These designed carbonyls readily release CO upon exposure to light (400−550 nm). The apparent CO release rates and quantum yield values at 509 nm (ϕ_{509}) of the photoCORMs increase steadily with rise in conjugation in the ligand frame and inclusion of a −SMe group. Addition of Br^- as an ancillary ligand also improves the CO-donating capacity. Results of density functional theory (DFT) and time dependent DFT (TDDFT) studies indicate that low energy metal-to-ligand charge transfer (MLCT) transitions from Mn-CO bonding into ligand-π orbitals lead to reduction of M-CO(π^*) back-bonding and loss of CO from these photoCORMs. Inclusion of −SMe and Br^- in the coordination sphere attenuates the energies of the HOMO and LUMO levels and causes further enhancement of CO photorelease. Collectively, the results of this work demonstrate that new photoCORMs with excellent sensitivity to visible light can be synthesized on the basis of smart design principles.

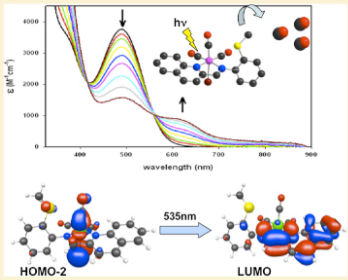

INTRODUCTION

Carbon monoxide (CO), the once obscure byproduct of heme catabolism by heme oxygenase (HO), has recently been the subject of intense scrutiny for its pertinent role in several physiological pathways.[1] Although substrates of CO may not be as diverse as that of another endogenously produced molecule nitric oxide (NO), CO has been known to mediate in key processes including vasorelaxation,[2] cell signaling,[3] and antiapoptotic activity.[4] In most cases, CO interacts with heme-containing metalloproteins. For instance, CO-induced vasodilation proceeds through binding to soluble guanylate cyclase (sGC) and to heme groups within the network of large conductance Ca^{2+}-activated potassium channels (BK_{Ca}).[2] A number of CO-dependent signaling processes include interaction of CO with mitochondrial cytochromes[5] and mitogen activated protein kinases (MAPK).[6] It is within these signaling cascades that CO imparts its protective action and establishes itself as a potent cytoprotective agent. Elevated CO levels concomitant with the induction of the stress protein HO have been associated with the attenuation of ischemia/reperfusion injury,[7] aid of organ graft survival,[8] and modulation of inflammatory conditions such as lung injury[9] and myocardial infarction.[10]

The salutary effects of endogenously produced CO have spurred efforts toward the preparation of exogenous CO donors to serve as novel therapeutics, as direct application of CO gas is often quite difficult. During the past few years, the CO complexes of low valent transition metals (metal carbonyls) have drawn attention as carbon monoxide releasing molecules (CORMs) that could serve as CO donors to biological targets.[11] Motterlini and co-workers synthesized the first in a series of water-soluble CORMs, $[Ru(glycinate)(CO)_3Cl]$ (often referred to as CORM-3),[12] by incorporating a glycine moiety to a typical Ru starting salt. Similar strategies were performed in the isolation of amino acid and amino ester-modified CORMs from group 6 metal centers.[13] These CORMs release CO upon dissolution to aqueous media. Solvent-assisted CO release was also achieved with the use of biocompatible pyrone groups and cyanocobalamin scaffolds in Fe/Mo[14] and Re-based[15] CORMs, respectively. Variation of ancillary ligands in the case of tetrachlorocarbonyliridates has resulted in a modulation of CO donation in aqueous media.[16] Our initial work on Fe-based CORMs derived from designed

Received: August 20, 2012
Published: October 22, 2012

ACS Publications © 2012 American Chemical Society

polypyridyl ligands have demonstrated the effect of trans ligands on the rates of CO release, as well as the role of K^+-channels in CO-induced vasodilation.[17] Although solvent-assisted CO release may be a desirable property in some cases, more control on initiating CO donation is necessary to achieve managed delivery of this potentially toxic gas.

Metal carbonyls have been known to release CO through photodissociation. The prototypical CORMs employed in previous biological assays were commercially available homoleptic metal carbonyls such as $[Mn_2(CO)_{10}]$[18] and $[Fe(CO)_5]$[19] which released CO upon laser flash photolysis. Ford and co-workers reported the photochemical reaction of a water-soluble salt $Na_3[W(CO)_5(TPPTS)]$ under UV irradiation and dubbed the term "photoCORM" to describe this type of light-triggered CO releasing compounds.[20] The iron carbonyl $[Fe(CO)(N4Py)](ClO_4)_2$, derived from a polypyridine ligand, also exhibits fast CO delivery upon illumination with UV light.[21] Sulfur-based ligands such as cysteamine and dithiocarbamate derivatives have recently been employed in the syntheses of photoactive Fe[22] and water-soluble Mn[23] photoCORMs, respectively.

Initial success in isolating photoCORMs has prompted research in exploring design principles that could provide ligands suitable for generating photosensitive metal carbonyls as suitable CO-delivery agents. Recently, a few manganese(I) tricarbonyl complexes derived from the tripodal ligands tris(pyrazolyl)methane and tris(imidazolyl)phosphane have been investigated by Schatzschneider and co-workers.[24] These photoCORMs release CO upon exposure to UV light much like $Na_3[W(CO)_5(TPPTS)]$ and $[Fe(CO)(N4Py)](ClO_4)_2$. We have utilized a series of tridentate polypyridine ligands with varying degree of conjugation to better understand the design principles that promote CO release from the subset of photoCORMs of the composition *fac*-$[Mn^I(L)(CO)_3]$ (L = tridentate ligands).[25] We discovered that increased conjugation in the ligand frame results in a systematic increase in absorptivity of the corresponding compounds in the longer wavelength region, thus generating photoCORMs more sensitive to light in the more desirable visible range. The carbonyl $[Mn(pqa)(CO)_3]ClO_4$ (where pqa = (2-pyridylmethyl)(2-quinolylmethyl)amine) which features both a pyridine and quinoline moiety (Figure 1), exhibits a strong

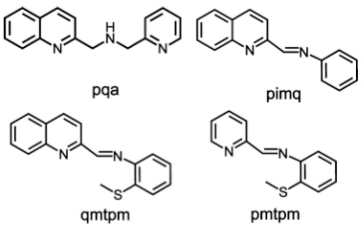

Figure 1. Structures of the ligands.

absorption band with λ_{max} at 360 nm. This is a notable red-shift in the absorption maximum when compared to the related carbonyl $[Mn(tpa)(CO)_3]ClO_4$ (where tpa = tri(2-pyridyl)-amine, λ_{max} = 330 nm) which comprises only pyridine donors in the otherwise similar ligand frame. Since the affinity of CO toward metals in low oxidation state arises predominantly from backbonding of electrons from the metal center to the π^* level of CO, we hypothesized that metal-to-ligand charge transfer (MLCT) transitions would reduce CO affinity of the metal center and result in CO photorelease. Indeed, increased CO photolability of $[Mn(pqa)(CO)_3]ClO_4$ compared to $[Mn(tpa)-(CO)_3]ClO_4$ indicates that facilitation of CO photorelease could arise from such transition(s).

To explore the validity of our hypothesis further, we have now designed a series of manganese(I) carbonyls featuring bidentate and potentially tridentate ligands that incorporate both conjugated aromatic nitrogen donors and an imine functionality (in place of the amine nitrogen) in the ligand framework. To probe the effects of ancillary ligands, a Br^- ligand has also been incorporated in the coordination sphere. Finally, a thioether moiety has been added to the ligand frame to compete for a coordination site and promote additional CO release. The structures of the ligands employed in the present work are shown in Figure 1. We herein report the syntheses, structures, and photochemical parameters of $[Mn(pimq)-(CO)_3(MeCN)]ClO_4$ (**1**, where pimq = (2-phenyliminomethyl)quinoline), $[Mn(qmtpm)-(CO)_3(MeCN)]ClO_4$ (**2**, where qmtpm =2-quinoline-*N*-(2′-methylthiophenyl) methyleneimine), $[Mn(qmtpm)(CO)_3Br]$ (**3**) $[Mn(pmtpm)(CO)_3(MeCN)]ClO_4$ (**4**, where pmtpm =2-pyridyl-*N*-(2′-methylthiophenyl)methyleneimine), and $[Mn-(pmtpm)(CO)_3Br]$ (**5**). The systematic changes in the ligand frame has afforded progressive red shift of the absorption band maximum from 390 nm (for **4**) to 535 nm (for **3**) in this set of photoCORMs. We have also attempted to correlate the CO photolability of these photoCORMs with the results of density functional theory (DFT) and time dependent DFT (TDDFT) calculations and confirm the nature of the MLCT associated with CO release.

EXPERIMENTAL SECTION

General Procedures. All experimental manipulations were performed under anaerobic conditions using standard Schlenk techniques and under limited light conditions. Manganese pentacarbonyl bromide ($[Mn(CO)_5Br]$) was purchased from Alfa Aesar. The ligands 2-pyridyl-*N*-(2′-methylthiophenyl)methyleneimine (pmtpm)[26] and 2-quinoline-*N*-(2′-methylthiophenyl) methyleneimine (qmtpm)[27] and the starting salt, *fac*-$[Mn(CO)_3(MeCN)_3](ClO_4)$[28] were synthesized following published procedures. Solvents were purified and/or dried by standard techniques prior to use.

Caution! *Transition metal perchlorates should be prepared in small quantities and handled with great caution as metal perchlorates may explode upon heating.*

2-(Phenyliminomethyl)quinoline (pimq). The synthesis and purification of pimq were modified to some extent compared to the procedure reported by Hamer.[29] Aniline (0.80 g, 8.60 mmol) was dissolved in 15 mL of MeOH followed by the addition of quinoline-2-carboxaldehyde (1.23 g, 7.81 mmol) in 15 mL of MeOH. The mixture was heated to reflux for 12 h, after which the solvent was removed under reduced pressure to obtain an orange-red oil. Upon addition of 30 mL of Et_2O and rapid scratching, the product separated as an orange powder. The solid was filtered and dried in vacuo (0.69 g, 60% yield). ^1H NMR (CD_3CN, 500 MHz), δ (ppm from TMS): 8.74 (s, 1H), 8.37 (d, 1H), 8.30 (d, 1H), 8.12 (d, 1H), 7.98 (d, 1H), 7.80 (t, 1H), 7.66 (t, 1H), 7.47 (t, 2H), 7.38 (d, 2H), 7.33 (t, 1H).

$[Mn(pimq)(CO)_3(MeCN)]ClO_4$ (1). A batch of $[Mn-(CO)_3(MeCN)_3]ClO_4$ (0.378 g, 0.97 mmol) was added to a degassed solution of pimq (0.225 g, 0.97 mmol) in 25 mL of $CHCl_3$. The clear yellow orange color of the solution deepened to red brown upon reflux under N_2 atmosphere. After 6 h, the solvent was removed under reduced pressure, and the residue was triturated three times with Et_2O to obtain a red orange powder (0.364 g, 90% yield). Slow diffusion of pentane into a dichloromethane solution of **1** afforded red blade-like

Table 1. Summary of Crystal Data, Intensity Collection, and Refinement Parameters for [Mn(pimq)(CO)$_3$(MeCN)]ClO$_4$ (1), [Mn(qmtpm)(CO)$_3$(MeCN)]ClO$_4$ (2), [Mn(qmtpm)(CO)$_3$Br] (3), [Mn(pmtpm)(CO)$_3$(MeCN)]ClO$_4$ (4), and [Mn(pmtpm)(CO)$_3$Br] (5)

	1	2	3	4	5
empirical formula	$C_{21}H_{15}ClMnN_3O_7$	$C_{22}H_{17}ClMnN_3O_7S$	$C_{20}H_{14}BrMnN_2O_3S$	$C_{18}H_{12}ClMnN_3O_7S$	$C_{16}H_{12}BrMnN_2O_3S$
FW.	511.75	557.85	497.24	504.77	447.19
cryst color	red blades	red orange blades	red blades	orange blades	red blades
T	296(2)	298(2)	296(2)	296(2)	296(2)
cryst syst	monoclinic	monoclinic	monoclinic	triclinic	triclinic
space grp	$C2/c$	$C2/c$	$P2(1)/n$	$P\bar{1}$	$P\bar{1}$
a (Å)	17.3321(6)	31.8928(8)	10.0170(8)	8.8047(6)	7.7145(6)
b (Å)	22.4429(8)	14.0999(4)	11.5945(10)	11.2528(8)	8.9929(6)
c (Å)	13.2943(5)	23.2818(6)	17.2755(14)	12.1033(8)	13.6094(10)
α (deg)	90	90	90	70.3630(10)	93.7460(10)
β (deg)	118.27	112.23	100.0900(10)	77.1640(10)	95.5470(10)
γ (deg)	90	90	90	88.6080(10)	106.1690(10)
V (Å^3)	4554.5(3)	9691.1(4)	1975.4(3)	1099.54(13)	898.36(11)
Z	8	16	4	2	2
d_{cal} (g/cm^3)	1.493	1.529	1.672	1.525	1.653
μ (mm^{-1})	0.744	0.789	2.820	0.861	3.090
GOF[a] on F^2	1.052	1.057	1.026	1.059	1.018
final R indices	R_1 = 0.0482	R_1 = 0.0460	R_1 = 0.0295	R_1 = 0.0430	R_1 = 0.0353
$[I > 2\sigma(I)]$	wR_2 = 0.1439	wR_2 = 0.1223	wR_2 = 0.0642	wR_2 = 0.1193	wR_2 = 0.0644
R indices[b]	R_1 = 0.0609	R_1 = 0.0703	R_1= 0.0451	R_1 = 0.0545	R_1 = 0.0670
all data[c]	wR_2 = 0.1567	wR_2 = 0.1380	wR_2 = 0.0704	wR_2 = 0.1288	wR_2 = 0.0731

[a] GOF = $[\sum[w(F_o^2 - F_c^2)^2]/(N_o - N_v)]^{1/2}$ (N_o = number of observations, N_v = number of variables). [b] $R_1 = \sum||F_o| - |F_c||/\sum|F_o|$. [c] $wR_2 = [(\sum w(F_o^2 - F_c^2)^2/\sum|F_o^2|)]^{1/2}$.

crystals suitable for X-ray studies. Anal. Calcd. for $C_{21}H_{15}ClMnN_3O_7$: C, 49.28; H, 2.93; N, 8.21. Found: C, 49.26; H, 2.87; N, 8.27. Electronic absorption spectrum in MeCN, λ_{max} (nm) [(ε (M^{-1} cm^{-1})]: 430 (3200), 345 (12 760), 260 (27 330). Selected IR frequencies (KBr disk, cm^{-1}): 2044 (s, ν_{CO}), 1970 (s, ν_{CO}), 1947 (s, ν_{CO}), 1593 (m), 1515 (m), 1374 (w), 1092 (s,ν_{ClO4}), 837 (w), 750 (m), 623 (s), 529 (w). ^{1}H NMR (CD_3CN, 500 MHz), δ (ppm from TMS): 9.00 (s, 1H), 8.82 (dd, 2H), 8.20 (dd, 2H), 8.12 (t, 1H), 7.92 (t, 1H), 7.62 (t, 2H), 7.56 (t, 3H).

[Mn(qmtpm)(CO)$_3$(MeCN)]ClO$_4$ (2). To a degassed solution of qmtpm (0.153 g, 0.55 mmol) in 25 mL of $CHCl_3$ was added a batch of $[Mn(CO)_3(MeCN)_3]ClO_4$ (0.200 g, 0.55 mmol), and the solution was heated to reflux under N_2 for 6 h. Solvent removal and subsequent trituration with Et_2O afforded **2** as a brick red solid (0.269 g, 88% yield). X-ray quality crystals (red orange plates) were grown by via diffusion of pentane into a CH_2Cl_2 solution of **2**. Anal. Calcd. for $C_{22}H_{17}ClMnN_3O_7S$: C, 47.37; H, 3.07; N, 7.53. Found: C, 47.26; H, 3.10; N, 7.57. Electronic Absorption Spectrum in MeCN, λ_{max} (nm) [ε (M^{-1} cm^{-1})]: 435 (3 680), 335 (10 400), 260 (33 670). Selected IR frequencies (KBr disk, cm^{-1}): 2046 (s, ν_{CO}), 1943 (s, ν_{CO}), 1516 (w), 1438 (w), 1094 (s, ν_{ClO4}), 822 (w), 750 (w), 623 (m). ^{1}H NMR (CD_3CN, 500 MHz), δ (ppm from TMS): 8.97 (s, 1H), 8.82 (t, 2H), 8.20 (t, 2H), 8.12 (t, 1H), 7.91 (t, 1H), 7.55 (d, 1H), 7.49 (t, 1H), 7.38 (t, 1H), 7.27 (s, 1H), 2.52 (s, 3H).

[Mn(qmtpm)(CO)$_3$Br] (3). A batch of $[Mn(CO)_5Br]$ (0.112 g, 0.41 mmol) was added to a degassed solution of qmtpm (0.113 g, 0.41 mmol) in 20 mL of $CHCl_3$. The solution developed a deep reddish purple hue upon reflux under N_2 atmosphere. After 4 h, the solvent was removed in vacuo, and the residue was triturated three times with Et_2O to obtain a red purple powder (0.219 g, 80% yield). Slow diffusion of pentane into a CH_2Cl_2 solution of **3** afforded red plates suitable for X-ray studies Anal. Calcd. for $C_{20}H_{14}BrMnN_2O_3S$: C, 48.31; H, 2.84; N, 5.63. Found: C, 48.24; H, 2.87; N, 5.52. Electronic Absorption Spectrum in $CHCl_3$, λ_{max} (nm) [ε (M^{-1} cm^{-1})]: 535 (2 235), 335 (9 050), 255 (26 710). Selected IR frequencies (KBr disk, cm^{-1}): 2022 (s, ν_{CO}), 1920 (s, ν_{CO}), 1514 (w), 1434 (w), 1262 (s, ν_{ClO4}), 828 (w), 752 (w), 680 (w).

[Mn(pmtpm)(CO)$_3$(MeCN)]ClO$_4$ (4). This complex was synthesized by following the procedure that afforded **2** (as described above). A batch of 0.148 g of pmtpm (0.65 mmol) and 0.236 g (0.65 mmol) of $[Mn(CO)_3(MeCN)_3]ClO_4$ afforded 0.269 g (82% yield) of the product as a yellow orange powder. Orange blades suitable for X-ray studies were grown by diffusion of pentane into a CH_2Cl_2 solution of **4**. Anal. Calcd. for $C_{18}H_{12}ClMnN_3O_7S$: C, 42.83; H, 2.40; N, 8.32. Found: C, 42.80; H, 2.46; N, 8.25. Electronic Absorption Spectrum in MeCN, λ_{max} (nm) [ε (M^{-1} cm^{-1})]: 390 (3 620), 270 (17 000). Selected IR frequencies (KBr disk, cm^{-1}): 2042 (s, ν_{CO}), 1945 (s, ν_{CO}), 1592 (w), 1470 (w), 1437 (w), 1307 (w), 1091 (s ν_{ClO4}), 768 (m) 623 (m). ^{1}H NMR (CD_3CN, 500 MHz), δ (ppm from TMS): 9.18 (d, 1H), 8.72 (s, 1H), 8.27 (t, 1H), 8.20 (d, 1H), 7.86 (t, 1H), 7.56 (d, 1H), 7.48 (t, 1H), 7.38 (t, 1H), 7.24 (s, 1H), 2.55 (s, 3H).

[Mn(pmtpm)(CO)$_3$Br] (5). This complex was synthesized by following the procedure that afforded **3** (as described above). A batch of 0.151 g (0.55 mmol) of $[Mn(CO)_5Br]$ and 0.125 g (0.55 mmol) of pmtpm afforded 0.257 g (47% yield) of **5** as an orange powder. Slow diffusion of pentane into a CH_2Cl_2 solution of **5** afforded red orange plates suitable for X-ray studies. Anal. Calcd. for $C_{16}H_{12}BrMnN_2O_3S$: C, 42.97; H, 2.70; N, 6.26. Found: C, 43.00; H, 2.66; N, 6.20. Electronic Absorption Spectrum in $CHCl_3$, λ_{max} (nm) [ε (M^{-1} cm^{-1})]: 500 (2 530), 380 (2 280), 315 (5 800), 285 (11 260). Selected IR frequencies (KBr disk, cm^{-1}): 2023 (s, ν_{CO}), 1934 (s, ν_{CO}), 1607 (w), 1468 (w), 1303 (w), 775 (w) 680 (w), 627 (w) 514 (w).

Physical Measurements. The ^{1}H NMR spectra were recorded at 298 K on a Varian Unity Inova 500 MHz instrument. A Perkin-Elmer Spectrum-One FT-IR was employed to monitor the FTIR spectra of the compounds. Electronic absorption spectra were obtained with a Varian Cary 50 Spectrophotometer. Room temperature magnetic susceptibility measurements were performed with the aid of a Johnson Matthey magnetic susceptibility balance.

Photolysis Experiments. For continuous wave photolysis experiments, a Newport Oriel Apex Illuminator (150 W xenon lamp) equipped with an Oriel 1/8 m Cornerstone monochromator (measured power 146−150 mW) was used as the light source. Standard ferrioxalate actinometry was performed to calibrate the light source at 509 nm (ϕ_{509}).[30] Samples of **1**−**5** were prepared under dim

Table 2. Selected bond Distances (Å) and Angles (deg) for 1−5

	1	2	3	4	5
Mn−N1	2.126(2)	2.120(2)	2.106(2)	2.054(2)	2.054(2)
Mn−N2	2.053(2)	2.063(3)	2.059(2)	2.069(2)	2.049(2)
Mn−N3	2.015(2)	2.013(3)		2.019(3)	
Mn−Br			2.5366(6)		2.5338(5)
Mn−C1	1.819(3)	1.810(4)	1.800(4)	1.810(3)	1.802(3)
Mn−C2	1.834(3)	1.831(4)	1.804(3)	1.803(3)	1.806(3)
Mn−C3	1.801(3)	1.803(4)	1.790(4)	1.801(3)	1.781(4)
C1−O1	1.139(3)	1.132(4)	1.149(4)	1.142(4)	1.148(3)
C2−O2	1.131(4)	1.134(4)	1.148(4)	1.150(4)	1.148(3)
C3−O3	1.136(4)	1.145(4)	1.146(4)	1.141(4)	1.148(4)
C1−Mn−N1	171.95(10)	169.99(14)	172.74(12)	173.86(12)	174.35(12)
C2−Mn−N2	175.85(12)	173.15(14)	170.35(12)	172.02(13)	171.15(12)
C3−Mn−N3	177.11(12)	176.07(14)		176.31(11)	
C1−Mn−C2	87.02(12)	86.82(18)	86.11(14)	88.96(16)	89.87(14)
C1−Mn−C3	87.56(14)	91.09(17)	89.42(15)	90.14(15)	88.92(14)
C1−Mn−N2	93.94(10)	91.75(15)	94.18(12)	95.77(12)	97.25(11)
C1−Mn−N3	94.28(11)	91.68(15)		93.41(13)	
C2−Mn−C3	87.51(15)	87.95(18)	89.48(14)	89.17(15)	91.25(14)
C2−Mn−N1	101.03(11)	102.79(14)	101.07(12)	97.05(13)	94.12(12)
C2−Mn−N3	94.80(12)	89.43(14)		89.88(13)	
C3−Mn−N1	92.61(12)	92.62(13)	91.68(12)	88.66(11)	94.98(12)
C3−Mn−N2	88.50(12)	98.73(14)	100.17(12)	97.23(11)	94.14(11)
Mn−C1−O1	177.4(3)	179.9(4)	175.1(3)	177.0(3)	176.9(3)
Mn−C2−O2	174.7(3)	173.8(4)	174.4(3)	177.9(4)	178.6(3)
Mn−C3−O3	177.2(3)	174.6(4)	174.9(3)	177.2(3)	176.0(3)
C1−Mn−Br			91.31(11)		88.55(10)
C2−Mn−Br			84.81(10)		86.97(10)
C3−Mn−Br			174.18(10)		176.91(10)

light conditions and placed in 2 × 10 mm quartz cuvettes positioned 2 cm away from the light source.

Because of differences in solubilities, the quantum yields (ϕ) of CO release for **1**, **2**, and **4** were measured in MeCN (1.10 mM), while that of **3** and **5** were measured in tetrahydrofuran (THF, 1.10 mM). Solutions were prepared to ensure sufficient absorbance (>90%) at the irradiation wavelength (509 nm), and changes in the electronic spectra in the 350−550 nm region (<10% photolysis) were used to determine the extent of CO release. Each sample was irradiated with the monochromatic light (power: 5 mW) at defined time intervals. Changes in the respective charge transfer bands of **1**−**5** were monitored along the 2 mm path.

The apparent rates of photolysis were monitored at an appropriate wavelength for each carbonyl, and the absorbance versus time plots were fitted to a the three parameter exponential equation $A(t) = A_\infty + (A_o - A_\infty)\exp\{-k_{CO}t\}$, where A_o and A_∞ are the initial and final absorbance values, respectively. The apparent rate of CO loss (k_{CO}) was calculated from the $\ln(C)$ versus time (T) plot for each carbonyl.

X-ray Crystallography. Diffraction data for **1**−**5** were collected at 296 K on a Bruker APEX-II instrument using monochromated Mo−K_α radiation (λ = 0.71073 Å). All data were corrected for absorption, and the structures were solved by direct methods using SHELXTL (1995−99) software package (Bruker Analytical X-ray Systems Inc.). Additional refinement details are contained in CIF files (Supporting Information). Crystal data, instrument and data collection parameters are summarized in Table 1. Selected bond distances and angles are listed in Table 2.

DFT and TDDFT Calculations. Density functional theory (DFT) and time dependent density functional theory (TDDFT) studies were executed with PC-GAMESS program[31] using the hybrid functional B3LYP. Optimizations for the Mn atom were performed by employing the LANL2DZ basis set and effective core potential (ECP). The Pople 6-311G* split-valence triple-ζ basis set with polarization was used for Br while for all other atoms, the 6-31G* basis set was employed with Valence Double-ζ polarization (VDZP). The X-ray crystal structure coordinates of complexes (**1**−**5**) were used as a starting point for the gas-phase geometry optimization of the low spin (S = 0) ground states. Electronic transition energies and oscillator strengths were then calculated for **1**−**5** at their B3YLP-optimized geometries using TDDFT. For these calculations the 40 lowest energy electronic excitations were calculated for each compound, and solvent effects were added using the Polarized Continuum Model (PCM)[32] using EtOH and THF as the solvents for the cationic and neutral species, respectively. The calculated molecular orbitals were visualized using MacMolPlt.

RESULTS AND DISCUSSION

To promote CO photorelease from our designed photo-CORMs through metal-to-ligand charge transfer (MLCT) transitions, we have introduced conjugated ring systems in addition to imine functionality in the ligand frames of the present work. Out of the set **1**−**5**, **1** contains the ligand pimq (Figure 1) in which a phenyl ring is bonded to a quinoline donor through an imine linker. This bidentate ligand provides a significant extent of conjugation. The next subset comprising **2** and **4** is derived from the potentially tridentate ligands qmtpm and pmtpm which includes a thioether moiety on the phenyl part of the ligand. The reasons for this inclusion are 2-fold. First, it is expected to add electron density to the π-frame of the ligand and second, it could bind to the Mn(I) center[33] and promote further CO release upon illumination. In addition, a pyridine donor in pmtpm (in complex **4**) has been replaced with a more-conjugated quinoline donor in qmtpm (in complex **2**) for enhanced absorptions in the visible range. Finally, in the subset consisting of **3** and **5**, a Br^- ligand replaces the

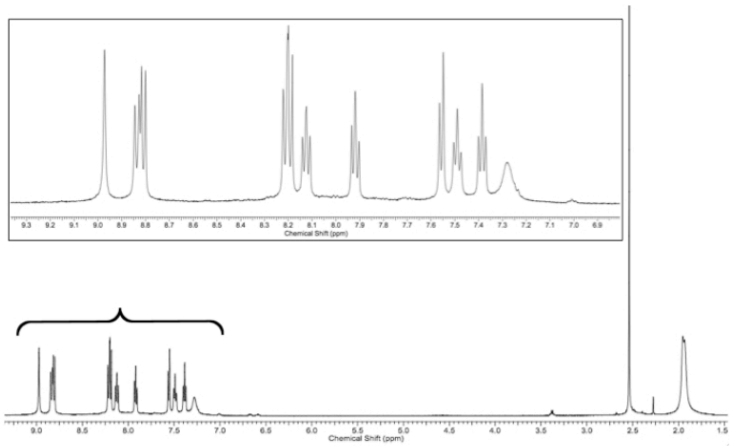

Figure 2. ^{1}H NMR (500 MHz) spectrum of [Mn(qmtpm)(CO)$_3$(MeCN)](ClO$_4$) (**2**) in CD$_3$CN (1.50−9.50 ppm range).

acetonitrile ligand. Introduction of this donor is intended to provide electron density to the Mn(I) center via σ-donation and modulate the MLCT transitions of the resulting carbonyls. In this subset, exchange of the pyridine donor with a quinoline donor has also been applied to correlate the CO photolability of the resulting carbonyls.

Treatment of *fac*-[Mn(CO)$_3$(MeCN)]ClO$_4$ with pimq or qmtpm in CHCl$_3$ under refluxing conditions afforded the cationic species [Mn(L)(CO)$_3$(MeCN)]$^+$, where L = pimq (**1**) or qmtpm (**2**). While qmtpm has potentially three coordination sites, only the nitrogen atoms of the ligand were found to bind to the metal center as evidenced by crystallographic data (vide infra). The use of a more suitable starting salt such as Mn(CO)$_5$Br under similar conditions also did not lead to the desired metal−sulfur binding and instead generated the neutral carbonyl [Mn(qmtpm)(CO)$_3$Br] (**3**, Figure 4). A similar trend was also observed with the less conjugated ligand pmtpm, wherein reaction with *fac*-[Mn(CO)$_3$(MeCN)]ClO$_4$ or Mn(CO)$_5$Br generated compounds **4** and **5**, respectively. This outcome was somewhat surprising since scrutiny of the literature revealed a few low valent manganese carbonyls in which multiple thioether groups are coordinated to the metal center in the presence of π-acceptor ligands.[31] We suspect that the rigid framework of the conjugated ligands of Figure 1 does not allow binding in the *facial* orientation and hence replacement of the MeCN or Br$^-$ ligand was not achieved in **2**−**5**. The utility of the −SMe moiety is however evident in the enhancement of the CO photorelease from these species thus indicating its electronic effect(s) on the overall CO- donating capacity of these photoCORMs (vide infra). All five carbonyls dissolve in organic solvents such as MeCN, DMSO, and CHCl$_3$ and in polar aprotic solvents such as MeOH. Such solutions are stable for hours when kept in the dark.

The IR spectra of carbonyls **1**−**5** exhibit two strong bands in the carbonyl region (Supporting Information), a pattern consistent with known *fac*-Mn(I) tricarbonyl complexes.[34] In the case the MeCN-adducts **1**, **2**, and **4**, the first ν_{CO} stretch appears as a sharp peak at 2042−2044 cm^{-1} pertaining to the axial CO ligand. The second broad ν_{CO} band noted at ∼1942−1947 cm^{-1} features a minor splitting pattern which suggests a distinction between the remaining CO groups in the equatorial plane. For the neutral compounds **3** and **5**, a similar pattern is observed, albeit slight shift to lower frequencies. The first sharp ν_{CO} stretch appears at 2020 cm^{-1} followed by the broad ν_{CO} stretch at 1920−1934 cm^{-1}.

Compounds **1**−**5** are diamagnetic in the solid state and in solutions. The S = 0 state of the compounds is readily evidenced by their clean NMR spectra. An example is shown in Figure 2. In this spectrum of **2** ligation of the qmtpm ligand to the Mn(I) center is indicated by the downfield shift of the imine proton (from 8.73 ppm in the free ligand) to 8.97 ppm. The aromatic protons spread over 7.30−9.00 ppm while the -SMe resonance of qmtpm remains unchanged and appears at 2.52 ppm.

Structures of the Complexes. The structures of the three MeCN-bound cationic carbonyls **1**, **2**, and **4** are discussed first. The cations of these carbonyls all adopt a similar motif wherein the designed ligands pimq (in **1**), qmtpm (in **2**), and pmtpm (in **4**) are coordinated in a bidentate fashion. The structures of **1** and **2** are shown in Figures 3 and 4 respectively while the

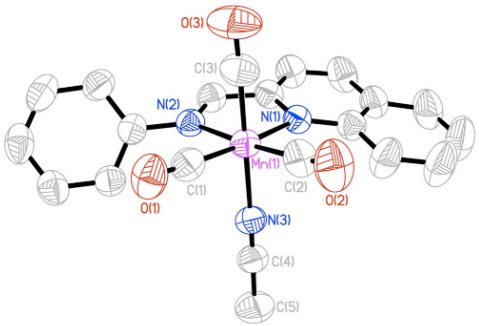

Figure 3. Thermal ellipsoid (probability level 50%) plot of [Mn(pimq)(CO)$_3$(MeCN)]$^+$ (cation of **1**) with select atom labeling. H atoms have been omitted for clarity.

structure of **4** is included in the Supporting Information, Figure S1. Three facially coordinated CO ligands force the bidentate ligands and MeCN to occupy different planes in the slightly distorted octahedral geometry. The Mn(I)-N_{imine} bond distances of **1** and **2** (2.053(2) and 2.063(3) Å respectively) are similar to such distances noted in other Mn(I) tricarbonyls featuring bidentate diimine ligands.[35] Also, the Mn(I)-$N_{quinoline}$ bond lengths for **1** and **2** (2.126(2) and 2.120(2) Å) compare well with Mn(I) complexes derived from quinoline-containing ligands.[36] These distances are however longer than the Mn(I)-N_{py} bond distance in **4** (2.054(2) Å) and confirm the superior coordinating ability of the pyridine N of the pmtpm ligand. In **2** (and **4**, Supporting Information, Figure S1), the thioether moiety is not coordinated despite the possibility of binding the metal center through displacement of a proximal CO (Figure 4). This presumably arises from the relatively low π-accepting capacity of the thioether S donor compared to CO.

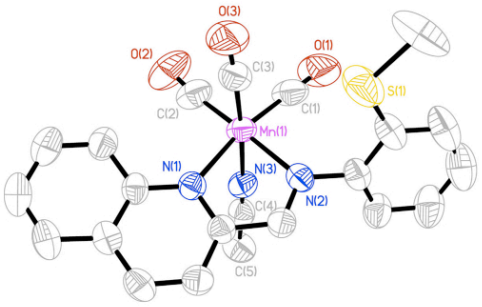

Figure 4. Thermal ellipsoid (probability level 50%) plot of $[Mn(qmtpm)(CO)_3(MeCN)]^+$ (cation of **2**) with select atom labeling. H atoms have been omitted for clarity.

The structure of the neutral carbonyl $[Mn(qmtpm)(CO)_3Br]$ (**3**) (shown in Figure 5) is very similar to that of **2** except for the replacement of the MeCN ligand with Br^-. The three CO ligands are coordinated in the same facial configuration, and the thioether moiety is not coordinated. In **3**, the Mn(I)-Br distance is 2.5366(6) Å, a value well within the range of Mn(I)-Br distances noted in compounds such as $[BrMn(CO)_2(N,N,N\text{-dapa})]$ [N,N,N-dapa = 2,6-diacetylpyridine-bis(aniline)].[37] The structure of the analogous neutral carbonyl $[Mn(pmtpm)(CO)_3Br]$ (**5**) has been included in the Supporting Information, Figure S2.

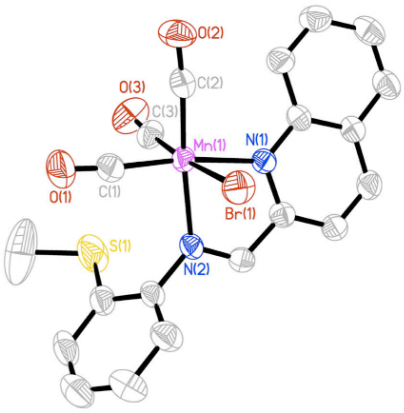

Figure 5. Thermal ellipsoid (probability level 50%) plot of $[Mn(qmtpm)(CO)_3Br]$ (**3**) with select atom labeling. H atoms have been omitted for clarity.

Electronic Spectra and CO Release in Solution. The electronic absorption spectra of compounds **1**−**5** have been recorded in MeCN, THF, and $CHCl_3$. A plot of the respective absorption maxima of **2**−**5** (solution in $CHCl_3$) in the visible region is shown in Figure 6. All absorption spectra were measured in the absence of room light since these carbonyls exhibit facile CO release (vide infra) upon illumination. The effect of increased conjugation in the ligand frame is readily indicated by the *red shift* of the absorption maximum of **2** (435 nm) compared to that of **4** (390 nm). Replacement of the MeCN ligand with the σ-donating Br^- ligand results in *further red shift* of λ_{max} of **3** and **5** to 535 and 500 nm, respectively. Carbonyls **1** and **2** exhibit similar absorption profiles (Supporting Information, Figure S3). with bands centered at ∼435, 335, and 265 nm. However, the addition of the −SMe group on the ligand frame leads to moderate increase in the extinction coefficient of **2** compared to **1**.

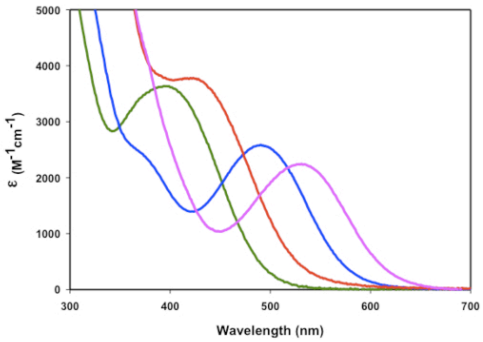

Figure 6. Electronic absorption spectra of $[Mn(qmtpm)(CO)_3(MeCN)]ClO_4$ (**2**, red trace), $[Mn(qmtpm)(CO)_3Br]$ (**3**, pink trace), $[Mn(pmtpm)(CO)_3(MeCN)]ClO_4$ (**4**, green trace), and $[Mn(pmtpm)(CO)_3Br]$ (**5**, blue trace) in $CHCl_3$.

The high extinction coefficient values for these bands in the 400−600 nm region confirm that they arise from charge transfer transition. Also, the red shift of these bands with more conjugation in the ligand frame (and/or electron-rich ligands or groups in the coordination sphere) readily identifies them as MLCT transition and results of theoretical calculations corroborate this assignment (vide infra).

Although solutions of **1**, **2**, and **4** in MeCN or MeOH are stable for several hours in the dark, exposure of such solutions to low power visible light leads to dramatic changes associated with CO release. Changes in the absorption spectrum of **2** upon illumination with 509 nm monochromatic light (5mW) are shown in Figure 7. Clean isosbestic points 500, 400, and 335 nm confirm that CO loss does not proceed via decomposition. Likewise, THF solutions of **3** and **5** exhibit

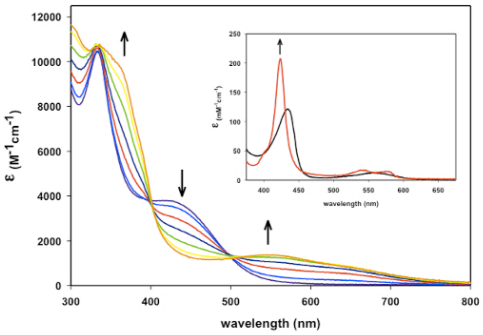

Figure 7. Changes in the electronic absorption spectrum of $[Mn(qmtpm)(CO)_3(MeCN)](ClO_4)$ (**2**) in MeCN upon exposure to monochromatic light (λ = 509 nm, 5mW). Inset: Formation of CO-Mb with light induced CO release from **2** in 100 mM phosphate buffer (pH 7.4).

stability in the dark, and CO release is only triggered upon illumination with 509 nm light with isosbestic points for **3** at 415 and 290 nm (Supporting Information, Figure S4).

Light-induced CO release of compounds **1**−**5** has been investigated by a modified myoglobin assay. In a typical experiment, MeCN or THF solutions of **1**−**5** were degassed and subsequently irradiated with a broadband light source fitted with a 400 nm cutoff filter. The resulting solution was flushed with N_2 gas, and the photogenerated CO was transferred via a cannula into a cuvette containing reduced myoglobin (Mb) in phosphate buffer (pH 7.4). In this method the possibility of carbonyl reduction by dithionite is eliminated.[38] In all cases, shift in the Soret band from 435 to 424 nm confirmed the formation of CO-Mb under anaerobic conditions (Figure 7 Inset). Because CO release takes place only upon light irradiation, it is evident that **1**−**5** comprise *an effective set of Mn-based photoCORMs*. Although the present carbonyls contain three CO ligands, we have not determined the exact number of CO molecules lost from each photoCORM under illumination. Ford and co-workers have commented on this issue in their work with the photoCORM $Na_3[W(CO)_5(TPPTS)]$. Exhaustive photolysis of this carbonyl afforded product(s) that still exhibited CO-related IR bands in its spectrum.[20] In our work, we have also noted that the exact amount of CO release from the photoCORMs upon illumination is quite difficult to quantify because of subsequent secondary reaction(s) of the initial photoproduct(s) with the oxygen, solvent, and other species in solution. Under strict anaerobic conditions, prolonged photolysis of the present carbonyls **1**−**5** in solvents like MeCN and THF afford products that exhibit weak CO stretching frequencies in the 2050−1950 cm^{-1} region. NMR measurements on these products indicated the presence of the intact ligand frames. When the photolysis experiments were performed with solutions in open vials, the final photoproducts exhibited strong EPR signals indicating formation of Mn(II) species. In a recent account, Kurt and Berends have reported the formation of both Mn(II) and Mn(III) species in photolysis of the photoCORM *fac*-$[Mn(CO)_3(tpm)]PF_6$ (tpm = tris(pyrazolyl)methane) under aerobic conditions.[39] Clearly, CO release from CORMs bearing multiple CO ligands follow complicated pathways leading to multiple photoproducts, and hence we have not attempted to characterize the photoproducts from **1**−**5** in the present study .

The CO release capacities of **1**−**5** under illumination with visible light have been determined in the present study to correlate the CO-releasing parameters with the features of the ligand (such as conjugation) and the nature of the sixth ligand (MeCN vs Br^-). For all these carbonyls, the rates of CO release obey a pseudo-first-order behavior (Supporting Information, Figure S4). The apparent rates of CO photorelease (k_{CO}) and the quantum yield values at 509 nm (ϕ_{509}) for **1**−**5** are shown in Table 3. The k_{CO} values of **1**, **2**, and **4** were measured in

Table 3. Apparent Rates of CO Release (k_{CO}) and Associated Quantum Yield Values at 509 nm (ϕ_{509}) of 1−5

compound	apparent rate (s^{-1}) (concentration = 1.10 mM)	quantum yield
1 (solv: MeCN)	$1.4 \times 10^{-3} \pm 0.1$	0.130 ± 0.010
2 (solv: MeCN)	$2.0 \times 10^{-3} \pm 0.1$	0.208 ± 0.010
3 (solv: THF)	$2.6 \times 10^{-3} \pm 0.1$	0.370 ± 0.010
4 (solv: MeCN)	$1.1 \times 10^{-3} \pm 0.1$	0.116 ± 0.010
5 (solv: THF)	$2.1 \times 10^{-3} \pm 0.1$	0.340 ± 0.010

CH_3CN, while those of **3** and **5** were obtained with THF solutions because of differences in solubility. As evident from Table 3, with increased conjugation in the ligand frame (going from **4** to **2**), the k_{CO} value increases from $1.1 \times 10^{-3} \pm 0.1$ to $2.0 \times 10^{-3} \pm 0.1$ s^{-1}. In addition, replacement of MeCN with Br^- (going from **2** to **3**) leads to a significant increase in the k_{CO} value (from $2.0 \times 10^{-3} \pm 0.1$ to $2.6 \times 10^{-3} \pm 0.1$ s^{-1}). The effect(s) of incorporating the −SMe group on the ligand frame is evident in the k_{CO} and ϕ_{509} values of **1** and **2**. The electron-rich S center enhances the ϕ_{509} value of **2** (0.208 ± 0.010) compared to **1** (0.130 ± 0.010) to a noticeable extent. Collectively, these correlations support our previous finding related to increased CO photolability with greater conjugation in the ligand frame.[25] In addition, the present results suggest that the ancillary ligands (like Br^-) can also influence the extent of CO photorelease. Since the −SMe donor is not coordinated to the Mn(I) center in **2**−**5**, it is not immediately evident why such modification of the ligand frames (as shown in Figure 1) affects the CO photolability of these photoCORMs. The results of DFT and TDDFT calculations, as described below, however provide valuable insight into the origins of such enhancement of CO photorelease in **2**−**5** (compared to **1**).

DFT and TDDFT Calculations. DFT and TDDFT calculations were utilized to obtain the optimized geometries, molecular orbital electron densities, and calculated electronic transitions for **1**−**5** to understand how the structural features of these photoCORMs correlate with their capacities of CO photorelease. The DFT optimized structures of **1**−**5** show good agreement with the bond lengths and bond angles observed in the corresponding crystal structure of each complex. Such data for **2**, **3**, and **5** are listed in Table 4 while the rest (for **1** and **4**) are included in Supporting Information, Table S1. The agreement supports the theoretical treatment of the molecules and allowed us to continue on with the TDDFT calculations. The calculated electronic transitions with oscillator strengths above 0.004 were collected, and those with energies falling within the range of the lowest energy experimental absorption band of each complex are presented in Table 5. For

Table 4. Selected Bond Distances (Å) and Angles (deg) of 2, 3, and 5 along with Optimized DFT Bond Distances and Bond Angles for Comparison

	complex **2**		complex **3**		complex **5**	
	X-ray	DFT	X-ray	DFT	X-ray	DFT
Mn−N1	2.120(2)	2.163	2.106(2)	2.166	2.054(2)	2.095
Mn−N2	2.063(3)	2.093	2.059(2)	2.088	2.049(2)	2.071
Mn−N3	2.013(3)	2.045				
Mn−Br			2.536(6)	2.586	2.5338(5)	2.581
Mn−C1	1.810(4)	1.831	1.800(4)	1.820	1.802(3)	1.828
Mn−C2	1.831(4)	1.823	1.804(3)	1.824	1.806(3)	1.820
Mn−C3	1.803(4)	1.852	1.790(4)	1.804	1.781(4)	1.803
C1−Mn−C2	86.82(18)	89.07	86.11(14)	88.12	89.87(14)	91.09
C1−Mn−C3	91.09(17)	97.25	89.42(15)	92.47	88.92(14)	91.69
C1−Mn−N2	91.75(15)	92.05	94.18(12)	93.25	97.25(11)	96.23
C1−Mn−N3	91.68(15)	90.05				
C2−Mn−C3	87.95(18)	96.14	89.48(14)	92.81	91.25(14)	93.07
C2−Mn−N1	102.79(14)	99.21	101.07(12)	100.18	94.12(12)	93.75
C2−Mn−N3	89.43(14)	85.77				
C3−Mn−N1	92.62(13)	84.85	91.68(12)	91.04	94.98(12)	94.45
C3−Mn−N2	98.73(14)	94.14	100.17(12)	100.16	94.14(11)	94.50
C1−Mn−Br			91.31(11)	89.97	88.55(10)	87.40
C2−Mn−Br			84.81(10)	82.30	86.97(10)	85.68

Table 5. Energies (*E*, nm) and Oscillator Strengths (*f*) of the Calculated (TDDFT) Electronic Transitions with the Molecular Orbitals Involved with Each Transition[a]

energy (nm)	oscillator strength (*f*)	transitions
	$[Mn(pimq)(CO)_3(MeCN)]^+$ (**1**)	
431.98	0.0259762	π(Q)-π(Ph)-π(MnCO)→π(Q)-π(SB)[HOMO→LUMO]
406.74	0.0573702	π(Q)-π(Ph)-d_{xz}(Mn)→π(Q)-π(SB)[HOMO-1→LUMO]
388.95	0.0307494	π(MnCO)-π(Ph)→π(Q)-π(SB)[HOMO-2→LUMO]
	$[Mn(qmtpm)(CO)_3(MeCN)]^+$ (**2**)	
533.21	0.0450962	π(PhS) →π(Q)-π(SB)[HOMO→LUMO]
459.29	0.0122483	π(MnCO)-π(Q)→π(Q)-π(SB)[HOMO-1→LUMO]
432.41	0.0189162	π(MnCO)-π(Q)→π(Q)-π(SB)[HOMO-2/HOMO-3→LUMO]
417.86	0.0334093	π(MnCO)-π(Q)→π(Q)-π(SB)[HOMO-2→LUMO]
	$[Mn(qmtpm)(CO)_3Br]$ (**3**)	
520.47	0.0046467	π(PhS)→π(Q)-π(SB)[HOMO→LUMO]
484.31	0.0166749	p(Br)-π(MnCO)→π(Q)-π(SB)[HOMO-1→LUMO]
460.92	0.0533586	p(Br)-π(MnCO)→π(Q)-π(SB)[HOMO-2→LUMO]
	$[Mn(pmtpm)(CO)_3(MeCN)]^+$ (**4**)	
484.60	0.0301023	π(PhS)→π(Pyr)−π(SB)[HOMO→LUMO]
372.72	0.0491039	π(MnCO)→π(Pyr)−π(SB)[HOMO-2→LUMO]
346.30	0.0606618	π(MnCO)-π(PhS)→π(Pyr)−π(SB)[HOMO-4→LUMO]
	$[Mn(pmtpm)(CO)_3Br]$ (**5**)	
491.25	0.0061503	π(PhS)→π(Pyr)-π(SB)[HOMO→LUMO]
446.20	0.0241548	π(MnCO)-p(Br)→π(Pyr)-π(SB)[HOMO-2→LUMO]

[a]Orbitals with greater contributions listed first. Only transitions with energies corresponding to the lowest energy absorption band observed experimentally for each complex are shown.

1, transitions of interest are the HOMO→LUMO (431 nm), HOMO-1→LUMO (406 nm), and HOMO-2→LUMO (388 nm). These correlate to the broad band observed at 430 nm for **1**. In case of **2**, HOMO→LUMO (533 nm), HOMO-1→LUMO (459 nm), combination orbital HOMO-2/HOMO-3→LUMO (432 nm) and HOMO-3→LUMO (417 nm) all fall under the experimental band at 435 nm. Similarly, the theoretical transitions HOMO→LUMO (520 nm), HOMO-1→LUMO (484 nm), HOMO-2→LUMO (460 nm) correlate to the 535 nm band observed experimentally for **3** while the 390 nm experimental band of **4** corresponds to HOMO→LUMO (484 nm), HOMO-2→LUMO (372 nm), and HOMO-4→LUMO (346 nm) transitions. And finally, the experimental band at 500 nm of **5** includes the theoretical transitions HOMO→LUMO (491 nm) and HOMO-2→LUMO (446 nm). Because these calculated transitions fall within the region of wavelengths that was employed to determine the capacity of CO photolability (as described above), we have examined the electron densities of the molecular orbitals that comprise these levels and check whether these transitions do labilize CO ligand(s) from these designed carbonyls. A complete list of transitions can be found in Supporting Information, Table S2.

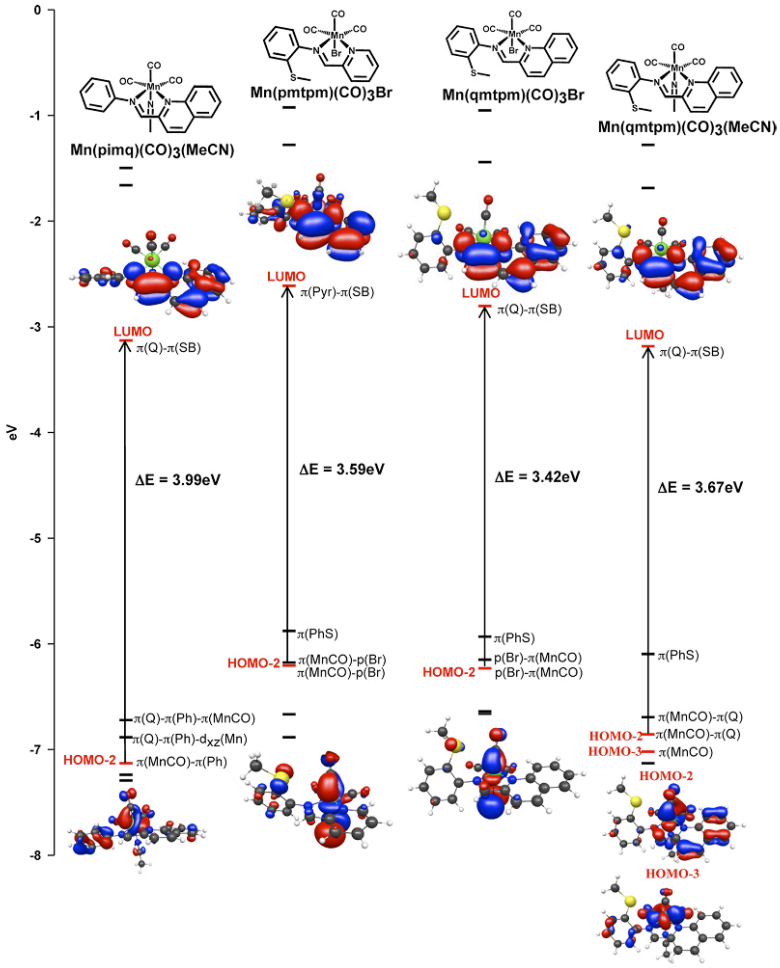

Figure 8. Calculated HOMO/LUMO energy diagram of complexes **1**, **5**, **3**, and **2** (from left to right). The most prominent MOs involved with transitions under the low energy band and their diagrams are shown. Transitions discussed in the text are shown in red (all other orbitals in TDDFT calculations are labeled in black).

The molecular orbital (MO) energy diagram, shown in Figure 8, displays the compositions of the three lowest occupied MOs and the LUMO of **1**, **2**, **3**, and **5**. The first and foremost point to note is that in each photoCORM, the lowest energy band corresponds to transitions that promote electron density from HOMO-2 (predominantly Mn-CO bonding character) to the LUMO mostly composed of the imine functionality and pyridine or quinoline ring. These MLCT transitions therefore shift electron density from the metal center to the ligand π frame, an event that is expected to curb the affinity of the Mn center toward CO (because of loss of π-backdonation from the metal). The CO photolability of the present photoCORMs observed at ~500 nm strongly suggests that these MLCT transitions are responsible for the observed CO photolability. As one goes from **5** to **3**, the change of the pyridine ring to more conjugated quinoline lowers the LUMO level and moves the λ_{max} from 500 to 535 nm. It is therefore evident that enhanced conjugation in the ligand frame sensitizes the resulting photoCORM more to the visible light. Inclusion of the electron-rich Br^- ligand raises both the HOMO-1 and HOMO-2 levels of **3** and **5** (both these MOs include contribution from Br^-, Table 5) compared to the MeCN-bound carbonyls. As a consequence, the MLCT transitions in the visible range are all red-shifted (Figure 8). This finding explains the red shift of these two photoCORMs (535 and 500 nm respectively) compared to **1** (430 nm), **2** (435 nm), and **4** (390 nm).

Although the −SMe group on the ligand frame does not participate in coordination in **2**−**5**, the HOMO of each of these carbonyls is composed of orbitals belonging to the phenyl ring

and the sulfur atom (Figure 8). Thus the HOMO→LUMO transition is an intraligand charge transfer that promotes electron density from the phenyl thioether moiety of the ligand frame to a MO associated mostly with the imine and the corresponding pyridine or quinoline functionality. A close scrutiny of the energy diagram however reveals that the absence of −SMe unit in **1** lowers the energy of the HOMO (consisting mostly of π(Ph) and π(Q) character) and leads to a slight blue shift of the low energy band (430 nm) compared to the analogous carbonyl **2** with −SMe unit on the ligand frame (435 nm). In addition, inclusion of the −SMe unit on the ligand frame enhances both the apparent rate of CO release and the ϕ_{509} value of **2** compared to **1** (Table 3). Since in all the present carbonyls the HOMO→LUMO transition contributes to the low energy band, it appears that the −SMe group enhances the overall CO photolability of **2**−**5** presumably through higher absorption of light in the visible region.

Taken together, the results of the theoretical calculations qualitatively support the hypotheses that guided our design principles. For example, it is evident that low energy MLCT transitions arising from MOs with metal-CO bonding character to MOs associated with the π-frame of the ligand could lead to scission of the Mn-CO bond(s) in the present photoCORMs **1**−**5** upon exposure to visible light. Increase in the CO photolability with more conjugated ligand frames further corroborates this conclusion. Baerends and Rosa have discussed the role of ligand-field and charge-transfer excited states in the photochemical dissociation of metal-CO bonds in metal carbonyls derived from α-diimine ligands.[40] The low energy MLCTs in such carbonyls also play key roles in the CO dissociation pathways. The results of the present work further indicate that inclusion of electron-rich functionality on ligands could enhance the CO photolability. In addition, ancillary ligands such as Br^- significantly augment the sensitivity of the designed photoCORMs (**1**−**5**) toward the visible light. More rigorous theoretical studies to establish the details of the mechanism of CO dissociation arising from the MLCT transition(s) are in progress in this laboratory.

SUMMARY AND CONCLUSIONS

The following are the summary and conclusions of this work.

(1) Five structurally related Mn(I) carbonyls **1**−**5** have been synthesized with a set of Schiff base ligands that contain pyridine and quinoline donors. The extent of conjugation has been systematically varied in these ligand frames. In addition, the effects of an electron-rich −SMe group on the ligand frame and an ancillary Br^- ligand in the coordination sphere have also been examined.

(2) The structures of the carbonyls indicate that the −SMe group does not bind the Mn(I) center in the equatorial plane because of its inability to replace a bound CO ligand. In addition to three facially ligated CO ligands, a MeCN or Br^- is also present.

(3) Although stable in the dark, solutions of all five carbonyls (in MeCN, MeOH, THF, or $CHCl_3$) rapidly release CO upon exposure to low power (5−15 mW) visible light (400−550 nm). These designed carbonyls could therefore be used as photoCORMs. The apparent rates of CO photorelease and quantum yield values at 509 nm (ϕ_{509}) increase linearly with increase in conjugation in the ligand frame. Replacement of MeCN with Br^- causes a significant red shift of the low energy band. Inclusion of the −SMe group on the ligand frame enhances both the apparent rate of CO release and the ϕ_{509} value.

(4) Results of density functional theory (DFT) and time dependent DFT (TDDFT) studies support the design principle that "transfer of electron density from the Mn(I) center to π orbitals of the ligand frame through MLCT transitions could curb the affinity of the metal center toward CO (requiring strong back bonding)". The calculated MO energy diagram also display proper alterations in the energy of the HOMO and LUMO levels upon inclusion of −SMe group and the Br^- ligand that lead to enhanced CO photolability of the respective photoCORMs.

(5) The excellent CO-releasing capacities of **1**−**5** and their sensitivity to visible light strongly support the design principles employed in the present work and provide further incentive toward isolation of new photoCORMs with predictable properties.

ASSOCIATED CONTENT

Supporting Information

X-ray crystallographic data (in CIF format) for $[Mn(pimq)(CO)_3(MeCN)]ClO_4$ (**1**), $[Mn(qmtpm)(CO)_3(MeCN)]ClO_4$ (**2**), $[Mn(qmtpm)(CO)_3Br]$ (**3**), $[Mn(pmtpm)(CO)_3(MeCN)]ClO_4$ (**4**), and $[Mn(pmtpm)(CO)_3Br]$ (**5**), thermal ellipsoid (probability level 50%) plots of **4** (Figure S1) and **5** (Figure S2), absorption profiles of **1** and **2** in MeCN (Figure S3), pseudo-first order plot of ln[**3**] vs time in THF (Figure S4), selected bond distances and angles of **1** and **4** with optimized DFT bond distances and angles (Table S1), complete list of energy and oscillator strength of the calculated (TDDFT) electronic transitions with the involved molecular orbitals (Table S2). This material is available free of charge via the Internet at http://pubs.acs.org.

AUTHOR INFORMATION

Corresponding Author

*E-mail: pradip@ucsc.edu.

Notes

The authors declare no competing financial interest.

ACKNOWLEDGMENTS

This research was supported by the NSF Grant CHE-0957251. M.G. was supported by the IMSD Grant GM-58903 and the NHGRI Grant HG002371. The X-ray facility at UCSC is supported by a NSF Major Research Instrumentation (MRI) Grant (CHE-0521569).

REFERENCES

(1) Kim, H. P.; Ryter, S. W.; Choi, A. M. K. *Pharmacol. Toxicol.* **2006**, *46*, 411−449.

(2) (a) Jaggar, J. H.; Li, A.; Parfenova, H.; Liu, J.; Umstot, E. S.; Dopico, A. M.; Leffler, C. W. *Circ. Res.* **2005**, *97*, 805−812. (b) Ndisang, J. F.; Tabien, H. E. N.; Wang, R. *J. Hypertens.* **2004**, *22*, 1057−1074. (c) Zhang, F.; Kaide, J.; Rodriguez-Mulero, F.; Abraham, N. G.; Nasjletti, A. *Am. J. Hypertens.* **2001**, *14*, 62S−67S. (d) McLaughlin, B. E.; Chretien, M. L.; Choi, C.; Brien, J. F.; Nakatsu, K.; Marks, G. S. *Can. J. Physiol. Pharmacol.* **2000**, *78*, 343−349. (e) Wang, R. *Can. J. Physiol. Pharmacol.* **1998**, *76*, 1−15. (f) Wang, R.; Wu, L.; Wang, Z. *Eur. J. Physiol.* **1997**, *434*, 285−291.

(3) (a) Kim, H. P.; Ryter, S. W.; Choi, A. M. K. *Annu. Rev. Pharmacol. Toxicol.* **2006**, *46*, 411−449. (b) Boczkowski, J.; Poderoso, J. J.; Motterlini, R. *Trends Biochem. Sci.* **2006**, *31*, 614−621. (c) Morse, D.; Sethi, J.; Choi, A. M. K. *Crit. Care Med.* **2002**, *30*, S12−S16.

(4) (a) Ahanger, A. A.; Prawez, S.; Leo, M. D. M.; Kathirvel, K.; Kumar, D.; Tandan, S. K.; Malik, J. K. *Eur. J. Pharmacol.* **2010**, *645*, 165−170. (b) Vieira, H. L. A.; Queiroga, C. S. F.; Alves, P. M. *J. Neurochem.* **2008**, *107*, 375−384. (c) Brouard, S.; Otterbein, L. E.; Anrather, J.; Tobiasch, E.; Bach, F. H.; Choi, A. M.; Soares, M. P. *J. Exp. Med.* **2000**, *192*, 1015−1026.
(5) Zuckerbraun, B. S.; Chin, B. Y.; Bilban, M.; de Costa d'Avila, J.; Rao, J.; Billiar, T. R.; Otterbein, L. E. *FASEB J.* **2007**, *21*, 1099−1106.
(6) Otterbein, L. E.; Bach, F. H.; Alam, J.; Soares, M.; Lu, H. T.; Wysk, M.; Davis, R. J.; Flavell, R. A.; Choi, A. M. K. *Nat. Med.* **2000**, *6*, 422−428.
(7) Kohmoto, J.; Nakao, A.; Stolz, D. B.; Kaizu, T.; Tsung, A.; Ikeda, A.; Shimizu, H.; Takahashi, T.; Tomiyama, K.; Sugimoto, R.; Choi, A. M. K.; Billiar, T. R.; Murase, N.; McCurry, K. R. *Am. J. Transplant.* **2007**, *7*, 2279−2290.
(8) Nakao, A.; Choi, A. M. K.; Murase, N. *J. Cell. Mol. Med.* **2006**, *10*, 650−671.
(9) (a) Ghosh, S.; Wilson, M. R.; Choudhury, S.; Yamamoto, H.; Goddard, M. E.; Falusi, B.; Marczin, N.; Takata, M. *Am. J. Physiol. Lung Cell Mol. Physiol.* **2005**, *288*, L1003−L1009. (b) Fujita, T.; Toda, K.; Karimova, A.; Yan, S. F.; Naka, Y.; Yet, S. F.; Pinsky, D. J. *Nat. Med.* **2001**, *7*, 598−604.
(10) (a) Stein, A. B.; Bolli, R.; Dawn, B.; Sanganalmath, S. K.; Zhu, Y.; Wang, O. L.; Guo, Y.; Motterlini, R.; Xuan, Y. T. *J. Mol. Cell. Cardiol.* **2012**, *52*, 228−236. (b) Stein, A. B.; Guo, Y.; Tan, W.; Wu, W. J.; Zhu, X.; Li, Q.; Luo, C.; Dawn, B.; Johnson, T. R.; Motterlini, R.; Bolli, R. *J. Mol. Cell. Cardiol.* **2005**, *38*, 127−134.
(11) (a) Romão, C. C.; Blättler, W. A.; Seixas, J. D.; Bernardes, G. J. L. *Chem. Soc. Rev.* **2012**, *41*, 3571−3583. (b) Alberto, R.; Motterlini, R. *Dalton Trans.* **2007**, 1651−1660. (c) Johnson, T. R.; Mann, B. E.; Clark, J. E.; Foresti, R.; Green, C. J.; Motterlini, R. *Angew. Chem., Int. Ed.* **2003**, *42*, 3722−3729.
(12) Johnson, T. R.; Mann, B. E.; Teasdale, I. P.; Adams, H.; Foresti, R.; Green, C. J.; Motterlini, R. *Dalton Trans.* **2007**, 1500−1508.
(13) Zhang, W. Q.; Whitwood, A. C.; Fairlamb, I. J. S.; Lynam, J. M. *Inorg. Chem.* **2010**, *49*, 8941−8952.
(14) Fairlamb, I. J. S.; Lynam, J. M.; Moulton, B. E.; Taylor, I. E.; Duhme-Klair, A. K.; Sawle, P.; Motterlini, R. *Dalton Trans.* **2007**, 3603−3605.
(15) Zobi, F.; Blacque, O.; Jacobs, R. A.; Schaub, M. C.; Bogdanova, A. Y. *Dalton Trans.* **2012**, *41*, 370−378.
(16) Bikiel, D. E.; González Solveyra, E.; Di Salvo, F.; Milagre, H. M. S.; Eberlin, M. N.; Corrêa, R. S.; Ellena, J.; Estrin, D. A.; Doctorovich, F. *Inorg. Chem.* **2011**, *50*, 2334−2345.
(17) Gonzalez, M. A.; Fry, N. L.; Burt, R.; Davda, R.; Hobbs, A. J.; Mascharak, P. K. *Inorg. Chem.* **2011**, *50*, 3127−3134.
(18) Herrick, R. S.; Brown, T. L. *Inorg. Chem.* **1984**, *23*, 4550−4553.
(19) Engelking, P. C.; Lineberger, W. C. *J. Am. Chem. Soc.* **1979**, *101*, 5569−5573.
(20) Rimmer, R. D.; Richter, H.; Ford, P. C. *Inorg. Chem.* **2010**, *49*, 1180−1185.
(21) Jackson, C. S.; Schmitt, S.; Dou, Q. P.; Kodanko, J. J. *Inorg. Chem.* **2011**, *50*, 5336−5338.
(22) Kretschmer, R.; Gessner, G.; Görls, H.; Heinemann, S. H.; Westerhausen, M. *J. Inorg. Biochem.* **2011**, *105*, 6−9.
(23) Crook, S. H.; Mann, B. E.; Meijer, A. J. H. M.; Adams, H.; Sawle, P.; Scapens, D.; Motterlini, R. *Dalton Trans.* **2011**, *40*, 4230−4235.
(24) (a) Pfeiffer, H.; Rojas, A.; Niesel, J.; Schatzschneider, U. *Dalton Trans.* **2009**, 4292−4298. (b) Kunz, P. C.; Huber, W.; Rojas, A.; Schatzschneider, U.; Spingler, B. *Eur. J. Inorg. Chem.* **2009**, 5358−5366.
(25) Gonzalez, M. A.; Yim, M. A.; Cheng, S.; Moyes, A.; Hobbs, A. J.; Mascharak, P. K. *Inorg. Chem.* **2012**, *51*, 601−608.
(26) Roy, S.; Mitra, P.; Patra, A. K. *Inorg. Chim. Acta* **2011**, *370*, 247−253.
(27) Castro, A. G.; Costa, J. S.; Pievo, R.; Massera, C.; Mutikainen, I.; Turpeinen, U.; Gamez, P.; Reedijk, J. *Z. Anorg. Allg. Chem.* **2008**, *634*, 2477−2482.
(28) Edwards, D. A.; Marshalsea, J. *J. Orgamomet. Chem.* **1977**, *131*, 73−91.
(29) Hamer, F. M. *J. Chem. Soc.* **1952**, 3197−3211.
(30) Montalti, M.; Credi, A.; Prodi, L.; Gandolfi, M. T. *Handbook of Photochemistry*, 3rd ed.; CRC Press: Boca Raton, FL, 2006.
(31) Nemukhin, A. V.; Grigorenko, B. L.; Granovsky, A. A. *Moscow Univ. Chem. Bull.* **2004**, *45*, 75−102.
(32) Miertus, S.; Scrocco, E.; Tomasi, J. *Chem. Phys.* **1981**, *55*, 117−120.
(33) (a) Patel, B.; Reid, G. *J. Chem. Soc., Dalton Trans.* **2000**, 1303−1307. (b) Connolly, J.; Genge, A. R. J.; Levason, W.; Orchard, S. D.; Pope, S. J. A.; Reid, G. *J. Chem. Soc., Dalton Trans.* **1999**, 2343−2351. (c) Connolly, J.; Goodban, G. W.; Reid, G.; Slawin, A. M. Z. *J. Chem. Soc., Dalton Trans.* **1998**, 2225−2231.
(34) (a) Kunz, P. C.; Huber, W.; Rojas, A.; Schatzschneider, U.; Spingler, B. *Eur. J. Inorg, Chem.* **2009**, 5358−5366. (b) Carlos, R. M.; Carlos, I. A.; Lima Neto, B. S.; Neumann, M. G. *Inorg. Chim. Acta* **2000**, *299*, 231−237. (c) Reger, D. L.; Grattan, T. C.; Brown, K. J.; Little, C. A.; Lamba, J. J. S.; Rheingold, A. L.; Sommer, R. D. *J. Organomet. Chem.* **2000**, *607*, 120−128. (d) Hyams, I. J.; Bailey, R. T.; Lippincott, E. R. *Spectrochim. Acta* **1967**, *23A*, 273−284.
(35) (a) García-Escudero, L. A.; Miguel, D.; Turiel, J. A. *J. Organomet. Chem.* **2006**, *691*, 3434−3444. (b) Valín, M. L.; Moreiras, D.; Solans, X.; Font-Altaba, M.; García-Alonso, F. J. *Acta Crystallogr., Sect. C* **1986**, *42*, 417−418.
(36) Zhang, J. A.; Pan, M.; Jiang, J. J.; She, Z. G.; Fan, Z. J.; Su, C. Y. *Inorg. Chim. Acta* **2011**, *374*, 269−277.
(37) Stor, G. J.; van der Vis, M.; Stufkens, D. J.; Oskam, A. *J. Organomet. Chem.* **1994**, *482*, 15−29.
(38) McLean, S.; Mann, B. E.; Poole, R. K. *Anal. Biochem.* **2012**, *427*, 36−40.
(39) Berends, H.-M.; Kurz, P. *Inorg. Chim. Acta* **2012**, *380*, 141−147.
(40) Baerends, E. J.; Rosa, A. *Coord. Chem. Rev.* **1998**, *177*, 97−125.

Chapter 4. Density Functional Theory Studies to elucidate origin of CO Photolability in d^6 Metal Carbonyls bearing the tridentate NNS ligand qmtpm

Part II: DFT and TDDFT Studies of Ruthenium qmtpm Carbonyl Complexes

4.II.1. Background

Renewed interest in the principles governing the photoreactivity of transition metal carbonyl complexes is attributed to the recent findings on the fundamental role of endogenously produced carbon monoxide (CO) in signaling pathways.[1] With the abundance of CO targets which include both metalloproteins and non-heme proteins such as mitogen-activated protein kinases (discussed in the introductory chapter), it is becoming clear that CO is essential in anti-inflammatory and immune response mechanisms. Interestingly, such CO-mediated processes appear to complement that of the more established signaling molecule, nitric oxide (NO). Given our lab's extensive work in the area of photolabile metal nitrosyls as NO-donors,[2] we decided to extend and test our design principles in the syntheses of photosensitive metal nitrosyls to the preparation of new metal carbonyl complexes as photoactive carbon monoxide releasing molecules (photoCORMs).

Optical excitation of transition metal carbonyl complexes typically results in the breaking of a metal–CO bond leading to CO photodissociation. CO loss and the inherent photosensitivity of this class of compounds has been attributed to metal-to-ligand charge transfer (MLCT) excited states, as MLCT electronic transitions are common in organometallic compounds bearing both low valent metal centers and electron-accepting ligand moieties (such as bipyridines, phenanthrolines and

polypyridines).[3] Singlet MLCT excited states have been determined to be more accessible than the associated ligand field (LF) excited states and it is from the primary MLCT excited state that other charge transfer excited states (such as ligand field) become accessible.[4] For metal carbonyl complexes, this single electron excitation into an MLCT excited state eventually culminates in metal–CO bond homolysis.

We postulated that tuning of MLCT states that govern CO photodissociation could be achieved with the incorporation of designed ligand frames and strategic placement of ancillary ligands. Specifically, we intended to utilize ligand frames and ancillary groups that reduce CO affinity to the metal center via MLCT interactions thereby generating more sensitized CO donors. By employing density functional theory (DFT) and time dependent density functional theory (TDDFT) calculations on selected photoCORMs, we can gain insight into the nature of the molecular orbitals and the respective electronic transitions that give rise to the observed MLCT photobands. DFT and TDDFT studies also provide the fractional contributions of the CO groups, metal center and associated ligands to the charge transfer band of interest. Such information could guide succeeding design strategies in the preparation of photoCORMs for use in physiologically relevant studies.

Because the inclusion of conjugated moieties seem vital in the preparation of photoCORMs with activities in the visible range, we employed the potentially tridentate ligand, 2-quinoline-N-(2'-methylthiophenyl) methyleneimine (qmtpm) in the syntheses of Mn(I)[5] and Ru(II) carbonyl complexes as detailed in the first section

of Chapter 4 and the second section of Chapter 3, respectively. This ligand features not only a quinoline group, but a thiophenyl and imine functionality in its framework as well. In part 1 of chapter 4, we report DFT and TDDFT studies on a series of Mn(I) qmtpm carbonyl complexes

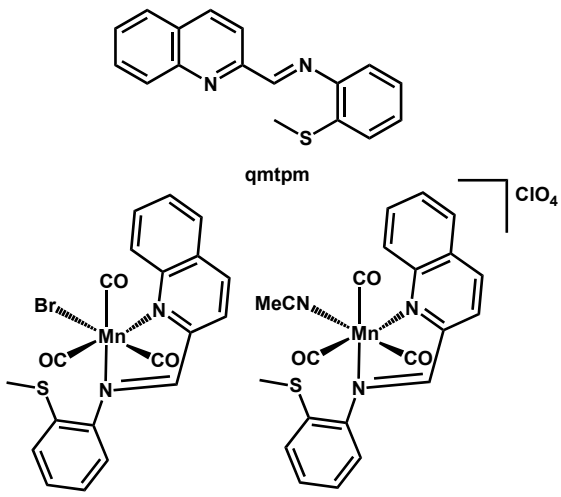

[Mn(qmtpm)(CO)$_3$Br] [Mn(qmtpm)(CO)$_3$(MeCN)]ClO$_4$

wherein qmtpm is bound only through the N-donors, leaving the thioether group uncoordinated. The qmtpm ligand and the corresponding cationic and neutral species [Mn(qmtpm)(CO)$_3$(CH$_3$CN)]ClO$_4$ and [Mn(qmtpm)(CO)$_3$Br], respectively are shown above. TDDFT analysis reveals that the inclusion of a quinoline moiety lowers the energy of the LUMO level while the presence of a Br^- raises the HOMO level of [Mn(qmtpm)(CO)$_3$Br]. The net result of which is an overall decrease in metal to ligand charge transfer energies as evidenced by the red shifted absorption maximum of [Mn(qmtpm)(CO)$_3$Br] (λ_{max} = 535 nm) when compared to that of [Mn(qmtpm)(CO)$_3$(CH$_3$CN)]ClO$_4$ (λ_{max} = 435 nm).[5]

It should be noted that although we achieved a progressive red shift in the MLCT band energies in this series of Mn(I) qmtpm carbonyl complexes, the thioether group remains unligated presumably due to the low affinity of Mn(I) centers for –SMe donors. Meridional binding of qmtpm was achieved with the use of Ru(II) centers that are isoelectronic with Mn(I), yet have a higher positive charge. In this

chapter, we examine the nature of the low energy charge transfer bands of $[Ru(Cl)(CO)(qmtpm)(PPh_3)]BF_4$, $[Ru(Cl)(CO)_2(qmtpm)]ClO_4$, $[Ru(Cl)(MeCN)(qmtpm)(PPh_3)]BF_4$ and $[Ru(MeCN)_2(qmtpm)(PPh_3)]ClO_4$ (shown in Figure 4.II.1) through DFT and TDDFT studies performed by a colleague, Samantha Carrington. We will correlate the observed CO photolability with the electronic transitions comprising their low energy photobands. By probing the character of the most red-shifted charge transfer bands, we can elucidate role of the qmtpm ligand frame and ancillary ligands in promoting CO labilization. In addition, we will examine the effect of increasing CO ligands on the photosensitivity and CO-donating capacities of $[Ru(Cl)(CO)(qmtpm)(PPh_3)]BF_4$ and $[Ru(Cl)(CO)_2(qmtpm)]ClO_4$, which incorporate one and two CO groups, respectively.

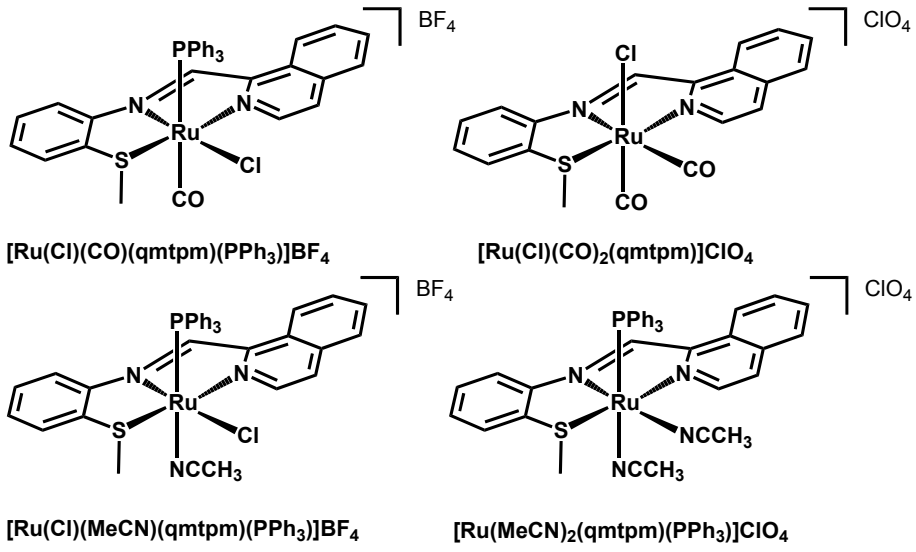

Figure 4.II.1. Structures of $[Ru(Cl)(CO)(qmtpm)(PPh_3)]BF_4$, $[Ru(Cl)(CO)_2(qmtpm)]ClO_4$, $[Ru(Cl)(MeCN)(qmtpm)(PPh_3)]BF_4$ and $[Ru(MeCN)_2(qmtpm)(PPh_3)]ClO_4$ utilized in DFT and TDDFT studies.

4.II.2. Geometry Optimizations of and Electronic Structure of the Complexes

The DFT-optimized geometries of $[Ru(Cl)(CO)(qmtpm)(PPh_3)]BF_4$, $[Ru(Cl)(CO)_2(qmtpm)]ClO_4$ and $[Ru(MeCN)_2(qmtpm)(PPh_3)]ClO_4$ were obtained using the hybrid functional PBE0. The calculated metric parameters shown in Table 4.II.1 are in good agreement with the experimental bond lengths and angles derived from the X-ray crystal structures of $Ru(Cl)(CO)(qmtpm)(PPh_3)]BF_4$, $[Ru(Cl)(CO)_2(qmtpm)]ClO_4$ and $[Ru(MeCN)_2(qmtpm)(PPh_3)]ClO_4$. The structure of $[Ru(Cl)(MeCN)(qmtpm)(PPh_3)]BF_4$ was obtained by exchanging an acetonitrile of $[Ru(MeCN)_2(qmtpm)(PPh_3)]ClO_4$ with Cl^- followed by optimization. The agreement supports the theoretical treatment of the molecules quite well.

Contour plots of selected molecular orbitals along with the contributions of the ligands and the metal centers in $[Ru(Cl)(CO)(qmtpm)(PPh_3)]BF_4$, $[Ru(Cl)(CO)_2(qmtpm)]ClO_4$, $[Ru(Cl)(MeCN)(qmtpm)(PPh_3)]BF_4$ and $[Ru(MeCN)_2(qmtpm)(PPh_3)]ClO_4$ are shown in Figures 4.II.2 – 4.II.5. The LUMO of the carbonyls $[Ru(Cl)(CO)(qmtpm)(PPh_3)]BF_4$ and $[Ru(Cl)(CO)_2(qmtpm)]ClO_4$ mostly consists of qmtpm ligand (π^*) character at 68% and 76%, respectively. Much of the calculated electron densities noted in these respective LUMOs of $[Ru(Cl)(CO)(qmtpm)(PPh_3)]BF_4$ and $[Ru(Cl)(CO)_2(qmtpm)]ClO_4$ are localized within the quinoline moiety (Figure 4.II.2 -4.II.3), suggesting that the inclusion of conjugated groups leads to a greater electron accepting character of the ligand frame

Table 4.II.1. A Comparison of Selected Experimental and Calculated Metric Parameters of $Ru(Cl)(CO)(qmtpm)(PPh_3)]BF_4$, $[Ru(Cl)(CO)_2(qmtpm)]ClO_4$, $[Ru(MeCN)_2(qmtpm)(PPh_3)]ClO_4$

$Ru(Cl)(CO)(qmtpm)(PPh_3)]BF_4$			**$Ru(Cl)(CO)_2(qmtpm)]ClO_4$**		
Bonds	**X-ray**	**Calculated**	***Bonds***	**X-ray**	**Calculated**
Ru - N1	2.1633(18)	2.188729	*Ru - N1*	2.1305(19)	2.134283
Ru - N2	2.0190(19)	2.026392	*Ru - N2*	2.060(2)	2.07098
Ru- S1	2.3166	2.339797	*Ru- S1*	2.3357	2.3595
Ru - C1	1.923(2)	1.883281	*Ru - C1*	1.903(3)	1.884492
Ru - C2	−−−	−−−	*Ru - C2*	1.890(3)	1.905
Ru - P1	2.4719(7)	2.511469	*Ru - P1*	−−−	−−−
Ru - Cl1	2.4352(6)	2.435748	*Ru – Cl1*	2.4176(7)	2.395094
C1 - O1	1.127(3)	1.147191	*C1 - O1*	1.137(3)	1.147559
C2 -O2	−−−	−−−	*C2 -O2*	1.130(3)	1.141917
Angles		***Angles***			
C1-Ru-Cl1	85.58(6)	85.0212	*C1-Ru-Cl1*	85.22(8)	85.3196
C1-Ru-S1	92.31(7)	93.23859	*C1-Ru-S1*	93.45(8)	93.33569
C1-Ru-N1	89.30(8)	89.04546	*C1-Ru-N1*	103.47(10)	102.88598
C1-Ru-N2	93.44(8)	94.33582	*C1-Ru-N2*	171.24(10)	169.41505
C1-Ru-P1	175.70(6)	174.83369	*Cl1-Ru-S1*	84.88(2)	84.96832
Cl1-Ru-S1	91.53(2)	90.61036	*N1-Ru-N2*	78.13(8)	78.61539
N1-Ru-N2	78.48(7)	78.55427	*N1-Ru-Cl1*	88.64(6)	86.40594
N1-Ru-Cl1	105.25(5)	106.01466	*N1-Ru-S1*	161.32(6)	160.92398
N1-Ru-S1	163.22(5)	163.3577	*N2-Ru-Cl1*	86.21(6)	84.31732
N2-Ru-Cl1	176.11(5)	175.35931	*N2-Ru-S1*	83.96(6)	83.61897
N2-Ru-S1	84.75(5)	84.83389	*C2-Ru-N1*	90.53(9)	91.60723
P1-Ru-Cl1	90.27(2)	89.81262	*C2-Ru-N2*	93.89(10)	94.71819
P1-Ru-S1	86.67(2)	86.85036	*C2-Ru-S1*	95.99(8)	96.75719
P1-Ru-N1	92.88(5)	92.34336	*C2-Ru-C1*	94.71(11)	95.70815
P1-Ru-N2	90.63(5)	90.8174	*C2-Ru-Cl1*	179.13(8)	177.92764
Ru-C1-O1	173.7(2)	177.9337	*Ru-C1-O1*	173.4(32)	175.62418
			Ru-C2-O2	175.6(2)	177.91805

$[Ru(MeCN)_2(qmtpm)(PPh_3)]ClO_4$

Bonds	**X-ray**	**Calculated**
Ru - N1	2.155(5)	2.153605
Ru - N2	2.017(2)	2.020038
Ru- S1	2.3137(18)	2.3371
Ru - N3	2.087(6)	2.084611
Ru - N4	2.056(6)	2.035621
Ru - P1	2.3485(19)	2.407833
Angles		
N1-Ru-N2	77.9(2)	78.436
N1-Ru-N3	84.5(2)	84.88618
N1-Ru-N4	104.7(2)	104.65232
N1-Ru-S1	162.87(15)	163.07243
N1-Ru-P1	94.12(14)	93.31152
N2-Ru-N3	91.2(2)	91.37872
N2-Ru-N4	176.4(2)	176.39006
N2-Ru-S1	85.29(15)	84.75707
N3-Ru-N4	86.7(2)	87.07103
N3-Ru-S1	92.46(16)	93.58776
N4-Ru-S1	91.89(17)	92.08205
P1-Ru-N2	91.92(15)	91.85065
P1-Ru-N3	176.21(16)	175.91472
P1-Ru-N4	90.24(16)	89.8455
P1-Ru-S1	89.89(7)	89.19897

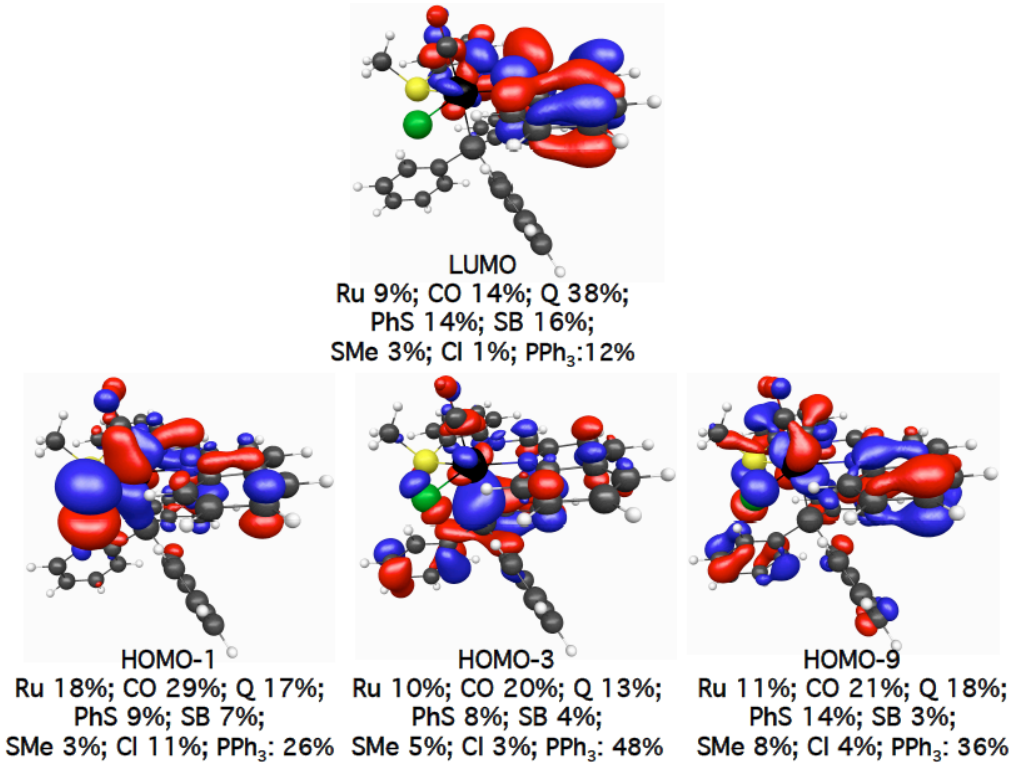

Figure 4.II.2. Contour plots of selected molecular orbitals of $[Ru(Cl)(CO)(qmtpm)(PPh_3)]BF_4$.

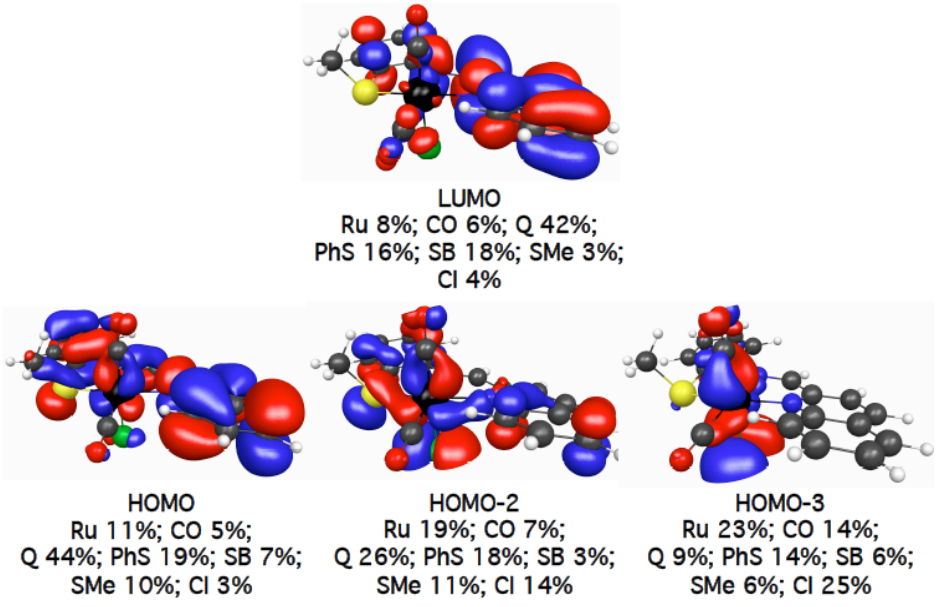

Figure 4.II.3. Contour plots of selected molecular orbitals of $[Ru(Cl)(CO)_2(qmtpm)]ClO_4$.

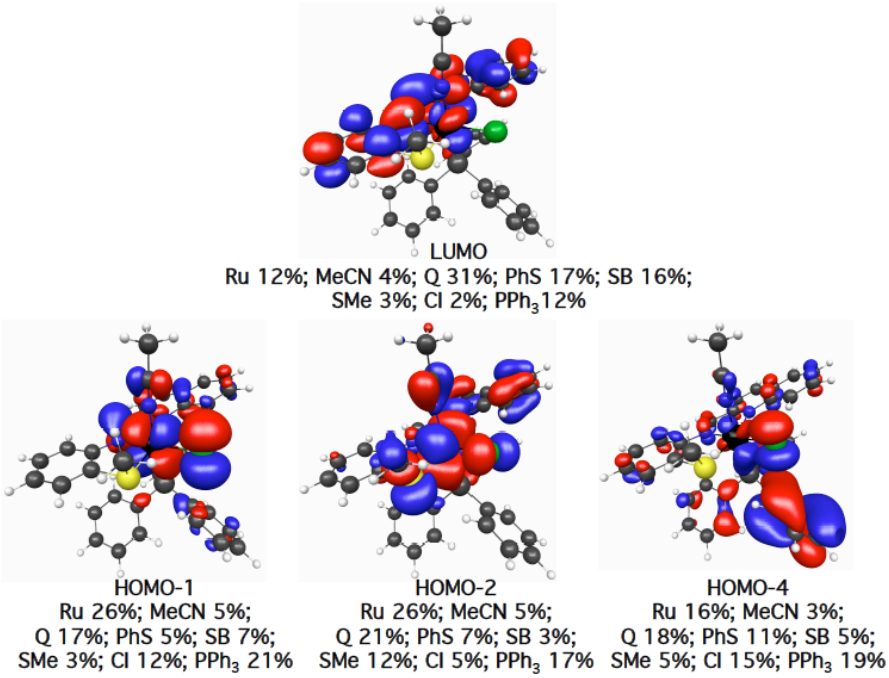

Figure 4.II.4. Contour plots of selected molecular orbitals of $[Ru(Cl)(MeCN)(qmtpm)(PPh_3)]BF_4$.

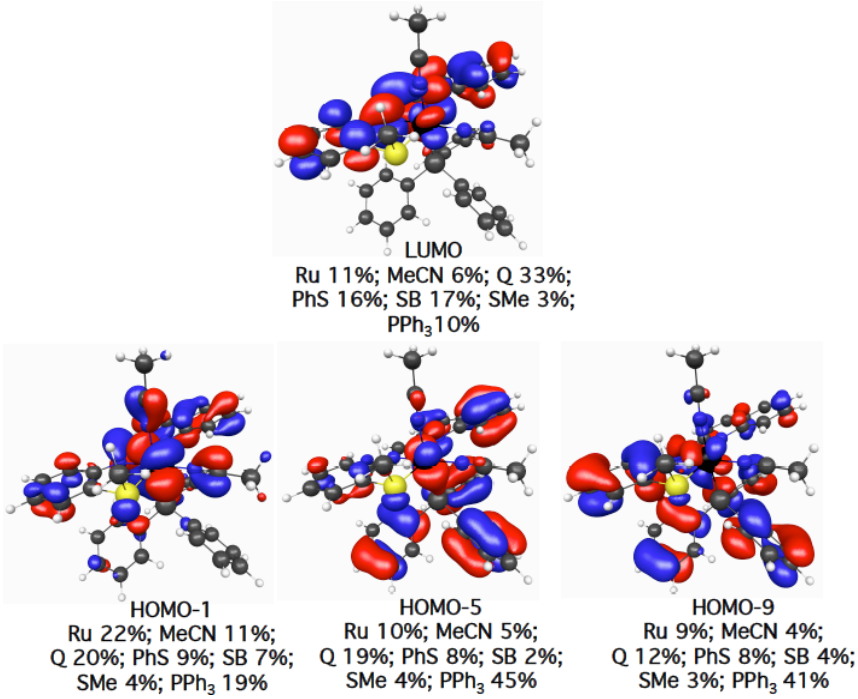

Figure 4.II.5. Contour plots of selected molecular orbitals of $[Ru(MeCN)_2(qmtpm)(PPh_3)]ClO_4$.

The HOMO-1 of $[Ru(Cl)(CO)(qmtpm)(PPh_3)]BF_4$ is mostly of metal and CO ligand character as seen in the calculated Ru and CO contributions (Figure 4.II.2).

In contrast, $[Ru(Cl)(CO)_2(qmtpm)]ClO_4$ exhibits a reduced degree of metal and CO ligand contribution in HOMO-2 and HOMO-3 even though it incorporates two CO groups. The contour plots of the solvato species $[Ru(Cl)(MeCN)(qmtpm)(PPh_3)]BF_4$ and $[Ru(MeCN)_2(qmtpm)(PPh_3)]ClO_4$ show similarities in molecular orbital composition. For instance, both LUMOs exhibit a comparable extent of quinoline, thiophenyl and imine contribution. Similarly, the HOMO-1 of both $[Ru(Cl)(MeCN)(qmtpm)(PPh_3)]BF_4$ and $[Ru(MeCN)_2(qmtpm)(PPh_3)]ClO_4$ are primarily Ru(II) and PPh_3 character (~40% in each case).

Table 4.II.2. Calculated (TDDFT) energies (E, nm), oscillator strengths (*f*), and nature of transitions[a] in the complexes.

Energy (nm)	Oscillator Strength	Transition
		$[Ru(Cl)(CO)(qmtpm)(PPh_3)]BF_4$
467	0.0489867	π(Ru-CO)-p(Cl)-π(Ru-PPh_3)→π^*(Q-PhS-SB)
431	0.0566891	π(PPh_3)-π(Ru-PPh_3)-π(Ru-CO)→π^*(Q-PhS-SB)
387	0.0302262	π(Ru-CO-SMe)→π^*(Q-PhS-SB)
381	0.0529700	π(PPh_3)-π(Ru-CO-SMe)→π^*(Q-PhS-SB)
374	0.0289463	π(PPh_3)-π(PhS)→π^*(Q-PhS-SB)
365	0.2146560	π(Ru-CO-SMe)-π(PPh_3)-π(PhS)→π^*(Q-PhS-SB)
323	0.0339253	π(Ru-Q-SMe-SB)-p(Cl)→π^*(Q-PhS-SB)
		$[Ru(Cl)(CO)_2(qmtpm)]ClO_4$
445	0.0275726	π(Q-PhS-SB)→π^*(Q-SB-PhS)
408	0.0165650	π(Q-PhS-SB)-π(Ru-CO-Cl)→π^*(Q-SB-PhS)
396	0.1794866	π(Ru-CO)-p(Cl)-π(PhS)→ π^*(Q-SB-PhS)
387	0.2110407	π(Ru-CO)-p(Cl)-π(PhS)→ π^*(Q-SB-PhS)
370	0.0729107	π(Ru-SMe-CO)-π(PhS)-p(Cl)→π^*(Q-SB-PhS)

		[Ru(Cl)(MeCN)(qmtpm)(PPh_3)]BF_4
589	0.0139661	π(Ru-SMe-MeCN-Cl)→π*(Q-PhS-SB)
539	0.0442363	π(Ru-Cl-SMe-MeCN)-π(Q)→π*(Q-PhS-SB)
414	0.0384803	π(Ru-PPh_3)→π*(Q-PhS-SB)
391	0.0905007	π(Ru-Cl-PPh_3)-π(Q)→π*(Q-PhS-SB)
382	0.0434632	π(PPh_3)-π(Ru-SB)→π*(Q-PhS-SB)
370	0.0384393	π(Ru-PPh_3)→π*(Q-PhS-SB)
365	0.0147778	π(Q)-π(Ru-PPh_3)→π*(Q-PhS-SB)
357	0.0790384	π(Ru-PPh_3-SMe)-p(Cl)→π*(Q-PhS-SB)
353	0.0131655	π(Ru-PPh_3-SMe)-p(Cl)→π*(Q-PhS-SB)
350	0.0223908	π(PPh_3)→π*(Q-PhS-SB)
342	0.0602548	π(PPh_3)- π(Sme)→π*(Q-PhS-SB)
		[Ru($MeCN)_2$(qmtpm)(PPh_3)]ClO_4
448.63	0.0787027	π(Ru-MeCN-PPh_3)→π*(Q-SB-PhS)
378.11	0.0210149	π(Ru-Q-PPh_3)→π*(Q-SB-PhS)
375.30	0.0685953	π(Ru-PPh_3)-π(PhS)→π*(Q-SB-PhS)
357.03	0.0148138	π(Ru-PPh_3)→π*(Q-SB-PhS)
346.99	0.2105311	π(PPh_3-PhS)-π(Ru-SB)→π*(Q-SB-PhS)
328.59	0.0473331	π(Ru-PhS-SMe)→π*(Q-SB-PhS)

[a] Orbitals with greater contributions listed first

4.II.3. TDDFT calculation and electronic spectra

The calculated electronic transitions of [Ru(Cl)(CO)(qmtpm)(PPh_3)]BF_4, [Ru(Cl)($CO)_2$(qmtpm)]ClO_4, [Ru(Cl)(MeCN)(qmtpm)(PPh_3)]BF_4 and [Ru($MeCN)_2$(qmtpm)(PPh_3)]ClO_4 with oscillator strengths above 0.0139 were collected, and those with energies falling within the range of the lowest energy absorption band of each complex are presented in Table 4.II.2. As shown in Figure 4.II.8, the theoretical electronic spectrum of [Ru(Cl)(CO)(qmtpm)(PPh_3)]BF_4 is in good agreement with the experimental spectrum obtained in acetonitrile. Complex [Ru(Cl)(CO)(qmtpm)(PPh_3)]BF_4 exhibits two major bands in the 300-500 nm region namely, the MLCT band at 460 nm and a higher energy absorption at 370 nm.

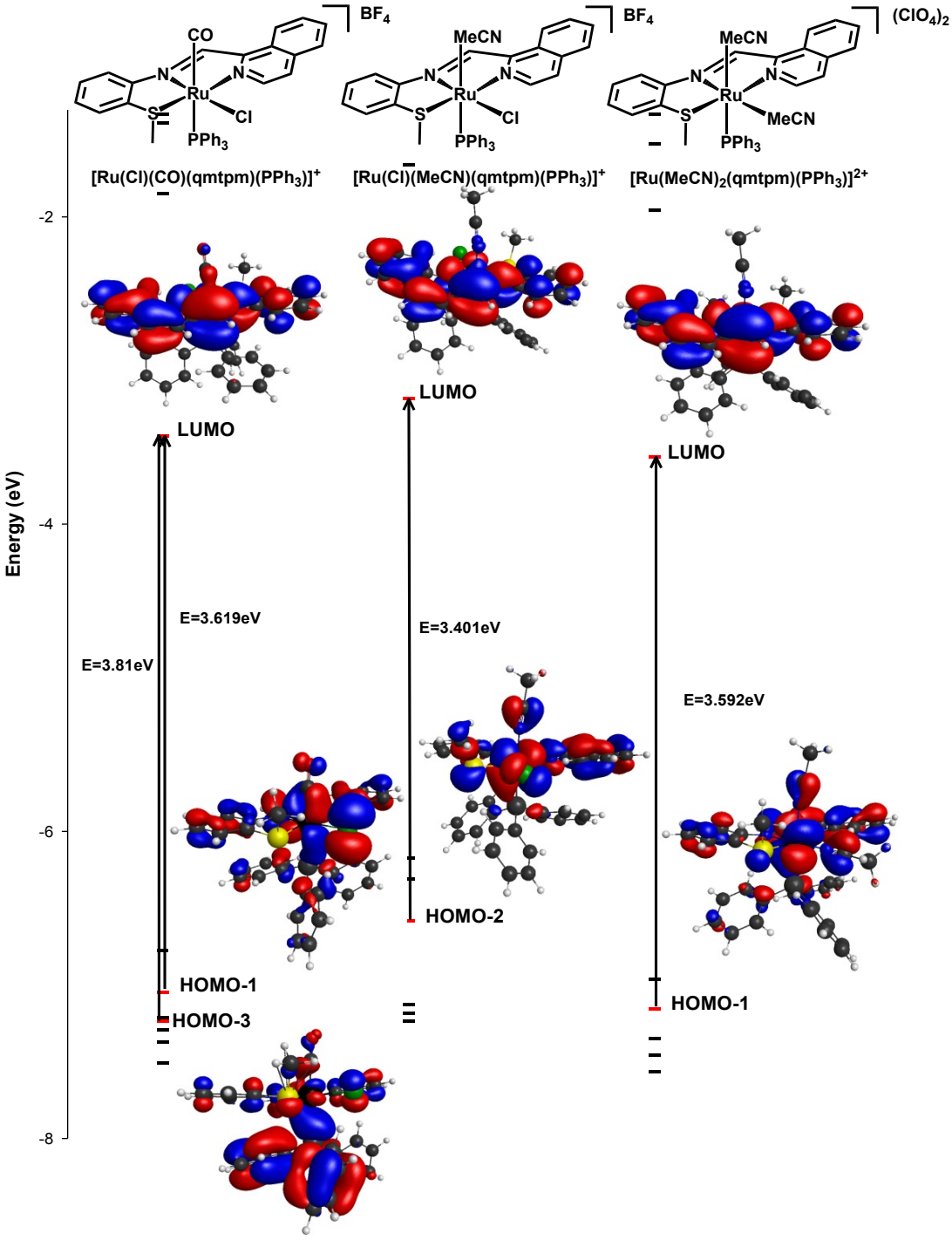

Figure 4.II.6. Calculated HOMO/LUMO energy diagram of $[Ru(Cl)(CO)(qmtpm)(PPh_3)]BF_4$, $[Ru(Cl)(MeCN)(qmtpm)(PPh_3)]BF_4$ and $[Ru(MeCN)_2(qmtpm)(PPh_3)]ClO_4$ (left to right). The most prominent MOs involved with under the low energy band and their diagrams are shown

TDDFT results indicate that for [Ru(Cl)(CO)(qmtpm)(PPh_3)]BF_4, two theoretical transitions in the ~460 nm region are the HOMO-1→LUMO (468 nm) and HOMO-3→LUMO (432 nm). The band at 370 nm corresponds to a HOMO-9→LUMO transition bearing the highest oscillation strength at 365 nm, along with a few weaker transitions (Figure 4.II.8). Close inspection of the molecular orbital (MO) energy diagram (Figure 4.II.6) displaying the electron densities of the MOs that comprise these levels reveal that HOMO-1 of [Ru(Cl)(CO)(qmtpm)(PPh_3)]BF_4 is mostly (π)Ru-CO bonding in character mixed with moderate (π)Ru-PPh_3 contribution while HOMO-3 is mainly (π)Ru-PPh_3 with modest (π)Ru-CO participation. The LUMO on the other hand is mostly composed of the ligand frame consisting of the π* orbital of the quinoline, the imine functionality, and the π* orbital of the thiophenyl (PhS) unit. It is important to note that exposure to visible light ($\lambda \geq 440$ nm) causes moderate CO photorelease from [Ru(Cl)(CO)(qmtpm)(PPh_3)]BF_4. The TDDFT results indicate that such Ru-CO bond labilization arises from shift of electron density from the Ru-CO moiety to the ligand frame. Partial reduction in Ru−PPh_3 backbonding also occurs during the 431 nm transition.

The much faster photorelease of CO from [Ru(Cl)(CO)(qmtpm)(PPh_3)]BF_4 upon exposure to light with $\lambda \geq 380$ nm stems from the predicted HOMO-9→LUMO transition at 365 nm. As previously shown in Figure 4.II.2, HOMO-9 also has a strong (π)Ru-CO character in addition to moderate contribution from the quinoline π orbital. Transfer of electron density from this orbital to the LUMO therefore results in

accelerated CO release. Taken together, these results suggest that transitions that shift electron density from the (π)Ru-CO moiety to the ligand frame promote CO release from photoCORMs like $[Ru(Cl)(CO)(qmtpm)(PPh_3)]BF_4$.

The photoproduct $[Ru(Cl)(MeCN)(qmtpm)(PPh_3)]BF_4$ exhibits its MLCT band at 535 nm (Figure 4.II.10). TDDFT results predict a theoretical HOMO-2→LUMO transition at 590 nm and a comparatively stronger HOMO-1/HOMO-2→LUMO transition at 539 nm. As evident from the MO diagram (Figure 4.II.6), replacement of CO with MeCN (a moderate π acceptor) raises the energies of the occupied MOs, while the LUMO (mostly comprised of the π* orbitals spread over the qmtpm ligand frame) are minimally affected. The net result is a lowering (red shift) of the electronic transition energies as reflected in the change of color from orange-yellow (in the case of $[Ru(Cl)(CO)(qmtpm)(PPh_3)]BF_4$) to magenta (in the case of $[Ru(Cl)(MeCN)(qmtpm)(PPh_3)]BF_4$) upon CO loss.

Replacement of a Cl^- (σ-donor) in $[Ru(Cl)(MeCN)(qmtpm)(PPh_3)]BF_4$ by MeCN (moderate π-acceptor) generates the complex $[Ru(MeCN)_2(qmtpm)(PPh_3)]ClO_4$ which features an absorption maximum at 495 nm and a higher energy band at 370 nm (Figure 4.II.11). TDDFT calculations for $[Ru(MeCN)_2(qmtpm)(PPh_3)]ClO_4$ predict the nature of the low energy band to be a HOMO-1→LUMO transition (~ 470 nm), while the HOMO-5→LUMO and HOMO-9→LUMO transitions give rise to the observed band at 370 nm. As depicted in the MO diagram in Figure 4.II.6, HOMO-1 is largely comprised of Ru, MeCN and PPh_3 π–orbitals with some and quinoline π–character. Contributions to the LUMO arise mainly from the π orbitals of the

quinoline, imine and thiophenyl groups making up the ligand frame. Low energy electronic transitions originating from HOMO-1 into the LUMO therefore appears to be of a mixed metal-to-ligand and intraligand charge transfer nature resulting in the deep red color of $[Ru(MeCN)_2(qmtpm)(PPh_3)]ClO_4$. The inclusion of two MeCN groups in $[Ru(MeCN)_2(qmtpm)(PPh_3)]ClO_4$ leads to a lowering of both the HOMO and LUMO levels (Figure 4.II.6) resulting in a slight blue shift of the low energy band (490 nm) compared to that of its precursor, $[Ru(Cl)(MeCN)(qmtpm)(PPh_3)]BF_4$ (535 nm).

The dicarbonyl complex $[Ru(Cl)(CO)_2(qmtpm)]ClO_4$ exhibits CO photorelease with UV light energies or higher as detailed in the second section of Chapter 3. We employed TDDFT to gain insight on the nature of the MOs involved in metal-CO bond homolysis and to explain the need for higher energy radiation to induce CO release from this photoCORM. The molecular orbitals involved in the transitions of $[Ru(Cl)(CO)_2(qmtpm)]ClO_4$ are displayed in Figure 4.II.7 alongside molecular orbitals corresponding to the low energy absorption band of $[Ru(Cl)(CO)(qmtpm)(PPh_3)]BF_4$ for comparison. Figure 4.II.9 shows the predicted energy transitions falling under both experimental and calculated electronic absorption traces of $[Ru(Cl)(CO)_2(qmtpm)]ClO_4$.

TDDFT studies predict that for $[Ru(Cl)(CO)_2(qmtpm)]ClO_4$, transitions originating from both HOMO-2 and HOMO-3 into the LUMO gives rise to the experimental absorption maximum at ~380 nm (Figure 4.II.9) and that illumination

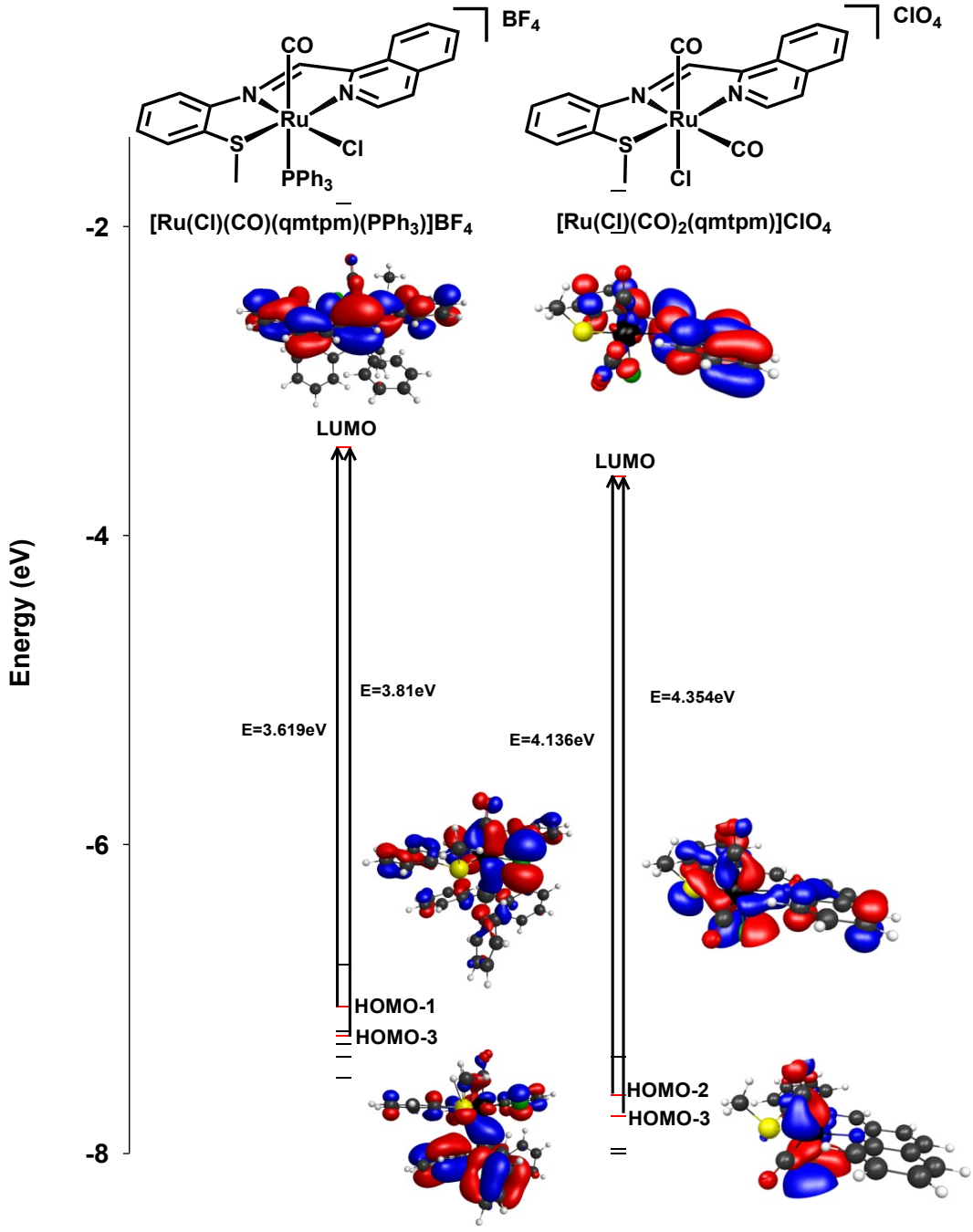

Figure 4.II.7. Calculated HOMO/LUMO energy diagram of $[Ru(Cl)(CO)(qmtpm)(PPh_3)]BF_4$ (left) and $[Ru(Cl)(CO)_2(qmtpm)]ClO_4$ (right). The most prominent MOs involved with under the low energy band and their diagrams are shown.

into this band gives rise to CO release. This HOMO-2/HOMO-3 transition into the antibonding orbitals of the ligand frame (LUMO) corresponds to a shift in electron density from the Ru(II) center to the qmtpm ligand frame, consistent with a metal to ligand charge transfer process. Scrutiny of the nature of HOMO-2 and HOMO-3 of $[Ru(Cl)(CO)_2(qmtpm)]ClO_4$ reveals a combined Ru-Cl and Ru-CO π-bonding character in these occupied orbitals, suggesting that backbonding interactions between the metal and the CO group is strengthened by the placement of a σ-donor trans to CO. It is these favorable interactions that must be overcome to promote a shift in electron density towards the π^* orbitals, hence the need for UV light energy in triggering CO photorelease from $[Ru(Cl)(CO)_2(qmtpm)]ClO_4$.

In the case of $[Ru(Cl)(CO)(qmtpm)(PPh_3)]BF_4$, the presence of a PPh_3 ligand (a strong π-acceptor) leads to a trans-labilizing effect that fosters rapid CO photorelease. Indeed, the nature of the HOMO-1 and HOMO-3 of $[Ru(Cl)(CO)(qmtpm)(PPh_3)]BF_4$ (Figure 4.II.2 and 4.II.7) exhibits some π(Ru-CO) and $\pi(PPh_3)$ character confirming the role of these two ligands CO labilization.

4.II.4 Conclusions

The primary objective of this study was to identify the electronic transitions that give rise to CO release from photoCORMs like $[Ru(Cl)(CO)(qmtpm)(PPh_3)]BF_4$ and $[Ru(Cl)(CO)_2(qmtpm)]ClO_4$ under illumination. Another major objective was to determine how the auxiliary ligands such as PPh_3, MeCN and Cl^- affect the MLCT transitions and facilitate Ru-CO bond scission. TDDFT results reveal that metal to

ligand charge transfer interactions facilitate CO photorelease. The predicted shift in electron density from the respective HOMOs of $Ru(Cl)(CO)(qmtpm)(PPh_3)]BF_4$ and $[Ru(Cl)(CO)_2(qmtpm)]ClO_4$ into the qmtpm ligand frame (LUMO) results in an electron deficient metal center that is not likely to bind CO. Such CO photorelease processes can be attenuated by the placement of trans-labilizing ligands. As evidenced in the case of $Ru(Cl)(CO)(qmtpm)(PPh_3)]BF_4$, a strong π-acceptor such as PPh_3 lessens the extent of π-backbonding interactions with the metal center, thereby making the resulting carbonyl complex susceptible to light-induced CO photorelease. The inclusion of a σ-donor such as Cl^- trans to a CO group on the other hand, strengthens such π-backbonding interactions that can only be overcome with the use of high energy radiation. The computational results provided in this section confirms our initial hypothesis that tuning of MLCT transitions involved in CO photodissociation can be achieved with the incorporation of designed ligand frames and strategic placement of auxiliary ligands.

4.II.5. Computational Methods

All computations were executed using PC Gamess program. The X-ray coordinates of $[Ru(Cl)(CO)(qmtpm)(PPh_3)]BF_4$, $[Ru(Cl)(CO)_2(qmtpm)]ClO_4$, and $[Ru(MeCN)_2(qmtpm)(PPh_3)]ClO_4$ were utilized as starting points for full geometry optimizations with the hybrid functional PBE0. Although the solid state structure of $[Ru(Cl)(MeCN)(qmtpm)(PPh_3)]ClO_4$ has not been characterized, geometry optimizations for this complex were built in analogy based on the structure of

$[Ru(MeCN)_2(qmtpm)(PPh_3)]ClO_4$ and the known Ru-Cl bond distances. DFT calculations were carried out using the double-ζ basis set 6-311G* basis set for all atoms with the exception of Ru, which utilized the quasi-relativistic Stuttgart−Dresden effective core potential (ECP). For TDDFT calculations, solvent (EtOH) effects were accounted for using the Polarized Continuum Model (PCM). Electronic transition energies and oscillator strengths above 0.0139 for $[Ru(Cl)(CO)(qmtpm)(PPh_3)]BF_4$, $[Ru(Cl)(CO)_2(qmtpm)]ClO_4$, $[Ru(Cl)(MeCN)(qmtpm)(PPh_3)]ClO_4$ and $[Ru(MeCN)_2(qmtpm)(PPh_3)]ClO_4$ were collected. MacMolPlt was used to view and calculate the fractional contributions of various groups to each molecular orbital.

4.II.6. Experimental Data: TDDFT Calculated and Experimental Electronic Absorption Spectra

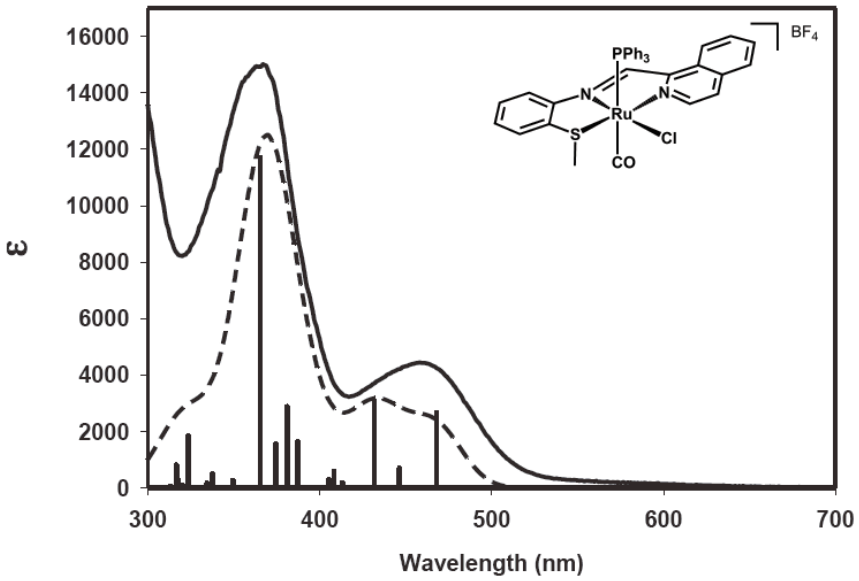

Figure 4.II.8. TDDFT calculated (dashed line) and experimental (solid line) electronic absorption spectrum of $[Ru(Cl)(CO)(qmtpm)(PPh_3)]BF_4$. Calculated energy transitions and oscillator strengths are shown as vertical lines.

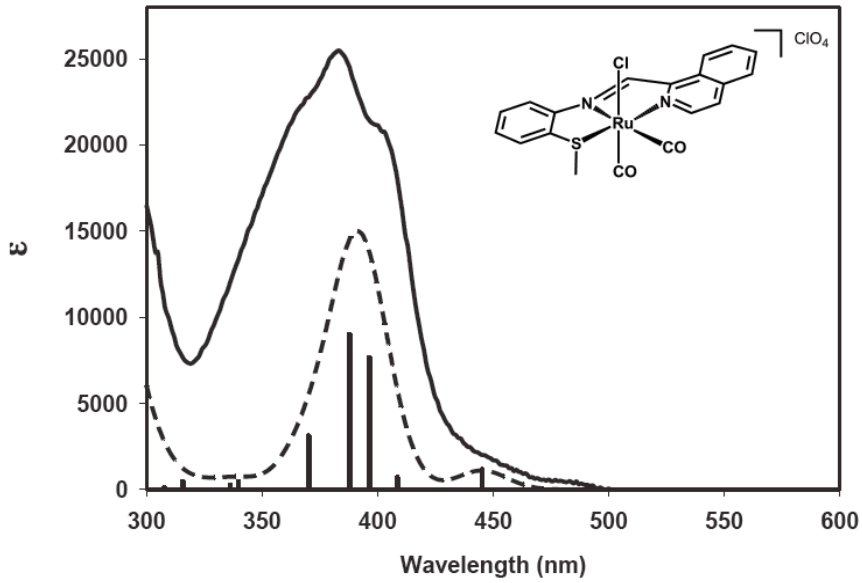

Figure 4.II.9. TDDFT calculated (dashed line) and experimental (solid line) electronic absorption spectrum of $[Ru(Cl)(CO)_2(qmtpm)]ClO_4$. Calculated energy transitions and oscillator strengths are shown as vertical lines.

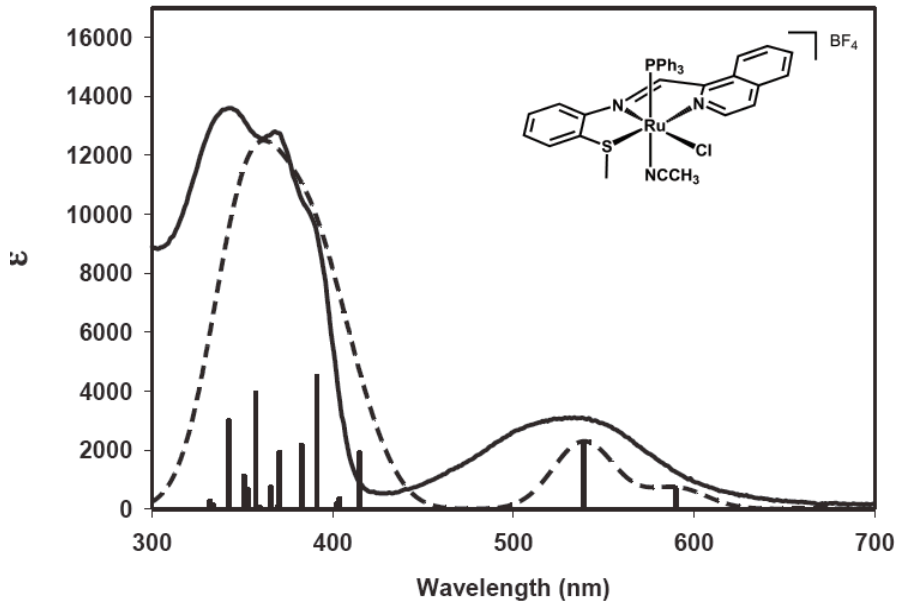

Figure 4.II.10. TDDFT calculated (dashed line) and experimental (solid line) electronic absorption spectrum of $[Ru(Cl)(MeCN)(qmtpm)(PPh_3)]ClO_4$. Calculated energy transitions and oscillator strengths are shown as vertical lines.

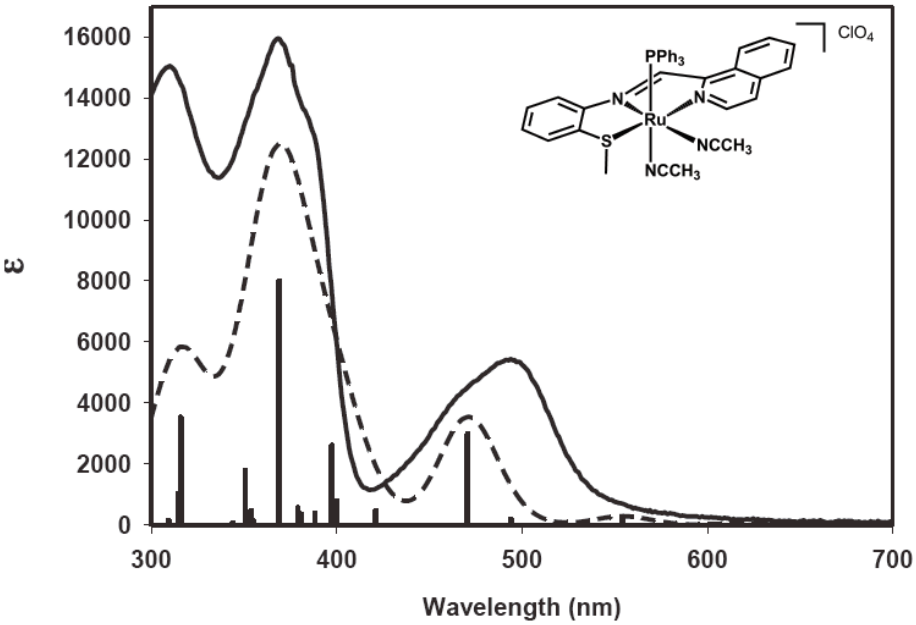

Figure 4.II.11. TDDFT calculated (dashed line) and experimental (solid line) electronic absorption spectrum of $[Ru(MeCN)_2(qmtpm)(PPh_3)]ClO_4$. Calculated energy transitions and oscillator strengths are shown as vertical lines.

4.II.7. References

(1) (a) Bauer, I.; Pannen, B. H. J., *Crit. Care*, **2009**, *13*, 220. (b) Kim, H. P.; Ryter, S. W.; Choi, A. M. K., *Annu. Rev. Pharmacol. Toxicol.*, **2006**, *46*, 411-449.

(2) (a) Eroy-Reveles, A. A.; Mascharak, P. K. *Future Med. Chem*. **2009**, *1(8),* 1497-1507. (b) Rose, M. J.; Mascharak, P. K. *Coord. Chem. Rev.* **2008**, *252*, 2093-2114. (c) Rose, M. J.; Mascharak, P. K. *Curr. Opin. Chem. Biol*. **2008**, *12*, 238-244.

(3) Vlček Jr., A., *Coord. Chem. Rev.*, **1998**, *177*, 219-256.

(4) (a) Villaume, S.; Strich, A.; Daniel, C.; Perera, S. A.; Bartlett, R. J., *Phys. Chem. Chem. Phys.*, **2007**, *9*, 6115-6122. (b) Ben Amor, N.; Villaume, S.; Maynau, D.; Daniel, C., *Chem. Phys. Lett.*, **2006**, *421*, 378-382.

(5) Gonzalez, M. A.; Carrington, S. J.; Fry, N. L.; Martinez, J. L.; Mascharak, P. K., *Inorg. Chem*., **2012**, *51*, 11930-11940.

Appendix A. Cell Protection Assay Utilizing $[Mn(pqa)(CO)_3]ClO_4$

A.1. Background

Much of the beneficial effects of carbon monoxide (CO) arise from its interaction with heme-dependent proteins involved in signaling pathways. By activation or inhibition of such proteins, CO is able to mediate a desired protective outcome. Low concentrations of CO for instance have been found to bind to cytochrome c oxidase, the terminal enzyme in the electron transport chain, leading to a surge of reactive oxygen species (ROS) that marks the onset of anti-inflammatory/immune response.[1] In these events of CO-mediated cytochrome c inhibition, a series of proteins constituting an adaptive response are upregulated. One such protein is the hypoxia-inducible factor (HIF1-α), a transcription factor responsible for the regulation of genes necessary in cell growth and angiogenesis.[2] CO in this case, by inactivation of cytochrome c oxidase, confers protection by stimulating anti-oxidant activity that includes HIF1-α expression.

When utilizing exogenous CO sources, the time of CO administration appears to be a critical factor in achieving the desired protective effect. Both preconditioning[3] and postconditioning[4] treatments employing CO gas have been found to attenuate damage and promote resilience against injury. To explore another potential application of our UV-active photoCORM: $[Mn(pqa)(CO)_3]ClO_4$, we developed a model of light-induced cell preconditioning to protect against subsequent oxidative damage. The compound $[Mn(pqa)(CO)_3]ClO_4$ has demonstrated efficient light-activated CO delivery in vasorelaxation studies due to its excellent stability and solubility in

biologically relevant media.[5] This section outlines the protocol on cell culture and treatment with various levels of photoCORM and the cytotoxic agent H_2O_2. Experimental details are provided herein to serve as a guide for future *in-vitro* studies on CO-mediated protection.

A.2. Findings

Human kidney embryonic cells (HEK-293T) were selected due to their ease of culture and proliferation. HEK-293T cells were plated on 96-well plates and allowed to reach a subconfluent state prior to treatments. We first identified a range of H_2O_2 concentrations that induce a noticeable, but not drastic reduction in cell viablility of HEK-293T cells. Figure A.1 shows that 200 μM and 500 μM H_2O_2 incubation for 4 hours results in ~ 10% and 50% decrease in cell viability, respectively. With the addition of 2000 μM H_2O_2 however, up to 85% cell death was noted.

The biocompatibility of our CO-donor, $[Mn(pqa)(CO)_3]ClO_4$ was initially assessed by incubation for 20 hours (Figure A.2) in the absence of light. This experiment, although not performed in triplicate, reflects the minimal damage effected by $[Mn(pqa)(CO)_3]ClO_4$ on HEK-293T cells. Specifically, the cells underwent up to a 15% reduction in viability when treated with concentrations of $[Mn(pqa)(CO)_3]ClO_4$ not exceeding 100 μM in a 20 hour period. With these results in hand, we determined a working range of 25-50 μM when performing pre-conditioning steps prior to an onslaught of H_2O_2-induced oxidative damage.

Preconditioning pertains to an injury-induced protection from a subsequent, more severe injury. We hypothesized that the light-induced administration of CO, through the application of $[Mn(pqa)(CO)_3]ClO_4$, can stimulate an anti-oxidant response from HEK-293T cells before a bolus addition of H_2O_2 thus rendering these cells more resilient against oxidative damage. In Figures A.3 and A.4, we show the response of preconditioned HEK-293T cells following an addition of 200 μM and 500 μM H_2O_2, respectively. In Figure A.4, it is clearly shown that upon bolus addition of 500 μM H_2O_2, cells preconditioned with 50 μM $[Mn(pqa)(CO)_3]ClO_4$ are ~22% more viable than their untreated counterparts. Similarly, HEK-293T cells preconditioned with 25 μM $[Mn(pqa)(CO)_3]ClO_4$ appear to resist damage by ~14% (Figure A.4). The effects of CO-preconditioning however are not as apparent when a bolus concentration of 200 μM H_2O_2 is applied. In Figure A.3, we can see that there is little difference between the untreated (control) and 50 μM pretreated HEK-293T cells.

A.3. Experimental Section

A.3.1. Materials

Plastic tissue culture plates (96 well, clear flat bottom Polystyrene TC-treated) were from Corning Incorporated. Fetal bovine serum (Thermo Scientific Hyclone) was obtained from Fisher Scientific. Dulbecco's Modified Eagle Medium (DMEM), Dulbecco's Phosphate Buffered Saline (PBS, Ca^{2+} and Mg^{2+} free), and 3-(4,5 dimethylthiazol-2-yl)-2,5-diphenyltetrazolium bromide (MTT) were purchased from Gibco, Invitrogen.

A.3.2. Cell Culture and Treatment

HEK-293T cells were obtained from the UCSC Chemical Screening Center facility and grown in DMEM supplemented with 10% fetal bovine serum without antibiotics and antifungal agents. All of the cells were maintained at 37°C in a humidified atmosphere of 5% CO_2. The cells in each culture flask were allowed to reach 80-90% confluence and passaged without trypsinization by rinsing with phosphate buffered saline (PBS) pH 7.4. The cells were seeded on 96 well plates at a density of 5 x 10^4 cells/ml (200 μL volume per well) and grown for 18-24 h to reach a subconfluent state prior to addition of $[Mn(pqa)(CO)_3]ClO_4$.

A stock solution of $[Mn(pqa)(CO)_3]ClO_4$ in DMSO was freshly prepared and diluted to different concentrations ranging from 25 μM to 200 μM with DMEM. The effective concentration of DMSO did not exceed 1% with each dilution to prevent solvent-related toxicities. After photoCORM addition, the cells were exposed to light from an LED worklamp for 15 min followed by 15 min of incubation in a humidified atmosphere. This irradiation-incubation cycle was repeated until a total irradiation period of 45 min was reached. Then, the media containing the photoproduct and possibly some unreacted $[Mn(pqa)(CO)_3]ClO_4$ was aspirated and replaced with fresh DMEM containing 200, 500 and 2000 μM of H_2O_2. After 6 h incubation with H_2O_2, the media was again aspirated and cell viability was assessed using the 3-(4,5-dimethylthiazol-2-yl)-2,5-diphenyltetrazolium bromide (MTT) assay described in the following section.

A.3.3 Cell Viability

The cell viability was measured by the 3-(4,5-dimethylthiazol-2-yl)-2,5-diphenyltetrazolium bromide (MTT) assay, modified from the procedure by Dinischiotu and co-workers.[6] Briefly, after the sequential preconditioning and H_2O_2 addition steps, the medium from each well was removed by aspiration and washed with 200 μL phosphate buffer saline (PBS). Fresh DMEM (150 μl) was added to each well, followed by 50 μl of MTT (5 mg/ml) in PBS. The cells were incubated for 2 h at 37°C to allow for metabolism of formazan dye by viable cells. The media containing unreacted MTT solution was then removed by aspiration and 50 uL of DMSO was added and the plate shaken to dissolve the formazan crystals. The optical density at 595 nm was taken using a plate reader (VersaMax ELISA Microplate Reader, Molecular Devices, LLC.) Absorbance corresponding to the control (untreated) cells was referenced as 100% cell viability.

A.4. Experimental Data: Cell Viability Measurements

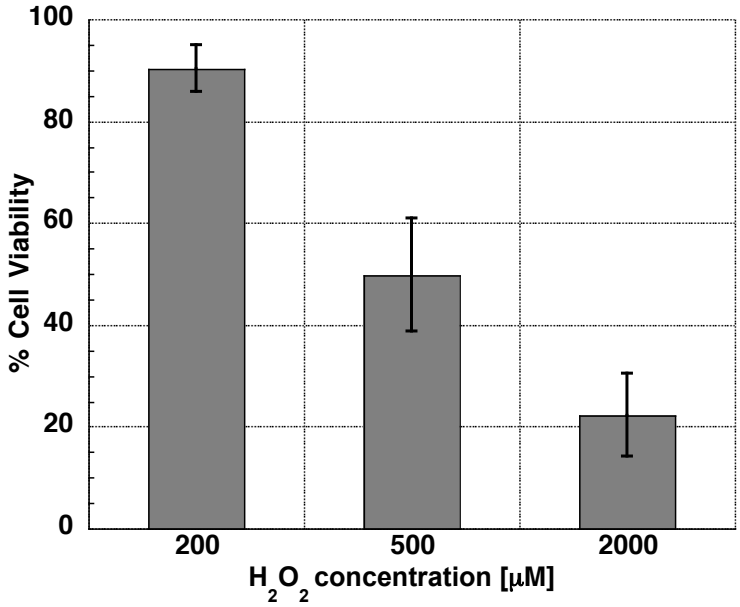

Figure A.1. Cell viability of HEK-293T cells after a 4 h exposure to H_2O_2 at 37°C in a humidified atmosphere of 5% CO_2.

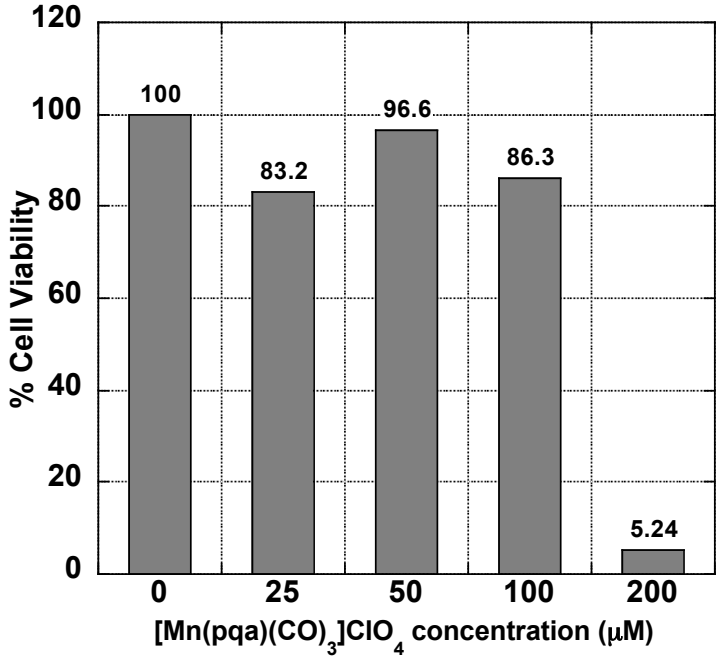

Figure A.2. Effects of $[Mn(pqa)(CO)_3]ClO_4$ incubation on HEK-293T cells in the absence of light.

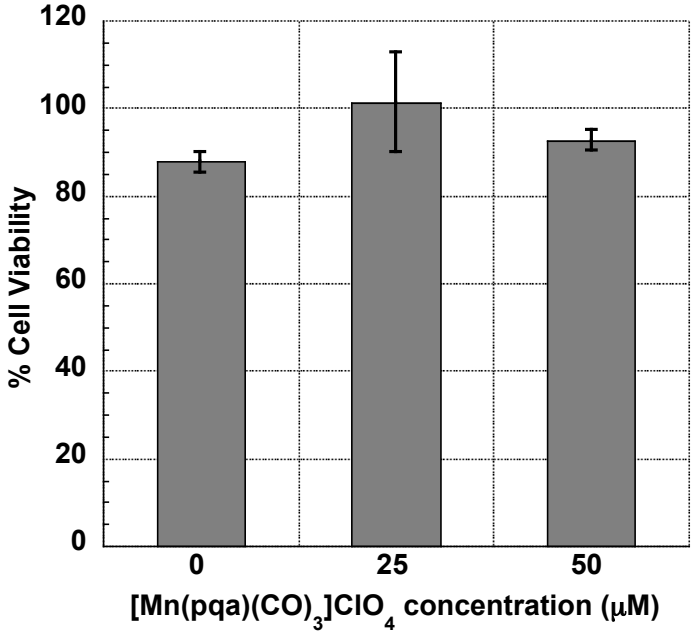

Figure A.3. Cell viability of $[Mn(pqa)(CO)_3]ClO_4$- preconditioned HEK-293T cells after addition of 200 μM H_2O_2.

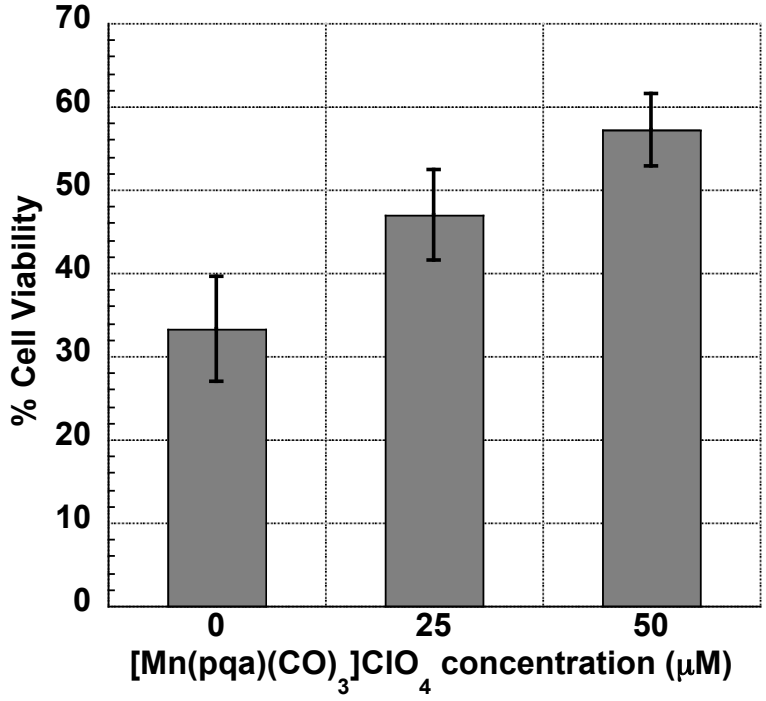

Figure A.4. Cell viability of $[Mn(pqa)(CO)_3]ClO_4$- preconditioned HEK-293T cells after addition of 500 μM H_2O_2.

A.5. References

(1) Zuckerbraun, B. S.; Chin, B. Y.; Bilban, M.; de Costa d'Avila, J.; Rao, J.; Billiar, T. R.; Otterbein, L. E., *FASEB J.*, **2007**, *21*, 1099-1106.

(2) (a) Chin, B. Y.; Jiang, G.; Wegiel, B.; Wang, H. J.; MacDonald, T.; Zhang, X. C.; Gallo, D.; Cszimadia, E.; Bach, F. H.; Lee, P. J.; Otterbein, L. E., *Proc. Natl. Acad. Sci*, **2007**, *104*, 5109-5114. (b) Chandel, N. S.; Maltepe, E.; Goldwasser, E.; Mathieu, C. E.; Simon, M. C.; Schumacker, P. T., *Proc. Natl. Acad. Sci.*, **1998**, *95*, 11715-11720.

(3) Vieira, H. L. A.; Queiroga, C. S. F.; Alves, P. M., *J. Neurochem.*, **2008**, *107*, 375-384.

(4) Schallner, N.; Fuchs, M.; Schwer, C. I.; Loop, T.; Buerkle, H.; Lagrèze, W. A.; van Oterendorp, C.; Biermann, J.; Goebel, U., *PLoS One*, **2012**, *7(9)*, e46479.

(5) Gonzalez, M. A.; Yim, M. Y.; Cheng, S.; Moyes, A.; Hobbs, A. J.; Mascharak, P. K., *Inorg. Chem.*, **2012**, *51*, 601-608.

(6) Dinu, D.; Bodea, G. O.; Ceapa, C. D.; Munteanu, M. C.; Roming, F. I.; Serban, A. I.; Hermenean, A.; Costache, M.; Zarnescu, O.; Dinischiotu, A., *Toxicon*, **2011**, *57*, 1023-1032.

Appendix B. PhotoCORM Entrapment within an Aluminosilicate Mesoporous Material

B.1. Background

The use of mesoporous silica nanoparticles (MSN) has been of interest in recent years as carrier materials for drug and nucleic acid delivery systems.[1] The favorable structural features of MSN that include (1) increased total surface area, (2) tunable pore diameter, (3) and monodisperse particle dispersion, make this class of materials ideal vehicles in the delivery of both hydrophobic and hydrophilic therapeutics. In addition, the physical properties of MSNs are readily modified with the incorporation of various functional groups such as amino[2] or mercapto moieties.[3] Nanoparticle surface functionalization has also been achieved with the use of more complex organic compounds such as β-cyclodextrin rings[4] or phenanthridine-based intercalating agents.[5]

MCM-41 (Mobile Crystalline Material) is a mesoporous silicate material that was developed in 1992 by Mobil Research and Development Corporation. It falls under the category of silicate/aluminosilicate mesoporous molecular sieves, designated as M41S,[6] that exhibits a hexagonal arrangement of pores whose dimensions can be altered depending on the synthetic conditions employed. Pérez-Pariente and co-workers first explored the potential of MCM-41 as a reservoir for controlled drug delivery, using ibuprofen as the model drug to be administered.[7] MCM-41-type of drug delivery systems have since become prevalent due to their ease of modification and biocompatibility. The typical synthesis of MCM-41 requires a silicate source,

organic surfactant and a base catalyst. Micellar rods are formed from the surfactant, which then arranges in a hexagonal array. The silicate source assembles about this hexagonal template. Calcination removes the pre-arranged micellar rods, leaving a porous structure characteristic of MCM-41. It is within these pores that the selected therapeutic is stabilized by surrounding silicate groups until controlled release is commenced.

A fellow graduate student, Howard Han, prepared a series of aluminum-doped MCM-41 (Al-MCM-41) particles with an average particle size of 50 nm to serve as mesoporous supports in the encapsulation of the selected photoactive carbon monoxide releasing molecule (photoCORM), $[Mn(pqa)(CO)_3]ClO_4$.[8] The recent emergence of CO as a potent signaling and cytoprotective molecule spurred our efforts towards the preparation of a light-activated CO-donating material. We selected MCM-41 because of its low toxicity, while $[Mn(pqa)(CO)_3]ClO_4$ was chosen because of its efficient CO photorelease characteristics. We report in this section some physical properties (leaching, CO-release, etc.) of the resulting photoCORM-loaded MCM-41 material ({Mn-CO}@Al-MCM-41). In addition, we evaluate the biocompatibility of the {Mn-CO}@Al-MCM-41 by measuring the viability of HeLa (human cervical carcinoma) cells after incubation with various particle loadings of this CO-donating material.

B.2. Findings

The negatively charged aluminum sites in Al-MCM-41 proved to facilitate loading of the manganese carbonyl complex, $[Mn(pqa)(CO)_3]ClO_4$, through a combination of

an ion-exchange mechanism and passive diffusion. The cationic species, $[Mn(pqa)(CO)_3]^+$, through exchange with Na^+ ions are successfully bound within the mesoporous support as evidenced by the presence of carbonyl stretching frequencies (ν_{CO}) in the FTIR spectra of {Mn-CO}@Al-MCM-41 (Figure B.1). The binding strength of $[Mn(pqa)(CO)_3]^+$ was assessed by measuring the extent of

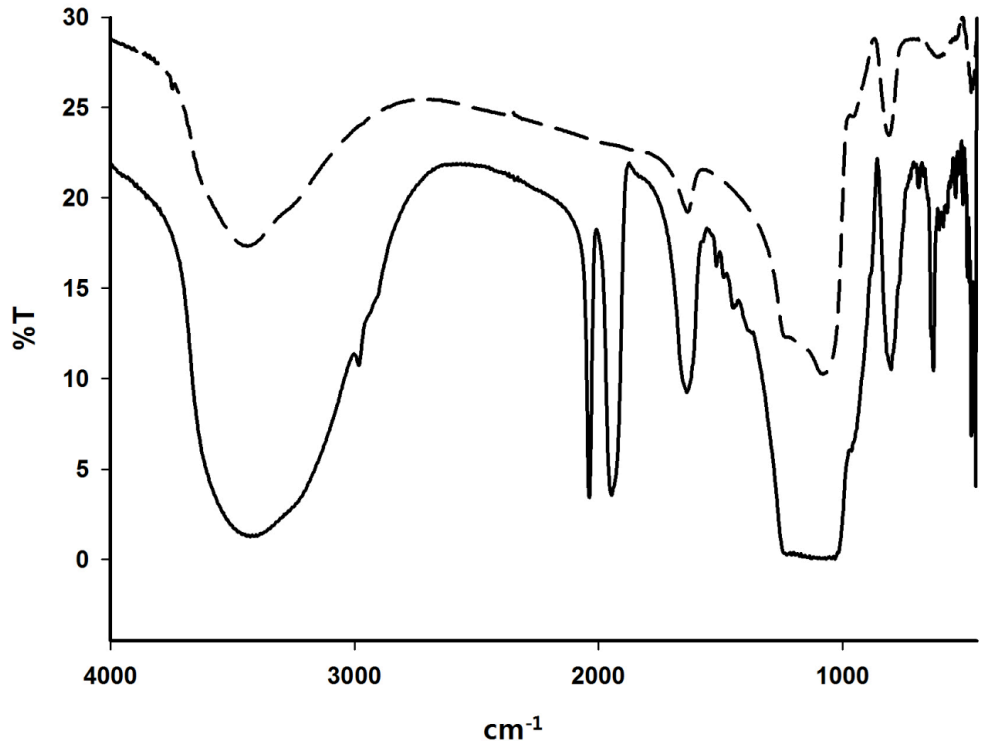

Figure B.1. FTIR spectra of Al-MCM-41 (black dashed) and loaded (black solid) {Mn-CO}@Al-MCM-41 in KBR Matrix.

leaching from the mesoporous support. The loaded materials were soaked in phosphate buffered saline (PBS, pH 7.4, 100 mM) for a total of 60 h with minimal agitation. As shown in Figure B.2, a total of ~12% $[Mn(pqa)(CO)_3]^+$ leached out of the matrix, confirming that the Al-MCM-41 is a suitable host in confining the

manganese carbonyl complex and preventing its degradation in aqueous media for an extended period of time.

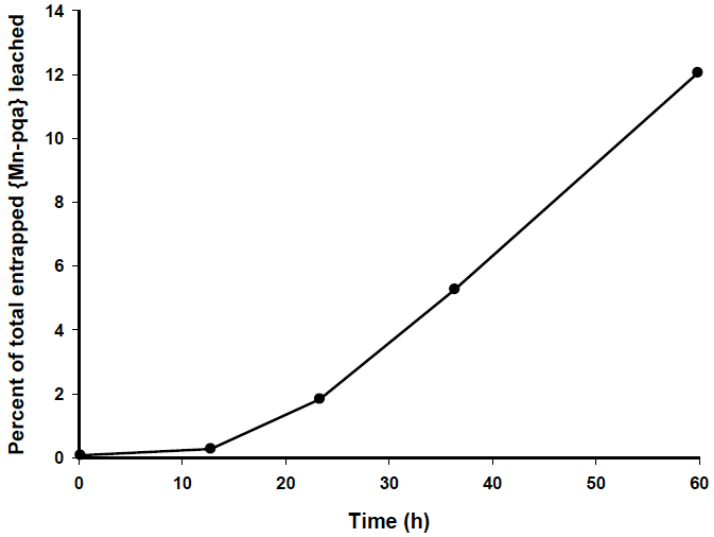

Figure B.2. Plot of leaching experiment showing the amount of $[Mn(pqa)(CO)_3]ClO_4$ loss from the Al-MCM-41 matrix.

The release of CO from {Mn-CO}@Al-MCM-41 was confirmed by means of myoglobin (Mb) assay employed as previously reported.[8] Briefly, {Mn-CO}@Al-MCM-41 was added to a solution of deoxymyoglobin (deoxy-Mb) in phosphate buffered saline (PBS, pH 7.4, 100 mM) and the particles were allowed to settle to the bottom of the cuvette. The suspension was then exposed to a broadband UV light source (λ >350 nm) at specified time intervals and the changes in the 520 nm- 600 nm region were monitored. A decrease in the absorbance at 540 nm, corresponding to that of deoxy-Mb was noted along with formation of new peaks the α (~542 nm) and β (578 nm) Q-bands. The spectrum shown in Figure B.3 is characteristic of carbonyl-

Mb formation from an exogenous CO source thus confirming the efficacy of {Mn-CO}@Al-MCM-41 as a light-activated CO-donating material.

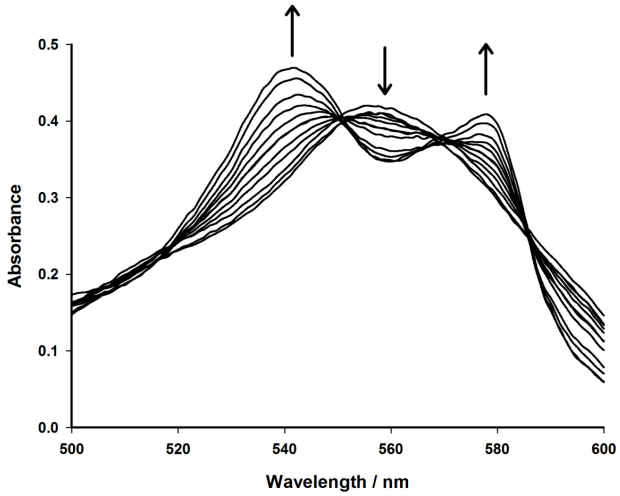

Figure B.3. Changes in Q-band region of horse heart myoglobin (Mb) (PBS, pH 7.4, 100 mM) upon addition of {Mn-CO}@Al-MCM-41 and subsequent irradiation (λ >350 nm).

With the goal of utilizing {Mn-CO}@Al-MCM-41 as a light-activated CO donor in physiologically relevant settings, we evaluated the biocompatibility of both {Mn-CO}@Al-MCM-41 and the mesoporous matrix, Al-MCM-41, by measuring the viability of HeLa cells (human cervical carcinoma). We found that incubation for longer periods of time (> 20 h) caused about 50% decrease in cell viability (not shown). Thus, we utilized a shorter time frame to minimize the inherent toxicity of these loaded nanoparticles. Figure B.4 shows that Al-MCM-41 particle loadings of up to 50 μg/ml cause a minimal dose-dependent reduction in viability. At 50 μg/ml for instance, 82-84% of the HeLa cells remained viable. Interestingly, a deviation in the expected viability was observed at 100 μg/ml (Figure B.4). One would expect that

higher particle loadings would decrease cell viability at this concentration. In the case of {Mn-CO}@Al-MCM-41, a similar dose-dependent decrease in viability was also observed (Figure B.5). The results shown in Figure B.5 closely resemble those noted within the group incubated with the unloaded particles. This suggests that Al-MCM-41 matrix effectively prevents leaching of the manganese carbonyl complex and that {Mn-CO}@Al-MCM-41 is a potential light-activated CO-donating material. Future work in this area entails studies exploring the protective (anti-apoptotic, anti-inflammatory) aspects of CO released from {Mn-CO}@Al-MCM-41.

B.3. Experimental Section

B.3.1. Materials

Tetraethyl orthosilicate was purchased from Acros Organics and sodium aluminate ($NaAlO_2$) from Strem Chemicals. Hexadecyltrimethylammonium bromide (C_{16}TMABr) was purchased from Aldrich Chemical. All chemicals were used without further purification. $[Mn(pqa)(CO)_3]ClO_4$ was synthesized from published procedure.[8]

B.3.2. Synthesis of spherical mesoporous supports (Al-MCM-41)

Mesoporous supports (Al-MCM-41) were synthesized using a procedure modified from that reported by Cai and co-workers.[9] Briefly, 3.5 mL of NaOH (2 M) solution was mixed with 480 mL of distilled water and 1.0 g of C_{16}TMABr was added to the solution at 80 °C with vigorous stirring for 15 minutes at 625 rpm. Then, 0.098 g of $NaAlO_2$ was added and 4.58 g of tetraethylorthosilicate (TEOS) was dropped in

slowly. The resulting slurry is expected to have a molar composition of 1.00 (TEOS) 0.13 (C_{16}TMABr) 1197.00 (H_2O) 0.31 (NaOH) 0.05 ($NaAlO_2$). The resulting product was filtered after 2 h, washed with distilled water, dried at 55 °C under vacuum. Calcination was performed in air at 823 K for 4 h with ramp rate of 1 °C/min.

B.3.3. Loading of $[Mn(pqa)(CO)_3]ClO_4$ to MSN ({Mn-CO}@Al-MCM-41)

A batch of 0.10 g of Al-MCM-41 was added to 5 mL of methylene chloride in a 50 mL Schlenk flask containing a magnetic stir bar. The mixture was degassed by freeze-pump-thaw method. A batch of $[Mn(pqa)(CO)_3]ClO_4$ (0.10 g) was added as a solid to the frozen Al-MCM-41 slurry under dinitrogen. The slurry was warmed to room temperature and stirred for 3 days with minimum light exposure. The loaded Al-MCM-41 was filtered using a fritted funnel. The light yellow product was washed with 3 x 3 mL of methylene chloride and dried in vacuo.

B.3.4 Physical Characterizations

Powder X-ray was XRD (Rigaku SmartLab diffractometer, CuKα radiation (λ = 1.5418 Å). The sample was scanned from 1.5° to 7° with a step size of 0.02° and a count time of 1 second at each point. Sample morphology and microstructure were examined by scanning electron microscopy, SEM (FEI Quanta 3D FEG dual beam SEM/FIB nanofabrication instrument, UCSC), and transmission electron microscopy, TEM (Philips CM200/FEG, National Center for Electron Microscopy). For SEM analysis, specimens were prepared by dispersing the as obtained powder in acetonitrile and was sonicated for ~20 minutes to completely disperse the particles. A

drop of the solution placed on a glass slide, followed by drying. The sample was sputtered with gold before SEM imaging. For TEM analysis, the specimens were dispersed in acetonitrile and drop coated on a copper grid. X-ray elemental maps were recorded (simultaneously) using a Hitachi HD-2000 dedicated stem equipped with an Oxford Inca EDS system. Infrared spectra of the materials (in KBr disks) were recorded on a Perkin-Elmer Spectrum-One FT-IR spectrometer.

B.3.5 Analysis of Manganese content of {Mn-CO}@Al-MCM-41

Analysis of Manganese content of the system was determined by inductively coupled plasma-optical emission spectroscopy, ICP-OES (PerkinElmer Optima 4300 DV ICO-OES). An acid digest procedure for ICO-OES was adapted from Heilman et *al.*[10] Batches of 35 mg of the loaded Al-MSN samples were added to the Teflon vessels of autoclave bombs, and to each was added 1 mL of a 1:3 mixture of concentrated HNO_3 and HCl. The samples were then frozen by dipping the vessels in liquid N_2. Once frozen, 0.125 mL of 40% aqueous HF was added, followed by immediately sealing the vessels and allowed to warm to room temperature. Vessels were placed in a 150 °C autoclave oven for 4 h, then allowed to cool to room temperature. Once it is safe to open the vessel, 12.5 mg of boric acid was added to each sample solution to complex free F^-. Finally the samples were diluted to 50 mL using Millipore water containing 1% HCO_3 and transferred to a polypropylene flask for analysis.

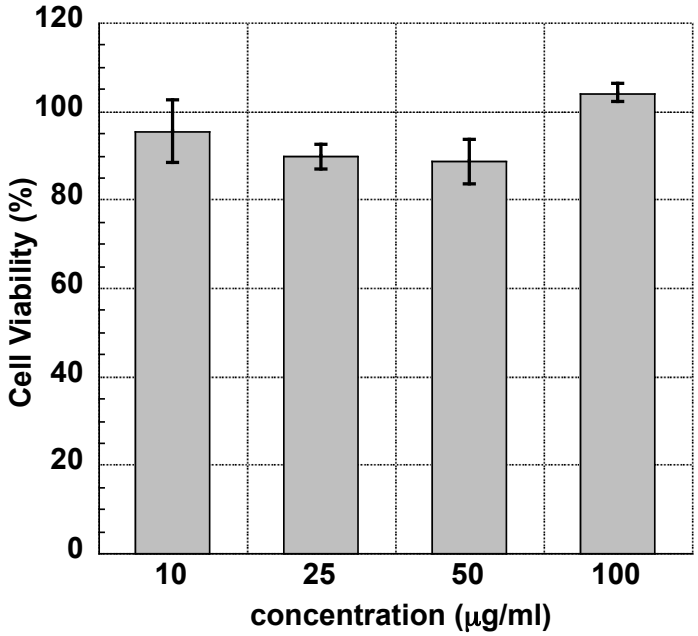

Figure B.4. Influence of different Al-MCM-41 concentrations on the HeLa cell viability after a 6 h incubation period.

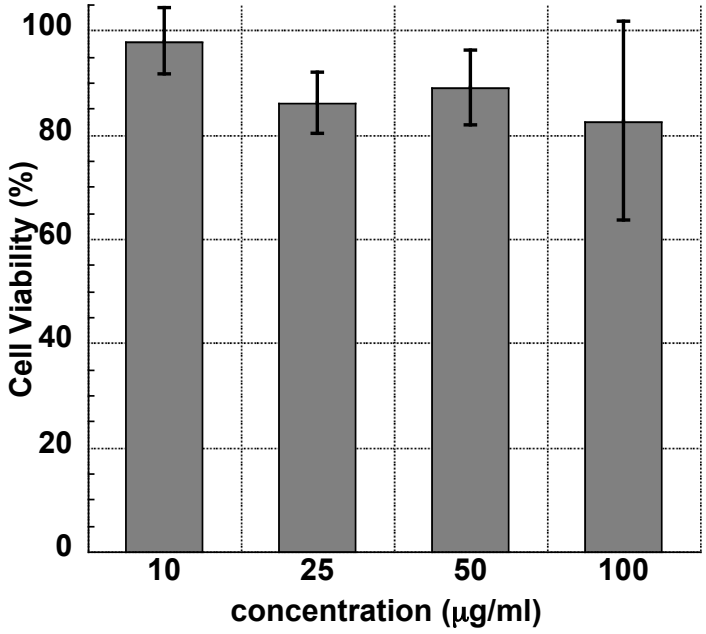

Figure B.5. Influence of different {Mn-CO}@Al-MCM-41 concentrations on the HeLa cell viability after a 6 h incubation period.

B.4. References

(1) (a) Li, L.; Guan, Y.; Liu, H.; Hao, N.; Liu, T.; Meng, X.; Fu, C.; Li, Y.; Qu, Q.; Zhang, Y.; Ji, S.; Chen, L.; Chen, D.; Tang, F., *ACS Nano*, **2011***, 5*, 7462-7470. (b) Slowing, I. I.; Vivero-Escoto, J. L.; Wu, C.-W.; Lin, V. S.-Y., *Adv. Drug Delivery Rev.,*, **2008**, *60*, 1278-1288.

(2) Cauda, V.; Schlossbauer, A.; Kecht, J.; Zürner, A.; Bein, T., *J. Am. Chem. Soc.*, **2009***, 131*, 11361-11370.

(3) Möller, K.; Kobler, J.; Bein, T., *J. Mater. Chem.*, **2007**, *17*, 624-631.

(4) Zhang, Q.; Liu, F.; Nguyen, K. T.; Ma, X.; Wang, X.; Xing, B.; Zhao, Y., *Adv. Funct. Mater.*, **2012**, *22*, 5144-5156.

(5) Vivero-Escoto, J. L.; Slowing, I. I.; Lin, V. S.-Y., *Biomaterials*, **2010**, *31*, 1325-1333.

(6) Beck, J. S.; Vartuli, J. C.; Roth, W. J.; Leonowicz, M. E.; Kresge, C. T.; Schmitt, K. D.; Chu, C. T.-W.; Olson, D. H.; Sheppard, E. W.; McCullen, S. B.; Higgins, J. B.; Schlenker, J. L., *J. Am. Chem. Soc.*, **1992**, *114*, 10834-10843.

(7) Vallet-Regi, M.; Rámila, A.; del Real, R. P.; Pérez-Pariente, J., *Chem. Mater.*, **2001**, *13*, 308-311.

(8) Gonzalez, M. A.; Yim, M. Y.; Cheng, S.; Moyes, A.; Hobbs, A. J.; Mascharak, P. K., *Inorg. Chem.*, **2012**, *51*, 601-608.

(9) Cai, Q.; Luo, Z.-S.; Pang, W.-Q.; Fan, Y.-W.; Chen, X.-H.; Cui, F.-Z., *Chem. Mater.*, **2001**, *13*, 258-263.

(10) Heilman, B. J.; St. John, J.; Oliver, S. R. J.; Mascharak, P. K., *J. Am. Chem. Soc.,*, **2012**, *134*, 11573-11582.